

Tarjei Heen
Kevin W. Kariuki

Investigative Study on Method for Approximating Nonlinear Material Behavior in Reinforced Concrete Structures Subjected to Seismic Ground Motions

Master's thesis in Civil and Environmental Engineering

Supervisor: Amir M. Kaynia

June 2019

Tarjei Heen
Kevin W. Kariuki

Investigative Study on Method for Approximating Nonlinear Material Behavior in Reinforced Concrete Structures Subjected to Seismic Ground Motions

Master's thesis in Civil and Environmental Engineering
Supervisor: Amir M. Kaynia
June 2019



Norwegian University of Science and Technology
Faculty of Engineering
Department of Structural Engineering

 **NTNU**
Norwegian University of
Science and Technology



MASTER THESIS 2019

| | | |
|---|-------------------------|--------------------------------------|
| SUBJECT AREA: Earthquake Engineering | DATE: June 11th 2019 | NO. OF PAGES: 105 + 51 (Appendix) |
|---|-------------------------|--------------------------------------|

| | |
|--|--|
| TITLE: Investigative Study on Method for Approximating Nonlinear Material Behavior in Reinforced Concrete Structures Subjected to Seismic Ground Motions Undersøkelse av metode for å tilnærme ikke-lineær materialoppførsel i betongkonstruksjoner utsatt for jordskjelvlaster | |
| BY: Tarjei Heen  | Kevin W. Kariuki  |

| |
|--|
| <p>SUMMARY:</p> <p>Nonlinear time history analyses are generally regarded as the most accurate way of predicting the dynamic response of a structure to a given seismic ground motion. Unfortunately, these types of analyses are computationally demanding and requires appropriate software. Therefore, the aim of this thesis is to investigate the feasibility and accuracy of an elastic analysis where material nonlinearities are accounted for iteratively through the use of secant stiffnesses, namely the Secant Method. The structure of focus is the South Pylon of the Chacao Bridge located in Chile. For comparative purposes, two models were created in the open-source framework OpenSees: a full nonlinear fiber model where nonlinear material behaviour is accounted for through distributed plasticity, and an elastic model where the element flexural stiffnesses are updated through the use of the Secant Method. For further verification, several pushover analyses were conducted on both models, with the inertial forces from the most unfavourable time-steps from the response histories providing the load distributions in the analyses.</p> <p>The results from seven averaged response history analyses show that the Secant Method is able to capture the maximum forces in the structure within an acceptable margin. The Secant Method is only able to emulate the stiffness reduction corresponding to maximum moments. The method is not able to capture regaining of stiffness once cracks are closed due to cyclic responses. Additionally, since the maximum moments for each element are picked independently of each other, the reductions obtained should be treated as a worst case scenario. With this in mind, the Secant Method is not recommended for studying the entire response history of the structure and should only be used when maximum responses are to be analyzed.</p> <p>The pushover analysis verified that the Secant Method was able to predict the response of the structure up until the steel reinforcement yields or crushing of the concrete. Nevertheless, the method was accurate for the loads representing the Most Probable Earthquake event and would be suitable for identifying possible plastic hinges, and to some degree assess the ductility of the structure.</p> <p>For design purposes, the concluding remarks of this confirm that the method is s a valid and code-compliant option to the full nonlinear analysis, according to the AASHTO Guide Specifications for LRFD Seismic Bridge Design and Eurocode 8.</p> |
|--|

| |
|--|
| RESPONSIBLE TEACHER: Prof. Amir M. Kaynia |
| SUPERVISOR(S) Prof. Amir M. Kaynia |
| CARRIED OUT AT: Department of Structural Engineering, NTNU |

Abstract

Nonlinear time history analyses are generally regarded as the most accurate way of predicting the dynamic response of a structure to a given seismic ground motion. Unfortunately, these types of analyses are computationally demanding and requires appropriate software. Therefore, the aim of this thesis is to investigate the feasibility and accuracy of an elastic analysis where material nonlinearities are accounted for iteratively through the use of secant stiffnesses, namely the Secant Method. The structure of focus is the South Pylon of the Chacao Bridge located in Chile. For comparative purposes, two models were created in the open-source framework OpenSees: a full nonlinear fiber model where nonlinear material behaviour is accounted for through distributed plasticity, and an elastic model where the element flexural stiffnesses are updated through the use of the Secant Method. For further verification, several pushover analyses were conducted on both models, with the inertial forces from the most unfavourable time-steps from the response histories providing the load distributions in the analyses.

The results from seven averaged response history analyses show that the Secant Method is able to capture the maximum forces in the structure within an acceptable margin. The Secant Method is only able to emulate the stiffness reduction corresponding to maximum moments. The method is not able to capture regaining of stiffness once cracks are closed due to cyclic responses. Additionally, since the maximum moments for each element are picked independently of each other, the reductions obtained should be treated as a worst case scenario. With this in mind, the Secant Method is not recommended for studying the entire response history of the structure and should only be used when maximum responses are to be analyzed.

The pushover analysis verified that the Secant Method was able to predict the response of the structure up until the steel reinforcement yields or crushing of the concrete. Nevertheless, the method was accurate for the loads representing the Most Probable Earthquake event and would be suitable for identifying possible plastic hinges, and to some degree assess the ductility of the structure.

For design purposes, the concluding remarks of this thesis show that the Secant Method is able to accurately predict maximum responses from time history analyses, pre-yielding behaviour and load distributions in static analyses. Hence, the method is a valid code-compliant option to a full nonlinear analysis, according to requirements from American Association of State Highway and Transportation Officials (AASHTO) Guide Specifications for LRFD Seismic Bridge Design and Eurocode 8.

Sammendrag

Ikke-lineære tidsplansanalyser blir generelt ansett som den mest nøyaktige metoden for å analysere responsen til konstruksjoner utsatt for seismiske laster. Dessverre er denne typen analyser svært krevende beregningsmessig, samt at det er nødvendig med passende spesialiserte verktøy. Målet med denne masteroppgaven er derfor å undersøke nøyaktigheten og brukbarheten av Sekantmetoden. Dette er en elastisk analyse, hvor de ikke-lineære effektene i konstruksjonens materiale blir tatt hensyn til gjennom bruken av sekantstivheter. Oppgavens fokus er rettet mot det søndre brutårnet på Chacao Bridge, en hengebru med beliggenhet i Chile. Til denne oppgaven ble det laget to modeller. Den første er en ikke-lineær fiber modell hvor ikke-lineæriteter i materialene er tatt hensyn til gjennom fordelt plastisitet. I tillegg ble det satt opp en elastisk modell, hvor bøyestivhetene til elementene ble oppdatert iterativt. Videre ble det utført ulike pushoveranalyser med hensikt av å danne et bredere sammenligningsgrunnlag.

Resultatene fra syv ulike tidsplansanalyser viste at Sekantmetoden er egnet til å beregne maksimum av bøyemomentene i konstruksjonen, innenfor en akseptabel feilmargin. Den endelige reduserte modellen representerer det verste tilfelle for samtlige elementer, og gir derfor en altfor myk konstruksjon sammenlignet med hva som i realiteten er tilfelle på et gitt tidspunkt under et jordskjelv. I tillegg evner ikke metoden å gjenskape lukking av riss i betongen grunnet osillerende svigninger. På grunnlag av dette egner metoden seg kun til å beregne maks momenter, og ikke hele respons historier.

Pushoveranalysene verifiserte Sekantmetodens egnethet til å beregne lastfordelingen i konstruksjonen fram til et lastnivå hvor knusing av betongen eller flyt i armeringen initieres. Metoden er likevel nøyaktig nok til å identifisere mulige flyteledd, og til en viss grad vurdere konstruksjonens duktilitet.

De konkluderende bemerkningene fra denne masteroppgaven viser at Sekantmetoden egner seg til analyser og prosjektering av konstruksjoner, da den evner seg å fange opp de største momentene som opptrer i konstruksjonen. I tillegg egner metoden seg til å beregne lastfordelingen i konstruksjonen før maks kapasitet nås i statiske analyser. På grunnlag av dette konkluderes det med at metoden gir et fullverdig alternativ til analyser ikke-lineær materialoppførsel. Dette er i samsvar med krav fra både Eurokode 8 og AASHTO Guide Specifications for LRFD Seismic Bridge Design.

Preface

This thesis is written as the finalization of the 5-year Master's Degree Program in Civil and Environmental Engineering at the Norwegian University of Science and Technology. Of the possible specializations, the authors have chosen Structural Engineering, with further specialization in Structural Dynamics. The interest in dynamics spring from a year abroad in California where Earthquake Engineering in particular is an important part of Structural Engineering. Coupled together with inspiring lectures from Professor Amir M. Kaynia, and the opportunity to work together with Aas-Jakobsen on the Chacao Bridge, the choice of writing a thesis on this subject was fairly simple.

We would like to extend our gratitude towards Aas-Jakobsen AS for granting us access to the finite element model and structural drawings for the Chacao Bridge. A special thanks to Lars Halvor Kaasa for his guidance in modelling and help choosing relevant topics of study, and for his willingness to contribute to the research in this thesis.

Finally, we would like to extend our thankfulness to our supervisor Professor Amir M. Kaynia for his involvement and guidance in our thesis work, as well as for his motivating meetings throughout the semester.

Trondheim, June 11th 2019



Tarjei Heen



Kevin W. Kariuki

Contents

| | |
|---|------------|
| Abstract | i |
| Sammendrag | iii |
| Preface | v |
| 1 Introduction | 1 |
| 1.1 Background | 1 |
| 1.2 Scope | 2 |
| 1.3 Structure of the thesis | 3 |
| 2 Theory | 5 |
| 2.1 Distributed Plasticity | 5 |
| 2.1.1 Displacement-Based Formulation | 6 |
| 2.1.2 Gaussian Quadrature | 7 |
| 2.1.3 Fiber Sections | 8 |
| 2.2 Nonlinear Material Models | 10 |
| 2.2.1 Concrete | 10 |
| 2.2.2 Structural Steel | 13 |
| 2.3 Nonlinear Geometry | 15 |
| 2.3.1 Corotational Formulation | 15 |
| 2.3.2 P-Delta | 17 |
| 2.4 Structural Damping | 18 |
| 3 Analyses in OpenSees | 19 |
| 3.1 Section Response Analysis | 19 |
| 3.2 Time History Analysis | 20 |
| 3.3 Secant Method | 21 |
| 3.4 Pushover Analysis | 24 |
| 4 Modelling in OpenSees | 27 |
| 4.1 Choice of Finite Element Software | 27 |
| 4.2 Modelling of the South Pylon | 27 |
| 4.2.1 Fiber Model | 29 |
| 4.2.2 Section Discretization | 33 |
| 4.2.3 Elastic Model | 34 |

| | | |
|----------|--|-----------|
| 4.2.4 | Mass and Gravity Loads | 35 |
| 4.3 | Synopsis of Mass and Stiffness | 35 |
| 4.3.1 | Boundary Conditions | 37 |
| 4.4 | Second Order Effects | 38 |
| 4.5 | Comparison of Modes | 39 |
| 4.6 | Structural Damping | 40 |
| 5 | Implementation of Analysis | 41 |
| 5.1 | Introduction | 41 |
| 5.2 | Time History Analysis | 42 |
| 5.2.1 | Input Ground Motion | 42 |
| 5.3 | Secant Method for Time History Analyses | 47 |
| 5.4 | Pushover Analysis | 51 |
| 5.4.1 | Longitudinal direction - L1 | 52 |
| 5.4.2 | Longitudinal direction - L2 | 53 |
| 5.4.3 | Transverse direction - T1 | 54 |
| 5.4.4 | Transverse direction - T2 | 55 |
| 5.4.5 | Transverse direction - T3 | 56 |
| 5.5 | Secant Method for Pushover Analysis | 57 |
| 6 | Results | 59 |
| 6.1 | Results from the Time History Analysis | 59 |
| 6.1.1 | Stiffness Ratios | 59 |
| 6.1.2 | Response History | 67 |
| 6.1.3 | Normalized Moment | 74 |
| 6.2 | Results from the Pushover Analysis | 76 |
| 6.2.1 | Longitudinal Analysis - L1 | 76 |
| 6.2.2 | Longitudinal Analysis - L2 | 78 |
| 6.2.3 | Transverse Analysis - T1 | 80 |
| 6.2.4 | Transverse Analysis - T2 | 82 |
| 6.2.5 | Transverse Analysis - T3 | 85 |
| 7 | Discussion | 89 |
| 7.1 | Discussion of the Secant Method | 89 |
| 7.2 | Discussion of Results From the THA | 91 |
| 7.3 | Discussion of Results From the Pushover Analysis | 95 |
| 7.4 | Further Work | 98 |
| 8 | Conclusion | 99 |

| | |
|------------------------------------|------------|
| Appendices | 105 |
| A Secant Procedure Results | A1 |
| B Mode shapes | B1 |
| C Cross sections | C1 |
| D Moment-Curvature Diagrams | D1 |
| E OpenSees Script | E1 |
| F MATLAB code | F1 |

Acronyms

| | |
|---|----|
| AASHTO American Association of State Highway and Transportation Officials..... | i |
| DB Displacement-Based..... | 6 |
| DOF Degree of Freedom..... | 19 |
| FE Finite Element..... | 18 |
| FEA Finite Element Analysis..... | 27 |
| FEM Finite Element Method..... | 6 |
| GMP Giuffré-Menegotto-Pinto..... | 13 |
| IP Integration Points..... | 7 |
| MDOF Multi Degree of Freedom..... | 20 |
| MPE Most Probable Earthquake..... | 25 |
| NTHA Nonlinear Time History Analysis..... | 2 |
| PEER Pacific Earthquake Engineering Research Center..... | 27 |
| RC Reinforced Concrete..... | 1 |
| SDOF Single Degree of Freedom..... | 24 |
| SSI Soil-Structure Interaction..... | 37 |
| THA Time History Analysis..... | 2 |

Chapter 1

Introduction

1.1 Background

In recent years, Aas-Jakobsen, a civil engineering consultancy based in Oslo, has been working on a suspension bridge that will connect the island of Chiloé to the Chilean mainland by crossing the Chacao channel. The suspension bridge, named Chacao Bridge, will at completion have a total length of approximately 2750 meters divided into two main spans of 1155 meters and 1055 meters, supported by three Reinforced Concrete (RC) pylons. Lying near the the subduction zone between the Nazca Plate and the South American Plate makes the Chacao Bridge building site one of the most seismically active regions on the planet [1]. The building site is shown in figure 1.1a, with an overview of the tectonic plate boundaries causing seismic activity in figure 1.1b.

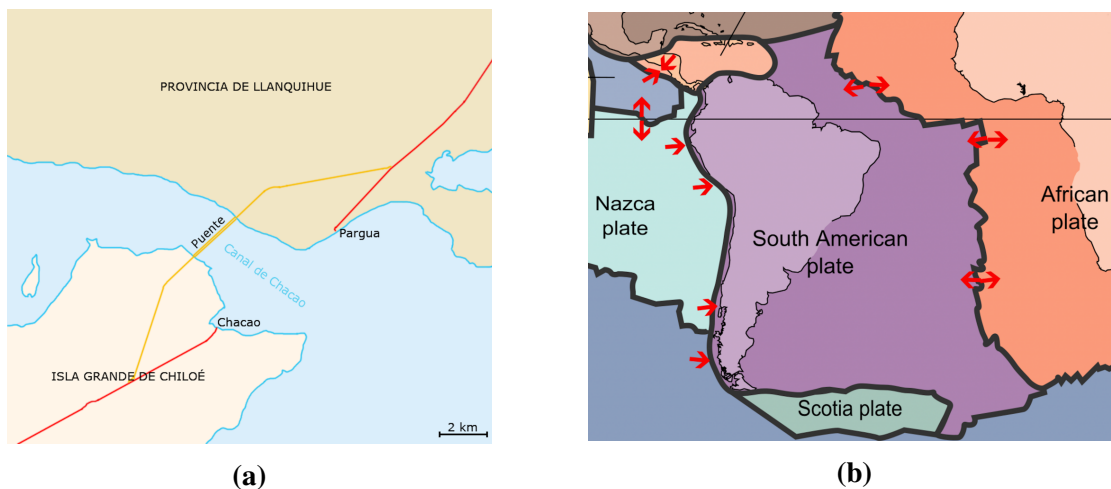


Figure 1.1: Chacao Bridge Building site [2]

Given the sites proximity to an area with high seismicity, both in frequency and magnitude, the design criteria for the structure have been strict and has forced the responsible engineers to be innovative in their work. One of the major issues surrounding the design process was whether or not to conduct a full nonlinear analysis of the structure. A full nonlinear analysis on a structure gives the most accurate information regarding the system's response to ground motion. However, for a structure of this size and complexity a full nonlinear analysis would take up to several days to complete, while an elastic analysis would complete in a fraction of the time. Thus, if possible it would be preferable to obtain the same results in a more efficient way. For



Figure 1.2: Chacao Bridge [4]

this reason, it was decided to conduct an elastic analysis of the bridge, while accounting for the cracked stiffness of the concrete sections through an iterative procedure based on the sections secant stiffnesses, which for this thesis will be named the Secant Method. This type of procedure is allowed in the design code used for the Chacao Bridge, namely the Guide Specifications for LRFD Seismic Bridge Design from the AASHTO, which states that:

The distribution of forces from an elastic analysis should be carefully reviewed to verify that the results are consistent with the expected nonlinear behavior of the earthquake resisting elements. [3]

Engineers at Aas-Jakobsen expressed interest in a further investigation into the procedure itself though a comparative study including a fully nonlinear model as baseline. Hence, this thesis will look into the accuracy of the Secant Method when compared to a full Nonlinear Time History Analysis (NTHA), as well conduct several pushover analyses for further verification. The Chacao Bridge is illustrated in figure 1.2, with the South Pylon in the foreground.

1.2 Scope

This thesis will focus on comparing a NTHA to a Time History Analysis (THA) run with elastic elements where the stiffness is updated iteratively to account for cracking of the concrete sections. To ensure that the various analyses are implemented correctly and constrict the area of focus, only the South Pylon will be analyzed. Two models are developed for this purpose. The first one is a fiber model with distributed plasticity, where each cross section consists of fibers modelled with nonlinear material models. The second one is an elastic model where an iterative procedure is developed to reduce the flexural stiffness of each element based on the maximum responses from the previous iteration. In addition, multiple pushover analyses will be carried

out on both models to attain further basis of comparison between models as well as to act as verification for the results from the THA. Both models are developed in the open source academic tool OpenSees [5]. The modelling of the South Pylon is carried out on the basis of a RM Bridge [6] model previously established by Aas-Jakobsen together with construction drawings from the bridge. Furthermore, several MATLAB scripts [7] are developed for iteration calculations, as well as for pre- and post-processing.

1.3 Structure of the thesis

The following list provides a description of the contents of each chapter:

- Chapter 2** lays out the fundamental theoretical background and descriptions of distributed plasticity, material models, time history analyses and the iterative procedure that this thesis will focus on.
 - Chapter 3** gives insight on how the South Pylon was modelled in OpenSees for both the fiber model and the elastic model.
 - Chapter 4** describes how the each of the analyses were implemented in OpenSees with focus on the iterative procedure for the Secant Method.
 - Chapter 5** provides the result from the time history and the pushover analyses, with plots comparing the response of the two models.
 - Chapter 6** presents a discussion of the results from both analyses, as well as a brief discussion of the methodology.
 - Chapter 7** concludes this thesis, and lays out the final thoughts on the Secant Method when compared to the full nonlinear model.
-

Chapter 2

Theory

2.1 Distributed Plasticity

The distributed plasticity element presented in this thesis is based on the Euler-Bernoulli beam theory. The theory behind the element will be presented for the three dimensional case, but is easily simplified for a two dimensional problem. These models assume a torsional response that is uncoupled from the axial and bending moment response. The element kinematics are described by the following displacement field

$$\mathbf{u}(x) = \begin{bmatrix} u(x) \\ v(x) \\ w(x) \end{bmatrix} \quad (2.1)$$

where $u(x)$, $v(x)$ and $w(x)$ are the axial and two transverse displacements in y and z-direction respectively. The section deformation vector \mathbf{e} is then given by

$$\mathbf{e}(x) = \begin{bmatrix} \varepsilon_a(x) \\ \kappa_y(x) \\ \kappa_z(x) \end{bmatrix} = \begin{bmatrix} \frac{\partial u}{\partial x} \\ \frac{\partial^2 v}{\partial x^2} \\ \frac{\partial^2 w}{\partial x^2} \end{bmatrix} \quad (2.2)$$

where κ denotes the curvature about the two axes and ε_a is the normal strain at the reference axis origin for an arbitrary element seen in figure 2.1.

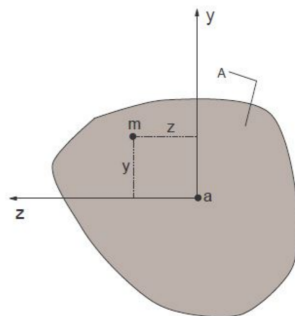


Figure 2.1: Strain at a point m in a section with bi-axial bending and axial load [8]

With the assumption from Bernoulli theory that plane sections remain plane after deformation, the strain at each point m on an arbitrary cross section can be found by

$$\varepsilon(x, y, z)_m = \varepsilon_a(x) + z\kappa_y(x) - y\kappa_z(x) = \begin{bmatrix} 1 & z & -y \end{bmatrix} \begin{bmatrix} \varepsilon_a(x) \\ \kappa_y(x) \\ \kappa_z(x) \end{bmatrix} \quad (2.3)$$

which by making use of the section kinematic vector \mathbf{a}_s can be expressed as

$$\varepsilon(x, y, z)_m = \mathbf{a}_s(y, z)\mathbf{e}(x) \quad (2.4)$$

Equation (2.4) above decomposes the general strain field of the frame element ε_m into functions over the cross section and along the x-axis of the element itself [8]. The section forces, also known as generalized stresses, are represented by the section force vector

$$\mathbf{s}(x) = \begin{bmatrix} N(x) \\ M_y(x) \\ M_z(x) \end{bmatrix} \quad (2.5)$$

where N is the axial force and M is the bending moment about the y and z-axis.

2.1.1 Displacement-Based Formulation

As with the classical Finite Element Method (FEM) beam formulations, the displacement fields for the Displacement-Based (DB) formulation are interpolated with linear Lagrangian polynomials for the axial deformation and cubic Hermite polynomials for the transverse deflection. With the chosen interpolation functions equation (2.1) can be expressed as

$$\mathbf{u}(x) \cong \mathbf{N}_U(x)\mathbf{U}^e, \quad (2.6)$$

where $\mathbf{N}_U(x)$ is the interpolation matrix and \mathbf{U}^e the vector contains element end displacements. The interpolation of the displacements along the element interior serves as an important source of approximation error for beams that are not prismatic and linear elastic [9]. By combining equations (2.2) and (2.6) we get the following relation between the element end displacements and the strain in a section

$$\mathbf{e}(x) = \mathbf{B}(x)\mathbf{U}^e \quad (2.7)$$

where \mathbf{B} is the strain-displacement transformation matrix, consisting of shape functions for section deformation. The section constitutive behaviour can be described by

$$\mathbf{s}(x) = \mathbf{k}_s(x)\mathbf{e}(x),$$

where $\mathbf{k}_s(x)$ is the section tangent stiffness matrix, taken as $\mathbf{k}_s(x) = \partial \mathbf{s} / \partial \mathbf{e}$ [8]. For homogeneous materials where the origin of the reference system coincides with the centroid of the section, \mathbf{k}_s becomes

$$\mathbf{s}(x) = \begin{bmatrix} EA(x) & 0 & 0 \\ 0 & EI_y(x) & 0 \\ 0 & 0 & EI_z(x) \end{bmatrix} \mathbf{e}(x) \quad (2.8)$$

where E is the tangent modulus of the σ - ε relation. In the nonlinear case, the incremental change in forces $\delta \mathbf{s}(x)$ is given by the product of the section tangent stiffness, $\mathbf{k}_s(x)$, and an incremental change in section strains $\delta \mathbf{e}(x)$ so that

$$\delta \mathbf{s}(x) = \mathbf{k}_s(x) \delta \mathbf{e}(x). \quad (2.9)$$

By making use of the principle of virtual displacement, the following equilibrium equations for the element force vector and stiffness matrix can be obtained

$$\mathbf{P}_e = \int_0^L \mathbf{B}^T(x) \mathbf{s}(x) dx \quad (2.10)$$

$$\mathbf{K}_e = \int_0^L \mathbf{B}^T(x) \mathbf{k}_s(x) \mathbf{B}(x) dx \quad (2.11)$$

where the section forces and stiffness matrix are integrated over the element length L .

2.1.2 Gaussian Quadrature

During structural analyses, equations (2.10) and (2.11) are solved with numerical integration, of which the most common is Gaussian quadrature. For distributed plasticity elements, two of the quadrature rules are the Gauss-Legendre and the Gauss-Lobatto rule. The first of the two is most commonly used for elastic FEM-formulations. The Gauss-Legendre rule is able to accurately integrate polynomials of order $2m - 1$, where m is the number of Gauss Integration Points (IP) along an element. [10]. The Gauss-Lobatto rule on the other hand has the advantage of always placing IPs at the element ends.[11] This makes it possible to capture exact forces and deformations at the element ends, where the forces and moments usually are the largest. This is especially useful for integration of inelastic elements. The downside of the Gauss-Lobatto is that the rule only integrates polynomials exactly up to order $2m - 3$. Table 2.1 and 2.2 summarize the IP locations and weights for $m = 3, 4, 5, 6$. Note that the location of the points are given in the isoparametric space with range $-1 \leq \xi \leq 1$.

Table 2.1: Gauss-Lobatto quadrature rule in isoparametric space

| Number of IP, m | IP location ξ_h | IP weight w_h |
|-------------------|---------------------|-----------------|
| 3 | 0.0 | 4/3 |
| | ± 1.0 | 1/3 |
| 4 | ± 0.447214 | 5/6 |
| | ± 1.0 | 1/6 |
| 5 | 0.0 | 32/45 |
| | ± 0.654654 | 49/90 |
| | ± 1.0 | 0.066667 |

Table 2.2: Gauss-Legendre quadrature rule in isoparametric space

| Number of IP, m | IP location ξ_h | IP weight w_h |
|-------------------|--------------------------|-----------------|
| 3 | 0.0 | 8/9 |
| | $\pm \sqrt{\frac{3}{5}}$ | 5/9 |
| 4 | ± 0.339981 | 0.652145 |
| | ± 0.861136 | 0.347855 |
| 5 | 0.0 | 128/225 |
| | ± 0.538469 | 0.478629 |
| | ± 0.906180 | 0.236927 |

2.1.3 Fiber Sections

Fiber sections is a way of discretizing cross sections to account for nonlinearities at any point of the element when using distributed plasticity. However, in practise, the element behaviour is only captured at the Gauss IPs, see figure 2.2. It can be shown that the section forces \mathbf{s} can be expressed as

$$\mathbf{s}(x) = \int_A \begin{bmatrix} 1 \\ z \\ -y \end{bmatrix} \sigma_m dA = \begin{bmatrix} N(x) \\ M_y(x) \\ M_z(x) \end{bmatrix} \quad (2.12)$$

where σ_m is the normal stress at point m . Further, by using equation (2.9) and the principal of virtual displacement, the following equation can be derived for the section state determination

$$\mathbf{k}_s(x) = \int_A \mathbf{a}_s(y, z)^T \frac{d\sigma}{d\varepsilon} \mathbf{a}_s(y, z) dA, \quad \frac{d\sigma}{d\varepsilon} = E_m \quad (2.13)$$

where the stress σ_m and the material tangent modulus E_m are determined by the material models. By discretizing the section into fibers the integrals above can instead be expressed as

$$\mathbf{s}_h = \sum_{fib=1}^{n_{fib}} (\mathbf{a}_{s,fib})^T (\sigma_{fib} A_{fib}) \quad (2.14)$$

and

$$\mathbf{k}_{s,h} = \sum_{fib=1}^{n_{fib}} (\mathbf{a}_{s,fib}(x))^T (E_{fib} A_{fib}) \mathbf{a}_{s,fib} = (E_{fib} A_{fib}) \begin{bmatrix} 1 & z_{fib} & -y_{fib} \\ z_{fib} & z_{fib}^2 & -z_{fib} y_{fib} \\ -y_{fib} & -z_{fib} y_{fib} & y_{fib}^2 \end{bmatrix} \quad (2.15)$$

for an arbitrary section h . As the equations above suggest, the section state is determined by looping over each discrete fiber in the section and calculating the section forces and tangent stiffness matrix, which in turn are used to calculate the element forces and stiffness by equations (2.10) and (2.11), respectively. The fiber variables σ_{fib} and $E_{T,fib}$ are found from the material models of each fiber. This allows the creation of composite sections consisting of different materials, such as RC sections. With this approach, no previous calibration of the moment-curvature hysteretic rule is required; therefore, there is no need for any semi-empirical decision [12].

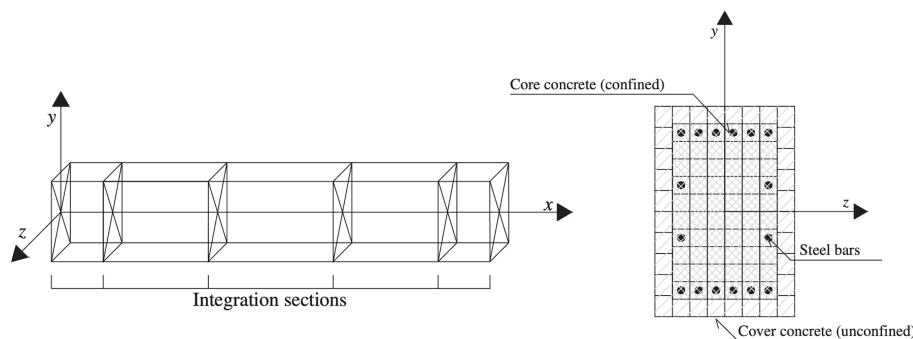
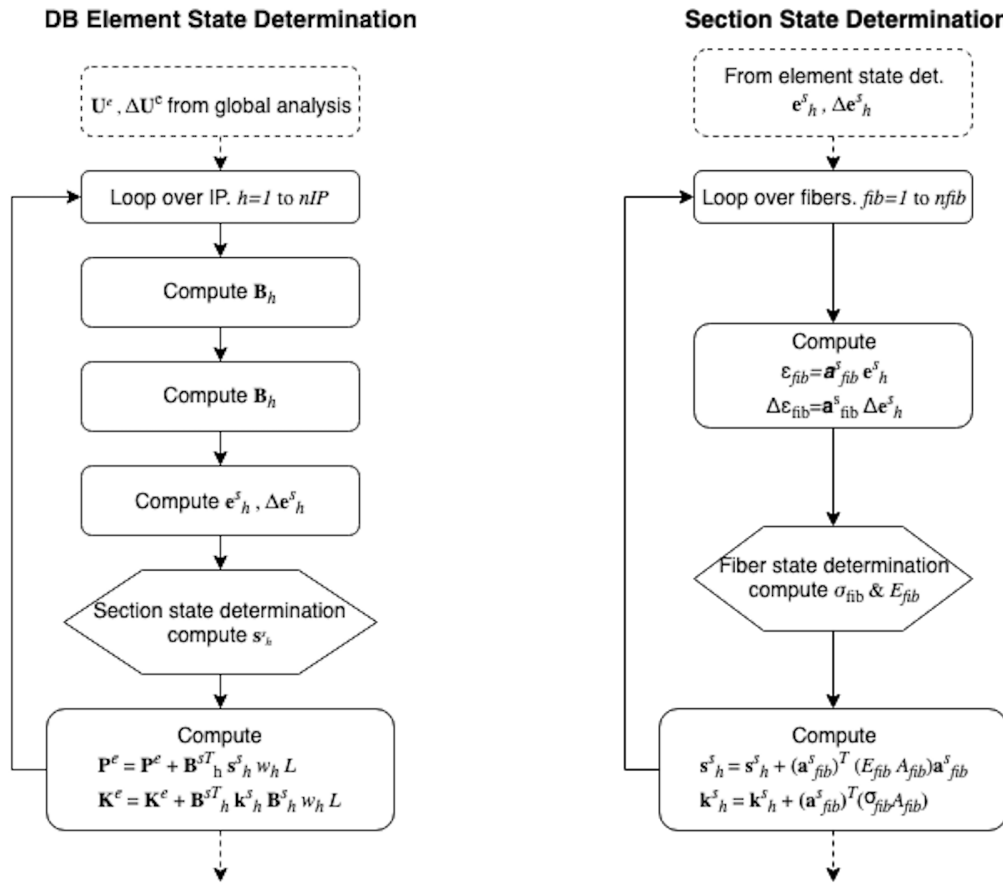


Figure 2.2: Example of controlling sections along the element and section fiber discretization [12]

Figures 2.3a and 2.3b summarize this theory by illustrating the element state and section state determination process. The fiber state determination is handled by the chosen material model in each fiber, which will be elaborated on in section 2.2



(a) Element state determination procedure

(b) Section state determination procedure

Figure 2.3

2.2 Nonlinear Material Models

2.2.1 Concrete

Concrete01

A widely used uniaxial concrete material model with both accuracy and simplicity is the Kent-Scott-Park concrete material object with degraded linear unloading/reloading stiffness, according to the work of Karsan and Jirsa, and no tensile strength [13, 14]. This material model, named *Concrete01* in OpenSees, requires minimal input to define the nonlinearity of the constitutive stress-strain law. The required input, as show in figure 2.4, are maximum stress f_{pc} , strain corresponding to maximum stress ε_{c0} , ultimate stress f_{pcu} and ultimate strain ε_{cu} . The initial

linear branch of the curve E_{cm} is defined as two times the maximum stress divided by the corresponding strain [15]. This allows some flexibility in modelling, since this makes it possible to use the elastic modulus as input, and defining the strain by the relation between stiffness and maximum stress. This property makes it possible to create a full nonlinear fiber model with the same exact initial stiffness as a linear elastic model. It should be noted that stresses and strains in compression are negative in figure 2.4.

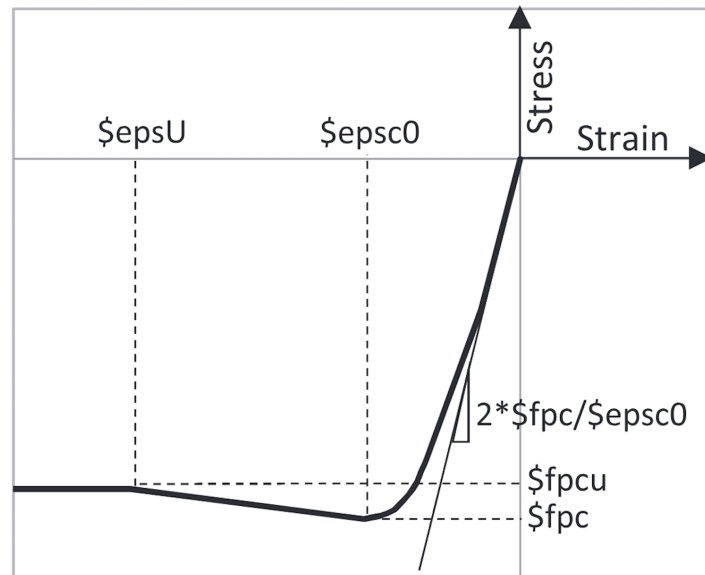


Figure 2.4: Concrete01 material model in OpenSees [15]

Concrete02

Another material model that is integrated in OpenSees is the *Concrete02* model. Similar to the previously mentioned *Concrete01* model, *Concrete02* is also based on the Kent-Scott-Park concrete material object with degraded linear unloading/reloading stiffness. However, unlike *Concrete01*, *Concrete02* has a bilinear relationship to represent the stress-strain relationship in tension and has bilinear unloading and linear reloading [16] properties. The material parameters for *Concrete02* are shown in figure 2.5. Again, note the sign for compressive stresses and strains. The additional parameters are the ratio between the unloading slope and the initial stiffness λ , the tension stress limit f_t and the slope of the linear tension softening branch E_{ts} .

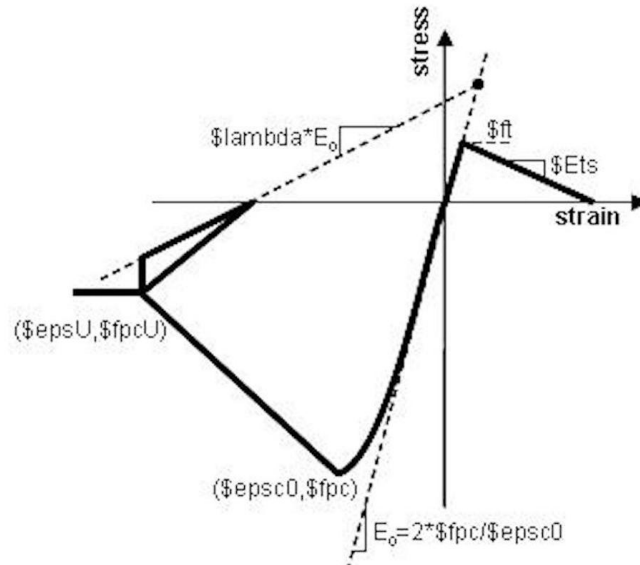


Figure 2.5: Concrete02 material model in OpenSees [5]

From figure 2.6 one can observe that the two models have exactly the same behaviour for monotonic compression forces. The differences occur during unloading and in tension, the latter not depicted in the figure. On a global scale, in the context of this thesis, the main difference among the two models is the initial stiffness contribution from the concrete fibers in tension. For elements without considerable axial forces, the loss of initial strength in tension should be considered when selecting the appropriate material model. This will be discussed in greater detail in chapter 4.

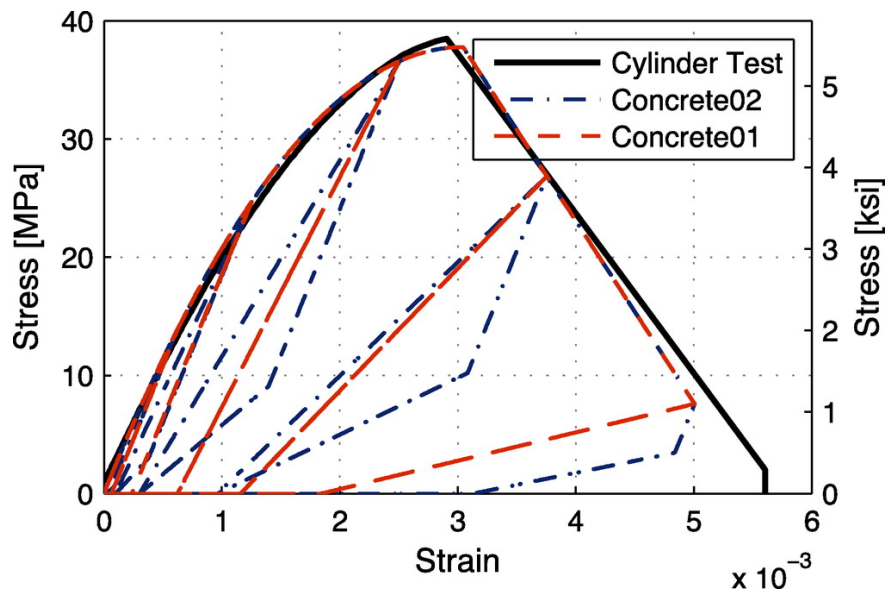


Figure 2.6: Comparison of Concrete01 and Concrete02 [17]

Concrete Confinement

The use of fiber section allows for the inclusion of additional strength of core concrete from transverse reinforcement as proposed by Mander, Priestley and Park [18]. Figure 2.7 shows the importance of considering this effect when analyzing concrete structures.

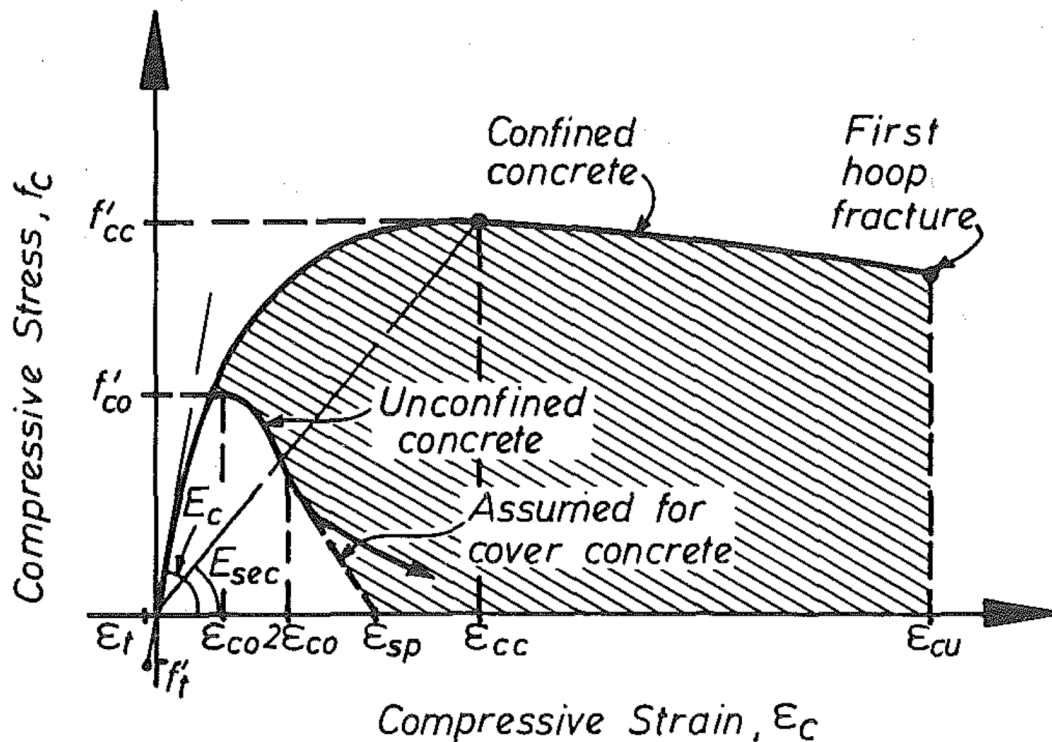


Figure 2.7: Stress-strain model proposed for monotonic loading of confined and unconfined concrete [18]

At low stress-levels, the transverse reinforcement is hardly stressed and the response thus behaves similar for both confined and unconfined concrete. At stresses close to the uniaxial stress limit of the concrete material, internal fracturing causes the concrete to dilate which in turn will induce confining action in the concrete [18]. By having a suitable distribution of stirrups, the strength as well as ductility of the concrete is significantly increased. This is an important aspect of concrete design for seismic action, and should be considered when there is a possibility of the concrete experiencing stresses close to the uniaxial strength limit as well as risks of brittle failure.

2.2.2 Structural Steel

Steel02

A uniaxial analytical material model for structural steel that offers numerical efficiency whilst agreeing well with experimental data from cyclic loading is the Giuffr -Menegotto-Pinto (GMP)

model [19], known as *Steel02* in OpenSees. By formulating the stress strain relationship explicitly with only a handful of parameters it offers a simple yet accurate way of describing the path dependent behaviour of steel. In its simplest form, assuming straight lines for the elastic yield line asymptotes, the normalized steel stress σ^* is defined as

$$\sigma^* = b\varepsilon^* + \frac{(1-b)\varepsilon^*}{(1+\varepsilon^{*R})^{\frac{1}{R}}} \quad (2.16)$$

where

$$\sigma^* = \frac{\sigma}{\sigma_y} = \frac{\sigma - \sigma_r}{\sigma_0 - \sigma_r} \quad (2.17)$$

and

$$\varepsilon^* = \frac{\varepsilon}{\varepsilon_y} = \frac{\varepsilon - \varepsilon_r}{\varepsilon_0 - \varepsilon_r} \quad (2.18)$$

Equation (2.16) describes a continuous function transitioning from a straight line with initial slope E_0 to a yield asymptote with slope $E_1 = bE_0$ where b is the post yield hardening ratio. The $(\varepsilon_0, \sigma_0)$ and $(\varepsilon_r, \sigma_r)$ pairs are located at the intersection of the asymptotic slopes and where the last strain reversal took place, respectively. The parameter R influences the transition between the two asymptotic lines and is defined as

$$R = R_0 - \frac{a_1\xi}{a_2 + \xi} \quad (2.19)$$

with R_0 as initial value and where ξ is the total plastic strain over the initial yield strain which is updated after each strain reversal. a_1 and a_2 are derived from empirical data. R influences the transition between the two asymptotes thus taking into account the Bauschinger effect, which alter the yield value of a steel member undergoing cyclic plastic deformations with opposite signs [20]. To allow for the effect of isotropic strain hardening, it is proposed to shift the yield line asymptote parallel to its direction following each strain reversal by an increment of σ_{st} [21]. This induces discrete stress and strain shifts on the monotonic envelope curve, given by

$$\sigma_{st} = a_3\sigma_{y0} \left(\frac{\varepsilon_{max}}{e_{y0}} - a_4 \right) \quad (2.20)$$

where ε_{max} is the absolute total strain value when the strain reversal occurs, ε_{y0} is the initial yield strain and a_3 and a_4 are found experimentally. When using the appropriate values for a_1 , a_2 , a_3 and a_4 , the GMP model is capable of incorporating several important properties of reinforcing steel mentioned above. Thus, its hysteric response following different load histories closely resembles experimental data [19], spite its simplicity. Figure 2.8 gives a summary of the GMP model.

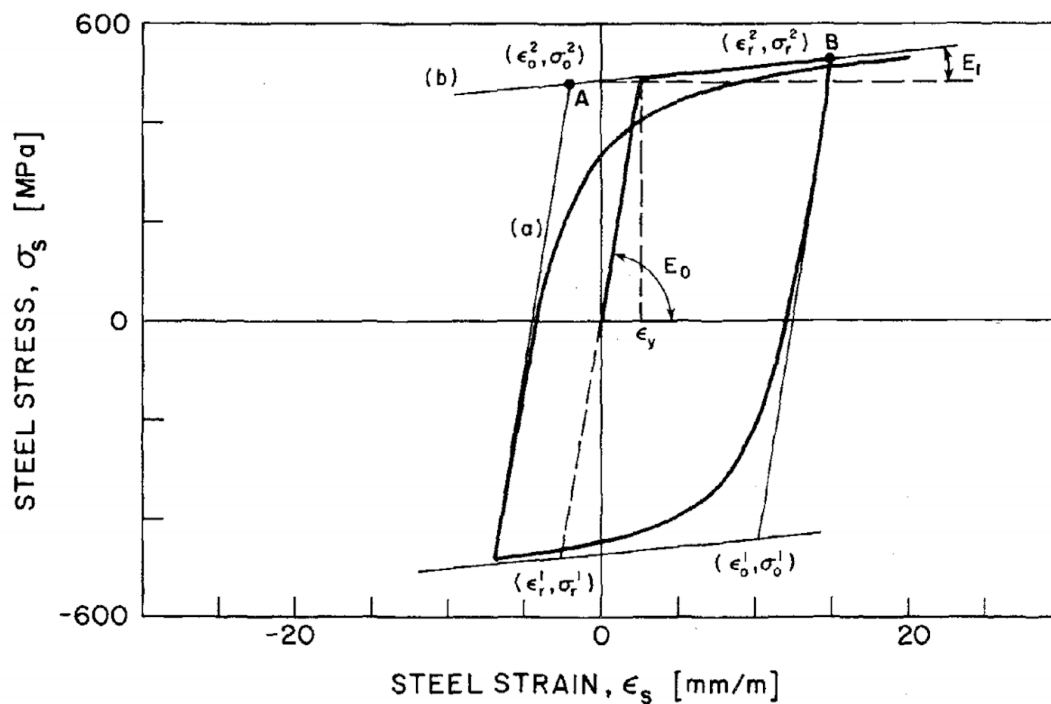


Figure 2.8: Menegotto-Pinto Steel Model [22]

2.3 Nonlinear Geometry

2.3.1 Corotational Formulation

Slender structural members undergoing large displacements and carrying high axial forces are prone to the effect of nonlinear geometry. Nonlinear chord geometry considers the relative translations of element ends. Using the principle of virtual work, the equilibrium relating the basic element forces \mathbf{q} to the end forces $\bar{\mathbf{p}}$ in the local reference system whilst taking this effect into account can be established [8]. The relation, seen below, show how the kinematic matrix $\mathbf{a}(\bar{\mathbf{u}})^T$ depend on the relative end displacements $\Delta\bar{\mathbf{u}}_x$ and $\Delta\bar{\mathbf{u}}_y$ in the element reference system. L_n is the deformed element length.

$$\bar{\mathbf{p}} = \mathbf{a}(\bar{\mathbf{u}})^T \mathbf{q} \quad (2.21)$$

$$\begin{bmatrix} \bar{p}_1 \\ \bar{p}_2 \\ \bar{p}_3 \\ \bar{p}_4 \\ \bar{p}_5 \\ \bar{p}_6 \end{bmatrix} = \begin{bmatrix} -\frac{L+\Delta\bar{u}_x}{L_n} & -\frac{\Delta\bar{u}_y}{L_n^2} & -\frac{\Delta\bar{u}_y}{L_n^2} \\ -\frac{\Delta\bar{u}_y}{L_n} & \frac{L+\Delta\bar{u}_x}{L_n^2} & \frac{L+\Delta\bar{u}_x}{L_n^2} \\ 0 & 1 & 0 \\ \frac{L+\Delta\bar{u}_x}{L_n} & \frac{\Delta\bar{u}_y}{L_n^2} & \frac{\Delta\bar{u}_y}{L_n^2} \\ \frac{\Delta\bar{u}_y}{L_n} & -\frac{L+\Delta\bar{u}_x}{L_n^2} & -\frac{L+\Delta\bar{u}_x}{L_n^2} \\ 0 & 0 & 1 \end{bmatrix} \begin{bmatrix} q_1 \\ q_2 \\ q_3 \end{bmatrix}$$

Figure 2.9 below depicts the element basic forces \mathbf{q} in the corotational frame and the the end forces \mathbf{p} in the global reference system. β is the chord rotation angle, taken from the undeformed orientation.

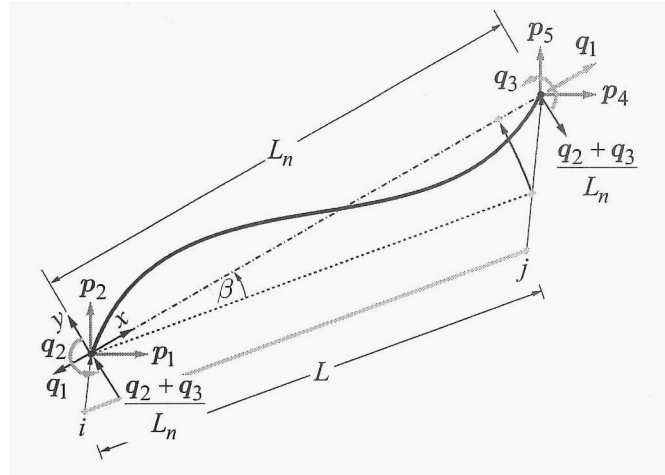


Figure 2.9: Relation between the element basic forces \mathbf{q} and end forces \mathbf{p} [8]

The tangent stiffness \mathbf{k}_e of the corotational frame element in the global coordinate system can be established by making use of the relation in equation (2.21), such that

$$\mathbf{k}_e = \frac{\partial \mathbf{p}}{\partial \mathbf{q}} = \frac{\partial [\mathbf{a}_g^T(\mathbf{u})] \mathbf{q}}{\partial \mathbf{u}} \quad (2.22)$$

where $\mathbf{a}_g^T(\mathbf{u})$ relates to $\mathbf{a}^T(\bar{\mathbf{u}})$ and \mathbf{p} to $\bar{\mathbf{p}}$ through linear transformation. By making use of the chain rule, the above equation can be expressed as

$$\mathbf{k}_e = \mathbf{a}_g^T(\mathbf{u}) \frac{\partial \mathbf{q}}{\partial \mathbf{v}} \mathbf{a}_g(\mathbf{u}) + \frac{\partial [\mathbf{a}_g^T(\mathbf{u})]}{\partial \mathbf{u}} \mathbf{q} = \mathbf{k}_m + \mathbf{k}_g \quad (2.23)$$

where \mathbf{v} is the element deformation, \mathbf{u} is the element end deformation in the global reference system, \mathbf{k}_m is the material stiffness matrix and \mathbf{k}_g the geometric stiffness matrix. Noting that $\mathbf{k} = \partial \mathbf{q} / \partial \mathbf{v}$, the material stiffness matrix \mathbf{k}_m may or may not include nonlinear element geometry effects also known as P- δ , depending on the axial force as well as element length and stiffness. The geometric stiffness \mathbf{k}_g can be further sub divided into the truss geometric stiffness

\mathbf{k}_{ga} and beam geometric stiffness \mathbf{k}_{gb} , relating to the contribution from the axial basic force and transverse end forces, respectively.

2.3.2 P-Delta

It can be shown that the truss geometric stiffness \mathbf{k}_{ga} derived in the previous section is much more significant than the beam geometric stiffness \mathbf{k}_{gb} [8]. Big P-Delta, denoted P- Δ , is an approximation of the nonlinear chord geometry effect which makes use of this fact by neglecting the contribution from the beam geometric stiffness and further simplifying the truss geometric stiffness. By neglecting axial deformation all together and assuming small $\Delta\bar{u}_y$ so that $L_n \approx L$, the relation in equation (2.21) can be simplified to

$$\begin{bmatrix} \bar{p}_1 \\ \bar{p}_2 \\ \bar{p}_3 \\ \bar{p}_4 \\ \bar{p}_5 \\ \bar{p}_6 \end{bmatrix} = \begin{bmatrix} -1 & 0 & 0 \\ 0 & \frac{1}{L} & \frac{1}{L} \\ 0 & 1 & 0 \\ 1 & 0 & 0 \\ 0 & -\frac{1}{L} & -\frac{1}{L} \\ 0 & 0 & 1 \end{bmatrix} \begin{bmatrix} \mathbf{q}_1 \\ \mathbf{q}_2 \\ \mathbf{q}_3 \end{bmatrix} + \begin{bmatrix} 0 \\ -\frac{\Delta\bar{u}_y}{L} \\ 0 \\ 0 \\ \frac{\Delta\bar{u}_y}{L} \\ 0 \end{bmatrix} \mathbf{q}_1$$

Here, the matrix multiplying the basic element end force vector \mathbf{q} is simply the static matrix \mathbf{a}^T under linear geometry. The last column multiplied with the axial basic force \mathbf{q}_1 considers the offset due to the relative end displacement $\Delta\bar{u}_y$ normal to the undeformed element chord. This gives rise to a moment, $\mathbf{q}_1\Delta\bar{u}_y$ and corresponding transverse element end forces. It can be shown that the approximate plane frame stiffness matrix \mathbf{k}_e in the global coordinate system is

$$\mathbf{k}_e = \mathbf{a}_g^T \mathbf{k} \mathbf{a}_g + \frac{\mathbf{q}_1}{L} \begin{bmatrix} (\mathbf{I} - \mathbf{i}\mathbf{i}^T) & \mathbf{0} & -(\mathbf{I} - \mathbf{i}\mathbf{i}^T) & \mathbf{0} \\ \mathbf{0} & 0 & \mathbf{0} & 0 \\ -(\mathbf{I} - \mathbf{i}\mathbf{i}^T) & \mathbf{0} & (\mathbf{I} - \mathbf{i}\mathbf{i}^T) & \mathbf{0} \\ \mathbf{0} & 0 & \mathbf{0} & 0 \end{bmatrix} = \mathbf{k}_m + \mathbf{k}_g \quad (2.24)$$

where \mathbf{I} is the identity matrix and the unit vector \mathbf{i} consists of the the direction cosines of the element chord in the original orientation,

$$\mathbf{i} = \begin{bmatrix} \frac{\Delta X}{L} \\ \frac{\Delta Y}{L} \end{bmatrix} \quad (2.25)$$

\mathbf{k}_g represent the approximation of the truss effect resulting from the nonlinear chord geometry. \mathbf{k} is the basic element stiffness matrix which again, may or may not include nonlinear element geometry, P- δ .

2.4 Structural Damping

In structural dynamics, damping plays an important role for the response of a structure excited by some dynamic action. The damping is a representation of all mechanisms causing energy dissipation in a structure during vibration. It is mathematically convenient to consider damping as a force proportional to the velocity, known as viscous damping. While this might not be the physically accurate, it gives a satisfactory representation of the inherent damping forces. [23]. In most cases, classical damping is an appropriate idealization, given similar materials over a structures height. The most common model for establishing a classical damping matrix is Rayleigh damping. The model expresses the damping matrix \mathbf{C} as a linear combination of the mass \mathbf{M} and stiffness \mathbf{K} matrices [24] so that

$$\mathbf{C} = a_0\mathbf{M} + a_1\mathbf{K} \quad (2.26)$$

where a_0 and a_1 are real valued scalars. These coefficients can be determined from specified damping ratios ξ for two arbitrary modes represented by their natural frequencies ω_i and ω_j . If both modes are assigned the same damping ratio the coefficients are found by the following equations [25]

$$a_0 = \xi \frac{2\omega_i\omega_j}{\omega_i + \omega_j}, \quad a_1 = \xi \frac{2}{\omega_i + \omega_j} \quad (2.27)$$

The damping ratio for modes i and j will be exactly ξ while outlying modes will be assigned either higher values if they are outside the interval $[i, j]$ or lower if they are inside the interval. For practical problems the modes i and j should be chosen to ensure reasonable values for the damping ratio at all significant modes. Figure 2.10 illustrates the process of distributing damping ratios.

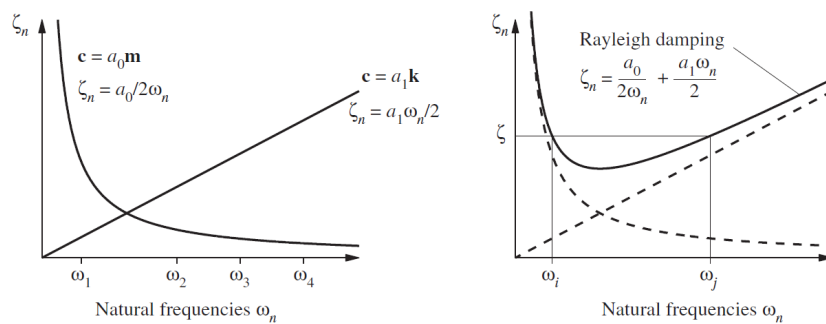


Figure 2.10: Variation of modal damping ratios with natural frequencies for Rayleigh damping [25]

There are two main ways to include Rayleigh damping in most Finite Element (FE) programs; either by assigning each element its own damping matrix by using the element modes or by constructing a global damping matrix. In OpenSees, only the latter option is available. Therefore, the damping model in OpenSees does not have the same damping ratio in all modes, but is rather chosen to achieve damping ratios close to the ones suitable for the materials used.

Chapter 3

Analyses in OpenSees

3.1 Section Response Analysis

A way to numerically evaluate the section response for a given fiber section in OpenSees is to perform a moment-curvature analysis. The section, complete with meshing and appropriate material models, is assigned to a theoretical zero length element. While one element end is fixed, the other is free to rotate about one or both of the local section axes. A load pattern consisting of an axial load may be applied perpendicular to the section face to induce initial strain in the section. Then, a unit rotational load about one of the section axis is applied, as well as a recorder to monitor the load and displacement values at the free Degree of Freedom (DOF). Target deformation is then defined along with the number of increments to be performed. The displacement step size is taken as their quotient, and remain constant during the analysis. When the analysis is initialized, a load factor is used to vary the unit rotation until the first curvature step is reached. The load along with the displacement value is then recorded, before the load factor increases so to reach the next curvature increment. This procedure continues until the target curvature is reached. A resulting text file contains the recorded values; the linearly increasing curvature values along with the corresponding bending moments. Figure 3.1 illustrates a moment-curvature diagram for an arbitrary cross section, where the curvature increment is set to $4 \times 10^{-6} \text{m}^{-1}$, with a final curvature target of $4 \times 10^{-3} \text{m}^{-1}$.

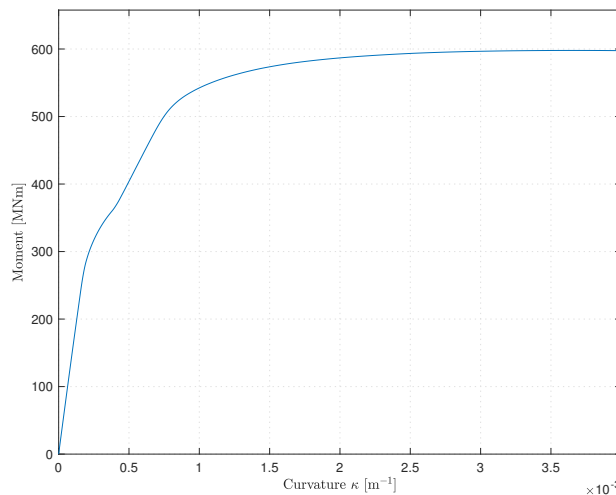


Figure 3.1: Moment-curvature diagram for arbitrary RC cross section

The same procedure can also be used to obtain the force-strain relation for a fiber section. A unit force is then applied perpendicular to the section face, and the translation DOF at the same end is left unrestrained. The sign of the force and target ductility determine whether a compression or tension analysis is to be performed. The analysis is then carried out for a number of linearly increasing strain steps for which the corresponding forces are recorded.

3.2 Time History Analysis

A THA is the most accurate way of predicting a structures response to a specific seismic event, especially when the structure is expected to deform beyond the limit of linear elastic behaviour. The governing equation for a linear Multi Degree of Freedom (MDOF) system subjected to arbitrary seismic loading is given by

$$\mathbf{m}\ddot{\mathbf{u}} + \mathbf{c}\dot{\mathbf{u}} + \mathbf{k}\mathbf{u} = -\mathbf{m}\mathbf{T}\ddot{u}_g(t) \quad (3.1)$$

where \mathbf{m} , \mathbf{c} , \mathbf{k} and \mathbf{T} are the mass matrix, damping matrix, stiffness matrix and influence vector, respectively. For inelastic systems, the nonlinear relation between resisting forces $\mathbf{r}(\mathbf{u})$ and displacements \mathbf{u} is path dependent, meaning that the relation depends on whether the deformation is increasing or decreasing, as well as the extent of previous deformations [25]. For a NTHA, (3.1) instead becomes

$$\mathbf{m}\ddot{\mathbf{u}} + \mathbf{c}\dot{\mathbf{u}} + \mathbf{r}(\mathbf{u}) = -\mathbf{m}\mathbf{T}\ddot{u}_g(t) \quad (3.2)$$

The solution of the nonlinear differential equation above is computationally demanding, since the resisting forces have to be computed and updated for all elements and fibers for every time or load step, elaborated in sections 2.1 and 2.2. The solution of equations (3.1) and (3.2) are usually handled by use of numerical time-stepping methods. In this thesis, Newmark's method will be utilized. More specifically the constant acceleration method, an implicit and unconditionally stable method, will be used. Large scale structural problems rarely requires small time steps. Even though other methods such as the linear acceleration method or the central difference method might be more accurate, the constant acceleration method is often more suitable for these types of problems given the restriction on time increments other methods inherent. Newmark's method with constant acceleration is summarized in figure 3.2

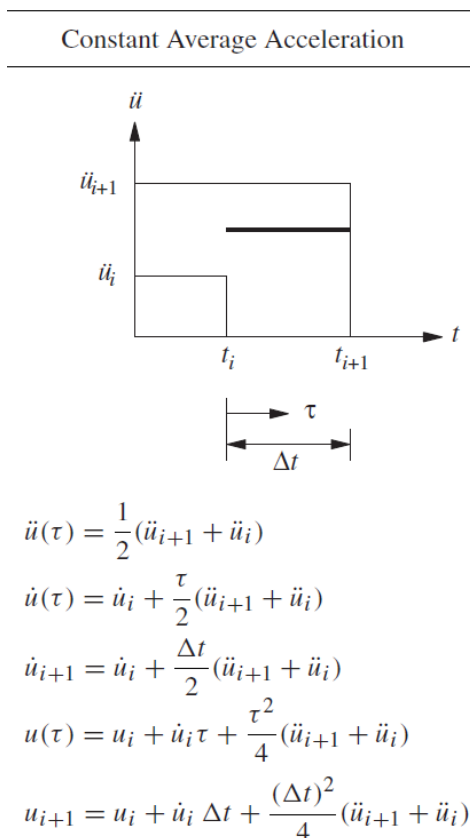


Figure 3.2: Newmark's method with constant acceleration [25]

3.3 Secant Method

The nonlinear material properties in a structure can be taken into account through an iterative procedure if certain nonlinear properties are known. This method, from now referred to as the Secant Method, uses the nonlinear moment-curvature relation of an element and the forces resulting from a linear THA to approximate its nonlinear response. As previously mentioned in chapter 1, an elastic analysis with secant stiffnesses is allowed by the AASHTO Seismic Design Manual, as long as the distribution of forces are verified to be consistent with expected nonlinear behaviour [3], which is what this thesis aims to examine. Eurocode 8 also states that if an elastic analysis is performed, it is preferable that the cracked stiffness of concrete sections are included in the analysis to account for including the influence of cracking on forces and deformations [26]. In the absence of an accurate evaluation of stiffness properties, the Eurocode also allows for a simplified method with 50% reduction of flexural stiffness in elements that are at risk of cracking. The simplified method will not be pursued further in this thesis, but it provides an indication of reasonable stiffness reductions in critical elements. Given that the Secant Method provides sufficiently accurate results compared to the nonlinear fiber model, the method is code-compliant for structures subjected to seismic loading that are design by following both the AASHTO Seismic Design Manual, as well as the Eurocode.

To perform the Secant Method, moment-curvature relations must first be established for all elements that potentially can become nonlinear during a seismic event. This relation depends on section properties such as reinforcement layout and material properties, as well as the axial forces acting on the section such as gravity loads. Then, a linear THA with the initial stiffnesses is conducted. The initial stiffnesses is taken as the slope of the tangent along the moment-curvature relation at the origin for each element in both directions.

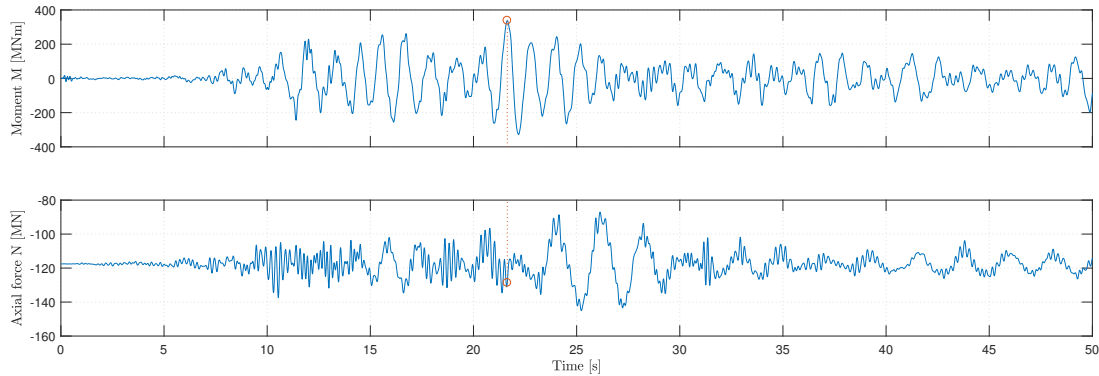


Figure 3.3: Moment and corresponding axial load for an element following a THA

Following the THA, each element has a series of resulting forces in the time domain, such as the ones in figure 3.3, from which the largest absolute bending moments about each section axis can be obtained. It should be noted that the largest absolute moment about the two principle axes does not necessarily occur simultaneously. Further, if the earthquake forces results in significant changes to the axial forces in the elements, the moment-curvature relations must be re-evaluated. The effect of the axial force on the moment-curvature relation, seen in figure 3.4a for an arbitrary RC element in compression, significantly influences the capacity of the element. For structures with frame-like configurations, horizontal translation of the girder can generate a tension-compression pair in the columns, which in turn will govern the ultimate strength of the these.

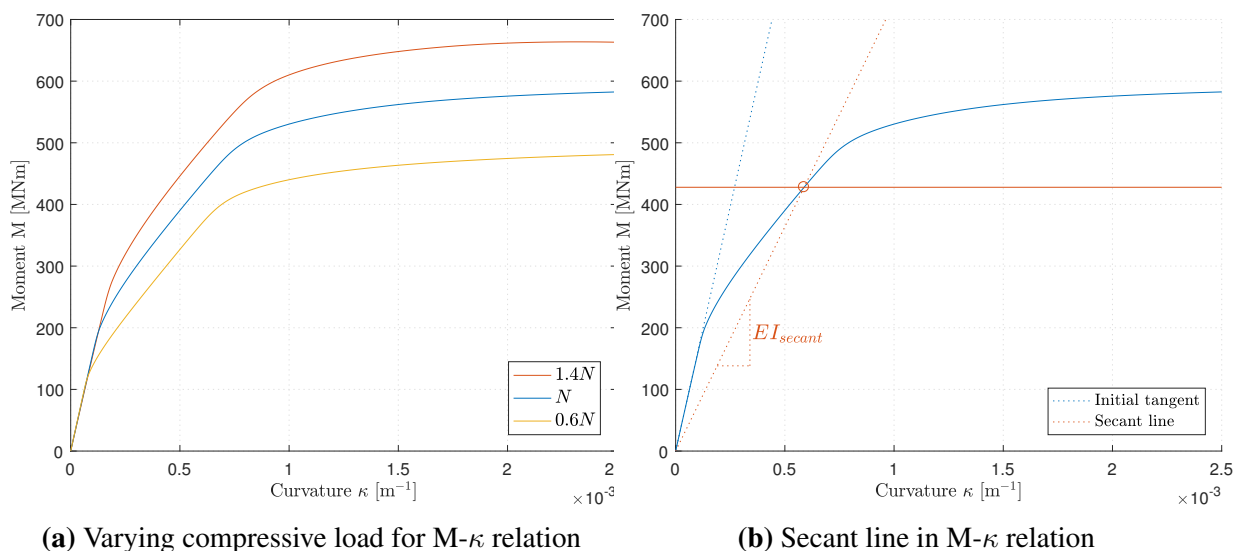


Figure 3.4: Determination of secant line using moment

The secant is taken as a line from the origin through the intersection point of the obtained moment and the correct moment-curvature relation, as seen in figure 3.4b. The new stiffness EI can then be found by making use of the relation

$$EI = \frac{M}{\kappa} \quad (3.3)$$

where M and κ is the moment and curvature about the appropriate axis. Thus, by calculating the slope of the secant line in both directions, the nonlinear flexural stiffness about both principle axes can be approximated. The updated stiffness of the structure can then be used in the next iteration of the procedure, replacing the initial stiffness.

This algorithm can be repeated for a certain number of iterations i or until a convergence criteria is met for the stiffness development. In theory this method should be able to approximate the nonlinear material response of a structure, since each elements' response is bounded by its inelastic moment-curvature relation. The final structure with reduced stiffnesses will in principal have the same maximum forces as a structure using full nonlinearity. The method has some weaknesses, however. If the moment value surpasses the peak of the moment-curvature relation, determining the secant line becomes significantly more cumbersome. Further, since the method only captures maximum deformation and forces, it is not able to take effects such as cyclic degradation and dissipation of energy due to cracking of the concrete into consideration. Furthermore, the method reduces each element on the basis of the maximum moments in the each element individually. Since the maximum response for all elements do not occur simultaneously during a THA and because a stiffness reduction of one element will affect the response of other elements, the response values following the each iteration of the Secant Method represents a worst-case scenario in regards to the stiffnesses in the structure. Additionally, the method is not able to account for the regaining of stiffness when cracks are closed under cyclic loading. These two effects in particular makes the final structure too soft, which must be taken

into consideration when evaluating the resulting stiffness values.

3.4 Pushover Analysis

The pushover analysis is a static incremental analysis with the goal of predicting the nonlinear behaviour of a structure. By incrementally increasing an applied horizontal load, it is possible to assess the structural performance of newly designed structures as well as to estimate potential plastic mechanisms and redistribution of forces [26]. Usually, a pushover analysis is conducted by converting the structural system into an equivalent Single Degree of Freedom (SDOF) system. Thereafter, a response spectrum analysis is conducted on the equivalent SDOF system to find displacement demands and corresponding load distributions, which are then applied to the entire structure. The loads are then incrementally increased until the target displacement is reached, and the residual strength of the structure is analyzed. This method is generally only applicable in structures where the fundamental mode shape dominates the response. Procedures such as the Modal Pushover Analysis have also been developed to account for all significant modes in the analysis by combining several pushover analyses, and therefore obtaining results that provide a better estimation of the forces from a THA [27].

For this thesis, the pushover analysis will hereby refer to the analysis procedure used by Aas-Jakobsen during the design of the Chacao Bridge. Rather than retrieving lateral loads from an equivalent SDOF system, the applied loads are instead set as the inertial forces retrieved at the most unfavourable time-steps from a THA. For a structure as complex as the Chacao Bridge, higher modes will significantly effect the response of the structure. It is also not certain that the fundamental mode shapes are the dominant response patterns with regards to the load distribution in various failure modes. By performing an analysis of this type, the exact acceleration profile and load distribution that might be detrimental to the structural integrity are easily identified and investigated. The process of establishing a pushover analysis of this type is explained in the list below [28].

1. Determine a critical element or section that is to be studied. For example the base of the pylon or one of the cross-beams.
2. Find the time-step t_{max} across all input ground motions where the maximum moment in the chosen section occurs.
3. Obtain the total acceleration profile, $\ddot{\mathbf{u}}^t(t_{max})$ for the ground motion that gives the maximum bending moment in the critical element.
4. Compute lateral inertial forces as $\mathbf{F} = \mathbf{m}\ddot{\mathbf{u}}^t(t_{max})$, and distribute the computed loads in the structure. This load level corresponds to a load step $\lambda = 1$.
5. Incrementally increase the load step, λ , by $\Delta\lambda$ from zero until ductile failure or until the analysis fails to converge.

6. Steps 1-5 are repeated for all critical elements or failure modes that are to be investigated.

This type of pushover analysis was performed by Aas-Jakobsen to enable the extraction of forces that are critical for various failure modes in the structure, demonstrate sufficient ductility and displacement capabilities. Furthermore, the pushover analysis is conducted to verify that nonlinear effects do not have a detrimental effect to the integrity of the structure [28]. The analysis is considered conservative, as the maximum response is retrieved from the worst-case time history for a specific element without averaging, which is allowed for design under Most Probable Earthquake (MPE). It has been verified that the applied loads reproduce the displacements and element forces when applied with a load factor $\lambda = 1$.

The pushover analysis described above was deemed preferable for this thesis over more conventional pushover analyses to stay consistent with the analyses used by Aas-Jakobsen in the actual design of the Chacao Bridge. The pushover analyses will be conducted to further verify the Secant Method, and control the results from the THA. Figure 3.5 illustrates an example of a capacity curve from a pushover analysis. In the fiber model, nonlinearities are handled internally by the solver in OpenSees, while nonlinearities in the elastic model will be handled by the Secant Method, which will be discussed further in the next chapter and in section 5.4.

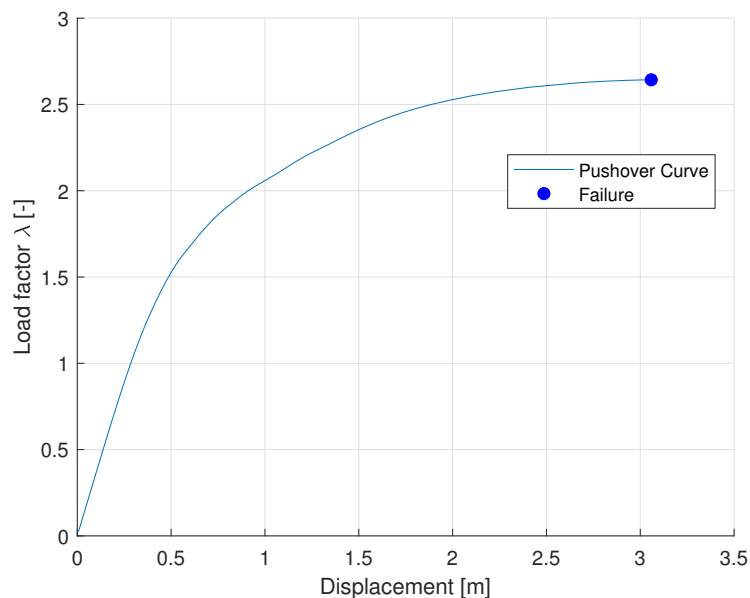


Figure 3.5: Pushover Curve

Chapter 4

Modelling in OpenSees

4.1 Choice of Finite Element Software

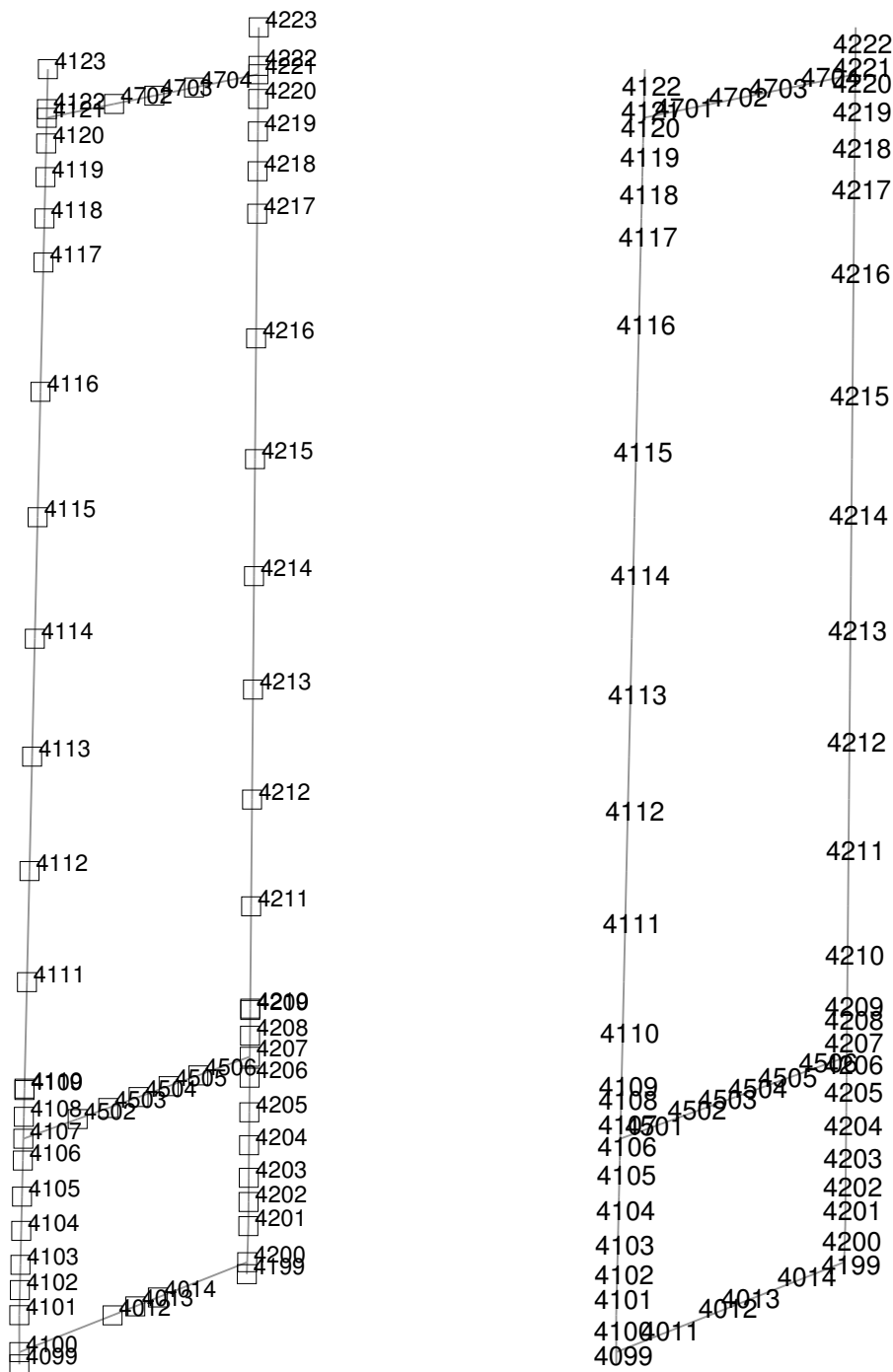
During the early stages of this report, several approaches were investigated to determine the best way to readily create a FE model with the desired requirements. Elements with distributed fiber sections were chosen to model the plastic behaviour of reinforced concrete due their ability to depict inelastic responses along an element for arbitrary cross sections. Because of the large axial loads imposed on the pylons, plastic deformations cannot be limited to certain element intervals which is the case for plastic hinge elements. An alternative way of modeling distributed plasticity is to model the entire beam as a solid with embedded reinforcement bars before creating solid FEs through meshing. This method is however computationally expensive and was disregarded after several trials in Abaqus.

An application with the necessary capability of using fiber sections is OpenSees. This open-source framework developed by the Pacific Earthquake Engineering Research Center (PEER) is an extension of the Tcl interpreter for Finite Element Analysis (FEA). With one of the authors having prior experience with the program after an exchange year abroad, some pre and post processing schemes in MATLAB [7] were obtainable. Preliminary knowledge, available tools and versatility thus made OpenSees the FE program of choice. Similar to most FE programs, OpenSees offers the possibility of defining a parametric input file, making it easy to alter properties in the element model. A drawback when using this approach in the design, however, is that any output value must be recorded manually and only data files are produced, limiting the amount of visual interface. For further post processing and visual interpretation of the data obtained, numerous MATLAB scripts have been developed.

4.2 Modelling of the South Pylon

The South Pylon along with the rest of the Chacao Bridge had previously been modeled by engineers at Aas-Jakobsen in the FEA program RM Bridge, and the parametric input file for this program laid the groundwork for establishing the OpenSees model. Data regarding geometry, boundary conditions and material properties were acquired from the parametric input file and related documentation. To accurately depict the geometry of the element model used by Aas-Jakobsen, the exact same node distribution was used in OpenSees. For easy comparison, node and element numbering were also kept alike. The elements connecting the nodes in the RM

Bridge model were designed as linear elastic for most of the bridge, including the South Pylon. For this thesis however, two FE models of the South Pylon were created; one with nonlinear material properties using fiber sections and one linear elastic. A pinned model showing the node and element numbering of the pylon can be seen in figure 4.1.



(a) Node numbering used in OpenSees

(b) Element numbering used in OpenSees

Figure 4.1

The naming convention used in this thesis and the local element axes related to the global coordinate system are elaborated in table 4.1. Here, the global Z-axis is upwards, while the global X and Y-axis are normal and parallel to the cross-beams, respectively.

Table 4.1: Naming convention and local element axes

| Structural Part | Elements | Local x | Local y | Local z |
|------------------|------------------------|--------------------|-----------------------------------|-------------------------------------|
| Pylon Legs | 4101-4122 4201-4222 | Along element axis | Transverse axis perp. to pylon | Longitudinal axis perp. to pylon |
| Lower Cross-Beam | 4501-4504 | Along element axis | Global longitudinal axis | Vertical |
| Upper Cross-Beam | 4701-4704 | Along element axis | Global longitudinal axis | Vertical |
| Pile Caps | 4099-4100 4199-4200 | Along element axis | Transverse axis perp. to pylon | Longitudinal axis perp. to pylon |
| Tie-beams | 4011-4014 | Along element axis | Global longitudinal axis | Vertical |
| SSI-springs | 34201 34202 | Global X | Global Y | Global Z |
| Cable Springs | 100 200 | Global X | Global Y | Global Z |

4.2.1 Fiber Model

Nonlinear RC fiber sections can readily be created in OpenSees by defining the concrete section dimensions and reinforcement layout. The pylon legs, for instance, were made using eight trapezoidal shaped segments, derived from structural drawings acquired from Aas-Jakobsen, seen in figure 4.2a for one of the pylon legs. The longitudinal reinforcement can then be mapped onto each segment by defining lines and specifying the distance between adjacent reinforcement bars. When combined, these segments make up a continuous reinforced concrete section, seen in figure 4.2b, which then can be meshed and assigned to one or more elements. To shorten the modelling process, some simplifications were made when creating the fiber elements, such as using only one row with twice the reinforcement area rather than two parallel bundled reinforcement groups. All fiber section can be found in appendix C.

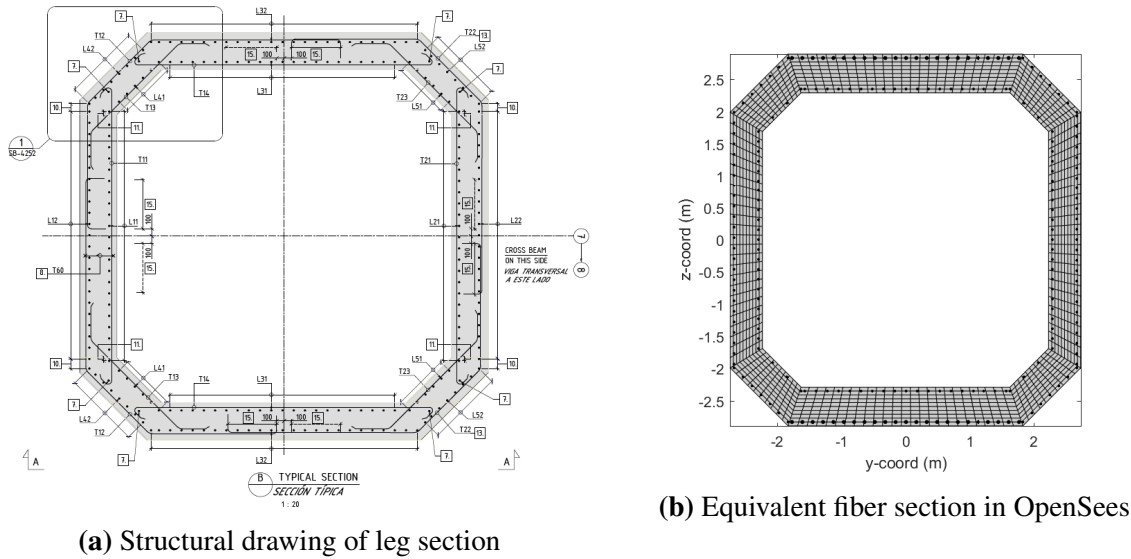


Figure 4.2: Comparison of construction drawings with fiber section in OpenSees

As mentioned in chapter 2.2, transverse reinforcement that confines the longitudinal bars can give a significant increase in strength and ductility of a concrete member, especially under large axial forces. This effect can be considered for uniaxial material models such as the ones used in OpenSees by distinguishing the concrete within and outside of the transverse shear reinforcement. The parameters for the confined concrete are largely based on the layout of the shear reinforcement, and formulas exist for several configurations. The hollow pylon legs are not among these, however, thus establishing a stress-strain relation for the confined concrete thus becomes a tedious task. Further, engineers at Aas-Jakobsen argued against including the effects of confinement, due to the unconventional section layout. When using thin walled sections as opposed to solid section, the effect can be unfavorable as the concrete cover spalls off resulting in a significant reduction of concrete area [29]. In addition to this, separating confined and unconfined concrete would have become a tedious task in OpenSees due to the complexity of the section layout. Therefore, no distinction was made on the concrete properties within and outside of the shear reinforcement and the concrete parameters for the entire pylon were based on the ones used by Aas-Jakobsen as well as values from the AASHTO Seismic Design Specifications [3], which was used as the design code for the bridge. While this does increase the capacity of the unconfined area in each cross section, the ratio of the unconfined area to the confined area is so small that this does not result in any considerable change to the overall response of the structure. At the same time, the compressive strength of the concrete was not scaled up to account for the confined strength of the core concrete, so that only the ductility benefits of confined concrete were kept. All in all, the choice of material parameters for the concrete was deemed conservative while preserving the efficiency of the modelling process.

Two relevant material models for concrete available in OpenSees are *Concrete01* and *Concrete02*, presented in section 2.2. The main distinction between these is that *Concrete02* bear some tensile strength, whereas *Concrete01* does not. Arguably, *Concrete02* provides a more

realistic concrete model, yet choosing one of the two has proven difficult. Figure 4.3a below shows the moment-curvature relation for a section belonging to the lower cross-beam which has relatively small compression forces resulting from gravity loads compared to the pylon legs. For moments larger than 150 MNm, the difference between the two curves are negligible, since the tensile part of the concrete section has cracked completely. For moments less than this value, however, there is a significant deviation between the two curves. This raises an issue when performing the Secant Method, for which *Concrete02* will yield a secant line significantly steeper than that of *Concrete01*, when using a moment less than 150 MNm. Since the two curves have the same initial stiffness, seen in figure 4.3b, the ratio of reduction from initial stiffness potentially depend on which material model is chosen. After switching between both material models for an extensive period, *Concrete02* was chosen, since it produced more realistic results for the cross-beams during the secant procedure. As shall be seen later, the secant procedure is extremely sensitive to crack development, and since the cross-beam have small axial forces, sometimes even in tension, cracking will occur for small and negligible moments when using *Concrete01*.

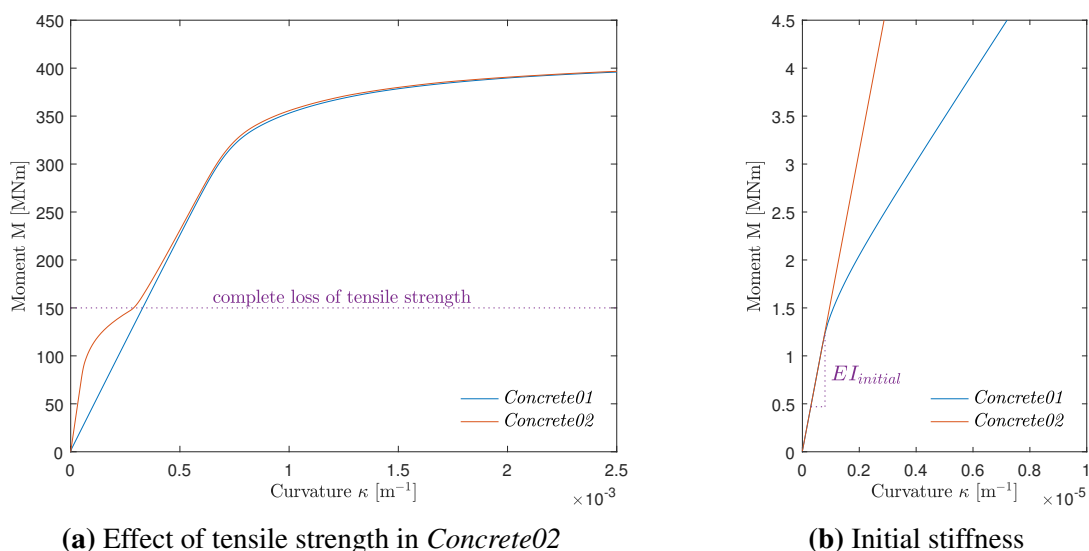


Figure 4.3: Moment-curvature analysis using *Concrete01* and *Concrete02*

The longitudinal reinforcement is modeled using the *Steel02* material model in OpenSees, presented in section 2.2.2. The bars are represented as 1D points along lines in the section, with capacity depending on the material model as well as the assigned diameter.

Tables 4.2 and 4.3 below summarize the choice of material parameters used for the fiber sections. The concrete compressive strength parameters correspond to concrete of type C45.

Table 4.2: *Concrete02* material parameters

| Parameter | Symbol | Value |
|---|--------------------|----------|
| Expected maximum compressive strength | f_{pc} | 58.5 MPa |
| Initial modulus of elasticity | E_{cm} | 32.1 GPa |
| Strain at maximum compressive strength | ε_{c0} | 3.64 ‰ |
| Ultimate compressive strength | f_{pcu} | 49 MPa |
| Ultimate compressive strain | ε_{cu} | 5 ‰ |
| Expected tensile strength | f_t | 4.05 MPa |
| Tensile softening stiffness | E_{ts} | 4.41 MPa |
| Ratio between unloading and initial slope | λ | 0.5 |

Table 4.3: *Steel02* material parameters

| Parameter | Symbol | Value |
|-------------------------------|-----------------|---------|
| Expected yield strength | f_y | 470 MPa |
| Young's modulus | E_s | 200 GPa |
| Yield strain | ε_y | 2.35 ‰ |
| Strain hardening ratio | b | 0.06 |
| Isotropic hardening parameter | a_1 | 0 |
| Isotropic hardening parameter | a_2 | 1 |
| Isotropic hardening parameter | a_3 | 0 |
| Isotropic hardening parameter | a_4 | 1 |
| Asymptote parameter | R_0 | 0.20 |
| Asymptote parameter | cR_1 | 0.925 |
| Asymptote parameter | cR_2 | 0.15 |

The material parameters for the steel fibers correspond to steel Grade 60. The values for a_1 - a_4 are kept as the default values for *Steel02*, while R_0 , cR_1 and cR_2 are chosen as the values recommended in the OpenSees manual [5].

Upon completion, all sections were assigned to elements, onto which they were distributed along IPs determined by the numerical integration algorithm. For this thesis, the Gauss-Lobatto rule was used, presented in table 2.1. Although less accurate than the Gauss-Legendre rule, it has the advantage of having IPs at the element ends. For the Hermite polynomials of the DB elements, the accuracy of the Gauss-Lobatto rule is sufficient with five IP along the element length. The outermost cross-beam elements were modeled with eccentricities so that their sections did not overlap with those of the pylon legs. The outer parts of the cross-beams which lack sections are rigid and follow the rotation of the leg nodes they are connected to.

Elements belonging to the foundation of the pylon were kept linear elastic. This decision was made on the notion that these elements were too complicated to be made into equivalent

fiber sections with similar properties. Further, these elements make up the pile caps and the tie-beam coupling them and will thus stay linear elastic behaviour due to their sheer size. Their properties were thus simply imported from the RM Bridge input file.

The local coordinate system for sections assigned to the pylon legs and cross-beams are depicted in figure 4.4 below, along with the global coordinate system seen with capital letters. The local x-axis coincides with the element vector, and its direction can be found using the right hand rule. The local coordinates are also shared by the linear elastic elements.

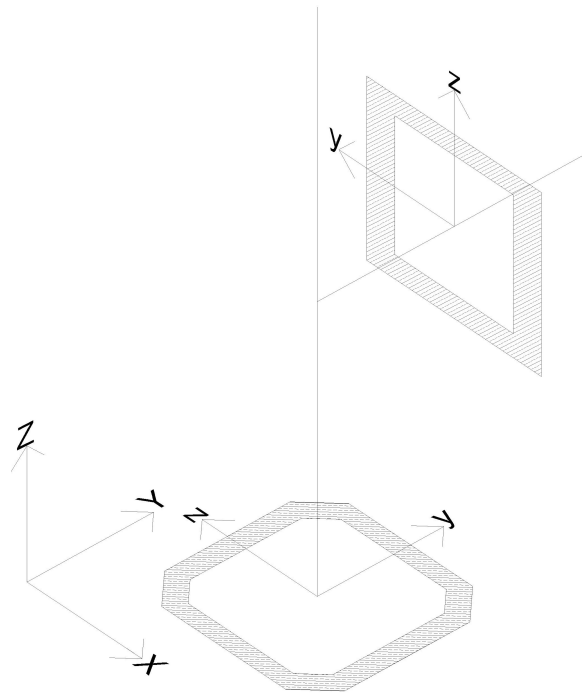


Figure 4.4: Local section coordinate systems

4.2.2 Section Discretization

Obtaining specific rules for the number and distribution of fibers over the section from literature was proven unsuccessful. These parameters effect the accuracy of the results and may also lead to convergence problems if the mesh is too coarse. On the other hand, increased mesh refinement leads to increased computational cost, eventually without significant improvements of accuracy [30]. During the early stages of development, it was decided upon using a 25×10 grid when meshing each of the four trapezoids making up the long sides of the leg sections. The mesh of the trapezoids which makes up the corners was scaled accordingly. This mesh size was deemed sufficiently small after a series of moment-curvature analysis was conducted, seen in figure 4.5 below. It shows the results following said analysis on element 4101, with varying axial forces and mesh sizes. The axial loads are in compression and represent 0.5,

1 and 1.5 times the gravity force on the element. For reference, the gravity load is -117.6 MN. Seen in figure 4.5, there is no significant difference among the section response using the 25×10 mesh or the more refined 50×20 mesh. Using a 5×2 grid or coarser however, result in divergence from the converged response. Since the 50×20 did not display great improvements in the results, the 25×10 mesh was deemed sufficiently accurate. The same element size was used when discretizing the cross-beam sections.

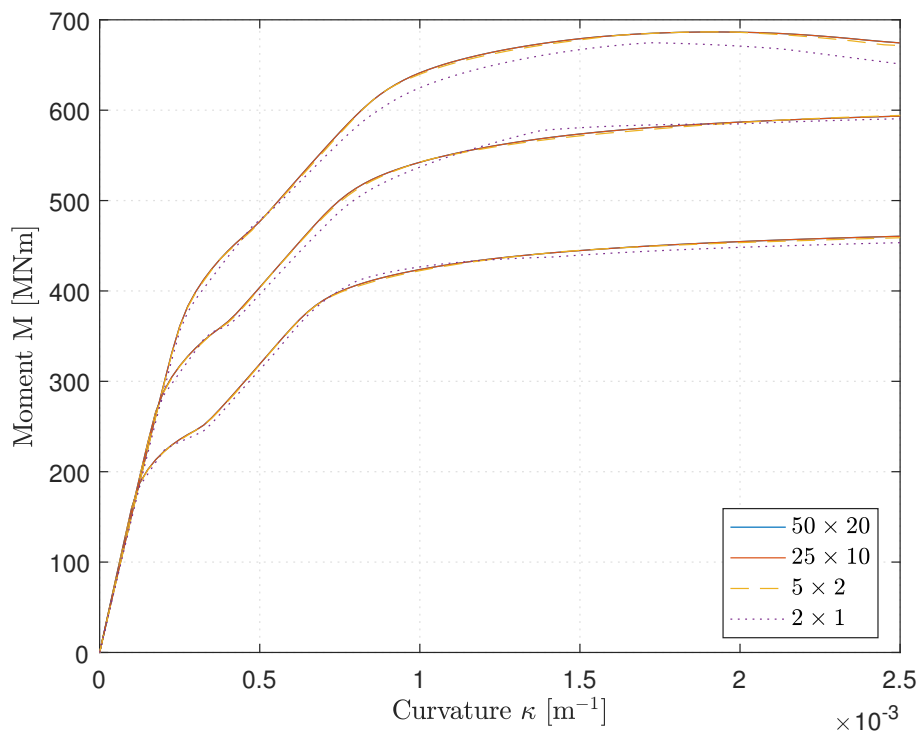


Figure 4.5: Moment-curvature relations for different meshing and axial load

4.2.3 Elastic Model

A linear elastic model of the South Pylon was also created in OpenSees, from now on referred to as the elastic model, onto which the Secant Method could be conducted. The elastic model was largely based on the fiber model, with elastic properties derived from the fiber model rather than from the RM Bridge input file. Doing so would remove potential sources of uncertainty when comparing the results of the Secant Method to those from the NTHA using the fiber model. The only distinction between the two models is how the elements are constructed. In the elastic model, these are defined as linear elastic, by specifying the elastic modulus along with the cross section area and the second moment of area about the two local element axes and the torsional constant. To obtain the second moment of area about the two transverse axes, each fiber section used in the fiber model underwent an moment-curvature analysis about both principle axes, described in detail in section 3.1. The slopes of the initial tangents from these curves provides the initial stiffness, EI , which divided by the elastic modulus becomes the effective second moment of area.

The fiber sections in OpenSees do not provide any inherent torsional stiffness. However, this can value can be attributed to a fiber section if an appropriate value can be obtained. In this thesis, these values were taken from the RM Bridge input file and assigned to all fiber sections as well as all elements in the elastic model.

Instead of assigning each element in the elastic model the area of the corresponding section in the fiber model, an equivalent area was obtained which included the stiffness contribution from the reinforcement. Same as for the transverse bending stiffnesses EI , the initial axial stiffness EA can be taken as the slope of the initial tangent from a section response analysis. As outlined in section 3.1, both a compressive and a tensile analysis can be conducted. The elements which make up the pylon legs will always remain in compression due to the large self weight of the structure and the cables during a THA. The cross-beams however, although mostly in compression, will occasionally be stretched under certain ground motions. This raises an issue since nonlinear RC sections have significantly different axial stiffness in tension and compression. Because the tensile stiffness for these sections typically was around ten percent of the compression stiffness if no tensile strength was attributed to the concrete, it was deemed too conservative to use this value for the cross-beams. Thus, all equivalent areas were taken from compression force-strain relations. When using the *Concrete02* material model in OpenSees, this simplification becomes slightly more correct as the material model carry some tensile strength.

4.2.4 Mass and Gravity Loads

Mass in OpenSees can either be assigned directly to nodes as point masses in directions of choice or distributed along the elements, then lumped to adjacent nodes automatically [5]. Both methods yield the same resulting mass matrix, and the second approach was applied for this thesis. The mass density per unit length was calculated using the sectional area times the mass density of RC, taken as $\rho_c = 2500 \text{ kg/m}^3$.

OpenSees does not have any functionality where the dead loads are calculated automatically from the mass of the structure. These must be defined separately as vertical point loads at each node. For both the fiber and elastic model the nodal gravity forces were obtained by lumping half of the weight of all elements connected to a node onto said node.

4.3 Synopsis of Mass and Stiffness

For completeness, some of the properties of the fiber and elastic model created in OpenSees are summarized in table 4.4 below. Due to symmetry only one of the two pylon legs are included as well as only one element from each cross-beam and the tie-beam. The two rightmost columns contains the stiffnesses used in the elastic model, derived from the sections in the fiber model using moment-curvature analysis. Elements marked with an asterisk (*) make up the foundation

and are modeled as linear elastic in both models, as elaborated in section 4.2.1. Element lengths include eccentricities. The total mass of the pylon structure ignoring cables and nonstructural components is 1.739×10^6 kg.

Table 4.4: Properties of the OpenSees models

| Element | Area [m ²] | Length [m] | Mass [kg $\times 10^3$] | I _y [m ⁴] | I _z [m ⁴] |
|-------------|------------------------|------------|--------------------------|----------------------------------|----------------------------------|
| 4011*-4014* | 12 | 2.80 | 84.35 | 9.00 | 16.00 |
| 4099* | 340.00 | 1.50 | 1275.00 | 11333.33 | 8188.33 |
| 4100* | 340.00 | 4.50 | 3825.00 | 11333.33 | 8188.33 |
| 4101 | 10.24 | 3.00 | 76.80 | 48.59 | 40.88 |
| 4102 | 10.22 | 3.00 | 76.68 | 47.18 | 40.57 |
| 4103 | 9.76 | 4.00 | 97.59 | 44.91 | 40.16 |
| 4104 | 9.29 | 4.00 | 92.92 | 44.51 | 40.05 |
| 4105 | 10.16 | 4.17 | 105.90 | 47.60 | 44.30 |
| 4106 | 11.04 | 2.50 | 69.00 | 63.44 | 53.98 |
| 4107 | 11.02 | 2.50 | 68.91 | 63.11 | 53.92 |
| 4108 | 10.12 | 3.03 | 76.70 | 47.47 | 47.04 |
| 4109 | 9.21 | 0.16 | 3.69 | 44.50 | 46.06 |
| 4110 | 9.18 | 11.84 | 271.90 | 39.31 | 39.43 |
| 4111 | 9.12 | 12.00 | 273.71 | 37.02 | 36.03 |
| 4112 | 9.06 | 12.00 | 271.83 | 36.03 | 35.66 |
| 4113 | 9.00 | 12.00 | 269.94 | 35.02 | 35.29 |
| 4114 | 8.93 | 12.00 | 268.06 | 34.07 | 34.92 |
| 4115 | 8.87 | 12.00 | 266.18 | 33.10 | 34.56 |
| 4116 | 8.81 | 12.00 | 264.30 | 32.15 | 34.23 |
| 4117 | 8.77 | 4.00 | 87.68 | 31.54 | 33.96 |
| 4118 | 8.75 | 3.71 | 81.14 | 31.73 | 36.51 |
| 4119 | 9.62 | 3.00 | 72.18 | 35.74 | 39.91 |
| 4120 | 10.50 | 2.27 | 59.47 | 43.26 | 45.08 |
| 4121 | 10.49 | 0.77 | 20.07 | 43.12 | 45.05 |
| 4122 | 26.42 | 3.50 | 231.21 | 52.39 | 59.20 |
| 4501-4506 | 9.50 | 3.63 | 86.26 | 48.98 | 64.89 |
| 4701-4704 | 8.46 | 4.23 | 89.52 | 33.21 | 43.62 |

4.3.1 Boundary Conditions

Main Cables

As mentioned, only the South Pylon of the Chacao Bridge is being assessed in this thesis. However, loads and stiffness contributions from the main cables play an important role in the response of the pylon. Therefore, the main cable has been modelled using one-dimensional springs in the longitudinal and transverse directions. That is, along the bridge axis and along the horizontal axis perpendicular to it. The springs were modelled using the zero-length elements in OpenSees [5]. These elements are defined by two nodes at the same location, which in this case is set at the top of each pylon leg. Thereafter, the element is assigned material properties in directions of choice. Computationally, the zero-length elements have unit length and area in all directions, meaning that the strain and axial displacement are the same, $\varepsilon = \frac{\Delta L}{L} = \Delta L$. Furthermore, the axial stiffness in each direction is defined by the Young's modulus in the corresponding direction, $\frac{EA}{L} = E$. From this it follows that the stiffness contributions from the cables, which were retrieved from the full Chacao Bridge model, could be inserted directly into the zero-length elements as their corresponding Young's modulus. This is summarized in tables 4.5 and 4.6 below. In addition to the cable springs, vertical point loads of -84 MN are placed on the top nodes of each leg to represent the vertical forces from the main cables.

Table 4.5: Longitudinal cable stiffness at each leg, with chosen E in OpenSees

| Pylon leg | Cable stiffness [kN/m] | E [N/m] |
|-----------|------------------------|----------|
| West Leg | 59012 | - |
| East Leg | 58964 | - |
| Mean | 58988 | 58988000 |

Table 4.6: Transverse cable stiffness at each leg, with chosen E in OpenSees

| Pylon leg | Cable stiffness [kN/m] | E [N/m] |
|-----------|------------------------|---------|
| West Leg | 523 | - |
| East Leg | 527 | - |
| Mean | 525 | 525000 |

Soil-Structure Interaction

The presence of soil or sedimentary rock layers above bedrock at a construction site will modify the ground motion characteristics [31]. The effect of this has been included by a previously conducted Soil-Structure Interaction (SSI) analysis in PLAXIS. In the RM Bridge model used by

Aas-Jakobsen, SSI have been implemented using matrix elements connected to the foundation elements. In OpenSees there are no such matrix elements that would suit this purpose. Instead, the SSI-matrices have been approximated using zero-length elements, as for the main cables. By extracting the stiffness used in RM Bridge directly from the matrix elements, it is possible to achieve the same stiffness in all diagonal terms. The off-diagonal terms have been neglected, as they are not as significant as the diagonal terms, and at the same time are more troublesome to include.

$$\begin{bmatrix} K_x & 0 & 0 & 0 & 0 & 0 \\ 0 & K_y & 0 & 0 & 0 & 0 \\ 0 & 0 & K_z & 0 & 0 & 0 \\ 0 & 0 & 0 & K_{xx} & 0 & 0 \\ 0 & 0 & 0 & 0 & K_{yy} & 0 \\ 0 & 0 & 0 & 0 & 0 & K_{zz} \end{bmatrix}$$

Figure 4.6: Coordinates in the OpenSees coordinate system

$$\begin{bmatrix} 113e5 & 0 & 0 & 0 & 0 & 0 \\ 0 & 159e5 & 0 & 0 & 0 & 0 \\ 0 & 0 & 111e5 & 0 & 0 & 0 \\ 0 & 0 & 0 & 11945e5 & 0 & 0 \\ 0 & 0 & 0 & 0 & 9580e5 & 0 \\ 0 & 0 & 0 & 0 & 0 & 14595e5 \end{bmatrix}$$

Figure 4.7: SSI matrix used in OpenSees [kN/m] & [kNm/rad]

4.4 Second Order Effects

As elaborated in section 2.3, slender structures subjected to large axial forces are susceptible to the effect of nonlinear geometry. Tall pylon structures definitively fall within this category, thus nonlinear geometry needs to be accounted for when analyzing the South Pylon. OpenSees accomplishes this through geometric transformation objects, which are attributed to each element. The main task of these is to transform global displacements to natural coordinates and to transform the resulting natural forces and stiffnesses obtained back to global coordinates [32]. When assembling an element in OpenSees, linear, P- Δ or corotational transformation can be chosen, which in turn determinate the kinematic transformation matrix. It should be noted that the nonlinear element geometry effect P- δ is not included in OpenSees, however this effect is usually several magnitudes smaller than the nonlinear chord geometry effect. The negative impact this will have on accuracy can be omitted by carefully selecting element lengths depending

on axial load and stiffnesses. This was not done for this thesis, but will be discussed further in section 7.4. After using alternating between the P- Δ and Corotational transformation for the leg sections over several analyses, it was observed that the two methods yielded almost identical results. Thus, it was decided to advance with the P- Δ transformation object, as it was faster.

4.5 Comparison of Modes

The first 20 modes computed for the linear elastic model and the nonlinear fiber model are shown in table 4.7. The results show that the two models behave similarly, with some differences that may stem from approximation when defining the elastic model. The results however, were deemed satisfactory for the purpose, with differences being so small that they will have negligible impact on the dynamic response. The mode shapes are illustrated in appendix B. Only the mode shapes for the fiber model have been included, as the mode shapes are similar for the elastic model.

Table 4.7: Comparison of modes for the two models

| Mode Nr. | Fiber Model [s] | Elastic Model [s] | Deviation [%] |
|----------|-----------------|-------------------|---------------|
| 1 | 2.181 | 2.139 | 1.929 |
| 2 | 1.145 | 1.132 | 1.090 |
| 3 | 0.794 | 0.793 | 0.225 |
| 4 | 0.596 | 0.591 | 0.829 |
| 5 | 0.491 | 0.484 | 1.563 |
| 6 | 0.415 | 0.408 | 1.767 |
| 7 | 0.376 | 0.376 | -0.025 |
| 8 | 0.284 | 0.280 | 1.440 |
| 9 | 0.240 | 0.236 | 1.607 |
| 10 | 0.215 | 0.212 | 1.366 |
| 11 | 0.193 | 0.189 | 2.083 |
| 12 | 0.176 | 0.173 | 1.696 |
| 13 | 0.163 | 0.162 | 0.928 |
| 14 | 0.161 | 0.159 | 1.526 |
| 15 | 0.136 | 0.135 | 0.658 |
| 16 | 0.131 | 0.129 | 1.186 |
| 17 | 0.127 | 0.125 | 0.934 |
| 18 | 0.116 | 0.114 | 1.253 |
| 19 | 0.107 | 0.106 | 0.950 |
| 20 | 0.104 | 0.102 | 2.150 |

4.6 Structural Damping

In section 2.4, it was shown how classical viscous damping is a practical way of including the various effect that cause dissipation of energy in a dynamic system. As seen in table 4.7, the natural modes of the two structures are sufficiently close. This allows the use of the same Rayleigh damping coefficients for both structures. The target damping ratio was set to 5 %, in accordance with recommendations in most codes [26, 3]. The calculation of the damping coefficients were performed by Aas-Jakobsen and inserted directly into OpenSees [31]. The damping matrix is then computed internally in OpenSees through utilizing the previously established equation (2.26). By using the same Rayleigh coefficients in both models, consistent damping forces are ensured through each iteration step in the Secant Method.

Chapter 5

Implementation of Analysis

5.1 Introduction

On a structure such as the Chacao Bridge, a full nonlinear time history analysis can take days to finish and convergence is not guaranteed. Therefore, Aas-Jakobsen deployed the Secant Method to investigate if some elements would get reduced stiffnesses due to cracking during an seismic event. This would in turn result in an overall softer structure and a reduction of element forces. Aas-Jakobsen used nonlinear moment-curvature relations for each section obtained in Nova Design and RM Bridge to run the elastic THA during each iteration [31]. The procedure was implemented on the South and North Pylon, as well as on the approach bridge piers, all of which showed a significant reduction of stiffness for certain elements after a number of iterations. However, since RM Bridge is unable to perform complete nonlinear analysis in a satisfactory manner, it is difficult to confirm these results. By ensuring that the reinforcement did not yield for any of the sections, engineers at Aas-Jakobsen concluded that the model remained consistent with elastic design assumptions. Further, the elements with reduced stiffness also had the largest moments for the fundamental mode shapes. The reduced stiffness was therefore assumed to be representative and used in further analyses after some modifications.

OpenSees, on the other hand, allows for the implementation of nonlinear material models and thus the possibility of a complete cross examination between the two approaches arises. Two models of the South Pylon were used during this analysis; one linear elastic with iterative stiffness updates based on the Secant Method, and one nonlinear fiber model used as a reference model. Both models were excited with seven earthquake records of large magnitude to ensure inelastic behavior, provided by Aas-Jakobsen. The elastic model underwent between 6-8 iterations depending on the earthquake record before the convergence criteria was met. Values such as largest absolute displacement and moment along the structure during the final iteration were then compared with the corresponding ones from the NTHA. Afterwards, the inertial forces which gave rise to the largest moments in the most critical sections were used as the basis of a pushover analysis, which was used as verification of the results, as well as a comparison of the two models in its own right.

5.2 Time History Analysis

The responses obtained from a THA is naturally sensitive to the chosen acceleration record, and in general, the likelihood of two identical seismic events is very low. For this reason, both the entire Chacao Bridge and the pylon structure in this thesis have been analyzed using seven different ground motion records. The results from these records will be averaged to give response values representative of the MPE, with a return period of 1030 years [31]. This is in accordance with the guidelines from the codes [26, 3]. The input ground motions were run with a full transient analysis in OpenSees with Newmark's constant average acceleration method as the time-stepping scheme, see section 3. OpenSees has the functionality of simultaneously running seismic ground motions in two directions. The accelerograms provided are generated with a time step of 0.01 seconds. This was initially done to prevent numerical damping of important high frequency modes for the entire Chacao Bridge. Since this thesis only considers the South Pylon, 0.01 seconds is not necessary. However, the time-step size is kept as-is to ensure convergence for the NTHA.

5.2.1 Input Ground Motion

Aas-Jakobsen have supplied the authors with seven pairs of horizontal ground motions for the South Pylon. The accelerograms were found by calculating the free-field ground motions at each location from rock motions, while taking into account the soil profile and foundation characteristics on site. For the South Pylon, the transverse ground motion, H2-components, was found with the assumption of one dimensional wave propagation, while the longitudinal, H1-component was found with two-dimensional site response analyses. [33]. The time-histories were then calculated using a computer code. The method used is not relevant for this thesis, and will therefore not be elaborated further. When the ground motions in the two directions have differing length, the analysis will use the shortest ground motion's duration.

A summary of the input ground motions used is shown in table 5.1, while the acceleration time histories themselves can be seen in the subsequent figures 5.1-5.7.

Table 5.1: Input Ground Motions

| Input Ground Motion | Direction | PGA [m/s ²] | Length [s] |
|---------------------|-----------|-------------------------|------------|
| SP1-H1 | Long. | 3.65 | 99.990 |
| SP1-H2 | Trans. | 3.64 | 141.630 |
| SP2-H1 | Long. | 4.04 | 75.000 |
| SP2-H2 | Trans. | 3.90 | 124.560 |
| SP3-H1 | Long. | 3.42 | 95.000 |
| SP3-H2 | Trans. | 3.70 | 201.960 |
| SP4-H1 | Long. | 4.16 | 50.010 |
| SP4-H2 | Trans. | 3.32 | 71.970 |
| SP5-H1 | Long. | 3.91 | 60.010 |
| SP5-H2 | Trans. | 4.12 | 64.420 |
| SP6-H1 | Long. | 3.76 | 30.000 |
| SP6-H2 | Trans. | 4.08 | 54.540 |
| SP7-H1 | Long. | 4.15 | 60.010 |
| SP7-H2 | Trans. | 4.55 | 88.650 |

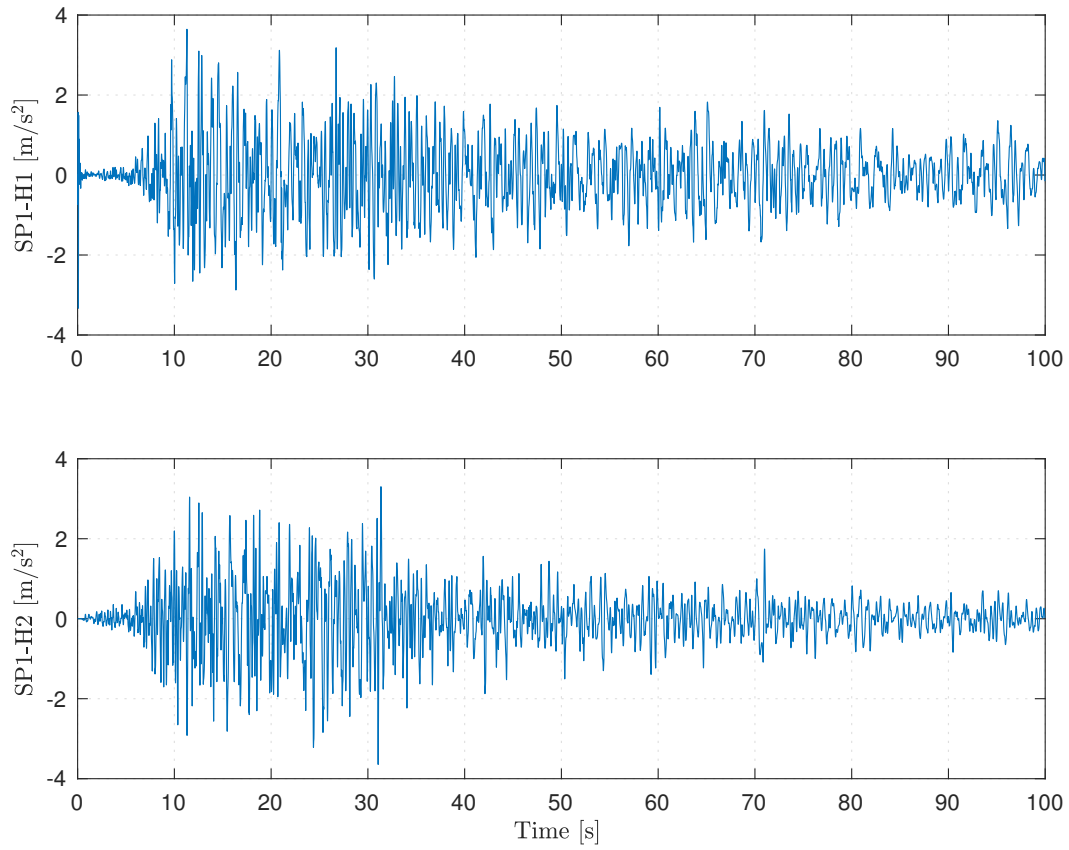


Figure 5.1: Input ground motion SP1

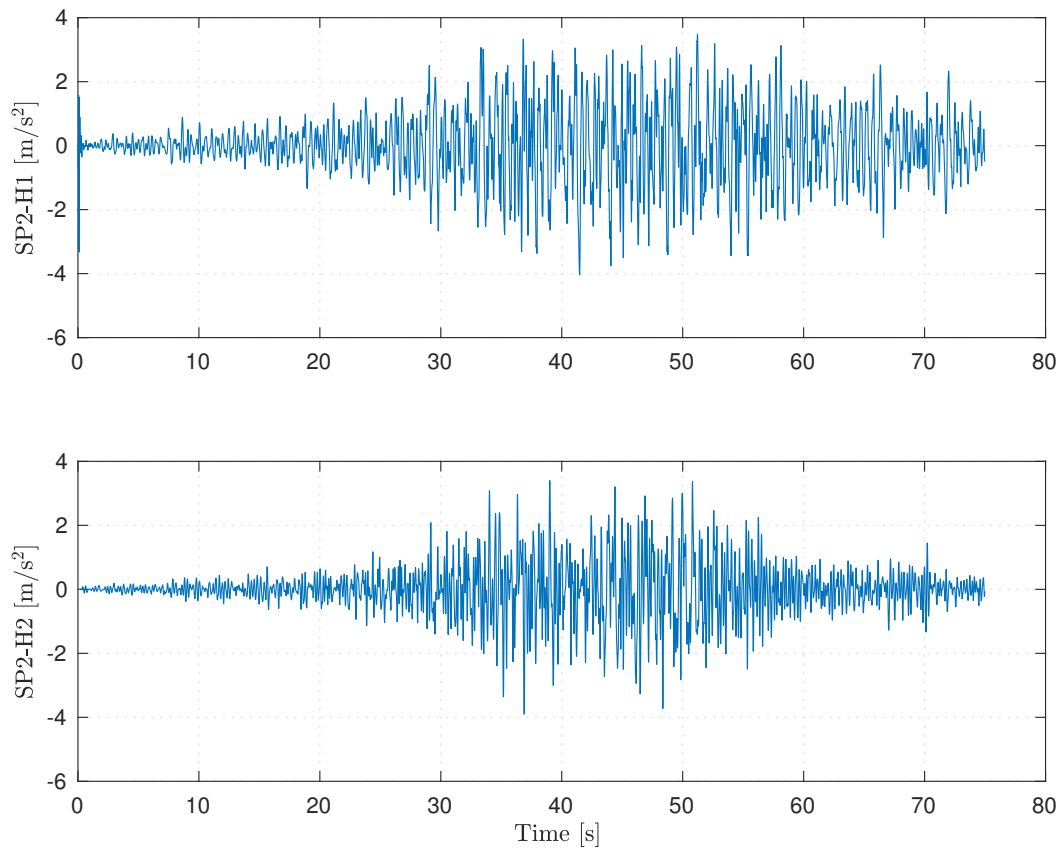
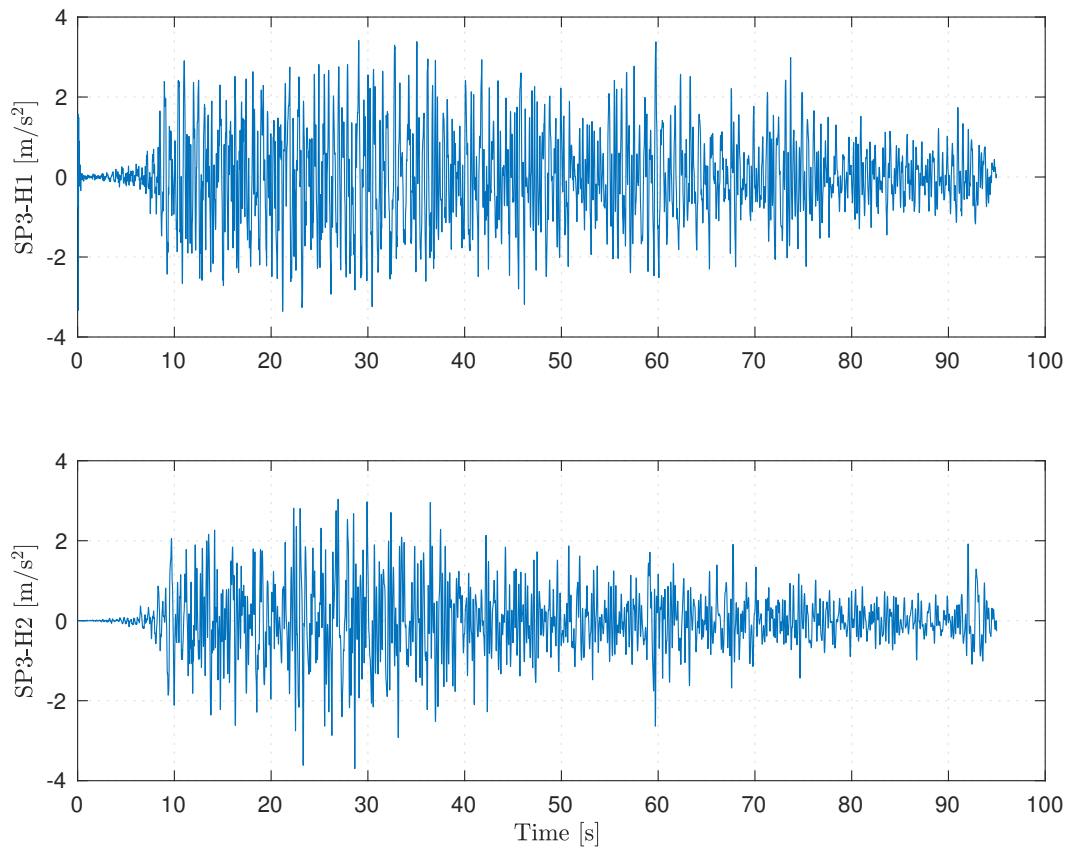
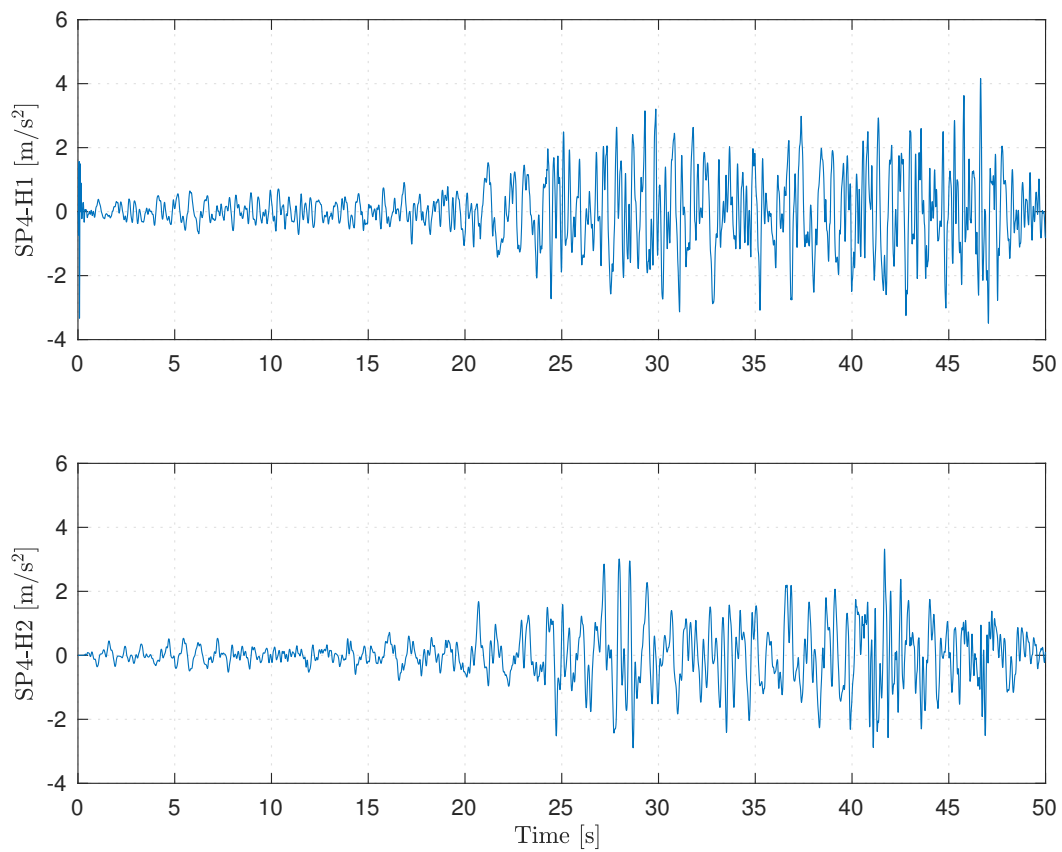


Figure 5.2: Input ground motion SP2

**Figure 5.3:** Input ground motion SP3**Figure 5.4:** Input ground motion SP4

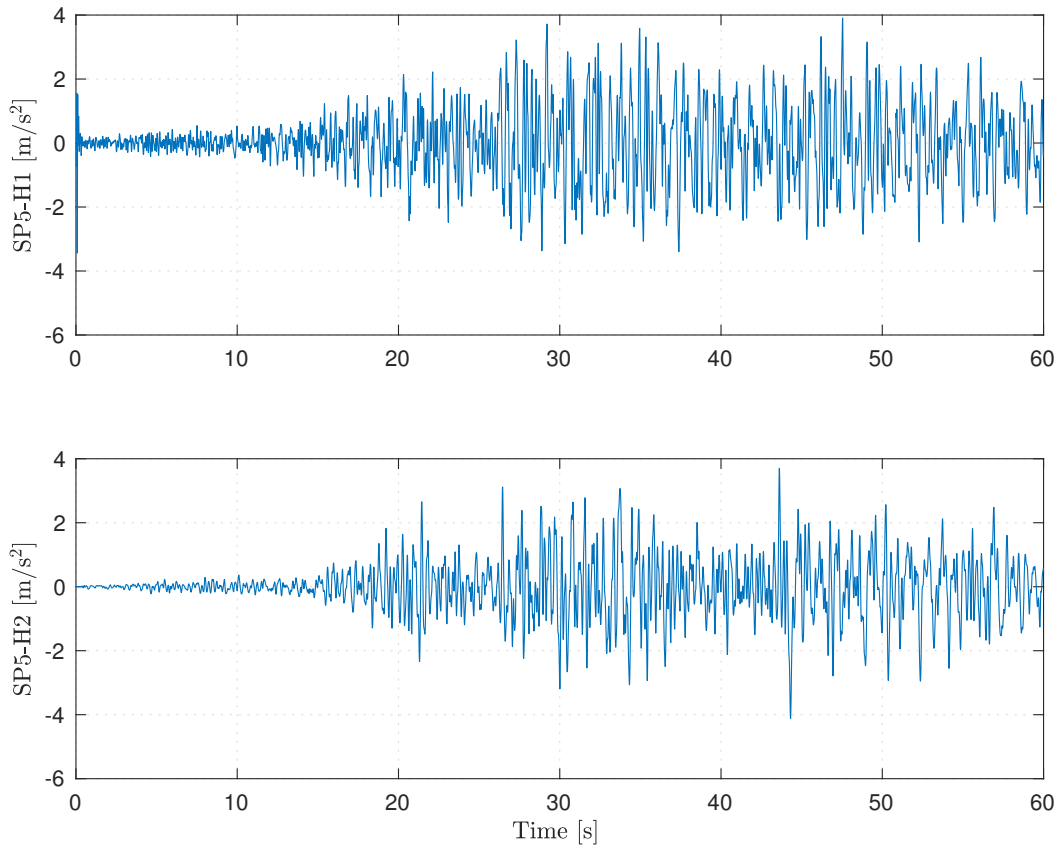


Figure 5.5: Input ground motion SP5

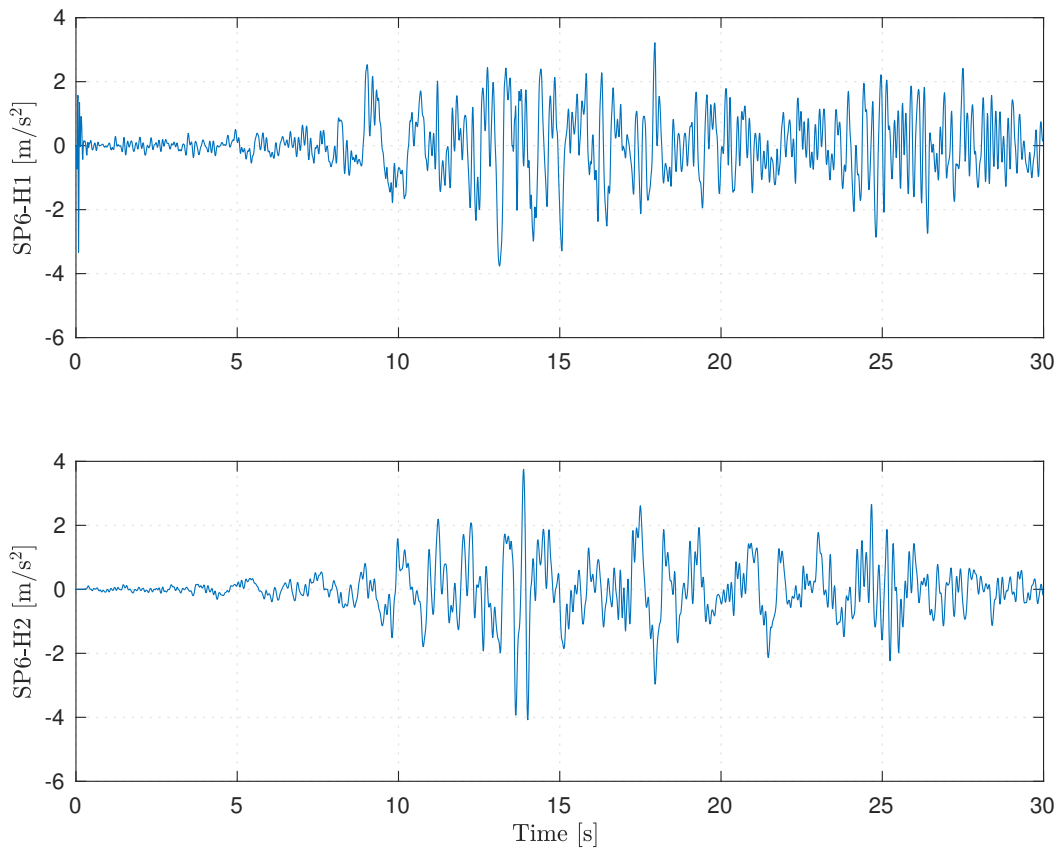


Figure 5.6: Input ground motion SP6

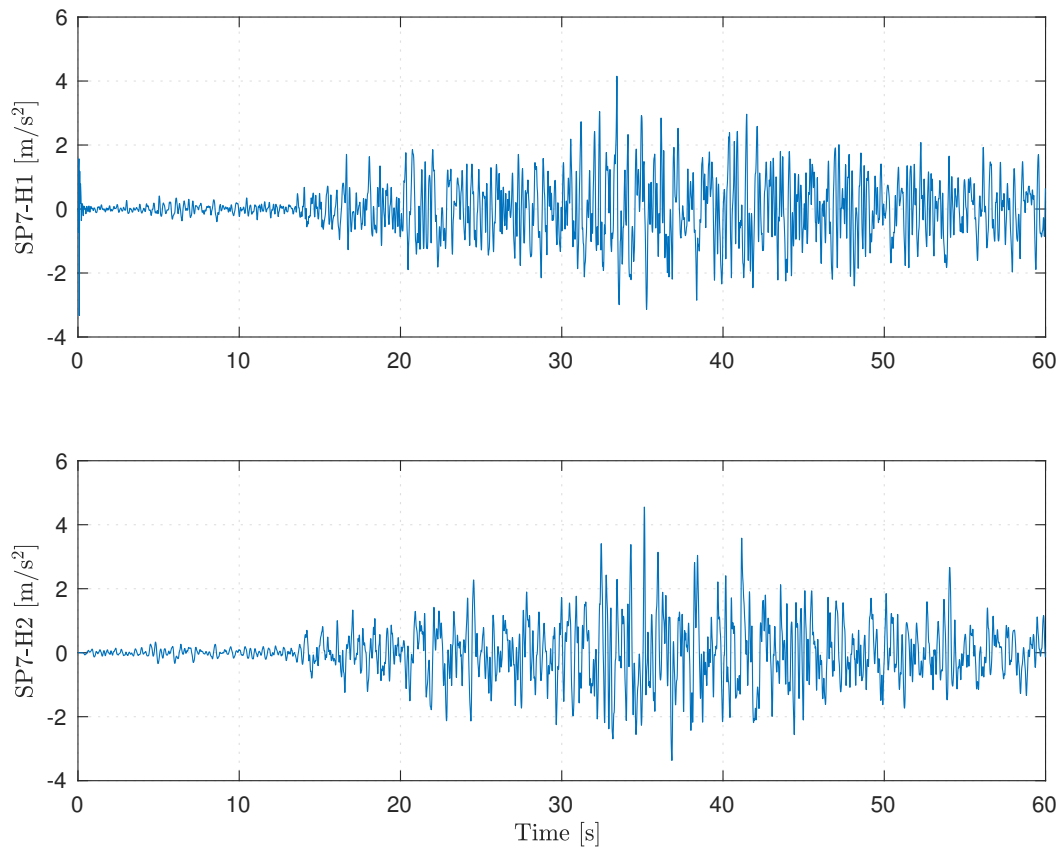


Figure 5.7: Input ground motion SP7

5.3 Secant Method for Time History Analyses

An OpenSees script was created to execute the Secant Method on the elastic pylon model through a series of iterations. However, due to limitations of the Tcl programming language, MATLAB was invoked during iterations to process the results before writing them to files that OpenSees subsequently would retrieve. The algorithm, which is also presented as a flow chart in figure 5.8, can be summarized as follows:

1. Perform several moment-curvature analyses in OpenSees for each section in the fiber model using gravity loads with different factors. Then, establish the initial bending stiffness for each element in both directions by calculating the slope of the tangent at the origin, using the moment-curvature relation with unit factor times the gravity load. All moment-curvature diagrams following these analyses can be found in appendix D.
2. Assemble the elastic model with the obtained initial stiffnesses. Define recorders to track values of interest, such as node displacements and accelerations as well as element forces. After applying gravity forces to the structure, perform a modal analysis to acquire eigen frequencies.
3. Conduct an elastic THA in both horizontal global directions simultaneously.

4. Invoke MATLAB to establish the axial forces corresponding to the largest absolute moments for each element in both directions. These forces include the axial loads resulting from self weight. Upon completion, MATLAB writes the results to text files.
5. Retrieve the axial forces in OpenSees and use these to conduct a new moment-curvature analysis for each section. This was only done for the cross-beams, as they experienced large variations in axial forces. The effect of varying axial force on the pylon legs was incorporated by interpolation between the different moment-curvature diagrams obtained in the first step. This could be justified seeing as the variation was relatively small and the method extremely time efficient.
6. Invoke MATLAB to calculate the updated stiffnesses. For the cross-beam elements, load the updated moment-curvature relations and find the intersection point of each curve and the corresponding moment resulting from the elastic THA. The secant line passes through the origin and this intersection point. The secant stiffness EI_{secant} is taken as the slope of the secant line. For the pylon legs, the intersection point is found using linear interpolation. To ensure stability and convergence, only a fraction $f = 0.5$ of the secant stiffness will be used. The updated stiffness EI_i of iteration i is taken as

$$EI_i = EI_{i-1} - f(EI_{i-1} - EI_{\text{secant}}) \quad (5.1)$$

where EI_{i-1} is the updated stiffness saved from the previous iteration $i - 1$. The ratio of updated stiffness to initial stiffness is then written to a file. The ratio R of initial stiffness about one of the two transverse element axes is taken as

$$R = \frac{EI_{\text{secant}}}{EI_{\text{Initial}}} \quad (5.2)$$

where EI_{secant} is the slope of the secant line and EI_{initial} is the slope of the initial tangent of the moment-curvature relation, using gravity forces only. If the change in updated stiffness is less than 5% from previous iteration, convergence is said to be met. The change is calculated as

$$\text{conv} = \left| \frac{|R_i| - |R_{i-1}|}{|R_{i-1}|} \right| \quad (5.3)$$

where conv denotes the percentage change and R the ratio of initial stiffness about local the y or z -axis. Convergence must be met for all elements about both transverse axes before a break statement can be passed to OpenSees, successfully terminating the script at the current iteration.

7. If no break statement has been passed to OpenSees upon completion of the MATLAB script, OpenSees will use the updated stiffness ratios in the next iteration, multiplying them with the initial stiffness. Entry 2 through 7 will then be repeated until convergence

is met or the maximum number of iterations is reached, which generally means that instability has occurred.

The above algorithm is in turn enveloped by a `for` loop in which the OpenSees script loops over all earthquake records, seen in section 5.2.1. Data regarding for instance maximum absolute moment is therefore saved specifying the *direction*, *element*, *iteration* and *earthquake record*, making it easy to retrieve and compare different data sets. If the procedure has reached convergence, the final elastic model with reduced flexural stiffnesses, from now on referred to simply as the reduced elastic model, will have properties which simulate nonlinear material behavior. The main OpenSees script used to perform the Secant Method can be found in appendix E along with the MATLAB script which is used to calculate the stiffness ratios in appendix F.

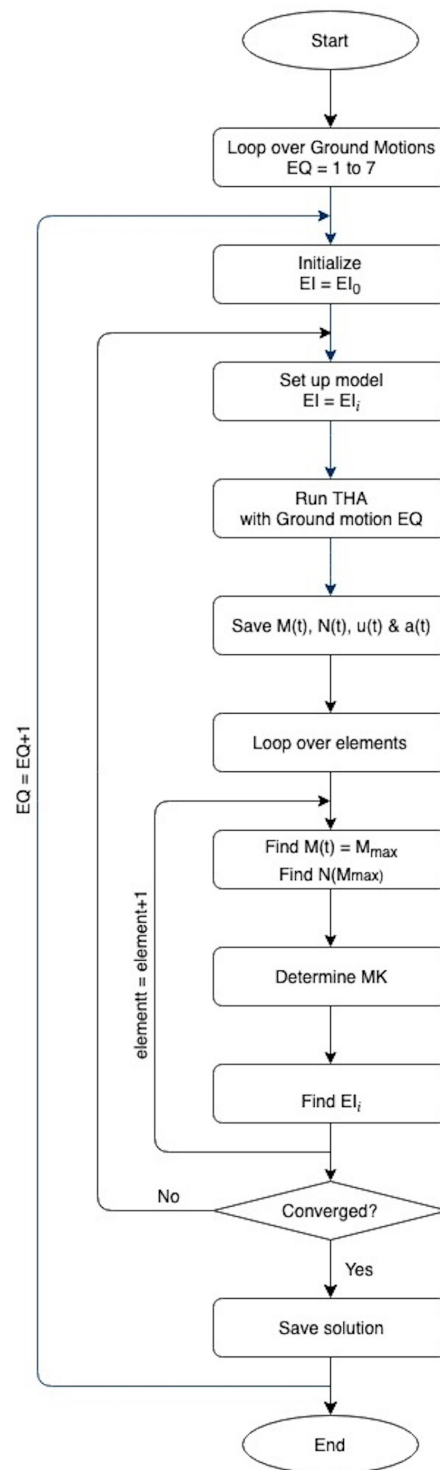


Figure 5.8: Flow chart showing the iteration procedure in detail

5.4 Pushover Analysis

Several pushover analyses were conducted to verify the models used for the THA, with the main objective being to control whether or not the iterative procedure is able to capture the nonlinear material behaviour of the pylon close to failure. Five different failure modes were selected to be analyzed further. For each of these modes, the applied forces were chosen as the lateral inertial forces corresponding to the most unfavourable time step in the response histories of the critical elements in the mode. Consequently, these response histories would correspond to the most critical ground motion for said elements. The inertial forces are extracted from the response histories of the fiber model, to remain consistent with the idea that the fiber model serves as the reference in this thesis. In practical cases, when a fiber model is not available, the force input should instead be taken from the response history of the reduced elastic model. In each analysis, the vertical forces, consisting of loads from the cables and the gravity loads, were held constant throughout the analysis. The sorting criteria for the failure modes, together with the earthquake record and corresponding time-step are shown in table 5.2 below.

Table 5.2: Sorting criteria and description of applied pushover loads

| Analysis | Description of sorting criterion | Direction | TH | Time [sec] |
|----------|---|-----------|-----|------------|
| L1 | Max moment in upper part of pylon leg (Max/min M_y for elements 4115 & 4215) | Long. | SP5 | 32.02 |
| L2 | Max moment at the base of pylon leg (Max/min M_z for elements 4101 & 4201) | Long. | SP2 | 35.37 |
| T1 | Max moment at the base of pylon leg (Max/min M_z for elements 4101 & 4201) | Trans. | SP2 | 48.43 |
| T2 | Max moment at lower cross-beam (Max/min M_y for elements 4501-4506) | Trans. | SP5 | 34.27 |
| T3 | Max moment at upper cross-beam (Max/min M_y for elements 4701-4704) | Trans. | SP1 | 26.16 |

5.4.1 Longitudinal direction - L1

The L1 analysis is based on the sorting criterion of finding the time-step across all 7 records where the maximum moment M_y occurs in the upper portion of the pylon leg, that is, in element 4115 and 4215. The acceleration profile and moment diagram for the given case are shown in figure 5.9. Governing values at corresponding elements:

- $M_y = 223$ MNm for west leg
- $M_y = 217$ MNm for east leg

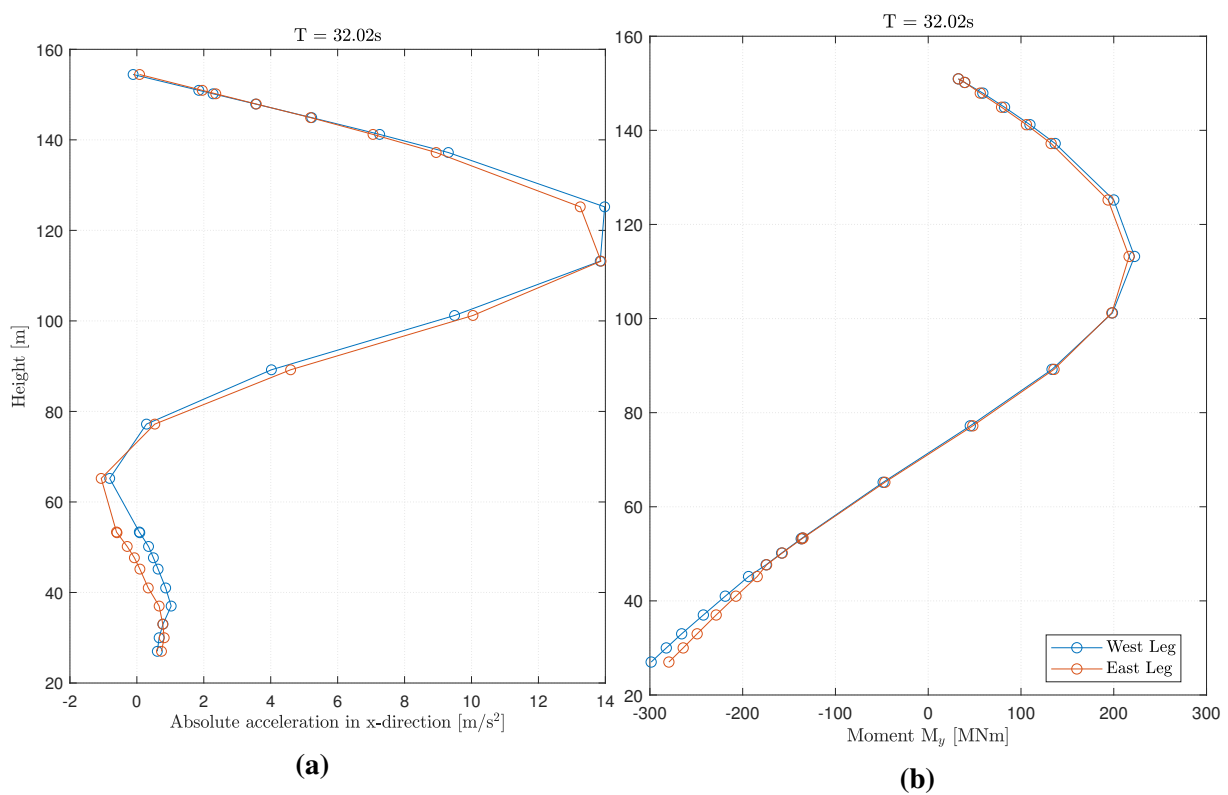


Figure 5.9: Acceleration profile and moment diagram for analysis L1

5.4.2 Longitudinal direction - L2

The L2 analysis is based on the sorting criterion of finding the time-step across all 7 records where the maximum moment M_y occurs at the base of the pylon legs, that is, in element 4101 and 4201. The acceleration profile and moment diagram for the given case are shown in figure 5.10. Governing values at corresponding elements:

- $M_y = 359$ MNm for west leg
- $M_y = 326$ MNm for east leg

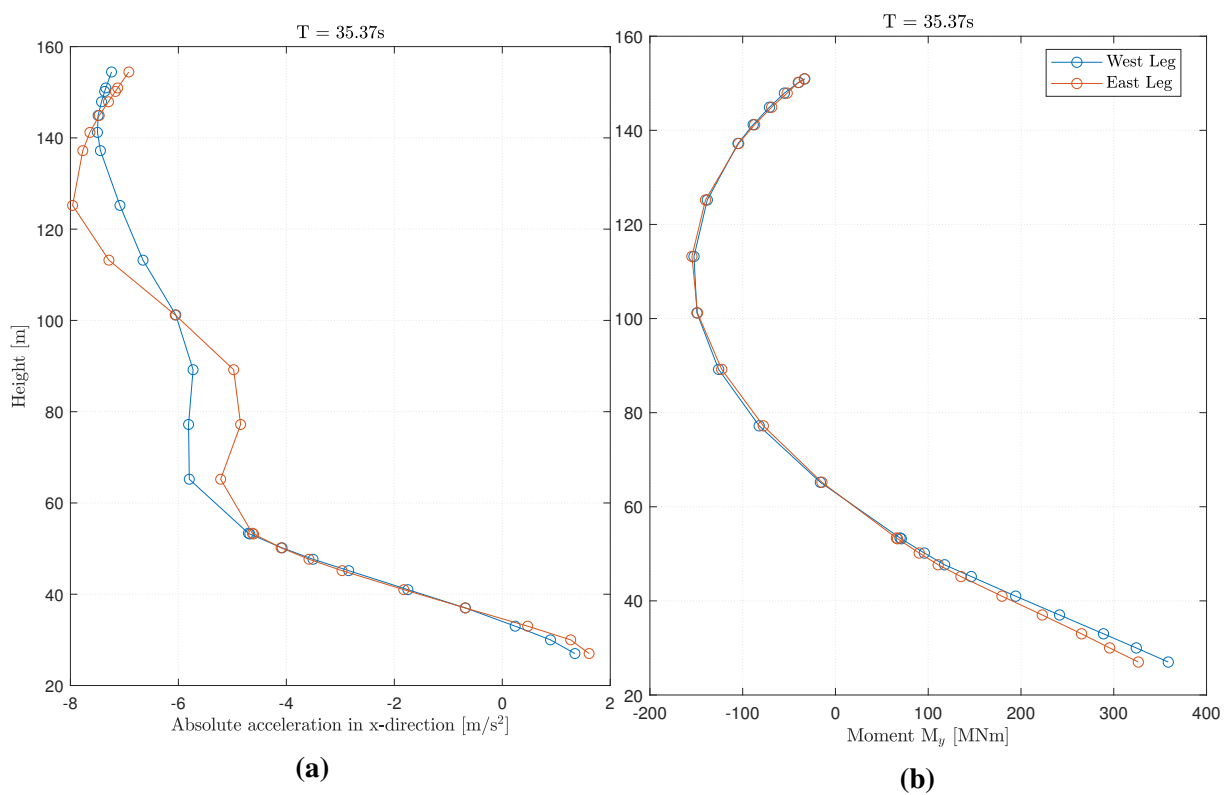


Figure 5.10: Acceleration profile and moment diagram for analysis L2

5.4.3 Transverse direction - T1

The T1 analysis is based on the sorting criterion of finding the time-step across all 7 records where the maximum moment M_z occurs in the lower portion of the pylon leg, in element 4101 and 4201. The acceleration profile and moment diagram for the given case are shown in figure 5.11. Governing values at corresponding elements:

- $M_z = 181$ MNm for west leg
- $M_z = 166$ MNm for east leg

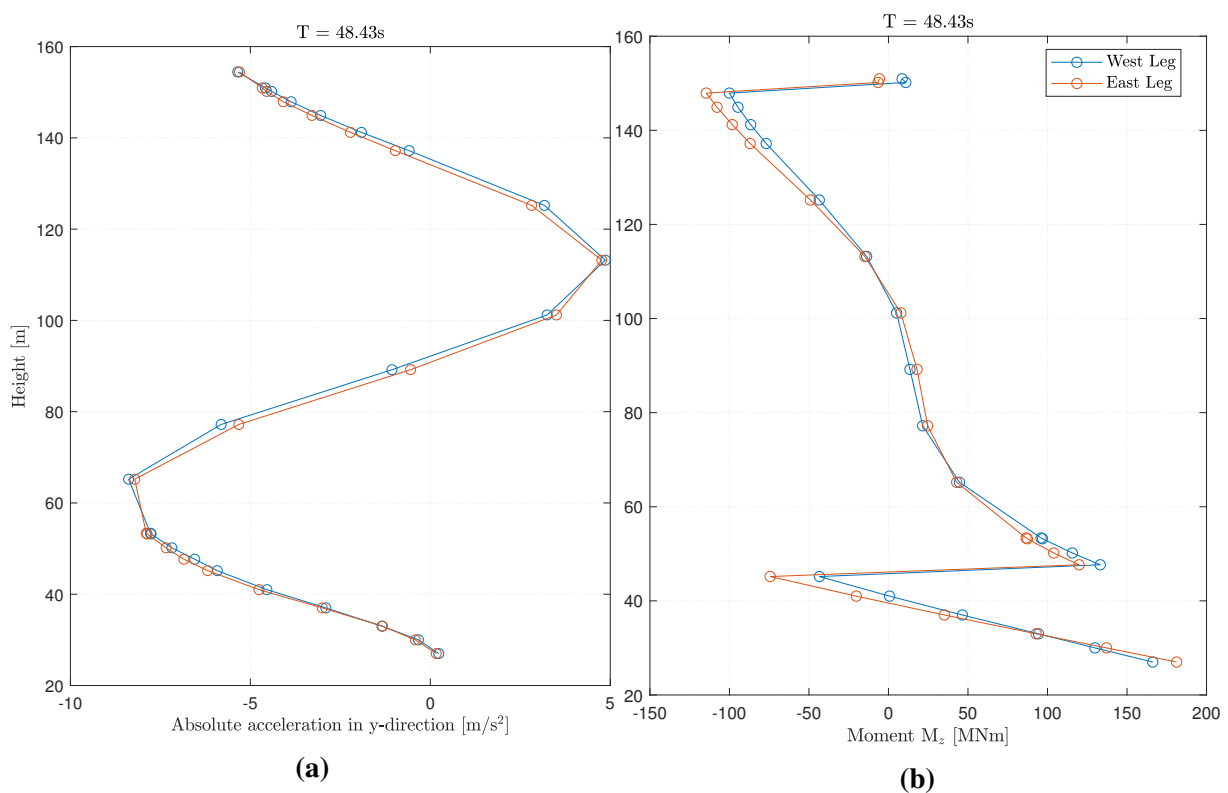


Figure 5.11: Acceleration profile and moment diagram for analysis T1

5.4.4 Transverse direction - T2

The T2 analysis is based on the sorting criterion of finding the time-step across all 7 records where the maximum moment M_y occurs in the lower cross-beam, elements 4501 to 4506. The acceleration profile and moment diagram along the height of the pylon for the given case are shown in figure 5.12. Governing values at corresponding elements:

- $M_y = 215$ MNm at the western end. Element 4501
- $M_y = 200$ MNm at the eastern end. Element 4506

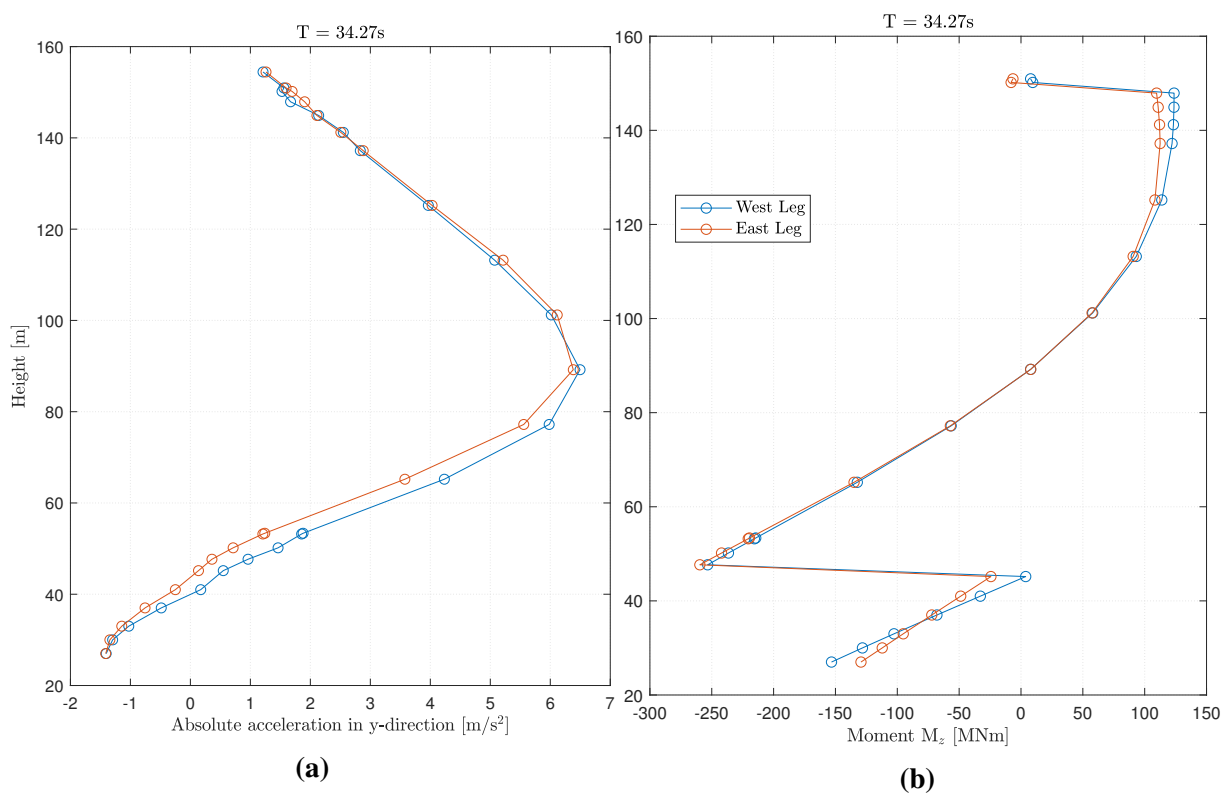


Figure 5.12: Acceleration profile and moment diagram for analysis T2

5.4.5 Transverse direction - T3

The T3 analysis is based on the sorting criterion of finding the time-step across all 7 records where the maximum moment M_y occurs in the upper cross-beam, elements 4701 to 4704. The acceleration profile and moment diagram along the height of the pylon for the given case are shown in figure 5.13. Governing values at corresponding elements:

- $M_y = 153$ MNm at the western end. Element 4701
- $M_y = 151$ MNm at the eastern end. Element 4704

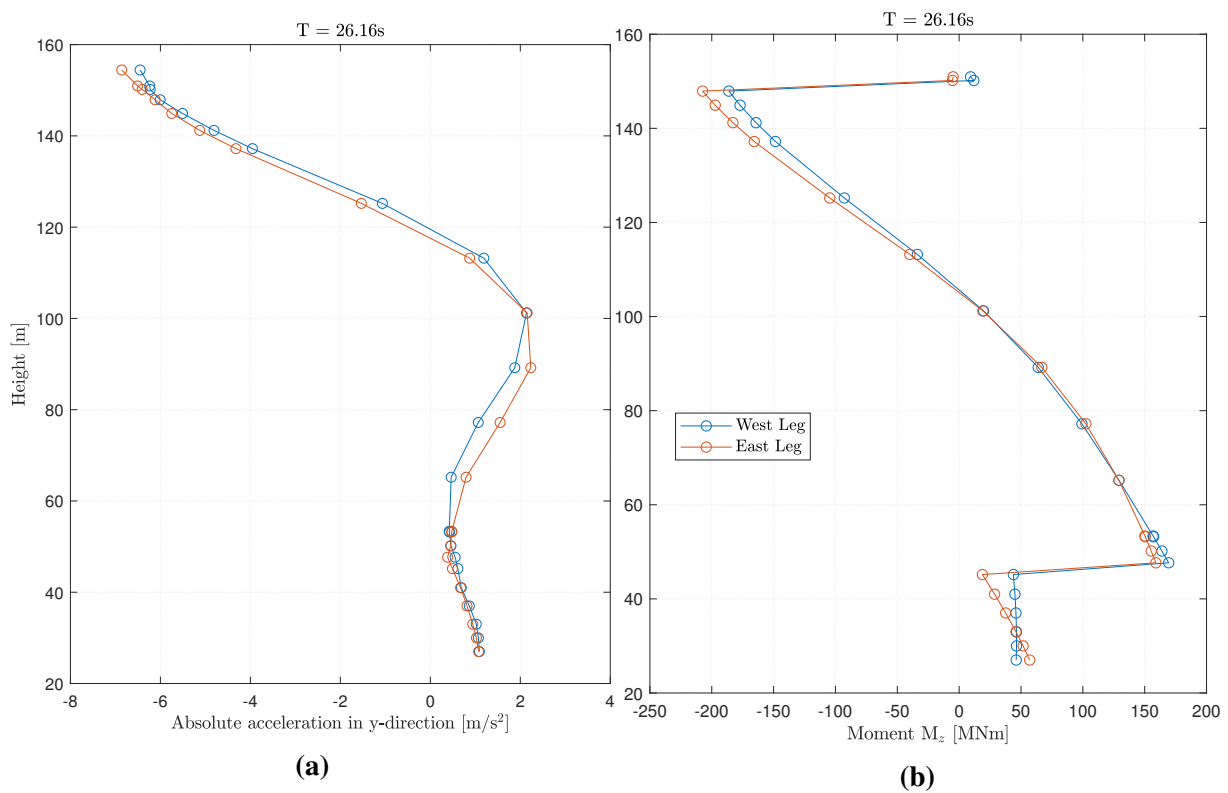


Figure 5.13: Acceleration profile and moment diagram for analysis T3

5.5 Secant Method for Pushover Analysis

The iterative procedure for calculating the secant stiffness of the RC sections is similar for both the pushover analysis and the method using THA, previously explained in section 5.3. There are some key differences, however. Thus, the following list will elaborate the algorithm in detail. The algorithm is also illustrated as a flow chart in figure 5.14. The load step increment, $\Delta\lambda$ is fixed as 0.05 for all the pushover analyses.

1. Perform a moment-curvature analysis in OpenSees for each section when subjected to various scaling of the gravity loads, and establish the initial stiffness for each element by calculating the tangent of the curve at the origin.
 2. Assemble the elastic model with obtained stiffnesses.
 3. Increment the load step $\lambda_i = \lambda_{i-1} + \Delta\lambda$.
 4. Define recorders tracking moment at all elements, and displacements in all nodes of interest. Run the analysis with the current value of λ .
 5. Start new iteration loop. Hold the value of λ constant throughout the iteration loop.
 - 5.1. Invoke MATLAB to compute the updated stiffness for each element based on their corresponding cross sectional forces. Calculate the secant stiffness EI_{secant} . The updated stiffness EI_i of iteration i is taken as equation (5.1).
 - 5.2. Check for convergence. If converged jump to point 6.
 - 5.3. Check if maximum number of iterations has been reached. If so exit the analysis
 - 5.4. If the convergence criteria has not been met, start iteration $i + 1$, using the updated stiffnesses EI_i .
 6. Increase the load step λ by $\Delta\lambda$, and start the next load step.
 7. Repeat points 2.-6. until OpenSees fails to converge within the maximum number of iterations.
-

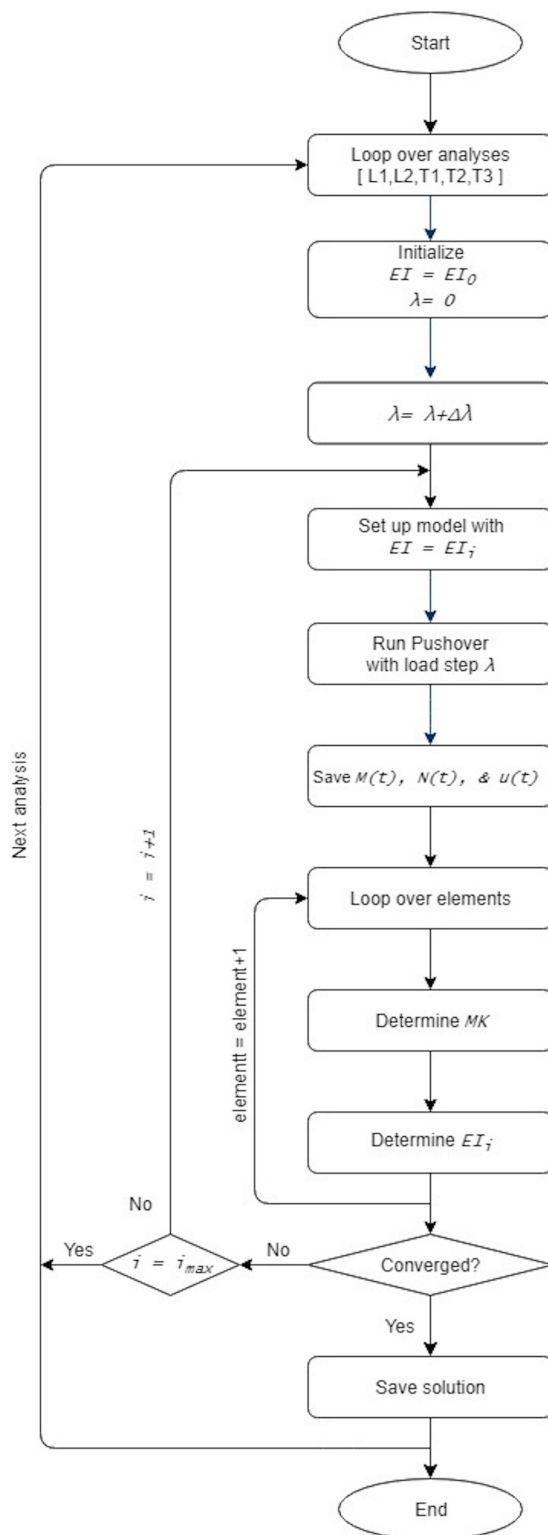


Figure 5.14: Flow chart showing the iteration procedure for the pushover analysis in detail

Chapter 6

Results

6.1 Results from the Time History Analysis

The results following the Secant Method, using the elastic model was compared to those resulting from the NTHA using the fiber model. Doing so for all seven ground motions established a solid base to further investigate if the Secant Method indeed carried out as expected. One of the goals of the Secant Method is to approximate the force distribution following a NTHA by simulating the nonlinear material behaviour in the structure. The development of the bending moments during the iterative procedure is therefore of high interest, specifically how well these values eventually compare to those following the NTHA. A vast library of data was available upon completion of the two fundamental different approaches which could be further processed in MATLAB.

In the following subsections, results for selected elements will be investigated further. These elements are located in segments with large bending moments about one or both transverse axes and are thus prone to undergo a reduction of stiffness. The selected elements are 4101, 4103, 4106, 4112, 4115, 4120, 4501 and 4701, which can be seen in figure 4.1b.

6.1.1 Stiffness Ratios

The figures and tables below summarize the core of the Secant Method itself for the selected elements upon completion of the entire procedure. The responses stem from 6 iterations where the ground motion record SP2 was applied in both horizontal directions. Only the response history about one of the two transverse axes for each element is shown. Each element history is summarized using three figures and one table. The first two figures, for example figure 6.1a and 6.1b, depict the approach to compute the secant line and the resulting reduction of stiffness, respectively. The solid blue line in figure 6.1a represent the moment-curvature relation for the corresponding section used in the fiber model, with normal forces from gravity only, obtained as described in section 3.1. The two adjacent dashed lines are moment-curvature relations using the same section but for increased and decreased normal forces, 0.8N and 1.2N. These, along with other similar lines that are not shown, have been used to incorporate the effect of varying axial forces by means of interpolation. Note that this is not the case for the cross-beam elements, discussed in section 5.3. The moment and the corresponding secant line following the initial and the final iteration are depicted as green and red solid lines, respectively. The gray

toned moment-secant pairs represent the intermediate values. Figure 6.1b to the right show the development of the section stiffness. The ratio is established using equation (5.2) after the secant slope has been determined during each iteration, seen as the red dots in figure 6.1b. Only a fraction of this value is carried to the next iteration, however, using equation (5.1). The resulting ratio used in the next iteration can be seen as the blue dots.

The moments and corresponding axial forces used in figure 6.1a can be seen in figure 6.2. The top sub figure shows the moment resulting from each THA, further used to establish secant lines. The solid blue line is the corresponding moment resulting from the NTHA, which the Secant Method is suppose to approximate. The sub plot below shows the axial force in the element, obtained at the same time instance during the THA as the moment. The solid gray toned line represent the axial force resulting from self weight only.

Table 6.1 further summarizes the data following each iteration. The first row specify the ground motion record used, local element axis depicted and the initial second moment of area about this axis. The last value is found by dividing the initial stiffness $EI_{initial}$ by the E-modulus of concrete. The first column shows the iteration number. The second and the third column shows the second moment of area in units of m^4 resulting from the secant line and the 50% weighted value, respectively. These values are also found by dividing the appropriate stiffnesses by the E-modulus of concrete. The fourth column shows the ratio, which again is after only using 50% of the new secant stiffness and thus are shown as the blue line in figure 6.1b. The fifth column also results from the blue line in figure 6.1b, and show the percentage change calculated using equation (5.3). This value is used as the convergence criteria and convergence is said to be met when it is below 5% or 0.05. As can be seen in table 6.1, however, iterations still continue after this value is passed. This is because the procedure does not stop until all elements in the structure have reached convergence. The sixth column show the axial force in the element following the THA normalized by the self weight axial load, both seen in figure 6.2. The final column shows the maximum moment values in units of MNm following the THA, also seen in figure 6.1a and 6.2.

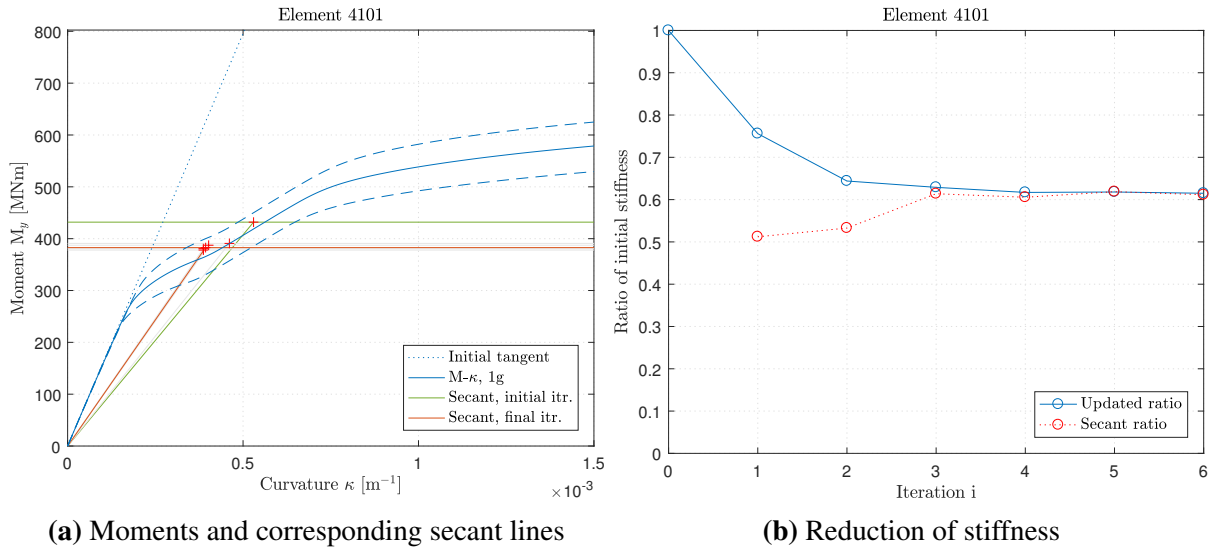


Figure 6.1

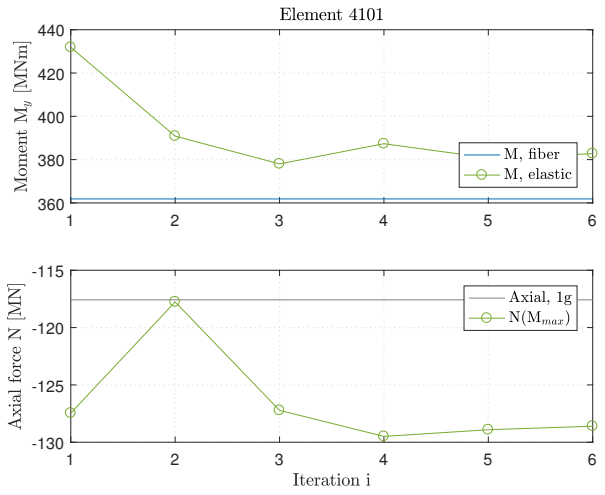


Figure 6.2: Max moment and axial forces

SP2, y-axis, $I_{initial} = 49.58 \text{ m}^4$

| i | I_{secant} | $I_{reduced}$ | ratio | conv | axial | M_y |
|---|--------------|---------------|-------|------|-------|-------|
| 1 | 25.39 | 37.48 | 0.76 | 0.24 | 1.08 | 432 |
| 2 | 26.41 | 31.94 | 0.64 | 0.15 | 1.00 | 391 |
| 3 | 30.43 | 31.18 | 0.63 | 0.02 | 1.08 | 378 |
| 4 | 30.02 | 30.60 | 0.62 | 0.02 | 1.10 | 387 |
| 5 | 30.68 | 30.63 | 0.62 | 0.00 | 1.10 | 381 |
| 6 | 30.32 | 30.48 | 0.61 | 0.01 | 1.09 | 383 |

Table 6.1: Summary of figure values

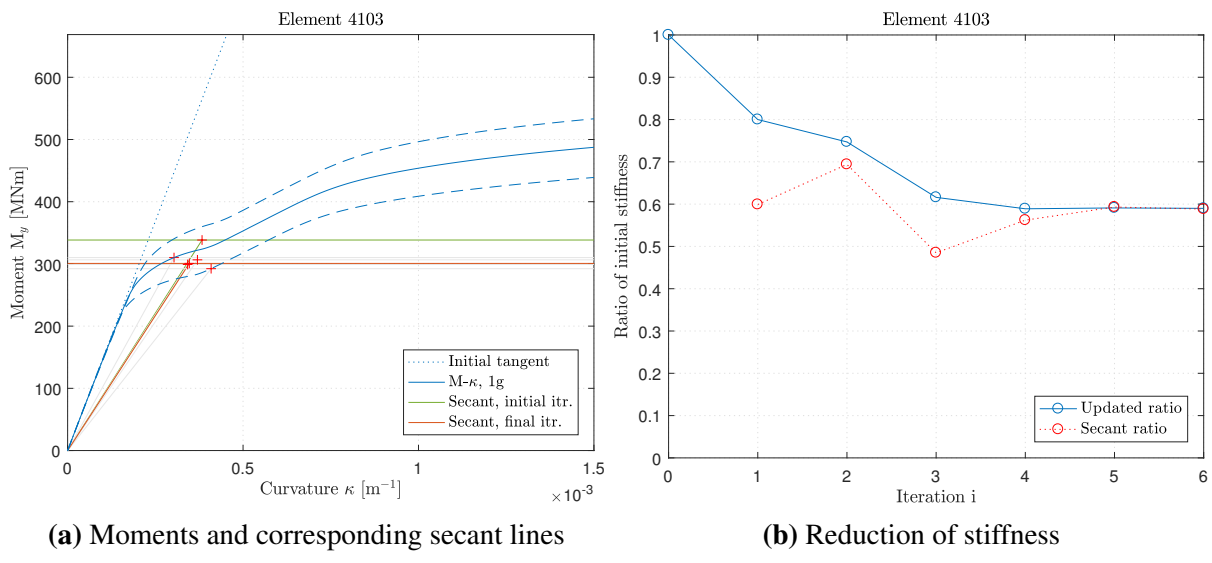


Figure 6.3

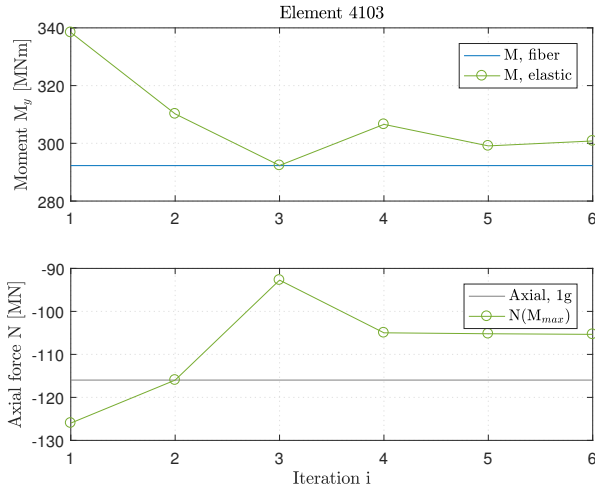
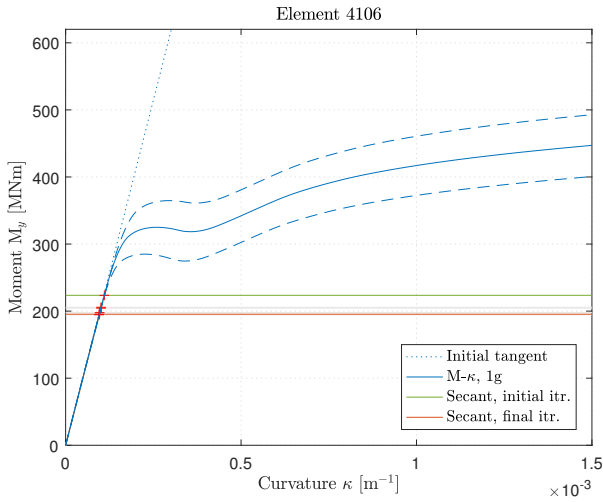


Figure 6.4: Max moment and axial forces

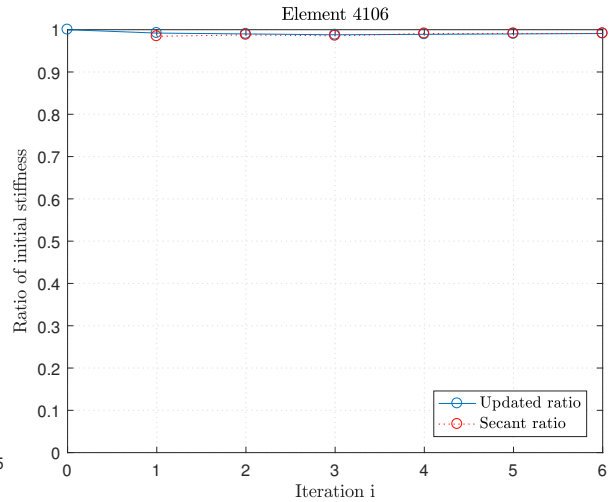
SP2, y-axis, $I_{initial} = 45.93 \text{ m}^4$

| i | I_{secant} | $I_{reduced}$ | ratio | conv | axial | M_y |
|---|--------------|---------------|-------|------|-------|-------|
| 1 | 27.52 | 36.72 | 0.80 | 0.20 | 1.09 | 338 |
| 2 | 31.87 | 34.30 | 0.75 | 0.07 | 1.00 | 310 |
| 3 | 22.27 | 28.29 | 0.62 | 0.17 | 0.80 | 292 |
| 4 | 25.81 | 27.05 | 0.59 | 0.04 | 0.91 | 307 |
| 5 | 27.24 | 27.15 | 0.59 | 0.00 | 0.91 | 299 |
| 6 | 27.02 | 27.08 | 0.59 | 0.00 | 0.91 | 301 |

Table 6.2: Summary of figure values



(a) Moments and corresponding secant lines



(b) Reduction of stiffness

Figure 6.5

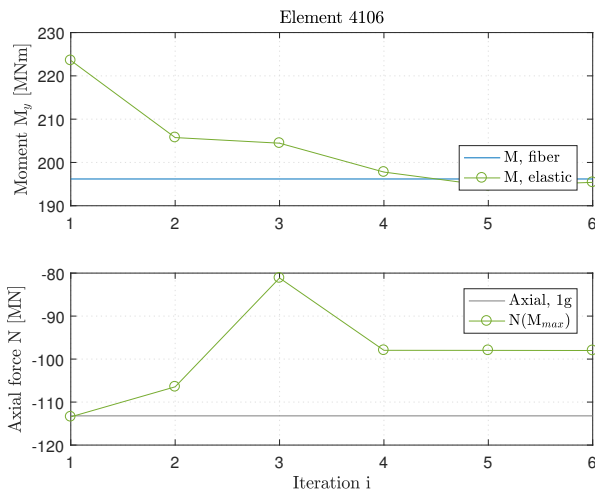
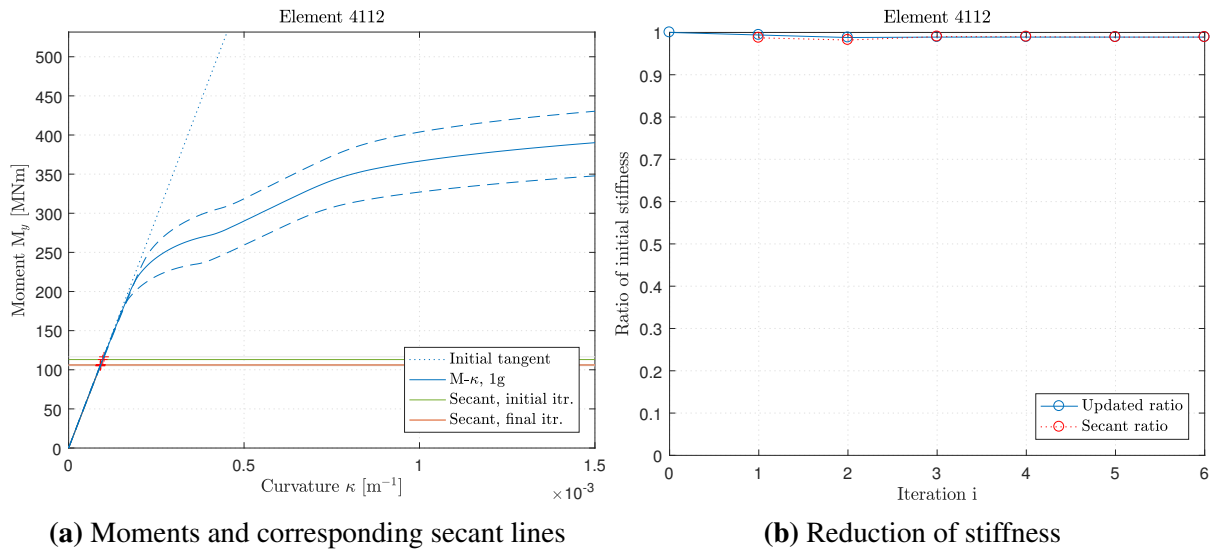


Figure 6.6: Max moment and axial forces

SP2, y-axis, $I_{initial} = 64.10 \text{ m}^4$

| i | I_{secant} | $I_{reduced}$ | ratio | conv | axial | M_y |
|---|--------------|---------------|-------|------|-------|-------|
| 1 | 63.09 | 63.60 | 0.99 | 0.01 | 1.00 | 224 |
| 2 | 63.31 | 63.45 | 0.99 | 0.00 | 0.94 | 206 |
| 3 | 63.17 | 63.31 | 0.99 | 0.00 | 0.72 | 204 |
| 4 | 63.51 | 63.42 | 0.99 | 0.00 | 0.87 | 198 |
| 5 | 63.53 | 63.46 | 0.99 | 0.00 | 0.87 | 195 |
| 6 | 63.52 | 63.49 | 0.99 | 0.00 | 0.87 | 195 |

Table 6.3: Summary of figure values



(a) Moments and corresponding secant lines

(b) Reduction of stiffness

Figure 6.7

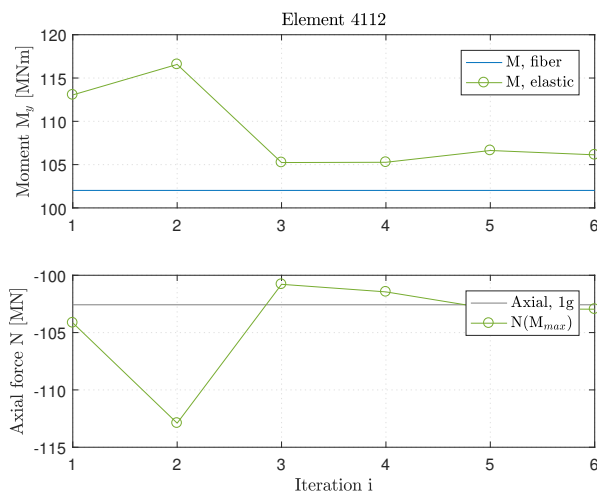
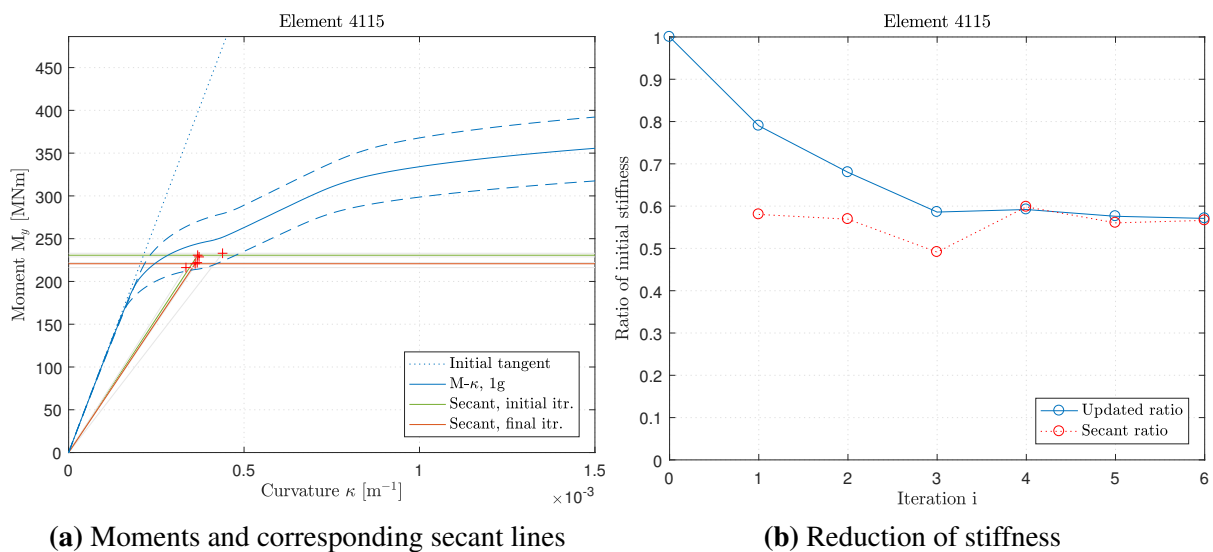


Figure 6.8: Max moment and axial forces

SP2, y-axis, $I_{initial} = 36.66 \text{ m}^4$

| i | I_{secant} | $I_{reduced}$ | ratio | conv | axial | M_y |
|---|--------------|---------------|-------|------|-------|-------|
| 1 | 36.19 | 36.43 | 0.99 | 0.01 | 1.02 | 113 |
| 2 | 36.01 | 36.22 | 0.99 | 0.01 | 1.10 | 117 |
| 3 | 36.30 | 36.26 | 0.99 | 0.00 | 0.98 | 105 |
| 4 | 36.29 | 36.27 | 0.99 | 0.00 | 0.99 | 105 |
| 5 | 36.25 | 36.26 | 0.99 | 0.00 | 1.00 | 107 |
| 6 | 36.26 | 36.26 | 0.99 | 0.00 | 1.00 | 106 |

Table 6.4: Summary of figure values



(a) Moments and corresponding secant lines

(b) Reduction of stiffness

Figure 6.9

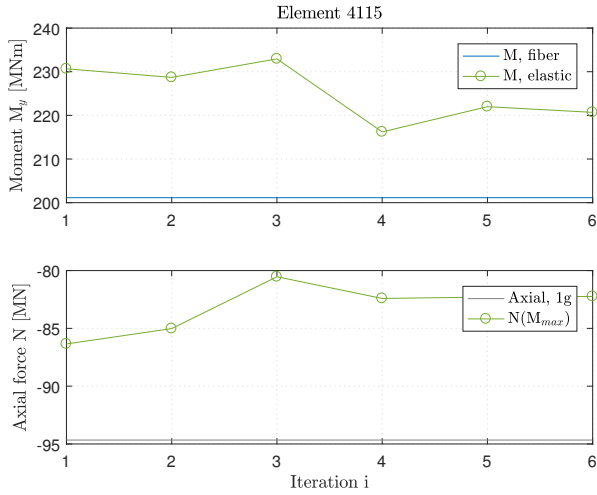
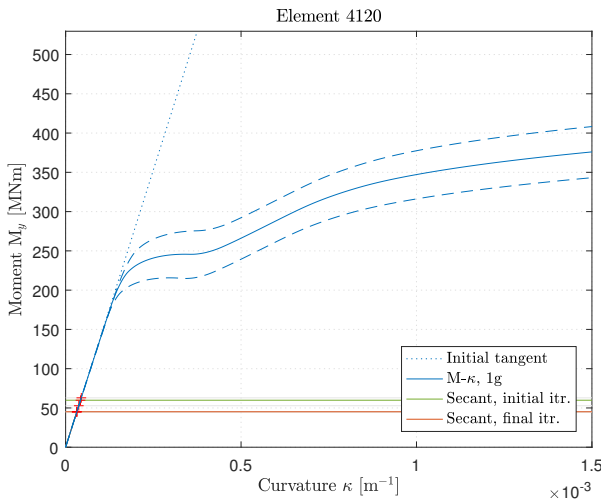


Figure 6.10: Max moment and axial forces

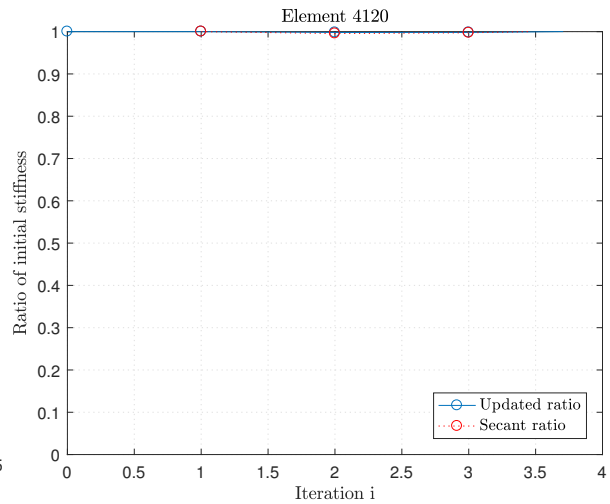
SP2, y-axis, $I_{initial} = 33.66 \text{ m}^4$

| i | I_{secant} | $I_{reduced}$ | ratio | conv | axial | M_y |
|---|--------------|---------------|-------|------|-------|-------|
| 1 | 19.54 | 26.60 | 0.79 | 0.21 | 0.91 | 231 |
| 2 | 19.16 | 22.88 | 0.68 | 0.14 | 0.90 | 229 |
| 3 | 16.54 | 19.72 | 0.59 | 0.14 | 0.85 | 233 |
| 4 | 20.14 | 19.93 | 0.59 | 0.01 | 0.87 | 216 |
| 5 | 18.87 | 19.40 | 0.58 | 0.03 | 0.87 | 222 |
| 6 | 19.06 | 19.23 | 0.57 | 0.01 | 0.87 | 221 |

Table 6.5: Summary of figure values



(a) Moments and corresponding secant lines



(b) Reduction of stiffness

Figure 6.11

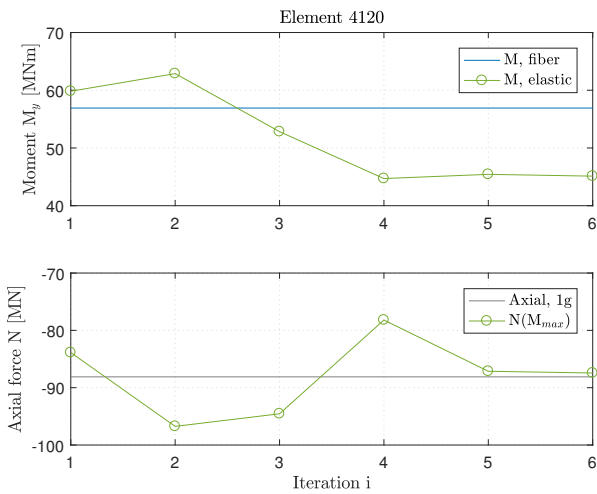


Figure 6.12: Max moment and axial forces

SP2, y-axis, $I_{initial} = 43.99 \text{ m}^4$

| i | I_{secant} | $I_{reduced}$ | ratio | conv | axial | M_y |
|---|--------------|---------------|-------|------|-------|-------|
| 1 | 43.99 | 43.99 | 1.00 | 0.00 | 0.95 | 60 |
| 2 | 43.79 | 43.89 | 1.00 | 0.00 | 1.10 | 63 |
| 3 | 43.87 | 43.88 | 1.00 | 0.00 | 1.07 | 53 |
| 4 | 44.14 | 44.02 | 1.00 | 0.00 | 0.89 | 45 |
| 5 | 44.01 | 44.02 | 1.00 | 0.00 | 0.99 | 45 |
| 6 | 44.00 | 44.02 | 1.00 | 0.00 | 0.99 | 45 |

Table 6.6: Summary of figure values

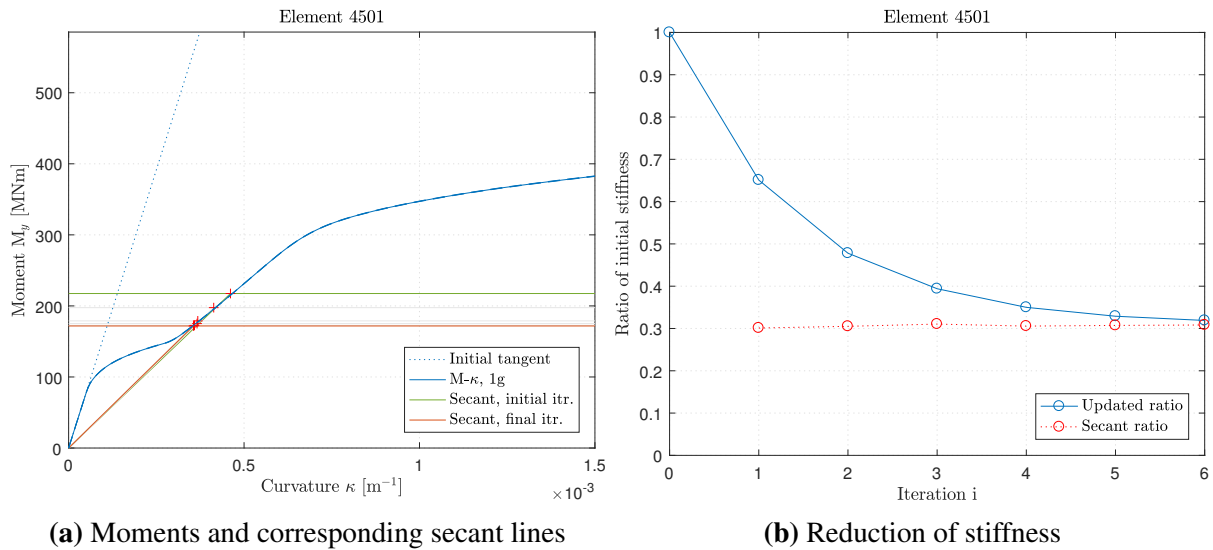


Figure 6.13

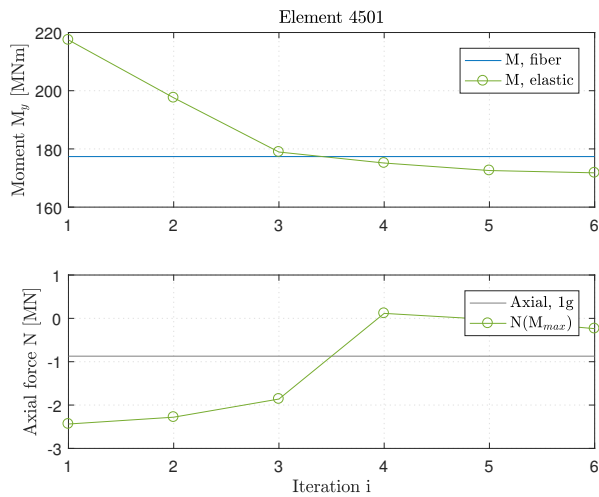


Figure 6.14: Max moment and axial forces

SP2, y-axis, $I_{initial} = 48.78 \text{ m}^4$

| i | I_{secant} | $I_{reduced}$ | ratio | conv | axial | M_y |
|---|--------------|---------------|-------|------|-------|-------|
| 1 | 14.69 | 31.73 | 0.65 | 0.35 | 2.90 | 217 |
| 2 | 14.88 | 23.32 | 0.48 | 0.27 | 2.66 | 198 |
| 3 | 15.14 | 19.23 | 0.39 | 0.17 | 2.16 | 179 |
| 4 | 14.91 | 17.06 | 0.35 | 0.11 | -0.13 | 175 |
| 5 | 14.99 | 16.03 | 0.33 | 0.06 | 0.03 | 173 |
| 6 | 15.04 | 15.54 | 0.32 | 0.03 | 0.28 | 172 |

Table 6.7: Summary of figure values

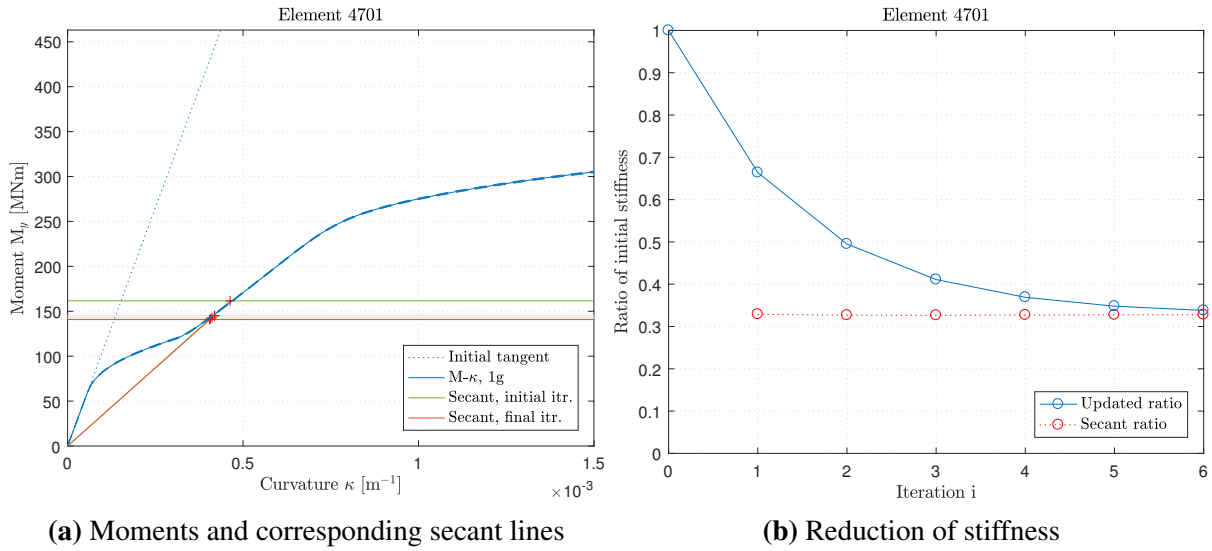


Figure 6.15

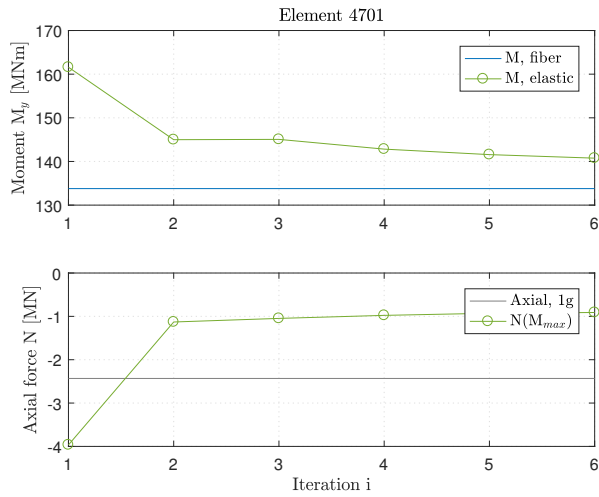


Figure 6.16: Max moment and axial forces

| SP2, y-axis, $I_{initial} = 33.04 \text{ m}^4$ | | | | | | |
|--|--------------|---------------|-------|------|-------|-------|
| i | I_{secant} | $I_{reduced}$ | ratio | conv | axial | M_y |
| 1 | 10.87 | 21.96 | 0.66 | 0.34 | 1.64 | 162 |
| 2 | 10.79 | 16.37 | 0.50 | 0.25 | 0.47 | 145 |
| 3 | 10.78 | 13.57 | 0.41 | 0.17 | 0.43 | 145 |
| 4 | 10.81 | 12.20 | 0.37 | 0.10 | 0.40 | 143 |
| 5 | 10.82 | 11.51 | 0.35 | 0.06 | 0.38 | 142 |
| 6 | 10.84 | 11.17 | 0.34 | 0.03 | 0.37 | 141 |

Table 6.8: Summary of figure values

6.1.2 Response History

The main parameters of interest during these procedures are displacements and bending moments about the two element axes, the latter used when calculating the secant stiffness. As stated in section 5.3, the moment values were obtained separately for both axes, independent of sign and time. The same applies for the maximum displacement values. Figures 6.17-6.33 summarize these values, for selected elements and one ground motion only; SP2. Each figure contains two sub figures, top and bottom, displaying the response at one node/element end in the local y and z direction, respectively. Each plot contains three response histories in the time domain; one resulting from the NTHA using the fiber model and two following a THA using the initial and the final elastic model. The initial elastic model refers to the first iteration of Secant Method, where all elements still retain their complete flexural stiffness. The final elastic model correspondingly refers to the elastic model following a number of iterations, during which several element stiffnesses have been reduced and eventually have converged to a steady stiffness reduction ratio. Only the first and the last response histories are included so to make the plots more comprehensible and because they to some extent envelope the intermediate results. Each plot contains the maximum absolute value for each of the result histories, marked with a circle. To further make the plots digestible, only a certain time interval of the original history is included. For each figure, this time frame includes all six maximum values, three in each direction. Since all figures stem from the same ground motion record, SP2, they have been subjected to the same number of iterations.

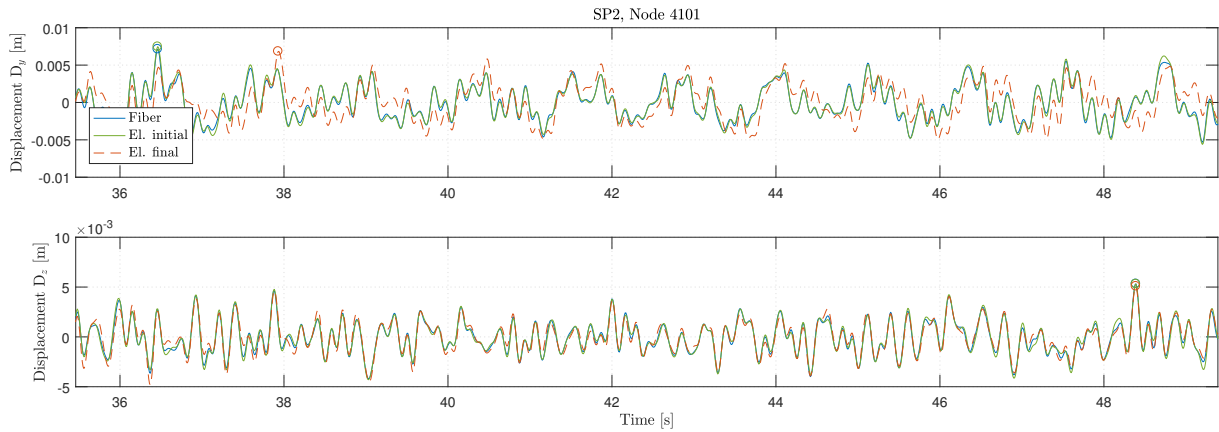


Figure 6.17: Displacement history from the first pylon leg node above foundation

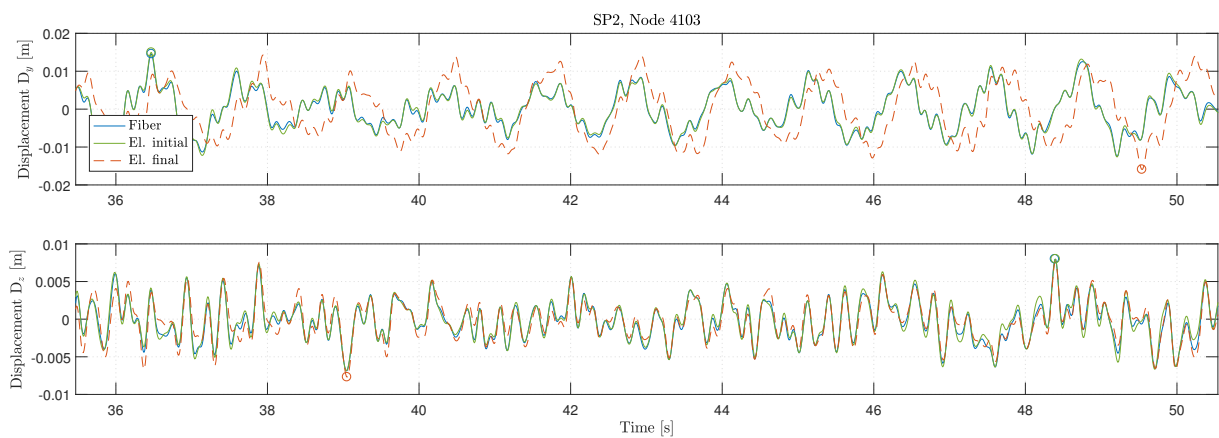


Figure 6.18: Displacement history from the middle of the leg segment connecting tie-beam and the lower cross-beam

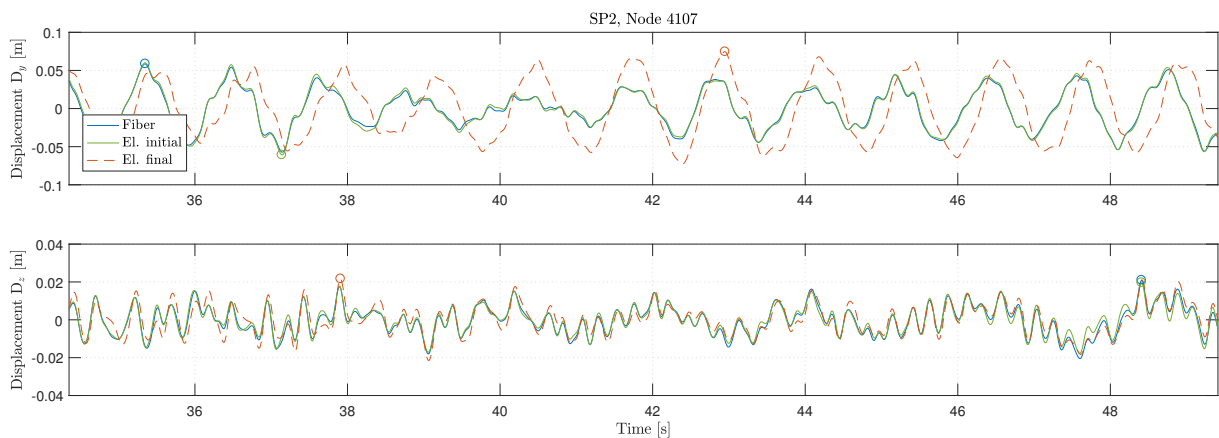


Figure 6.19: Displacement history from the node connected to the lower cross-beam

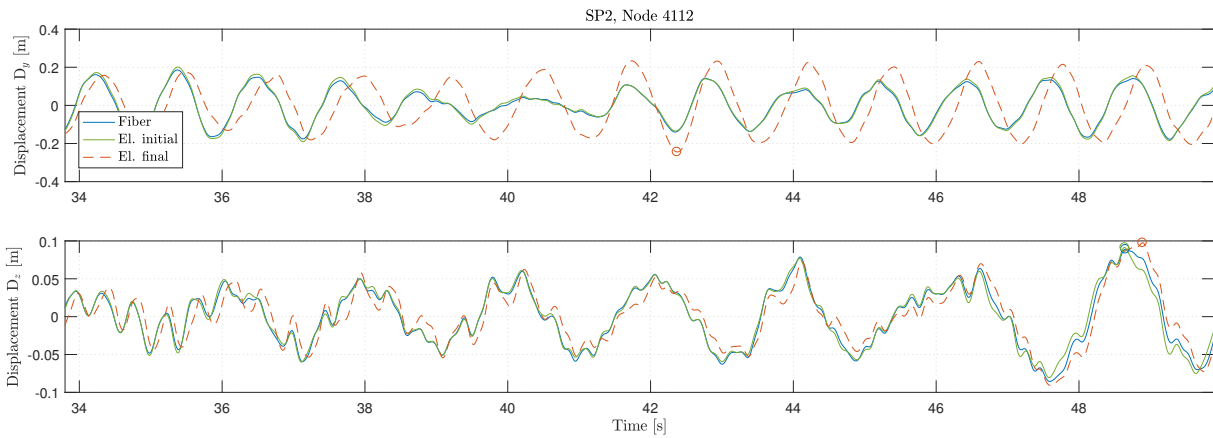


Figure 6.20: Displacement history from intermediate node along the leg segment connecting the lower and upper cross-beam

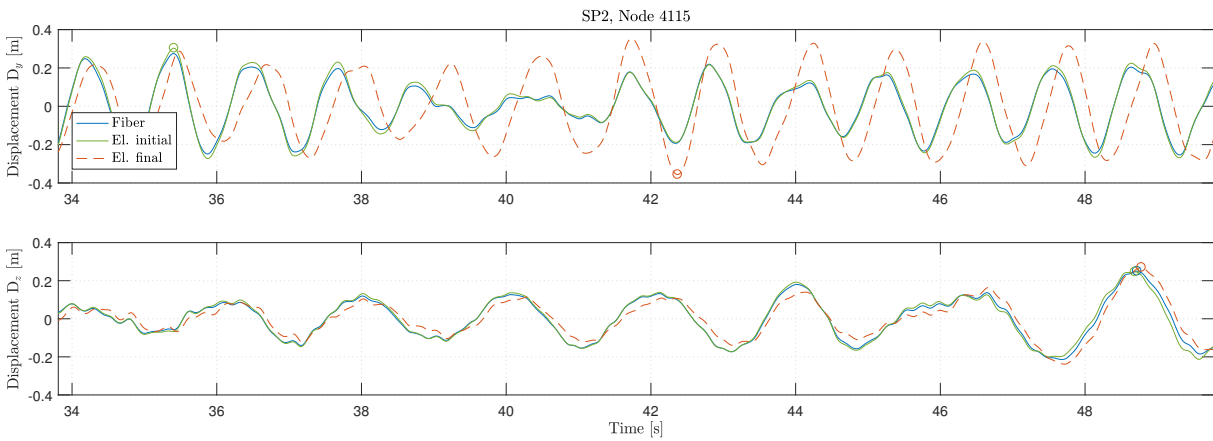


Figure 6.21: Displacement history from intermediate node along the leg segment connecting the lower and upper cross-beam

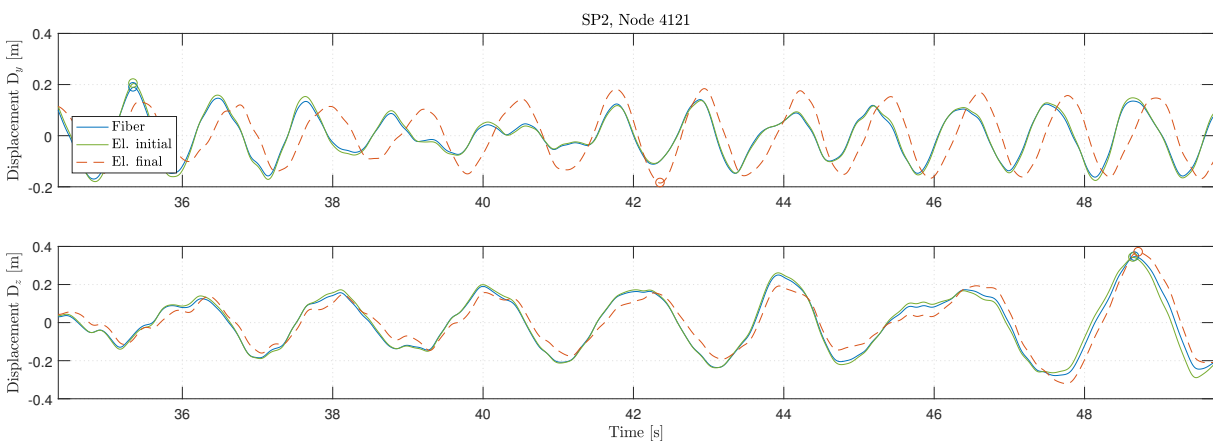


Figure 6.22: Displacement history from the node connected to the upper cross-beam

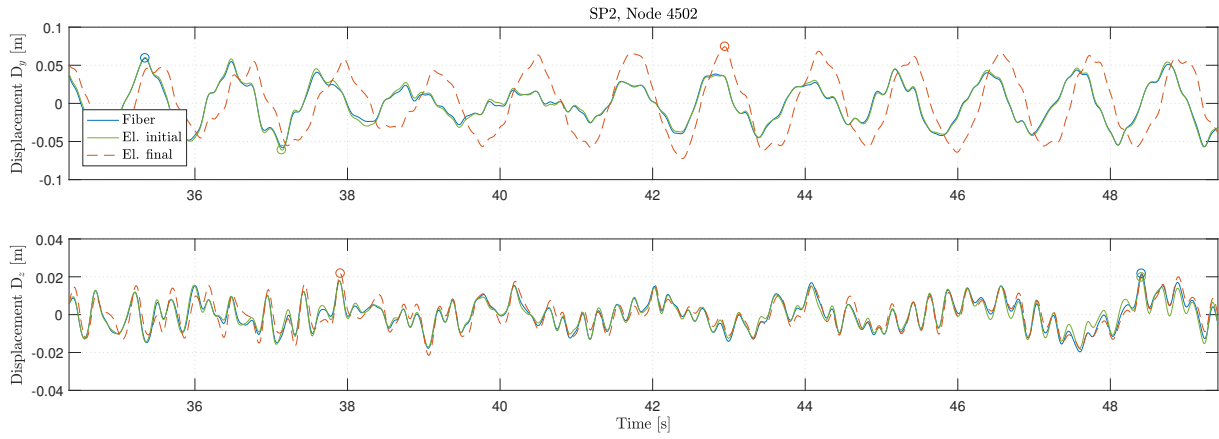


Figure 6.23: Displacement history from the 2nd node of the lower cross-beam

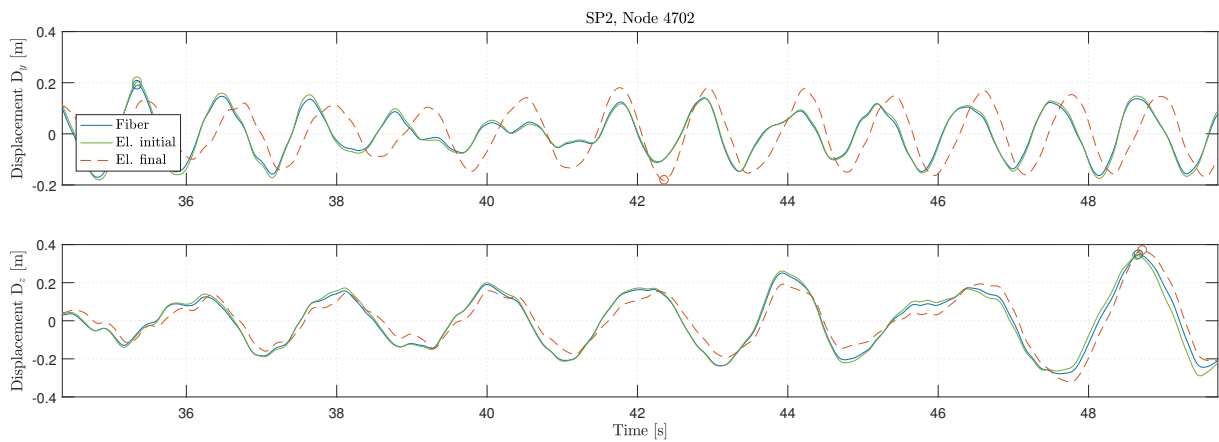
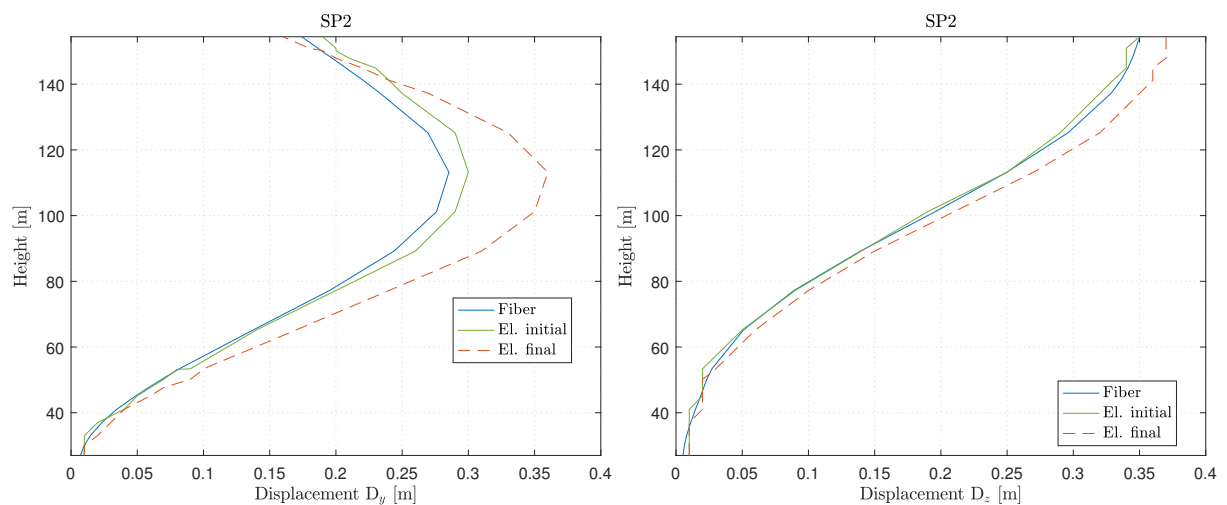


Figure 6.24: Displacement history from the 2nd node of the upper cross-beam

Figure 6.25 below depicts the maximum absolute displacement values for one of the pylon legs along the height of the pylon. Using the same notation as in the figures above, it compares the displacement values from the initial and final elastic model with those from the fiber model.



(a) Maximum displacement in the local y direction **(b)** Maximum displacement in the local z direction

Figure 6.25

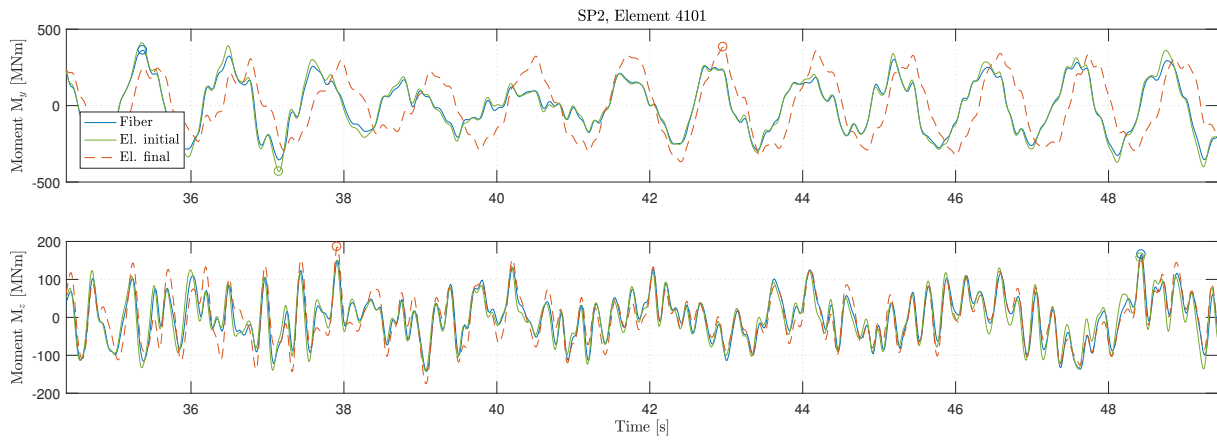


Figure 6.26: Moment history from the first pylon leg element above foundation

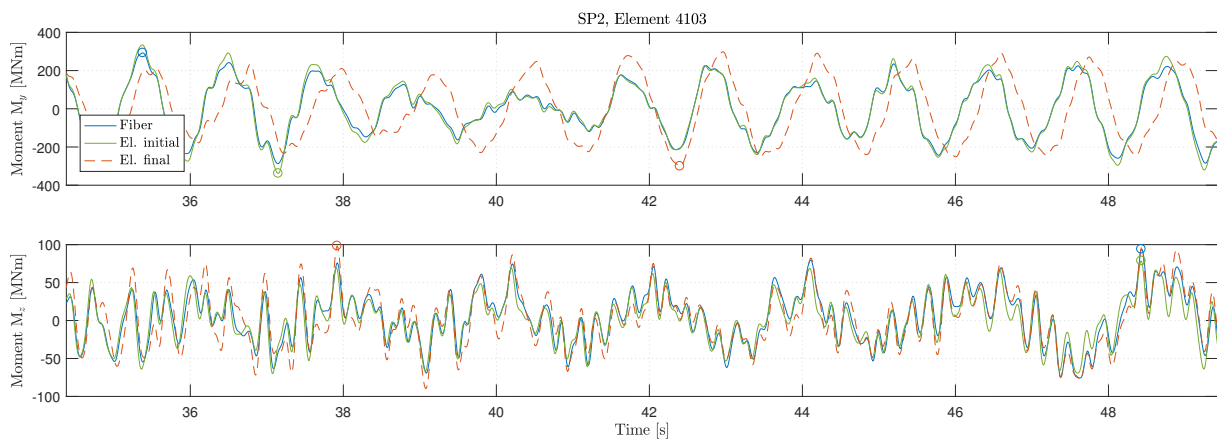


Figure 6.27: Moment history from the middle of the leg segment connecting tie-beam and the lower cross-beam

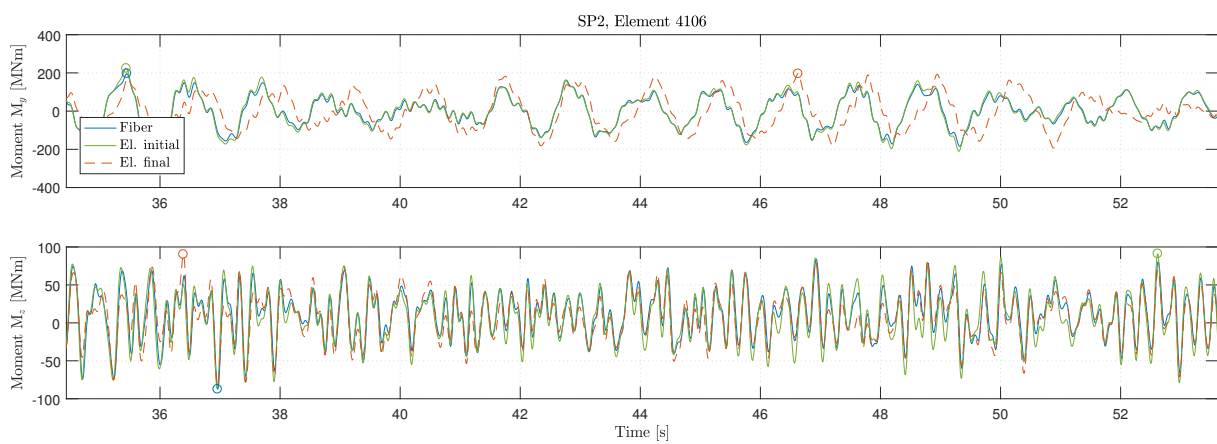


Figure 6.28: Moment history from the lower element connected to the lower cross-beam

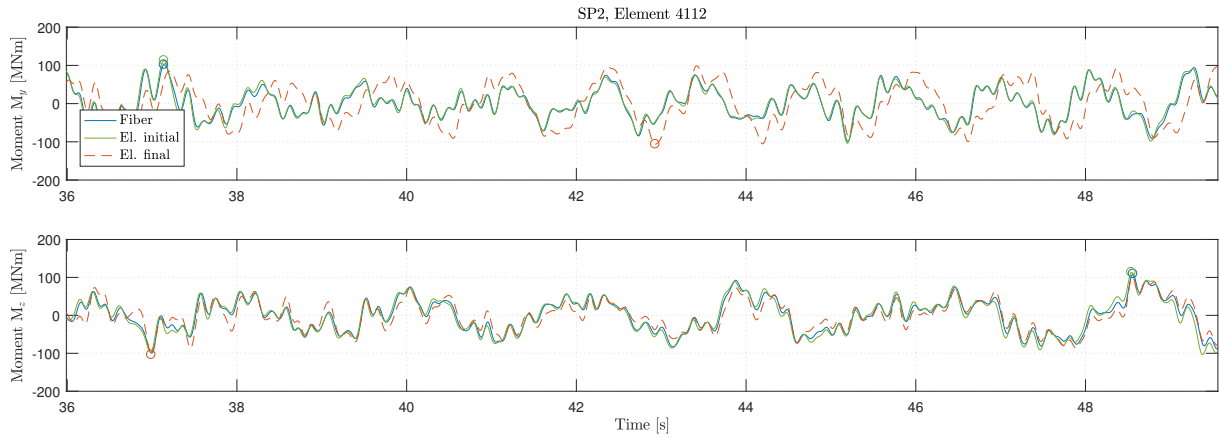


Figure 6.29: Moment history from intermediate element along the leg segment connecting the lower and upper cross-beam

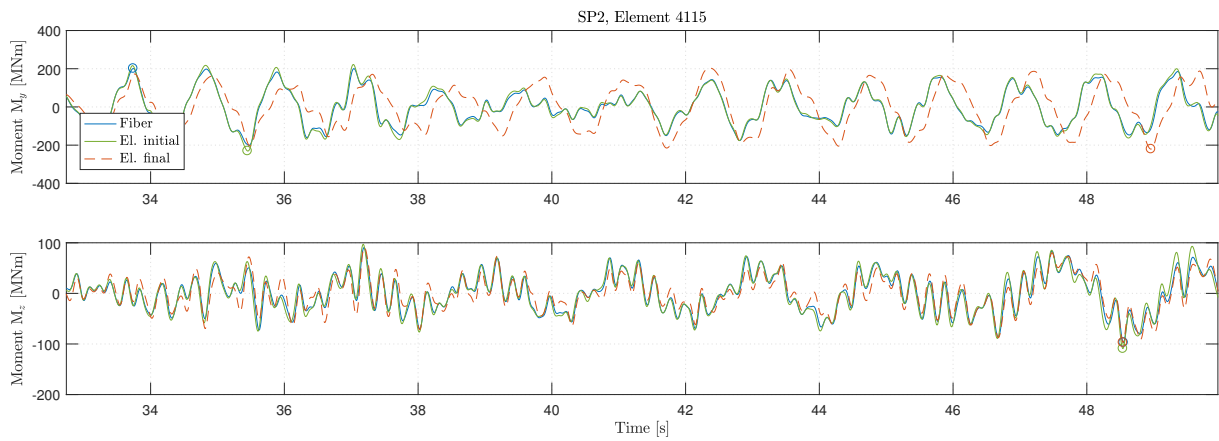


Figure 6.30: Moment history from intermediate element along the leg segment connecting the lower and upper cross-beam

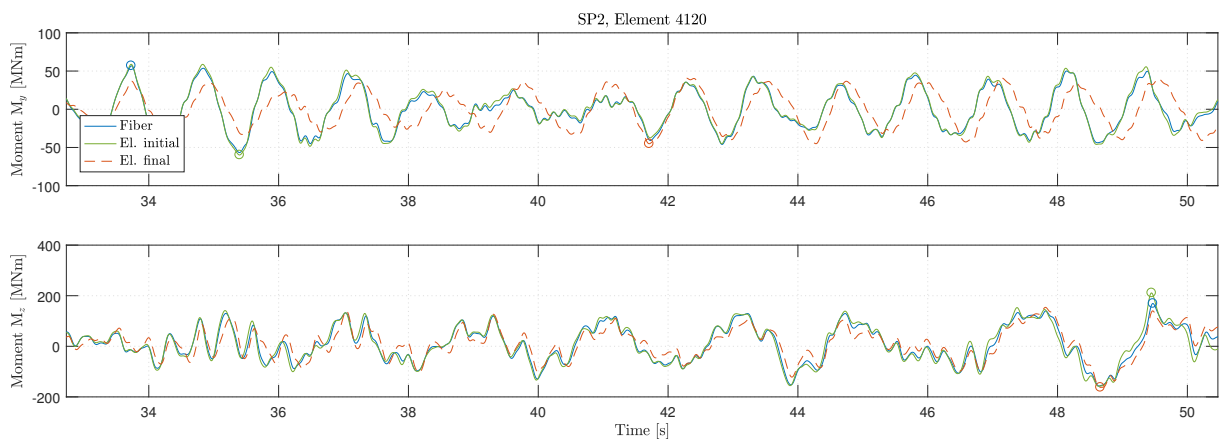


Figure 6.31: Moment history from the lower element connected to the upper cross-beam

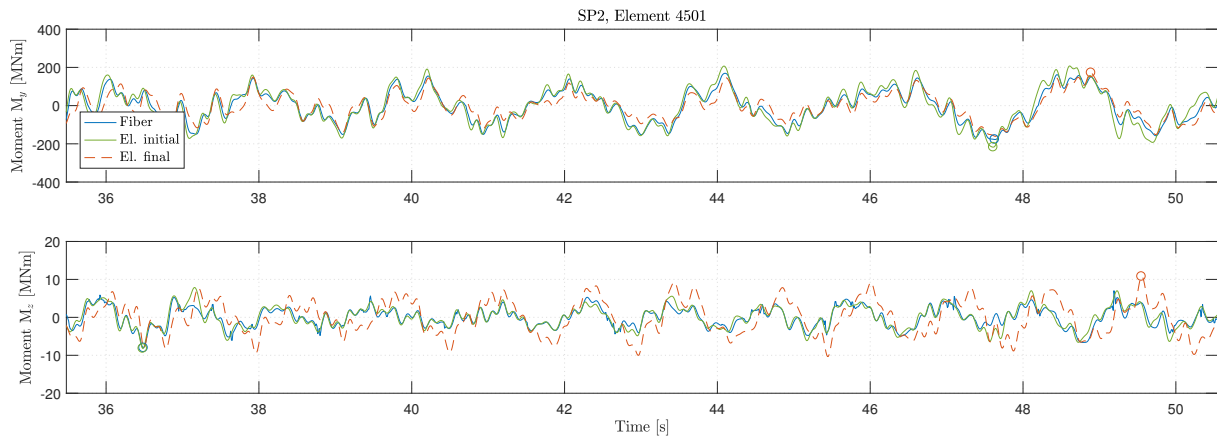


Figure 6.32: Moment history from the outer most element on the lower cross-beam

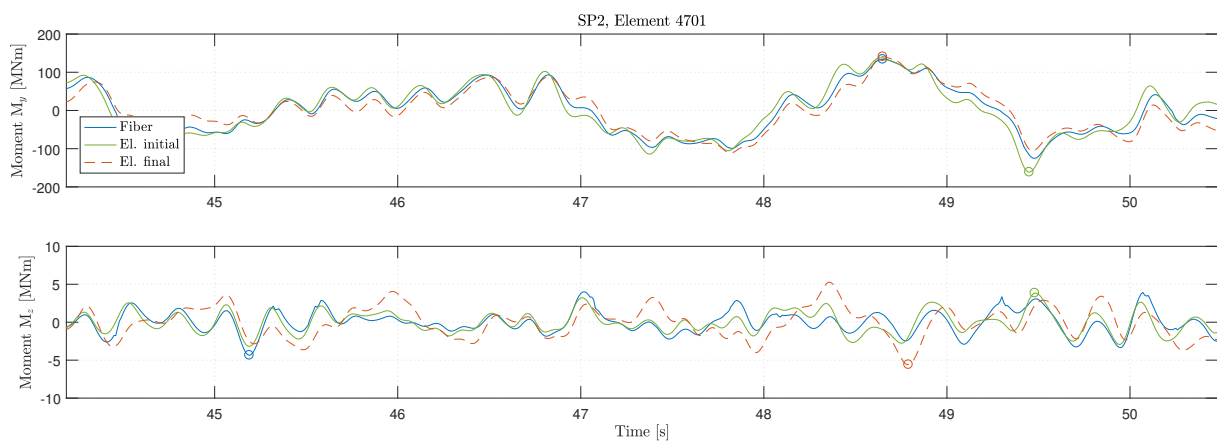
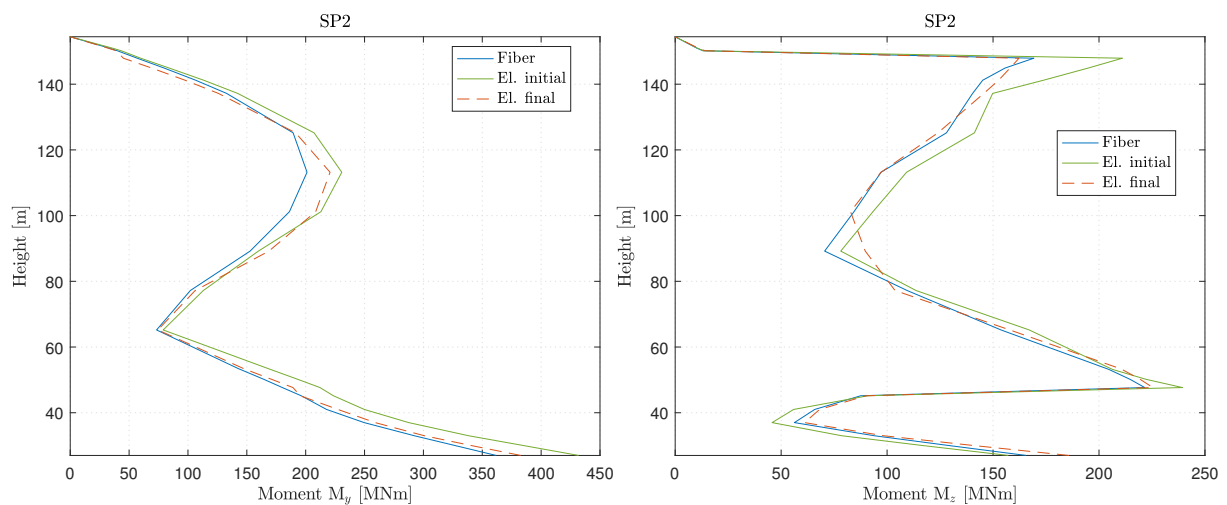


Figure 6.33: Moment history from the outer most element on the upper cross-beam

Figure 6.34 below depicts the maximum absolute moment values for one of the pylon legs along the height of the pylon. Using the same notation as in the figures above, it compares the moment values from the initial and final elastic model with those from the fiber model.



(a) Maximum moment about the local y-axis

(b) Maximum moment about the local z-axis

Figure 6.34

6.1.3 Normalized Moment

Figures 6.35-6.38 below summarize the results from all moment histories for the selected elements. The figures contain three maximum moment values following each of the seven ground motion records, SP1 to SP7, about both axes. All moment values are normalized by the corresponding maximum moment following the NTHA for each ground motion. The maximum moment from fiber model thus becomes unity, and the moments from the two elastic models are expressed factors of the response following the NTHA. Denoted $M_{i,itr}^*$, the normalized moment about axis i following iteration itr is taken as

$$M_{i,itr}^* = \frac{M_{i,itr}}{M_{i,fiber}} \tag{6.1}$$

where the maximum absolute moment following the NTHA is the denominator. itr equal to *initial* represent the first, unreduced iteration and itr equal to *final* the last, converged iteration. The horizontal axis show the deviation among the values while the vertical axis represent different ground motion records. Along the horizontal axis, two diamond shaped markers identify the mean value of both the initial and the final moment, taken over all ground motion records. The top plot in each figure display the bending moment about the local y-axis for the appropriate element while the bottom plot about the local z-axis. A summary of the values can be found in table 7.1.

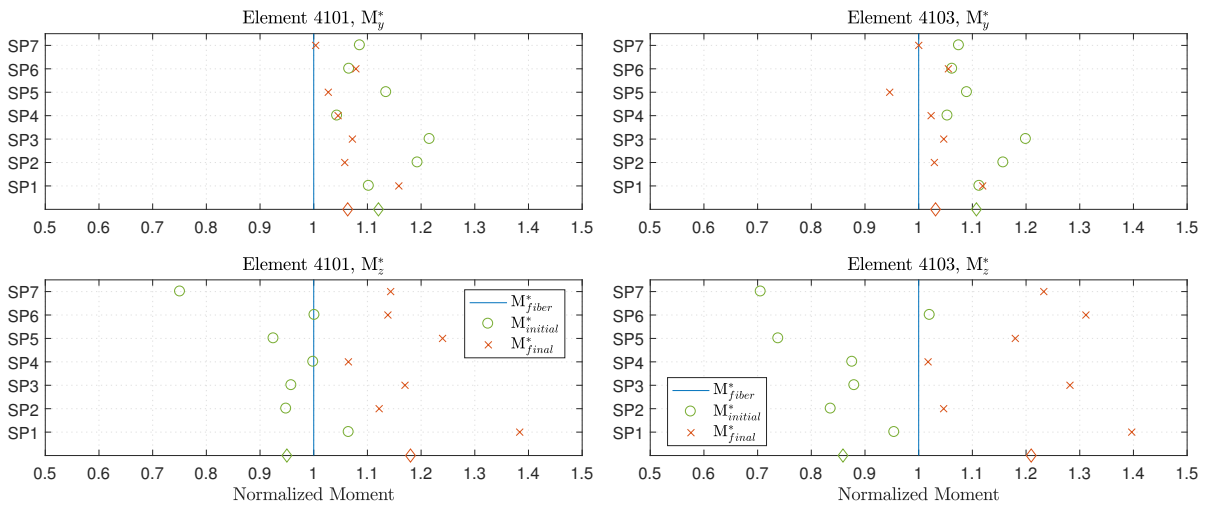


Figure 6.35

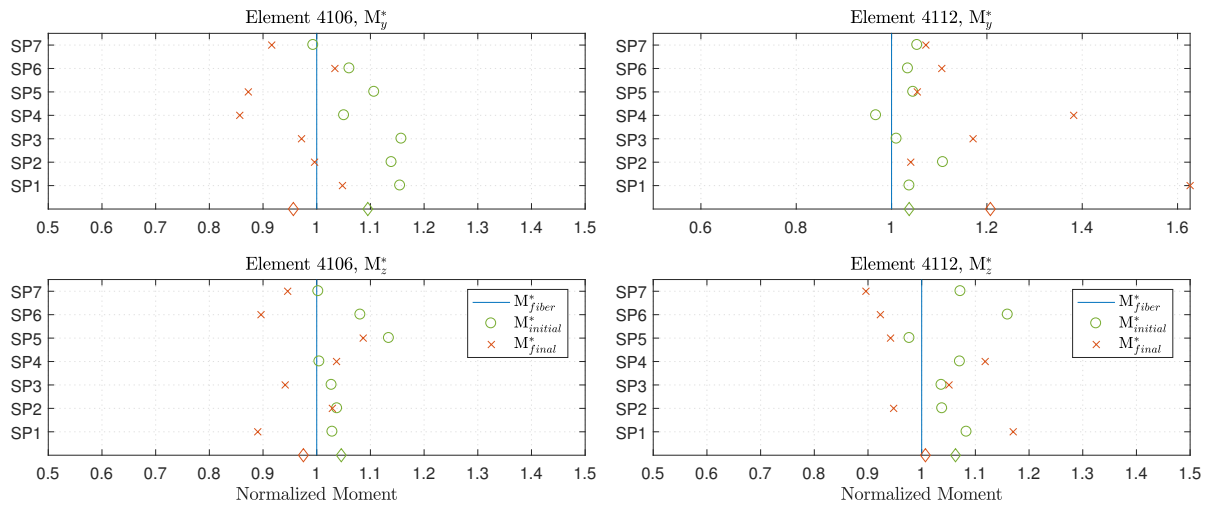


Figure 6.36

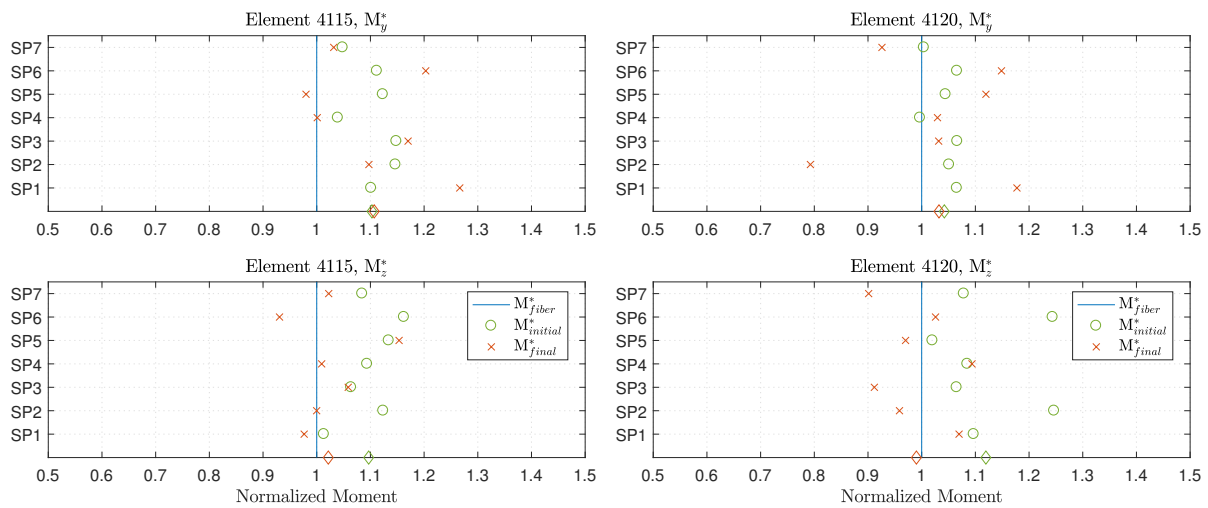


Figure 6.37

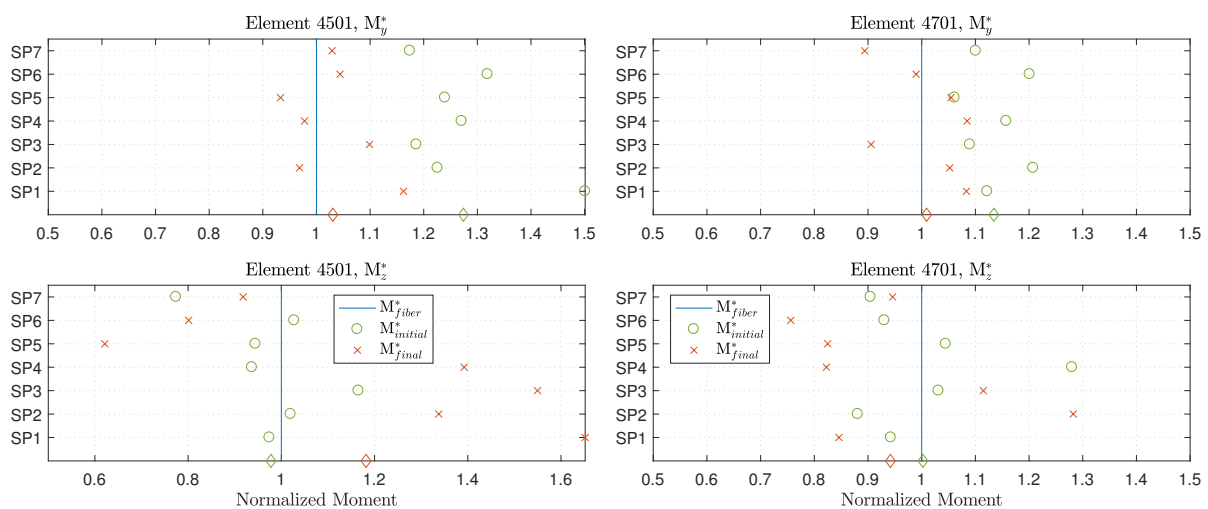


Figure 6.38

6.2 Results from the Pushover Analysis

The results from the pushover analyses using the elastic model with updated stiffnesses are compared to the responses from pushover analyses using fiber model with the same load distribution. At the beginning of each subsection below, a pushover curve is presented, showing the displacement of the structure against load step, as well as the bending moment in the governing element, also against the load step, for both methods. The governing elements for each analysis can be found in section 5.4. As for the THA, the main parameter that forms the basis for comparing the responses from the nonlinear fiber model and the elastic model is the bending moment about the relevant axis, given by the push direction for each element. The moment diagram of the structure is therefore presented both for the load step $\lambda = 1$, which corresponds to the maximum moments from the input ground motions, and for the last converged load step for the elastic model. To easily assess the accuracy of the Secant Method on the elastic model, the normalized moment as presented in equation (6.1) will be presented in tables for the critical elements for each analysis.

6.2.1 Longitudinal Analysis - L1

Table 6.9 summarizes the results from the longitudinal analysis L1. The governing elements for this analysis are located in the upper portion of the pylon legs, elements 4115 and 4215. The final converged load step for the elastic model is $\lambda = 1.5$. Elements 4101 and 4201 are also deemed critical for this analysis and will be included in the table below.

Table 6.9: Summary of critical element for pushover analysis L1

| Element | Ratio $\lambda = 1$ | $M_{\lambda=1}^*$ | Ratio $\lambda = 1.5$ | $M_{\lambda=1.5}^*$ |
|---------|---------------------|-------------------|-----------------------|---------------------|
| 4101 | 0.95 | 0.99 | 0.47 | 1.03 |
| 4201 | 0.95 | 1.00 | 0.47 | 1.04 |
| 4115 | 0.92 | 1.02 | 0.47 | 1.05 |
| 4215 | 0.93 | 1.01 | 0.31 | 1.04 |

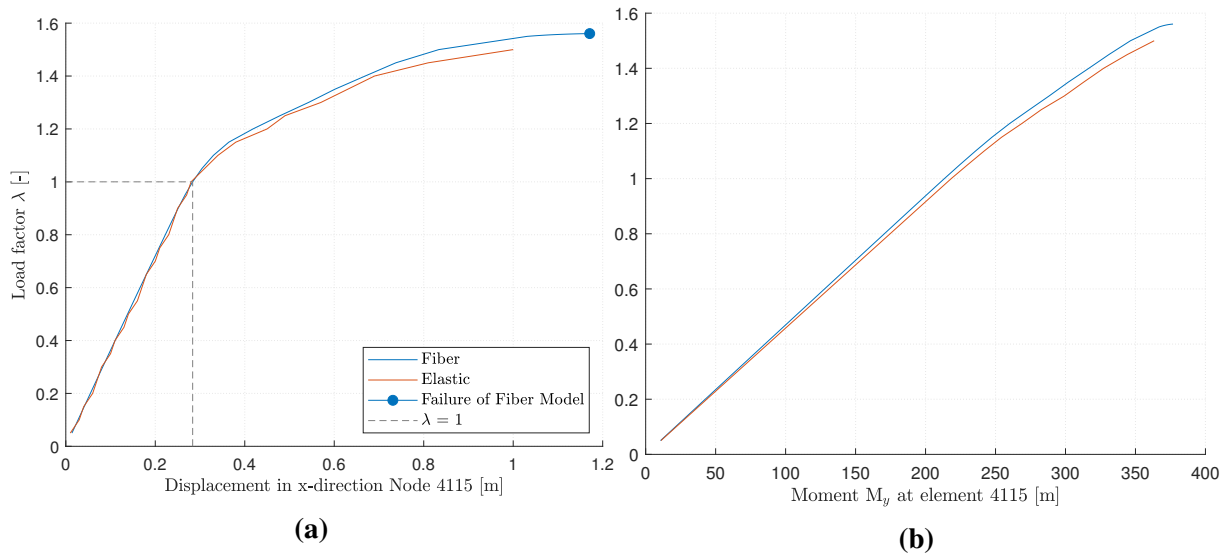


Figure 6.39: Pushover curves for analysis L1

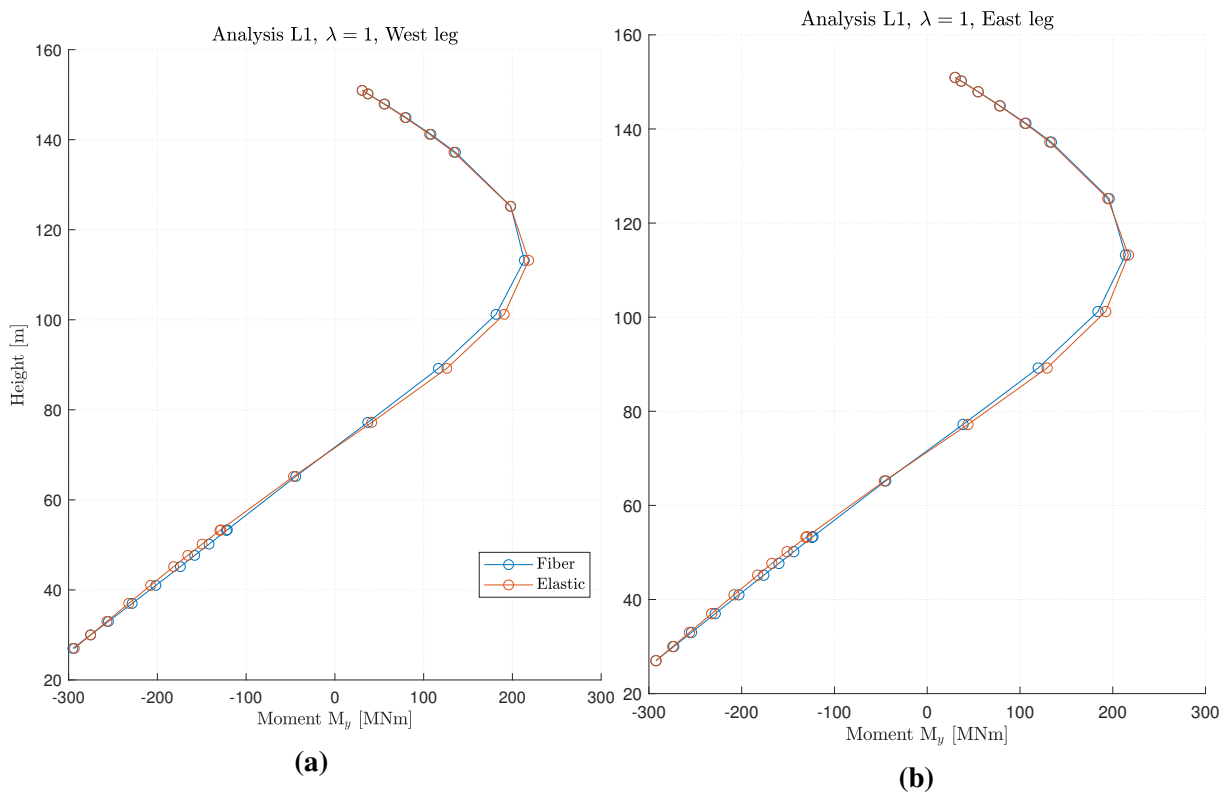


Figure 6.40: Moment distribution for the pylon legs

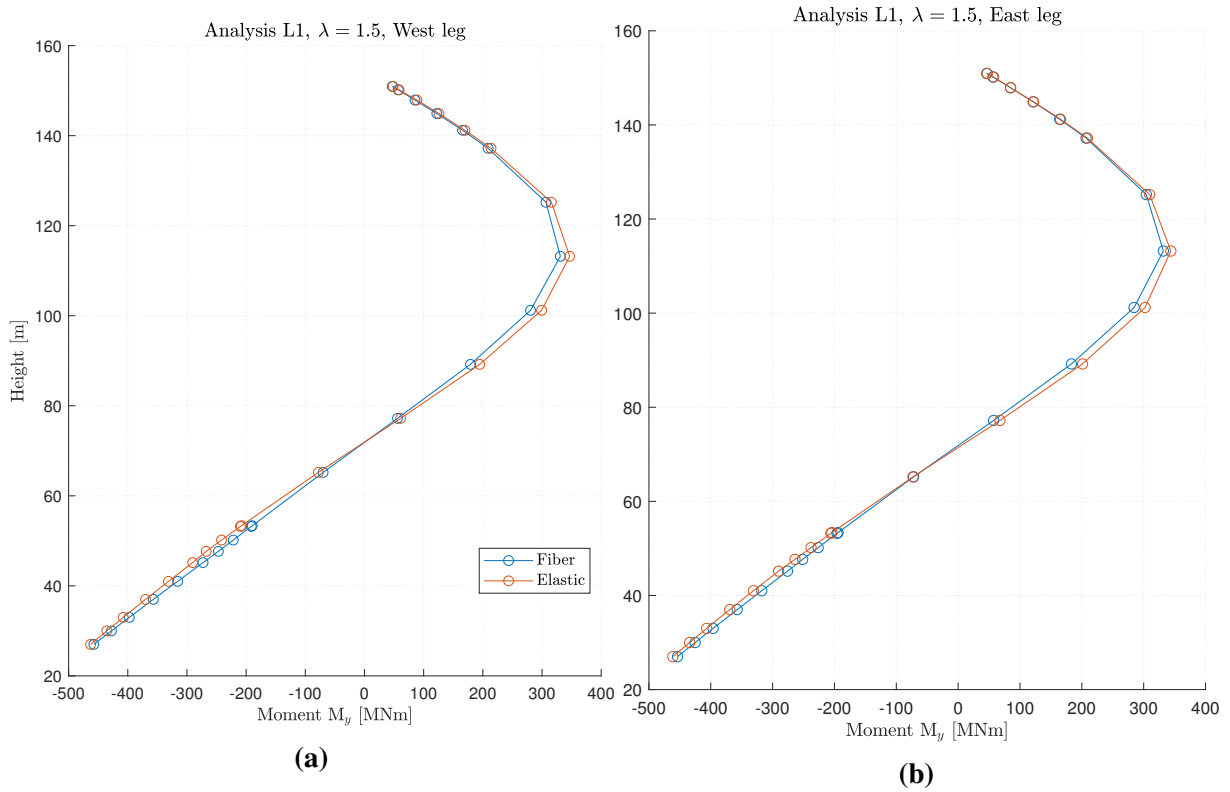


Figure 6.41: Moment distribution for the pylon legs

6.2.2 Longitudinal Analysis - L2

Table 6.10 summarizes the results from the longitudinal analysis L2. The governing elements for this analysis are located at the base of the pylon legs, elements 4101 and 4201. The final converged load step for the elastic model is $\lambda = 1.8$. Elements 4115 and 4215 are also deemed critical for this analysis and will thus be included in the table below.

Table 6.10: Summary of critical elements for pushover analysis L2

| Element | Ratio $\lambda = 1$ | $M_{\lambda=1}^*$ | Ratio $\lambda = 1.8$ | $M_{\lambda=1.8}^*$ |
|---------|---------------------|-------------------|-----------------------|---------------------|
| 4101 | 0.81 | 1.00 | 0.34 | 1.01 |
| 4201 | 0.83 | 1.00 | 0.34 | 1.01 |
| 4115 | 0.98 | 1.00 | 0.36 | 1.08 |
| 4215 | 0.98 | 1.00 | 0.36 | 1.07 |

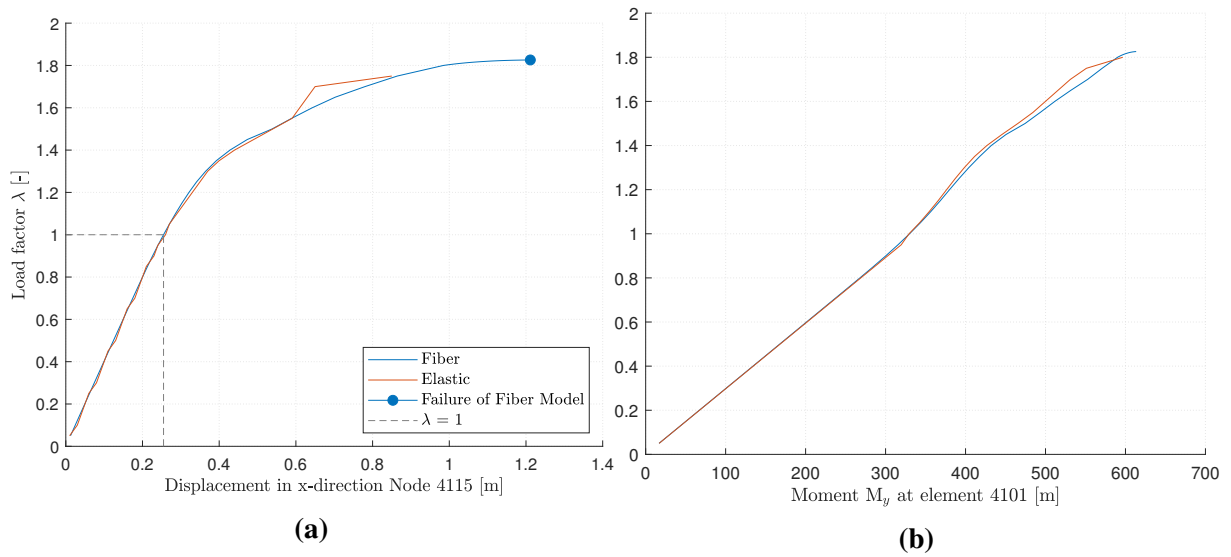


Figure 6.42: Pushover curves for analysis L2

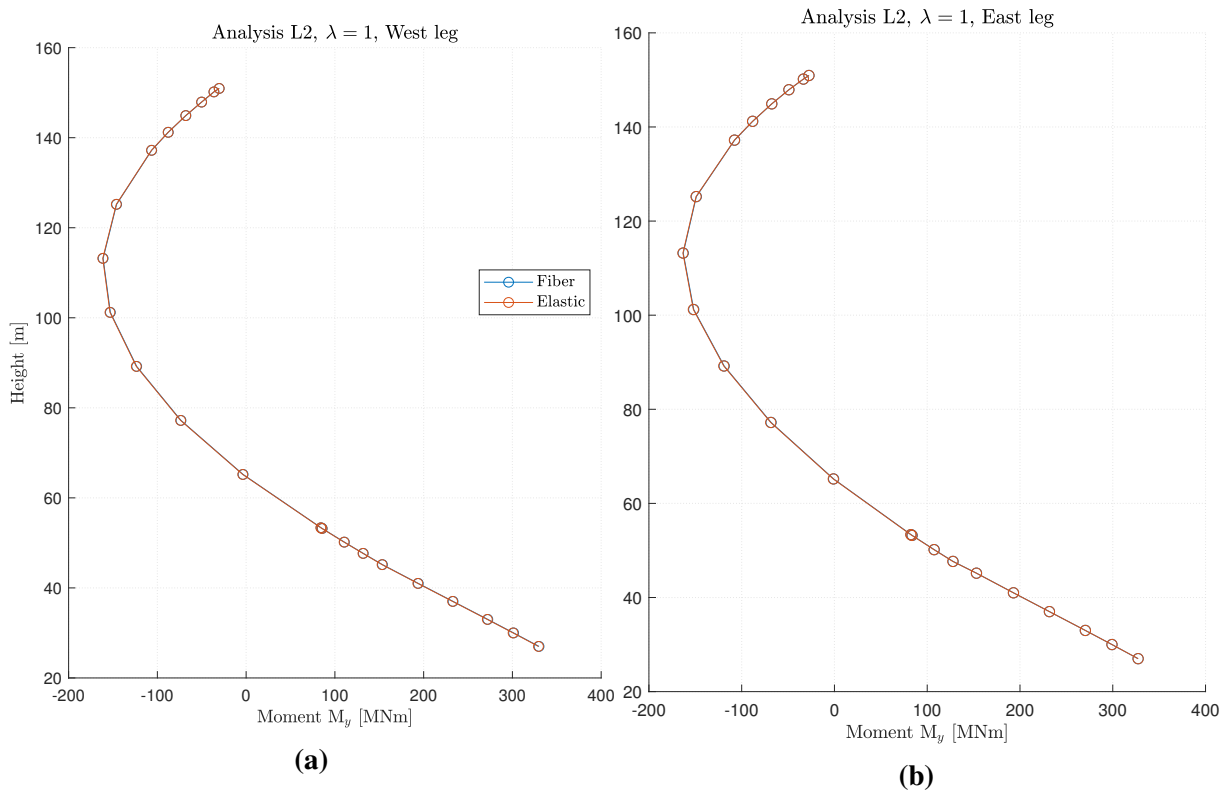


Figure 6.43: Moment distribution for the pylon legs

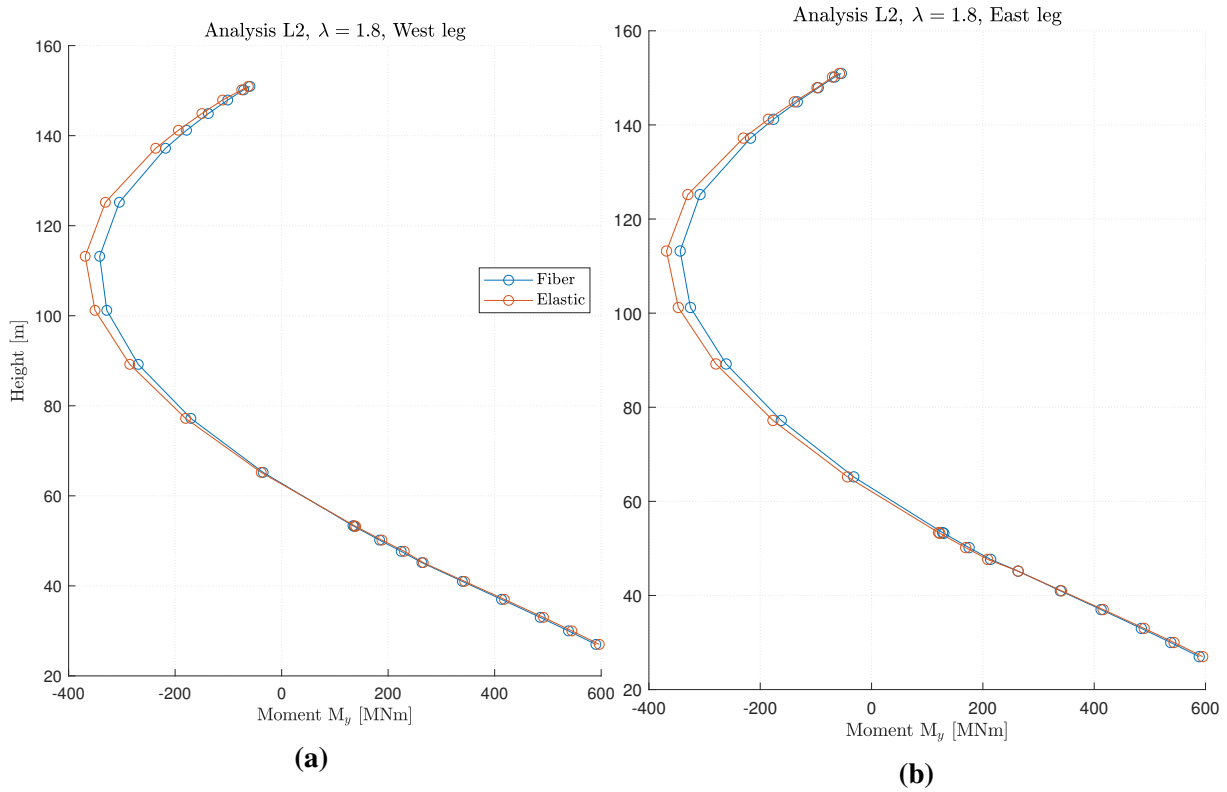


Figure 6.44: Moment distribution for the pylon legs

6.2.3 Transverse Analysis - T1

Table 6.11 summarizes the results from the transverse analysis T1. The governing elements for this analysis are at the base of the pylon legs, elements 4101 and 4201. The final converged load step for the elastic model is $\lambda = 4.4$. The cross-beam end elements are also deemed critical for this analysis and will be included in the table below.

Table 6.11: Summary of critical elements for pushover analysis T1

| Element | Ratio $\lambda = 1$ | $M_{\lambda=1}^*$ | Ratio $\lambda = 4.4$ | $M_{\lambda=4.4}^*$ |
|---------|---------------------|-------------------|-----------------------|---------------------|
| 4101 | 0.98 | 1.00 | 0.47 | 0.94 |
| 4201 | 1.00 | 0.98 | 0.27 | 1.03 |
| 4501 | 0.86 | 1.01 | 0.16 | 0.89 |
| 4506 | 0.99 | 1.01 | 0.28 | 1.13 |
| 4701 | 1.00 | 1.00 | 0.33 | 1.01 |
| 4704 | 1.00 | 0.99 | 0.48 | 1.05 |

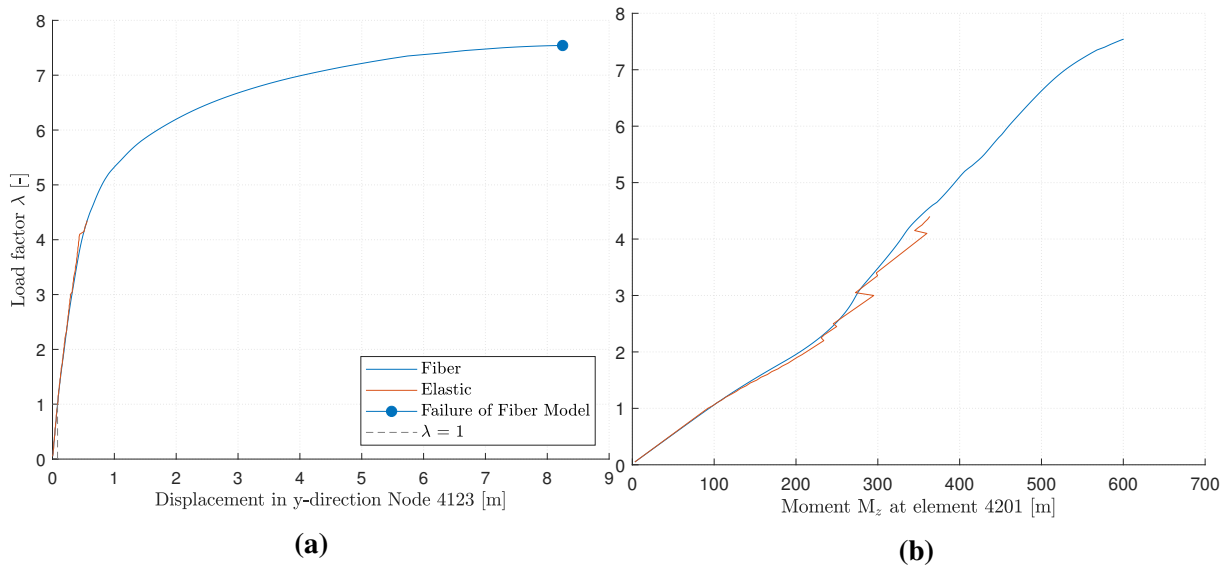


Figure 6.45: Pushover curves for analysis T1

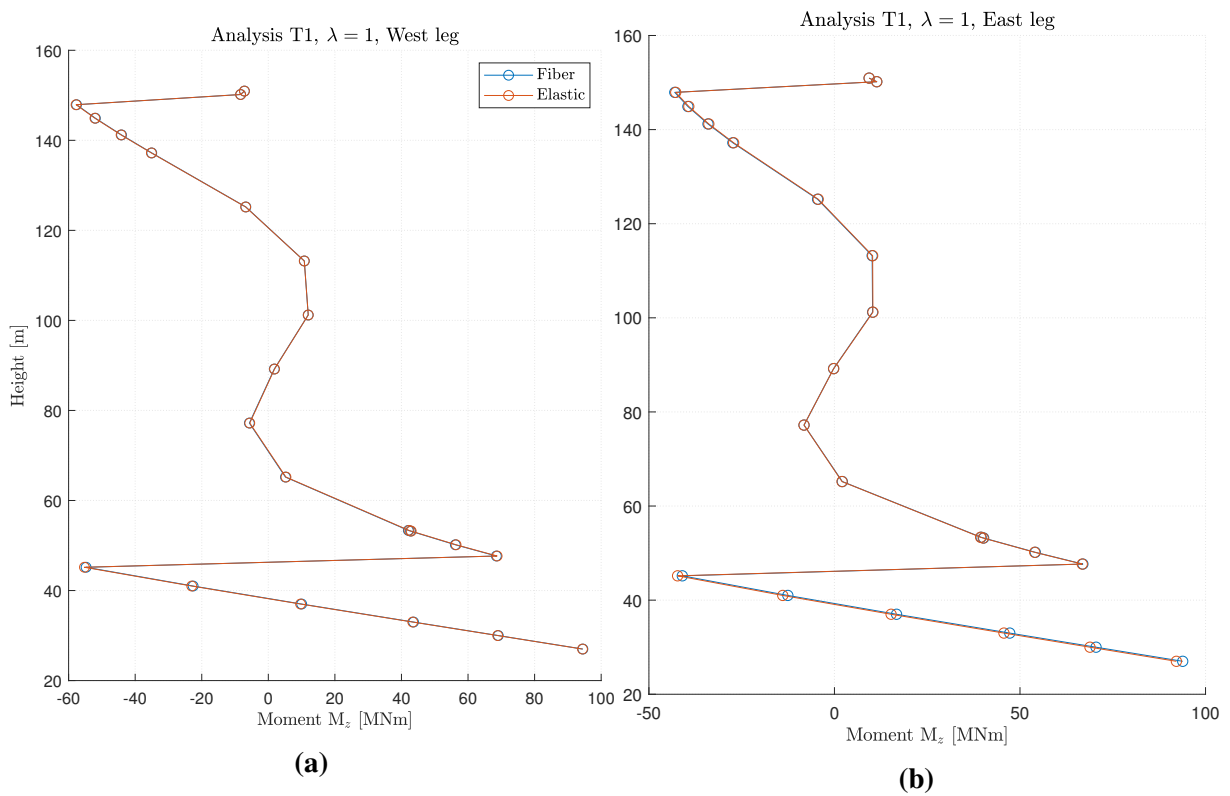


Figure 6.46: Moment distribution for the pylon legs

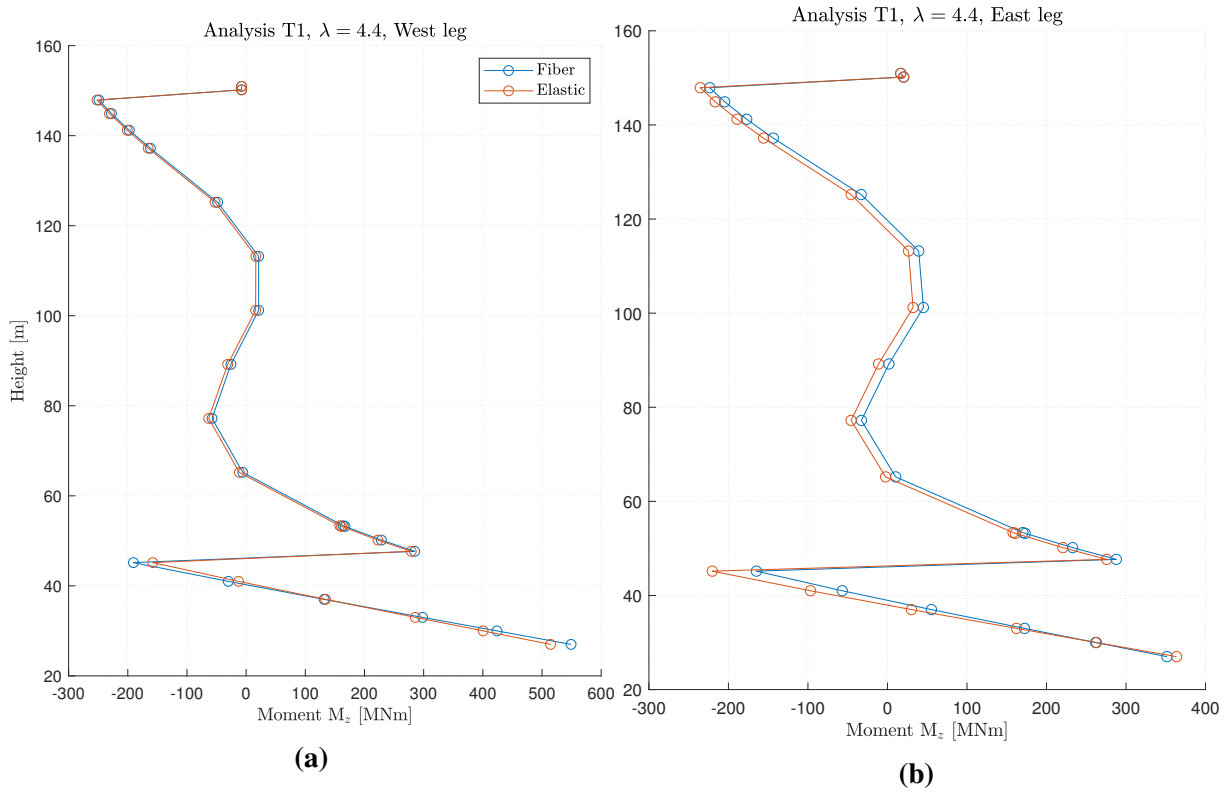


Figure 6.47: Moment distribution for pylon legs

6.2.4 Transverse Analysis - T2

Table 6.12 summarizes the results from the transverse analysis T2. The governing elements for this analysis are the lower cross-beam ends, elements 4501 and 4506. The final converged load step for the elastic model is $\lambda = 1.35$. Elements 4101, 4201, 4701 and 4704 are also deemed critical for this analysis and will be included in the table below.

Table 6.12: Summary of critical elements for pushover analysis T2

| Element | Ratio $\lambda = 1$ | $M_{\lambda=1}^*$ | Ratio $\lambda = 1.35$ | $M_{\lambda=1.35}^*$ |
|---------|---------------------|-------------------|------------------------|----------------------|
| 4101 | 0.92 | 1.06 | 0.53 | 0.99 |
| 4201 | 0.96 | 0.91 | 0.94 | 0.91 |
| 4501 | 0.30 | 0.93 | 0.27 | 0.95 |
| 4506 | 0.30 | 1.03 | 0.29 | 1.02 |
| 4701 | 0.35 | 0.96 | 0.32 | 1.01 |
| 4704 | 0.87 | 1.13 | 0.34 | 1.12 |

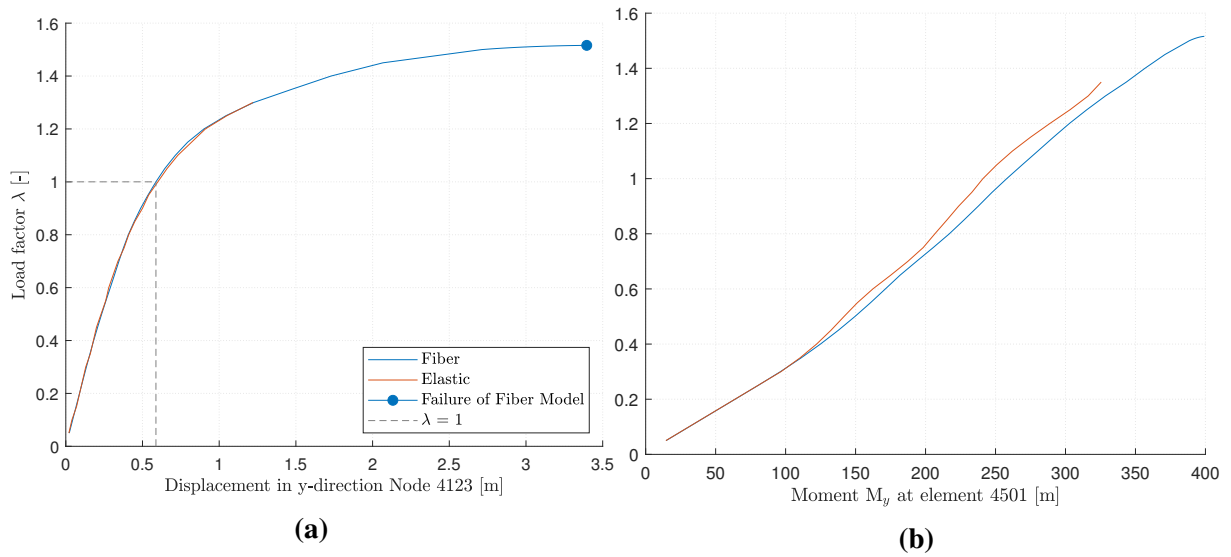


Figure 6.48: Pushover curves for analysis T2

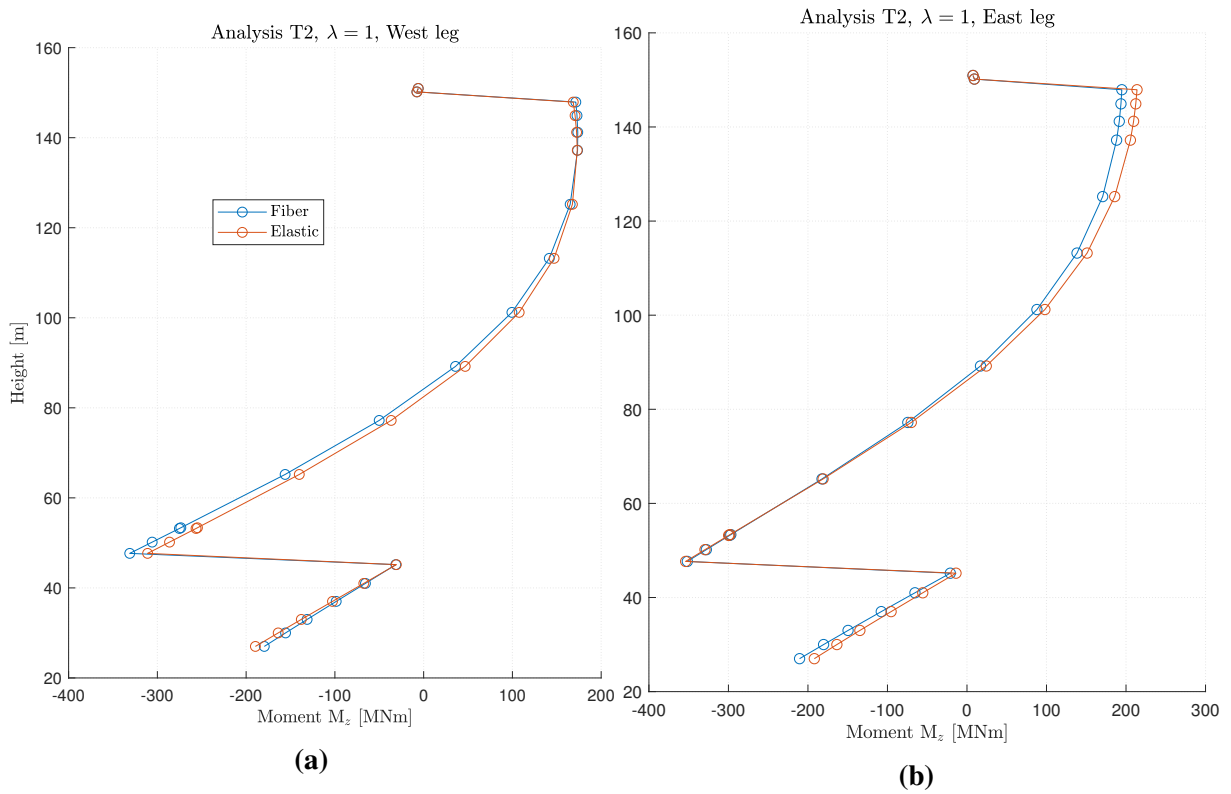


Figure 6.49: Moment distribution for the pylon legs

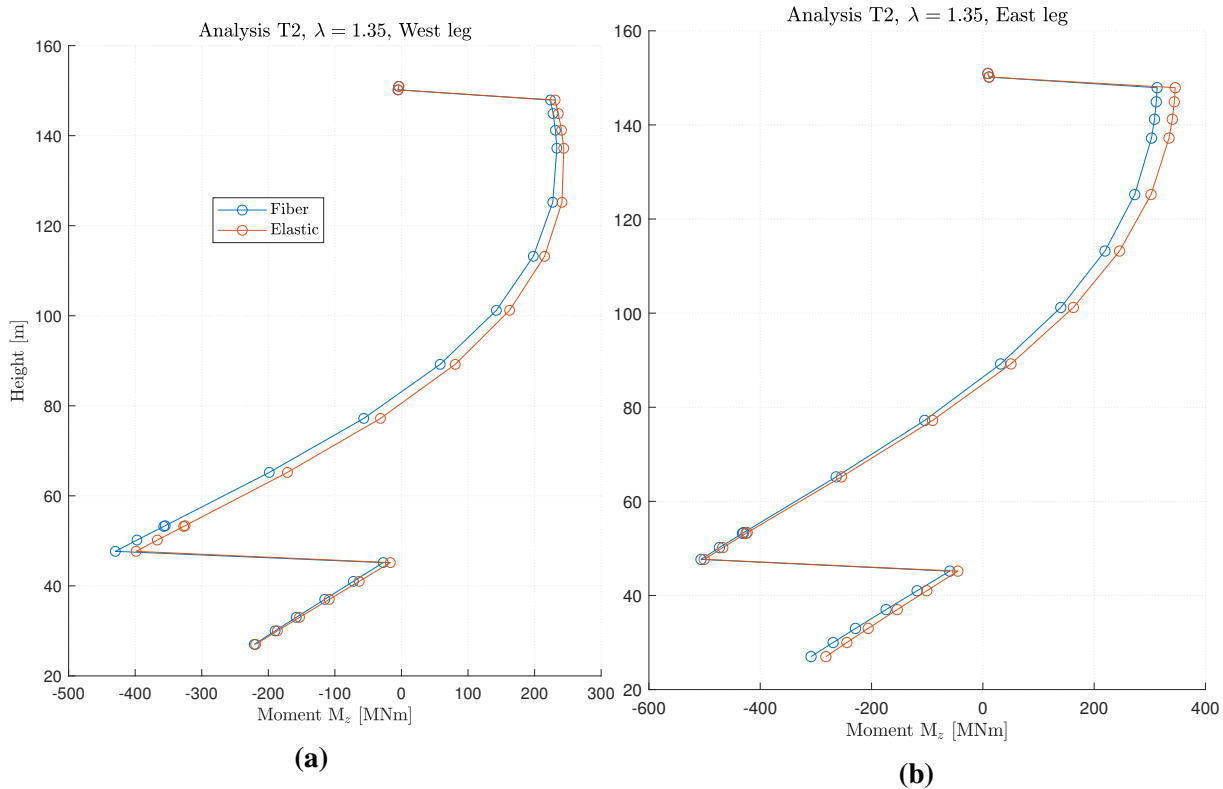


Figure 6.50: Moment distribution for the pylon legs

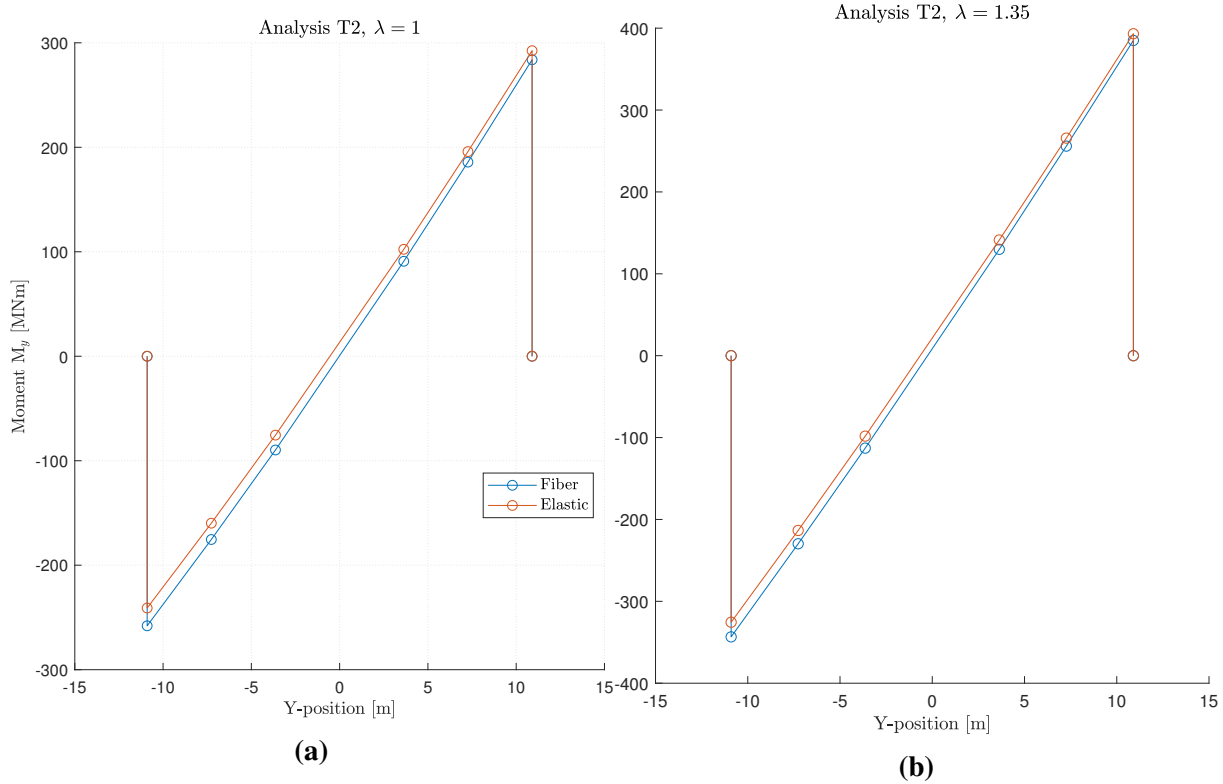


Figure 6.51: Moment distribution for the lower cross-beam

6.2.5 Transverse Analysis - T3

Table 6.13, summarizes the results from the transverse analysis T3. The governing elements for this analysis are the upper cross-beam ends, elements 4701 and 4704. The final converged load step for the elastic model is $\lambda = 2.6$. Elements 4101, 4201, 4501 and 4506 are also deemed critical for this analysis and will be included in the table below.

Table 6.13: Summary of critical elements for pushover analysis T3

| Element | Ratio $\lambda = 1$ | $M_{\lambda=1}^*$ | Ratio $\lambda = 2.6$ | $M_{\lambda=2.6}^*$ |
|---------|---------------------|-------------------|-----------------------|---------------------|
| 4101 | 0.99 | 1.02 | 0.96 | 0.87 |
| 4201 | 1.00 | 0.95 | 0.95 | 1.1 |
| 4501 | 0.85 | 0.97 | 0.29 | 0.86 |
| 4506 | 0.99 | 1.03 | 0.29 | 0.99 |
| 4701 | 0.46 | 0.94 | 0.10 | 1.02 |
| 4704 | 0.90 | 1.06 | 0.32 | 1.07 |

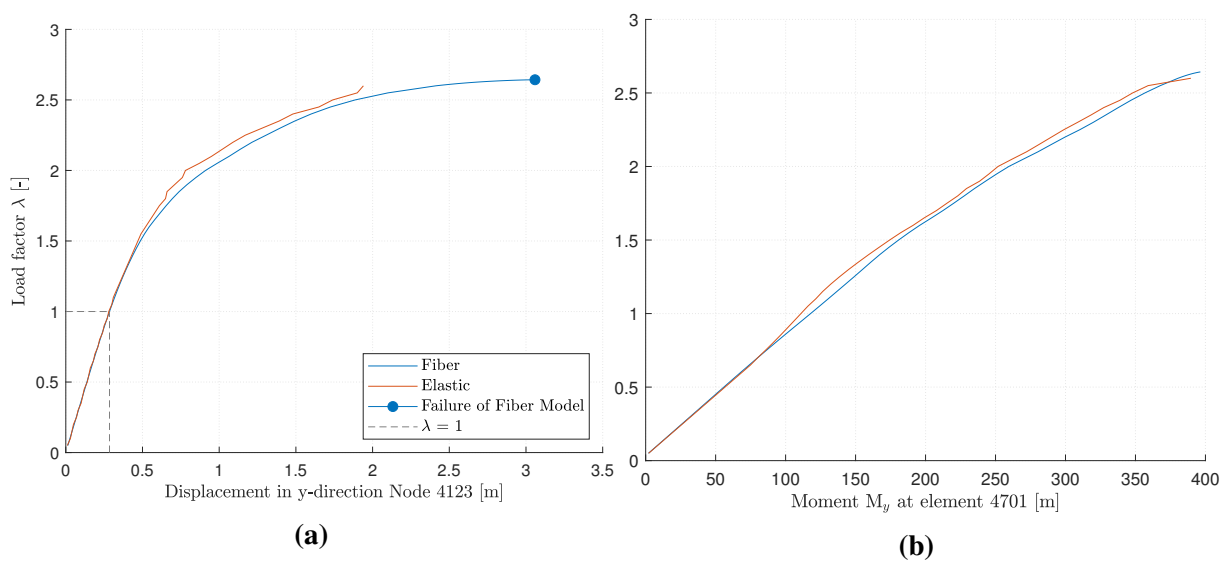


Figure 6.52: Pushover curves for analysis T3

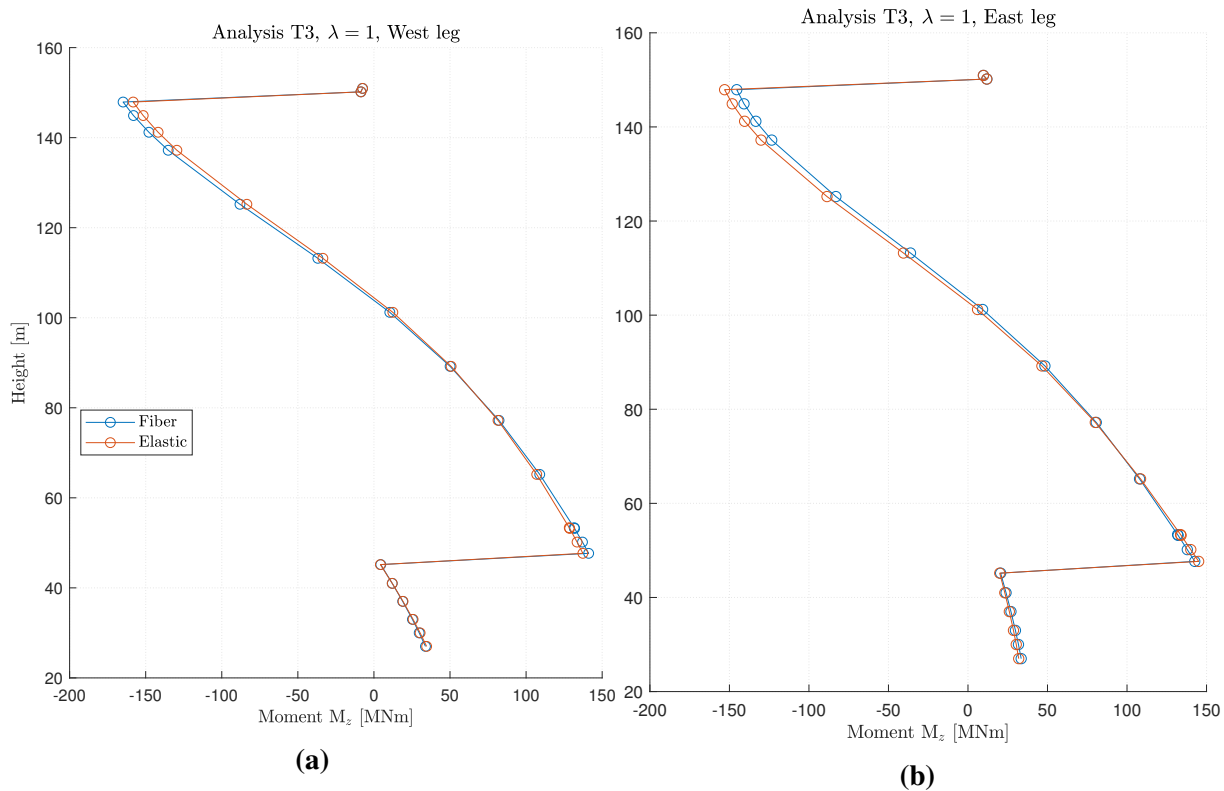


Figure 6.53: Moment distribution for the pylon legs

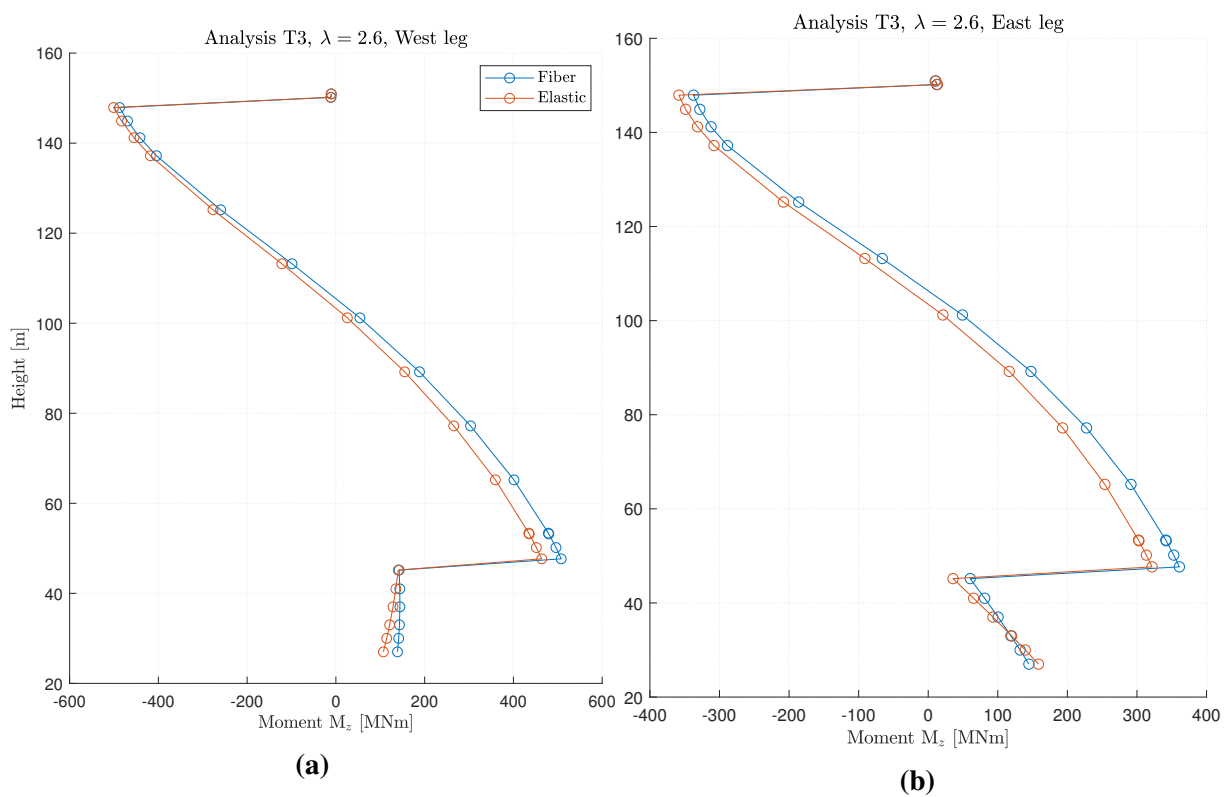


Figure 6.54: Moment distribution for the pylon legs

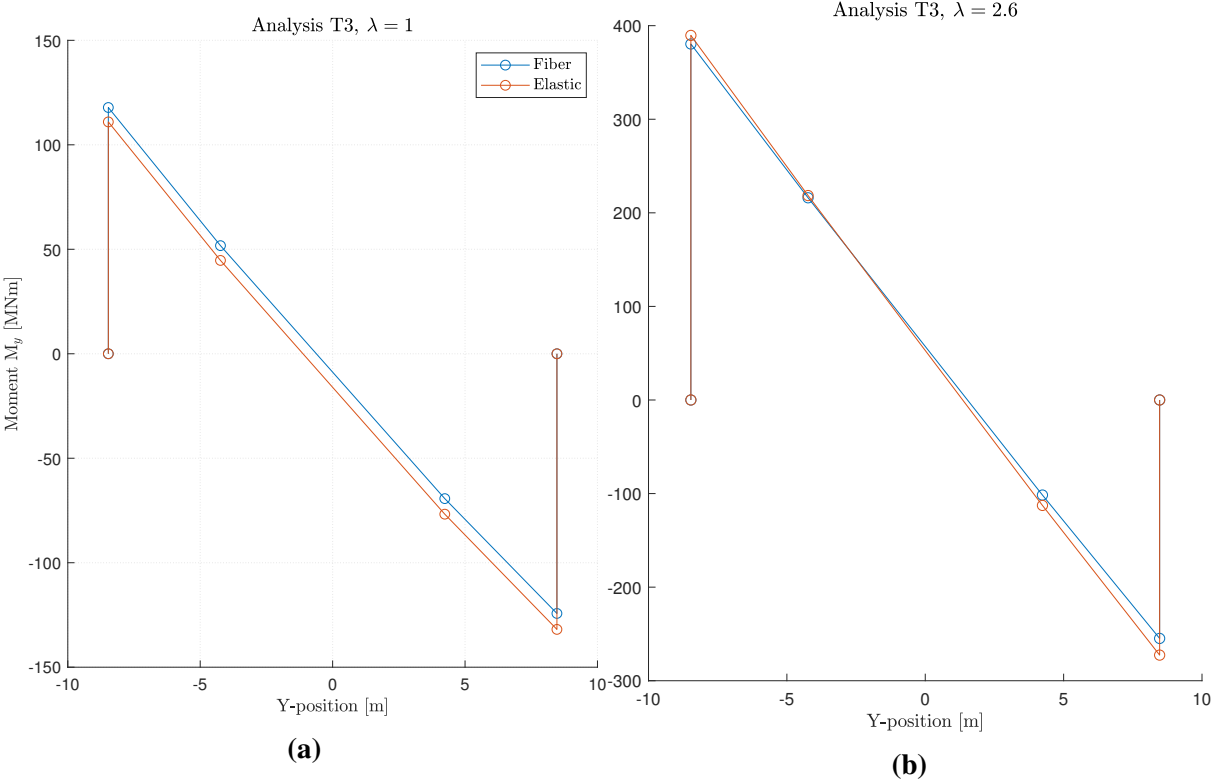


Figure 6.55: Moment distribution for the upper cross-beam

Chapter 7

Discussion

7.1 Discussion of the Secant Method

In the following, a brief discussion of the Secant Method itself will be conducted, before the various results following said procedure will be examined in detail. One of the main objectives of the Secant Method is to give an indication of the nonlinear material behavior in certain elements when a full nonlinear analysis either is unfeasible or too computationally demanding to perform. There are several approaches to develop this procedure, and as discussed in 5.3, an OpenSees script which invoked MATLAB was used for this thesis. A downside of this approach is that a new instance of MATLAB needed to be booted at least once during each iteration. This was in itself time consuming, and likely could have been avoided if more research had been put into the functionality of the Windows Command Prompt, from which MATLAB was invoked.

Other efforts to cut iteration time was instead pursued, most notably was the change from calculating new moment-curvature diagrams each iteration to instead use interpolation between pre-existing ones, when capturing the effect of the axial load. This modification removed about two-three minutes off each iteration which in turn reduced the entire procedure using all seven ground motions with about two hours. The downside of this measure is however the possibility of encountering issues in determining the stiffness by interpolation, especially for high moments in elements with substantial axial forces. Figure 7.1 shows the moments-curvature diagrams used for determining the stiffness at the base of the pylon legs, elements 4101 and 4201, about the local z-axis. For axial forces 1.6-2 times the gravitational load, the maximum moment capacity correspond to relatively small curvatures. The algorithm is implemented in such a way that if the moment obtained from the analysis exceeds the maximum moment value of one of the interpolating curves, the secant stiffness is taken as the maximum moment of the lowest curve divided by the corresponding curvature. This effectively caps the possible reduction in the relevant elements, and reduces the elastic models ability to deform in a ductile manner, post yielding of concrete fibers. This effect is mostly relevant for the transverse pushover analyses, as large transverse forces gives rise to high compressive axial forces in one of the pylon legs, and is a possible explanation for the instability seen in the transverse analysis T1, and why the updated elastic model is as ductile as the fiber model. Similar moment-curvature diagrams as the one in figure 7.1 are shown in appendix D for all elements.

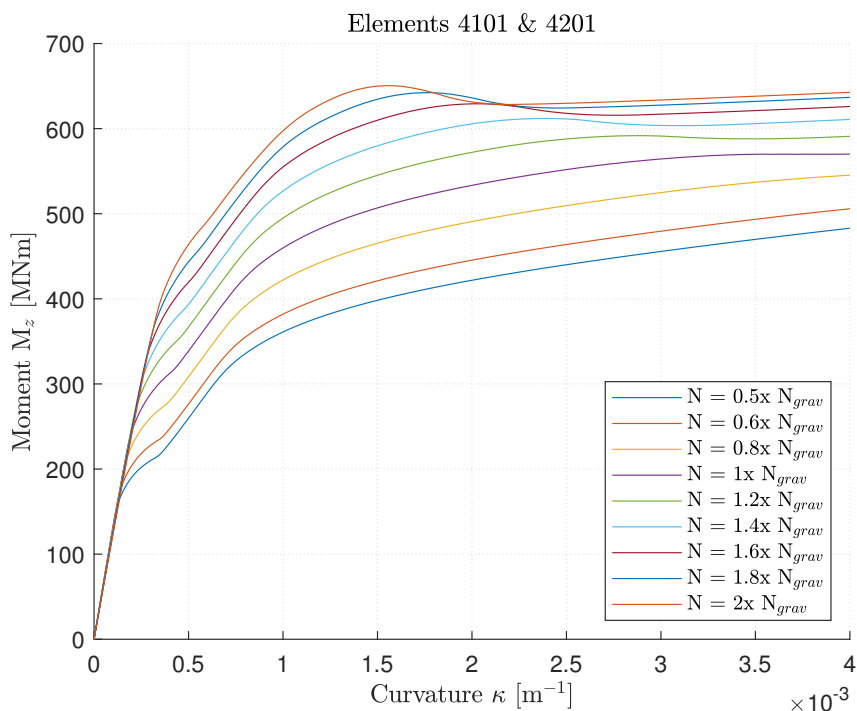


Figure 7.1: Moment-curvature diagrams about local z-axis for varying axial loads

The factor used in equation 5.1 to ensure stability also impacted the total run time of the Secant Method. Choosing a low factor, say 30%, generally resulted in a higher number of iterations than when using a higher factor, for instance 50%. When using a lower factor, the updated ratio carried to the next iteration will be more similar to the previous one, thus yielding a lower percentage change. The ratio will consequently spend additional iterations to reach a given value, but once close to the value, it will converge faster due to the nature of the convergence criteria. Of these two opposing effects, it becomes clear from figure 7.2 that it is the descending speed that is the dominant one. The figure shows the development of the stiffness reduction for the same element following a series of iterations where only the factor varies. Using a too large of a factor may lead to instability issues, as seen for the curves using a factor of 0.6 and 0.7. A factor yielding convergence for all 7 ground motions whilst being as large as possible was therefore preferable, and 0.5 was determined after trial and error. Another advantage of choosing the largest possible factor is that the final ratio will be closer to whichever value it was approaching.

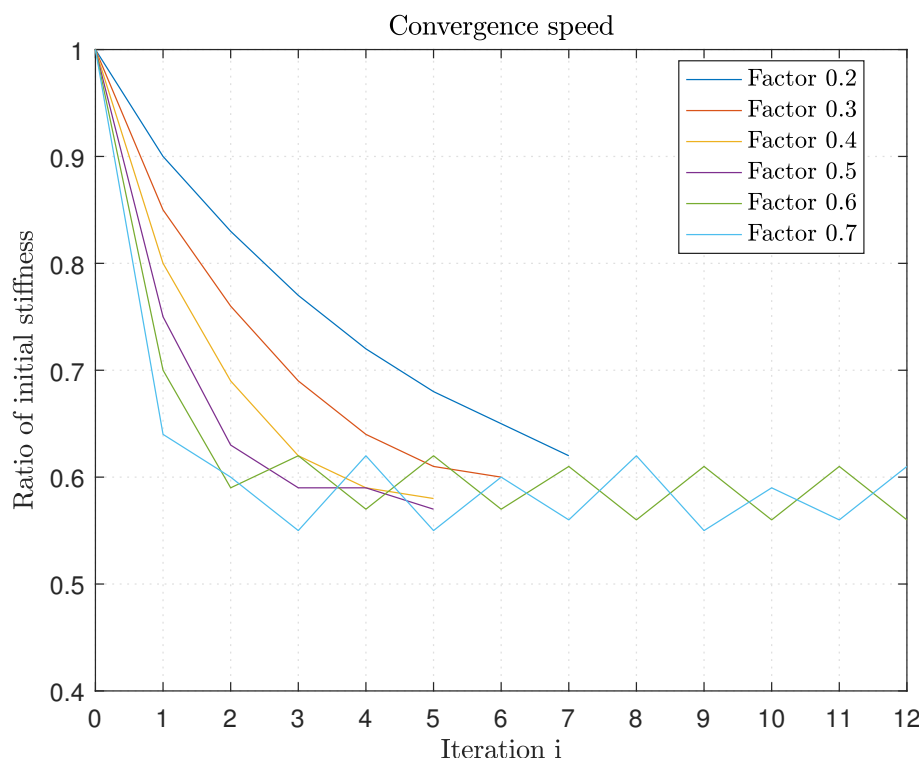


Figure 7.2: Stiffness ratios from procedures using different factors

Since it is such an essential part of the entire secant procedure, some final remarks regarding the convergence test are in order. The convergence value, calculated for all elements during each iteration using equation (5.3), evaluates the percentage change of the updated ratio with regards to the previous one. This means that an increase of say 0.1 in the stiffness ratio will render a lower percentage change for a high number than for a low number. A justification for using this bias criteria is that elements which stiffnesses are substantially reduced during the procedure will have stricter convergence requirements, thus ensuring that they indeed have converged properly before terminating the iteration scheme.

7.2 Discussion of Results From the THA

The reduced elastic model, that is, the elastic model with reduced flexural stiffness values following the Secant Method, should in theory mimic the behavior of a model where nonlinear material models have been accounted for. The potential success of the iterative secant procedure using THA can best be investigated referencing figures 6.1-6.15. By depicting the maximum moment following the initial and the final iteration for each ground motion, these figures provides an overview of how well the benchmark moment values resulting from the NTHA are approximated by these values. The extreme moment values in each element upon convergence of the secant procedure should in theory be closer to the corresponding ones following the NTHA, in this case unity. Suggested for instance by the top sub figure in figure 6.1, this is a general trend, supported by the mean values along the horizontal axis. It does not hold

true for all of the ground motion records, however, as seen for the moment following ground motion record SP1 which shifts further away from the benchmark value after the elastic model stiffnesses have been reduced.

Moving on to the top sub figure in figure 6.7, the mean values along the horizontal axis suggests a trend moving away from the NTHA value of unity. The stiffness of this element, 4112, about the y-axis is not reduced significantly during the procedure for any input ground motion, seen in table A.1. The steady increase in moments can thus be a result of stiffness reduction in other elements and consequently a redistribution of forces. Second order chord geometry may also contribute to the increase in bending moments. Stiffness reductions in certain elements result in an overall softer structure and consequently larger deformations, seen in figures 6.25a and 6.25b. Some elements may thus experience larger second order moments due to the substantial compression loads combined with increasing relative end displacements. Unlike element 4101 located near the base of the pylon, element 4112 is located halfway to the top and is thus significantly more susceptible to this effect. Again looking at figures 6.25a and 6.25b, it becomes clear that the Secant Method in fact increases the between the gap between the displacements following the NTHA and the THA. This emphasizes a key property of the procedure; while it gives better approximations for the maximum moment response, displacements tends diverge further from their true value. If accurate displacement values are sought after, fundamental refurbishment is needed throughout the procedure.

Table 7.1 below summarizes the mean values found in figures 6.35-6.38, taken over all seven responses in both in each direction. It also displays the mean initial stiffness ratio obtained after the final iteration along with the mean maximum moment values resulting from the NTHA in units of MNm.

Table 7.1: Summary of mean values from figures 6.35-6.38

| Element | y-axis | | | | z-axis | | | |
|---------|--------|-----------------|---------------|-------------|--------|-----------------|---------------|-------------|
| | Ratio | $M_{initial}^*$ | M_{final}^* | M_{fiber} | Ratio | $M_{initial}^*$ | M_{final}^* | M_{fiber} |
| 4101 | 0.63 | 1.12 | 1.06 | 338 | 0.95 | 0.95 | 1.18 | 159 |
| 4103 | 0.80 | 1.11 | 1.03 | 274 | 1.00 | 0.86 | 1.21 | 90 |
| 4106 | 0.99 | 1.10 | 0.96 | 187 | 0.99 | 1.05 | 0.98 | 82 |
| 4112 | 0.99 | 1.04 | 1.21 | 92 | 0.98 | 1.06 | 1.01 | 107 |
| 4115 | 0.82 | 1.10 | 1.11 | 192 | 0.99 | 1.10 | 1.02 | 92 |
| 4120 | 1.00 | 1.04 | 1.03 | 53 | 0.94 | 1.12 | 0.99 | 181 |
| 4501 | 0.31 | 1.27 | 1.03 | 185 | 1.00 | 0.98 | 1.18 | 7 |
| 4701 | 0.35 | 1.13 | 1.01 | 137 | 1.00 | 1.00 | 0.94 | 4 |

Looking at table 7.1 above, several observations can be made. Moment values about the local y-axis for elements close to the pylon base are generally nudged closer to NTHA moments following the Secant Method. This also holds true for the lower and upper cross-beam elements.

The y-axis bending moments along the intermediate pylon leg elements, however, are either not significantly affected by the Secant Method, or drifting further away from the benchmark values, as seen for element 4112. This is likely due to increased second order geometry effects.

The moments about the local z-axis, on the other hand, stray further away from the NTHA values near the pylon foundation. This is likely due to the severe reduction of the cross-beam ends, acting as hinges and redistributing much of the moments about the global x-axis to the pylon legs. The z-axis moments at the intermediate elements along the legs are nudged slightly closer to the NTHA values, also likely due to the reduction of cross-beam ends about the local y-axis. The moments about the local z-axis for the cross-beam elements are too random to infer any general behavior from, when looking at figures 6.13 and 6.15, but since these moments are relatively small, they are not of importance in this context. It is interesting to see, however, that the cross-beams remain uncracked about this axis, which would not have been the case if *Concrete01* had been used. There are, without a doubt many effects to account for when looking at these results. Many of which can be attributed to the crude nature of the Secant Method, which, by assessing each element individually, fails to account for relations among elements in the structure.

The normalized extreme values in figures 6.1-6.15 are obtained from moment histories such as the ones seen in the preceding figures, 6.26-6.33, for ground motion SP2 only. Based on these response histories, several observations can be made. Looking at the periods of the responses, these correspond to some degree to that of the two first eigen periods, which oscillates in the global y and x direction, respectively. Although less visible for the response about the local z-axis, it shows that these periods indeed are present in the response.

The two solid lines representing the dynamic response from the NTHA and the THA using initial stiffness values are in phase, indicating similar vibration properties among the two models. The response amplitude from the linear elastic model is consistently larger than the response from the fiber model, which is to be expected. In the majority of the cases, the maximum response also occurs simultaneously for the two curves. The dashed line, showing the response following the last iteration of the secant procedure, does not coincide as well with the NTHA response. Further, for certain segments, this response is larger in magnitude than that following the unreduced elastic response, yet the absolute maximum is lower. This observation can be attributed to the different stiffness properties between the two models, which also explains why the maximum values seldom occur simultaneously.

For the moment about the local y-axis, M_y , the final elastic response experiences a significant increase in phase angle, which illustrates another limitation of the Secant Method. While the nonlinear fiber model is able to capture crack opening and closing, the Secant Method merely captures crack opening, which results in a reduced section area even after the crack closes up and is in compression. Thus, the Secant Method underestimates the effective stiffness. The moment history following the final iteration therefore resembles a more conservative model where permanent degradation has occurred, such as crushing of concrete and yielding

of reinforcement. This can be confirmed by comparing the two elastic moment histories to a NTHA using the same earthquake ground motion but with increased amplitude. Figure 7.3 illustrates this for element 4101, which experiences the largest moments in the structure. While the two elastic moment histories still result from the secant procedure using SP2, the fiber moment history uses $1.5 \times \text{SP2}$, to invoke permanent deformations. What becomes clear from the top figure, representing the moment about the local y-axis, is that the fiber moment history initially coincides with the initial elastic one. After reaching its maximum value, however, it gradually changes its phase, increasingly aligning with the final elastic curve. Two assumptions can be deduced from this realization. First, as expected, the reduced stiffnesses obtained following the Secant Method are conservative, as they mimic the nonlinear behavior following a stronger earthquake. Second, the earthquakes used during this analysis does not inflict permanent degradation beyond cracking, as the fiber moments stay aligned with the initial elastic moment in figures 6.26-6.33. Consequently, consistency with elastic design can be assumed.

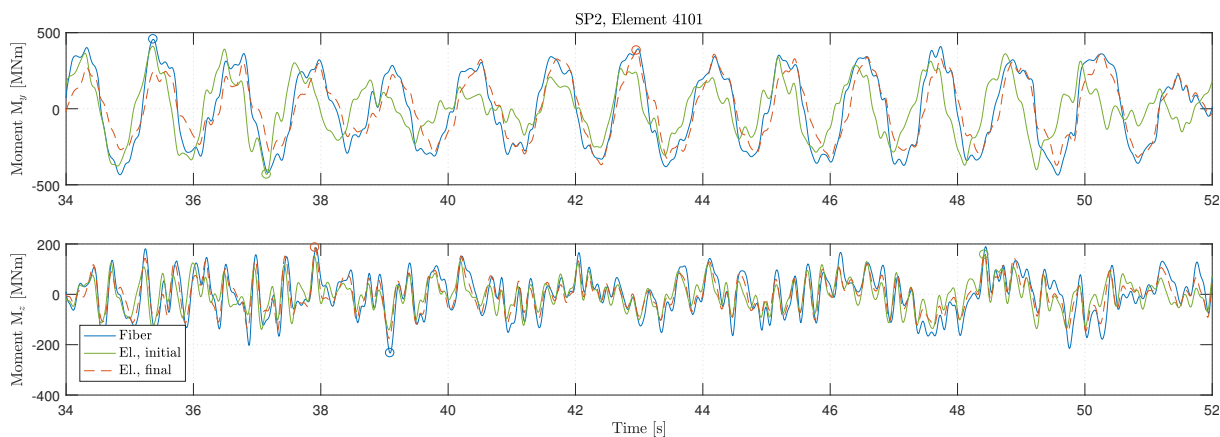


Figure 7.3: Moment history using 1.5SP2 as input during NTHA

Cracking of RC sections largely depends on the development of tensile stress. This in turn is determined by the moment and axial force as well as the section layout. Although the sections near the foundation are under extreme axial compression, it is evident that cracking indeed occurs, confirmed by table 7.1. Tables A.1-A.4 in Appendix A gives a complete summary of the stiffness ratios obtained. Despite the fact that the axial forces and section properties vary along the pylon leg, it is apparent that the the reduction ratio to some degree follow the NTHA moment distribution, as seen in these tables. The elements connecting the cross-beam to the pylon legs receive the largest reduction in the entire structure, even though their maximum bending moment values about the local y-axis are relatively low. This can be attributed to the section properties, but more importantly is a result of the oscillating axial forces, seen in tables 6.7 and 6.8. Even reaching tensile forces during some iterations, these sections are significantly exposed to cracking, also for small bending moment values.

The observation made regarding the reduced stiffness values coincides with what can intuitively be expected. Yet, the question remain weather they represent a valid assumption or

not and if the reduced elastic model is representative of the inelastic behavior. As previously discussed, the stiffness reductions are on the larger side, resulting a structure which is too soft. This consequently increases the the deflections, which in turn introduces additional forces due to the large compression forces. However, using the initial stiffness in further analysis will also undoubtedly introduce errors, as the structure will be too stiff. A structure whose stiffness is enveloped by these two outer limits can therefor be of interest. By merely using the reduced stiffnesses as guidelines, the effect of cracking can be implemented whilst to some degree counteracting the overestimated reductions.

7.3 Discussion of Results From the Pushover Analysis

By using the fiber model as reference for the performance of the elastic model, it is safe to say that the Secant Method in general is able to capture the material nonlinearities of the structure caused by concrete cracking, while the method struggles when yielding of the cross section has to be accounted for. For all pushover analyses, the response of the two models are approximately the same for the MPE level inertial forces corresponding to load step $\lambda = 1$, while there are some variations as λ surpasses this value.

For the longitudinal analysis L1, both the bending moment M_y at the base and the upper part of the pylon legs return results that were about equal to the nonlinear model response for the seismic level load step, see table 6.9 and figure 6.40. For the elements where there are deviations in the moment response, the results are slightly on the conservative side, that is, higher for the iterative elastic model. For load levels beyond the MPE, the Secant Method is to some extent able to reproduce the same responses as the fiber model. The moments in the elements are around 3-5% higher for all the critical elements in this analysis, seen in figure 6.41 and table 6.9, which confirms that the reduced elastic model still is able to mimic the nonlinear behavior of the structure. The maximum deviation at the final load step is 5%, which can be considered acceptable. The pushover curves in figure 6.39 also present the same results as mentioned above. The curves for the two models are similar up to $\lambda = 1$. Onwards, the elastic model begins to deviate from the reference results in the fiber model, and produce conservative responses. That is, for a given load step, the reduced elastic model is produces larger deflections and bending moments.

The longitudinal analysis L2 shows the same tendencies as L1. For the earthquake level forces, both structures yield identical results. All the critical elements have bending moments that match the moments appearing in the fiber model exactly. The stiffness of the base elements 4101 and 4201 have been reduced to 81% and 83% of their initial stiffnesses, which means that parts of the concrete section has reached its tensile strength and that the Secant Method has been able to emulate this effect, see table 6.10 and figure 6.43. When moving towards the final converged load step of the elastic model, $\lambda = 1.8$, the elastic model begins to diverge slightly from the nonlinear results. This is most likely because further reductions of the base

elements lead to increased displacements in the upper part of the pylon, which in turn due to P- Δ effects increases the secondary moments in the pylon. Despite of this, the maximum deviation for the moments in the critical elements is only 8%, while giving conservative results for this analysis as well. The pushover curves following the analysis in figure 6.48b illustrate this behavior. The displacement of node 4115 is for all practical purposes the same up to a load step of approximately $\lambda = 1.5$. For lambda values beyond this stiffening behavior of the elastic model can be observed. This is purely a numerical issue, which is likely caused by the Secant Methods apparent restrictions in emulating proper yielding and ductile behavior, similar to the case for analysis L1. Another possible explanation for the deviations in the longitudinal analyses for higher load levels is that for large deflections P- Δ effects plays a significant role. This makes the moment response at high load levels sensitive to deflections, which in turn will influence the stiffness reduction. The analyses might therefore struggle to converge within the accepted number of iterations.

At the MPE level inertial forces in analysis T1, the only considerable reduction of stiffness is in the western end of the lower cross-beam; 14% reduction of element 4501 compared to its initial stiffness. Given the relatively small reductions it is not surprising that the bending moment from the elastic model matches the nonlinear one, with the base of eastern pylon leg deviating less than 2%. By looking at the pushover curve in figure 6.45, one can observe that the two models produce similar results up to a load level of approximately $\lambda = 2$. From that point and onward, some numerical issues can be spotted in the load-moment curve for element 4201, which carries on until convergence failure at $\lambda = 4.4$. This issue might stem from the way the algorithm was implemented, as well as restrictions on the method's ability to capture ductile yielding as previously mentioned. The elements with the largest stiffness reductions are also the elements where the deviations in the moment values are the largest; namely the cross-beam elements. This support the assumption that the numerical instabilities seen in the pushover curves stem from shortcomings in the Secant Method when approaching the ultimate strength of the section. It is noteworthy how the cross-beams ends reduced the most, with an 84% and 72% stiffness reduction in elements 4501 and 4506 respectively, even though the governing failure mode for this analysis is failure at the base of the pylon legs. This can also serve as an explanation to why this analysis fails to converge relatively early compared to the fiber model, see table 6.11.

For analysis T2 it can be observed that the cross-beams already are reduced to about 30% of their initial stiffness for $\lambda = 1$. This can be explained by their relatively low axial forces, which make them susceptible to cracking. Despite this, the Secant Method yields accurate results throughout the analysis, alternating between conservative and unconservative results for the critical elements seen in table 6.12. The same goes for the results when the load step increases towards 1.35. The force-displacement curve in figure 6.48a shows that the Secant Method accurately approximates the displacement of the top node all the way up to the last converged load step. However, the procedure again falls short of following the curve all the way up to

$\lambda = 1.5$ at which the fiber model fails. At the last converged load step for the elastic model, the results from both models are fairly similar, with the exceptions being the base of the eastern pylon leg and the eastern end of the upper cross-beam; element 4201 with 9% underestimation and element 4504 with 12% overestimation.

The results at $\lambda = 1$ following analysis T3 bears some resemblance to the results from T2. That is, significant stiffness reduction of the cross-beams and decent approximations. More specifically, the upper cross-beam, element 4701, which also is the governing elements for this analysis, is reduced to 46% of its initial stiffness, see table 6.13. At the same time the deviation between the moments in the fiber and elastic model is within 6%. From approximately $\lambda = 1.5$, significant deviations in the deflection start to occur, which can be seen in figure 6.52a. The elastic model yields some unconservative results, which can also be seen in the 6.13 for $\lambda = 2.6$, where the base element 4101 as well as the lower cross-beam element 4501 have deviations of 13-14%. The upper cross-beam, however, have a resulting moment on the conservative side, which consequently renders larger stiffness reductions than what can be expected. This will affect the magnitude of the bending moments carried by the lower part of the pylon and hence be an explanation for the deviations found in these elements.

In general the Secant Method was able to accurately estimate the response of the South Pylon when the nonlinear fiber model is used as a reference. For the load level corresponding to the inertial forces from the seismic ground motion, all critical elements are within an tolerable margin, the exception being element 4701 in analysis T2. As the elements approach their final converged steps, the method seems to somewhat destabilize and give less accurate results. As mentioned, this is likely due of the algorithm itself, which struggles to capture the ductile yielding behavior of the structure. Despite these numerical issues, the method serves its purpose by being able to accurately approximate the response of the cracked concrete sections and force distribution in the pylon up to the MPE level. Further, the procedure is to some extent able to provide reasonably accurate, though slightly conservative, force distributions for the nonlinear branch of the analysis.

It should be noted that the resulting stiffness reductions following the pushover analyses were in general somewhat lower than than the corresponding mean element reductions following the THA. For example, from table 7.1, element 4101 has experienced a mean stiffness of 0.63 times its initial stiffness, while the pushover analysis L2 where element 4101 is the critical element resulted in a ratio of 0.81 for $\lambda = 1$. This can also be observed for the critical elements in other pushover analyses. The explanation for this is that inertial forces used in the pushover analyses are obtained from the response history using the fiber model rather than the reduced elastic model. The accelerations history for the reduced elastic model were in general larger than the accelerations from the fiber model, which in turn leads to lower inertial forces when using the latter. By using a force input with lower load levels, the reductions at the chosen load level are consequently smaller. The choice to use the accelerations from the fiber model was made because this model acts as a reference for the analysis, and it would therefore be suitable

to use the forces extracted from this model. Because the results showed that the Secant Method was still relatively accurate for loads up to at least $\lambda = 1.2$, the force input was kept as is. With more time in hand, it would have been possible to run the analyses with inertial force input from the response history of both models to further analyze their differences.

7.4 Further Work

If more time was available at hand, several improvements likely could have been made to both the fiber and the elastic model. A more uniform node distribution could for instance have been applied to cope with the absence of nonlinear element geometry effects. By using linear interpolation to calculate new node coordinates while maintaining geometry, element lengths can be decided based on their stiffness and anticipated axial load. By ensuring that ψ given by

$$\psi = \sqrt{\frac{|\mathbf{q}_1|L^2}{EI}} \quad (7.1)$$

where \mathbf{q}_1 is the axial basic force, is less than 0.5, first order stiffness coefficients can be used [8]. Solving equation 7.1 for the element length L using $\psi=0.5$ thus gives the upper limit for element lengths for which the basic axial force \mathbf{q}_1 has negligible influence on the flexural stiffness \mathbf{k} . This will potentially provide more accurate results, but depending on the refinement also come at the expense of computational cost.

Looking at the fiber model, the effect of confinement could have been taken into consideration if more time had been set aside to calculate the different parameters needed and subdividing the section mesh. This would yield a more realistic model, but it should be emphasized that the main importance for this thesis is the similarity between the elastic model and the fiber model.

OpenSees provides the possibility of recording the stress and strain in each individual fiber during analyses. Although a tedious task to implement, this would have provided a necessary tool which could have been used when investigating convergence failure in the Secant Method and section response close to the ultimate strength of the sections.

It must be stressed that the different OpenSees scripts containing the model and running analyses are complex and as new layers of code were added, it became increasingly harder to modify the older parts. If the modifications previously mentioned had been taken into account from the beginning, it would have been significantly easier to implement them.

Using the final structure with reduced stiffness in other analyses such as for instance a response spectrum analysis to see how the results hold up against those following a NTHA is in itself an interesting subject. This can further confirm the assumptions made about the reduced model or find shortcomings with it. It would also be beneficial to investigate the effect increased eigen periods due to reduced stiffness will have on accelerations during such an analysis.

Chapter 8

Conclusion

The goal of this study has been to assess if the the secant stiffness could provide a reasonable approximation to the nonlinear material behavior of structures. Naturally, a good indication of this is that the responses following the secant procedure coincides with the ones following a NTHA. The results presented in previous section indicate that the approximation is satisfactory for the majority of the elements, but there are also anomalies where the secant procedure increases the gap between the THA and NTHA responses. These may occur for a number of reasons, most of which are rooted in the shortcomings of the Secant Method itself, which are summarized in section 3.3 and further discussed in section 7.1. Despite these observations, discrepancies between the moment values from the two models should not render the reduced stiffnesses incorrect. The reduced stiffness values obtained following the secant procedure merely indicate whether or not nonlinearities have occurred during the THA, that is, cracking of concrete and yielding of reinforcement. As discussed in the previous section, the observations made regarding the reduced stiffness values coincides with what can intuitively be expected. Further, if the results are assessed properly, the linear elastic model with reduced flexural stiffnesses may be utilized in further analysis. Clearly, using the initial, unreduced linear elastic model in say a response spectrum analysis will yield conservative forces if cracking is indeed expected to occur. Use of the reduced linear elastic model with the associated increased periods of the structure will produce more realistic results by capturing the crack distribution. Additionally, as seen throughout the results presented in this thesis, discrepancies between the results of NTHA and the reduced elastic model tends to be on the conservative side. That is, the elastic model with reduced stiffnesses tends to produce higher maximum moments than the fiber model. As discussed, this follows from the fact that use of the Secant Method often results in a structure that is too soft. Thus, rather than simply using the stiffness values obtained following the Secant Method, it is proposed in this study to use these as guidelines for creating new stiffnesses. By selecting stiffnesses enveloped by the initial and reduced values, more towards the latter, the overestimated reduction is to some degree counteracted. If the relative magnitude among the stiffness reductions remain the same, a structure which contains a realistic representation of the crack distribution will then result.

The numerical tool was also used in the pushover analyses. The results from the pushover analysis indicated that the Secant Method is capable of accurately producing the same bending moments and displacement patterns as the nonlinear fiber model up to and slightly beyond the load levels corresponding the maximum loads from various THA. When reaching load levels

where post-yield capacity was expected, the Secant Method produced bending moments with slightly higher values in the elements experiencing the largest reductions. This may be due to a number of effects, most important of which is the way the Secant Method obtains stiffnesses for moments close to the ultimate section capacity. Nevertheless, the general trend from the pushover analyses, both for $\lambda = 1$, and for higher load levels is that the force distribution, as well as deflections to a certain degree are approximated to a sufficient level, especially in the most critical elements. Overall, the Secant Method has proved to be a valid option to the full nonlinear analysis. The method is also code-compliant as it satisfies the requirements from both Eurocode 8 and the AASHTO Guide Specifications for LRFD Seismic Bridge Design with regards to providing results that are consistent with expected nonlinear material behaviour.

Bibliography

- [1] S.E. Barrientos. Earthquakes in Chile. *Geological Society Special Publication*, 01 2007.
- [2] Andrew Randell. Chile Gives Us A Lesson in Plate Tectonics | Geology for Investors. Available from: <https://www.geologyforinvestors.com/chile-lesson-plate-tectonics/>. [2019-05-02].
- [3] American Association of State Highway, Transportation Officials. Subcommittee on Bridges, and Structures. *AASHTO Guide Specifications for LRFD Seismic Bridge Design*. American Association of State Highway and Transportation Officials, 2011.
- [4] Aas-Jakobsen. Chacao bridge. Available from: <https://www.aaj.no/prosjekter/chacao/>. [2019-05-05].
- [5] Frank McKenna, Silvia Mazzoni, Michael H. Scott, and Gregory L. Fenves. Opensees command language manual. *Open System for Earthquake Engineering Simulation*, 2006.
- [6] RM Bridge. *Connect Edition*. Benteley Systems Incorporated, Exton, Pennsylvania, 2019.
- [7] MATLAB. *version 9.1.0 (R2016b)*. The MathWorks Inc., Natick, Massachusetts, 2016.
- [8] Filip C. Filippou. *Lecture Notes from CE220N Nonlinear structural analysis*. University of California, Berkeley, Department of Civil and Environmental Engineering, 2018.
- [9] Joel P. Conte. *Reader-SE201B Nonlinear Structural Analysis*. University of California, San Diego, Department of Structural Engineering, 2018.
- [10] Milton Abramowitz and Irene A Stegun. *Handbook of mathematical functions: with formulas, graphs, and mathematical tables*, volume 55. Courier Corporation, 1965.
- [11] A. Quarteroni, R. Sacco, and F. Saleri. *Numerical Mathematics*. Texts in Applied Mathematics. Springer Berlin Heidelberg, 2010.
- [12] Armando Calabrese, João Pacheco Almeida, and Rui Pinho. Numerical issues in distributed inelasticity modeling of rc frame elements for seismic analysis. *Journal of earthquake engineering : JEE.*, 14(S1), 2010.
- [13] I Demir Karsan and James O Jirsa. Behavior of concrete under compressive loadings. *Journal of the Structural Division*, 1969.
- [14] Dudley Charles Kent and Robert Park. Flexural members with confined concrete. *Journal of the Structural Division*, 97(7), 1971.

- [15] Nurbaiah Mohammad Noh, Laura Liberatore, Fabrizio Mollaioli, and Solomon Tesfamariam. Modelling of masonry infilled rc frames subjected to cyclic loads: State of the art review and modelling with opensees. *Engineering Structures*, 150, 2017.
- [16] Yassin MH Mohd. Nonlinear analysis of prestressed concrete structures under monotonic and cyclic loads. *PhD Thesis*, 1995.
- [17] Vesna Terzic and Bozidar Stojadinovic. Calibration and validation of analytical models for predicting the seismic and axial-load response of circular bridge columns. *Journal of Bridge Engineering*, 20(9), 2015.
- [18] John B Mander, Michael J.N Priestley, and R Park. Theoretical stress-strain model for confined concrete. *Journal of structural engineering*, 114(8), 1988.
- [19] Filip Filippou, A D'Ambrisi, and A Issa. Effects of reinforcement slip on hysteretic behavior of reinforced concrete frame members. *ACI Structural Journal*, 96, 05 1999.
- [20] Wai-Fah Chen. *Plasticity in reinforced concrete*. J. Ross Publishing, 2007.
- [21] Enrico Spacone, Filip Filippou, and F F. Taucer. Fiber beam-column model for nonlinear analysis of r/c frames. *Earthquake Engineering & Structural Dynamics*, 25, 07 1996.
- [22] Filip C Filippou, Vitelmo Victorio Bertero, and Egor P Popov. Effects of bond deterioration on hysteretic behavior of reinforced concrete joints. *National Technical Information Service*, 1983.
- [23] A.P. Jeary. Damping in structures. *Journal of Wind Engineering and Industrial Aerodynamics*, 72, 1997. Selected papers from the Ninth International Symposium on Wind Engineering.
- [24] Emrah Erduran. Evaluation of rayleigh damping and its influence on engineering demand parameter estimates. *Earthquake Engineering & Structural Dynamics*, 41(14), 2012.
- [25] A.K. Chopra. *Dynamics of Structures: Theory and Applications to Earthquake Engineering*. Civil Engineering and Engineering Mechanics Series. Prentice Hall, 2012.
- [26] Standard Norge. *Eurocode 8: Design of structures for earthquake resistance - Part 1: General rules, seismic action and rules for buildings*. NS-EN 1998-1:2004+A1:2013+NA:2014, 2014.
- [27] Anil K Chopra and Rakesh K Goel. A modal pushover analysis procedure for estimating seismic demands for buildings. *Earthquake engineering & structural dynamics*, 31(3), 2002.
-

-
- [28] Aas-Jakobsen, SYSTRA, Hyundai Engineering & Construction, and OAS. *Global Analysis, Pushover Analysis South Pylon*. Report CHB-SAJ-DGN-DOC-GB-0107, 2018. Not publicly available.
- [29] Aas-Jakobsen, SYSTRA, Hyundai Engineering & Construction, and OAS. *Pylons Seismic Design Approach*. Technical Memo CHB-SAJ-DGN-TME-GB-0066-0A, 2016. Not publicly available.
- [30] Khalid M. Mosalam. *Lecture Notes from CE222 Finite Element Methods*. University of California, Berkeley, Department of Civil and Environmental Engineering, 2018.
- [31] Aas-Jakobsen, SYSTRA, Hyundai Engineering & Construction, and OAS. *Global Analysis, Dynamic Seismic Analyses Results*. Report CHB-SAJ-DGN-DOC-GB-0106, 2018. Not publicly available.
- [32] Jerome F. Hajjar. Description of geometric nonlinearity for beam-column analysis in opensees september 2013. 2013.
- [33] Aas-Jakobsen, SYSTRA, Hyundai Engineering & Construction, and OAS. *Dynamic Impedances and Foundation Input Motions*. Report CHB-SAJ-DGN-DOC-GB-0223, 2018. Not publicly available.
-

Appendix

Appendix A

Secant Procedure Results

Tables A.1-A.4 below summarize the converged ratios of initial stiffness for each element in both directions calculated using equation 5.2 and 5.1. The ratios thus results from the final iteration of the Secant Method, for each ground motion record SP1-SP7. Column 2-8 in each table depicts an individual ground motion record and the reduction about one axis. The second to last column shows the mean values of the ratios, take over all ground motions, and the last column the mean moment of all seven NTHA using the fiber model, in units of MNm.

Table A.1: Ratios of initial stiffness, y-direction, element 4101-4122, 4501-4506

| Element | SP1 | SP2 | SP3 | SP4 | SP5 | SP6 | SP7 | Ratio | Ave |
|---------|------|------|------|------|------|------|------|-------|-----|
| 4101 | 0.52 | 0.61 | 0.54 | 0.54 | 0.65 | 0.81 | 0.74 | 0.63 | 338 |
| 4102 | 0.55 | 0.71 | 0.62 | 0.59 | 0.78 | 0.90 | 0.83 | 0.71 | 306 |
| 4103 | 0.61 | 0.59 | 0.73 | 0.92 | 0.90 | 0.95 | 0.91 | 0.80 | 274 |
| 4104 | 0.89 | 0.79 | 0.96 | 0.96 | 0.97 | 0.97 | 0.98 | 0.93 | 239 |
| 4105 | 0.98 | 0.94 | 0.98 | 0.98 | 0.98 | 0.98 | 0.99 | 0.98 | 211 |
| 4106 | 0.99 | 0.99 | 0.99 | 0.99 | 0.99 | 0.99 | 1.00 | 0.99 | 187 |
| 4107 | 0.99 | 0.98 | 0.99 | 0.99 | 0.99 | 0.99 | 1.00 | 0.99 | 171 |
| 4108 | 0.99 | 0.99 | 0.99 | 0.99 | 0.99 | 0.99 | 1.00 | 0.99 | 155 |
| 4109 | 0.99 | 0.99 | 0.99 | 0.99 | 0.99 | 0.99 | 1.00 | 0.99 | 134 |
| 4110 | 0.99 | 0.99 | 0.99 | 0.98 | 0.99 | 0.99 | 1.00 | 0.99 | 133 |
| 4111 | 1.00 | 0.99 | 1.00 | 1.00 | 0.99 | 1.00 | 0.99 | 1.00 | 72 |
| 4112 | 0.99 | 0.99 | 0.99 | 0.99 | 0.99 | 0.99 | 0.99 | 0.99 | 92 |
| 4113 | 0.97 | 0.97 | 0.98 | 0.98 | 0.98 | 0.98 | 0.99 | 0.98 | 143 |
| 4114 | 0.87 | 0.77 | 0.94 | 0.97 | 0.96 | 0.98 | 0.98 | 0.93 | 180 |
| 4115 | 0.80 | 0.57 | 0.78 | 0.95 | 0.89 | 0.89 | 0.88 | 0.82 | 192 |
| 4116 | 0.94 | 0.93 | 0.90 | 0.97 | 0.91 | 0.90 | 0.92 | 0.92 | 176 |
| 4117 | 0.98 | 0.98 | 0.98 | 0.98 | 0.97 | 0.98 | 0.99 | 0.98 | 123 |
| 4118 | 0.99 | 1.00 | 0.99 | 0.99 | 0.99 | 1.00 | 1.00 | 0.99 | 99 |
| 4119 | 1.00 | 1.00 | 1.00 | 0.99 | 0.99 | 1.00 | 1.00 | 1.00 | 74 |
| 4120 | 1.00 | 1.00 | 1.00 | 1.00 | 1.00 | 1.00 | 1.00 | 1.00 | 53 |
| 4121 | 1.00 | 1.00 | 1.00 | 1.00 | 1.00 | 1.00 | 1.00 | 1.00 | 36 |
| 4122 | 1.00 | 1.00 | 1.00 | 1.00 | 1.00 | 1.00 | 1.00 | 1.00 | 30 |
| 4501 | 0.30 | 0.32 | 0.31 | 0.32 | 0.31 | 0.32 | 0.32 | 0.31 | 185 |
| 4502 | 0.33 | 0.62 | 0.57 | 0.69 | 0.45 | 0.69 | 0.51 | 0.55 | 127 |
| 4503 | 0.99 | 1.00 | 0.99 | 1.00 | 0.99 | 0.99 | 0.99 | 0.99 | 67 |
| 4504 | 1.00 | 1.00 | 1.00 | 1.00 | 1.00 | 1.00 | 1.00 | 1.00 | 14 |
| 4505 | 0.91 | 0.99 | 0.98 | 0.98 | 0.93 | 0.98 | 0.97 | 0.96 | 68 |
| 4506 | 0.31 | 0.43 | 0.36 | 0.41 | 0.33 | 0.37 | 0.35 | 0.37 | 120 |

Table A.2: Ratios of initial stiffness, y-direction, element 4201-4222, 4701-4704

| Element | SP1 | SP2 | SP3 | SP4 | SP5 | SP6 | SP7 | Ave | Ave |
|---------|------|------|------|------|------|------|------|------|-----|
| 4201 | 0.54 | 0.52 | 0.60 | 0.68 | 0.56 | 0.68 | 0.81 | 0.63 | 331 |
| 4202 | 0.58 | 0.72 | 0.70 | 0.81 | 0.64 | 0.82 | 0.90 | 0.74 | 299 |
| 4203 | 0.63 | 0.87 | 0.81 | 0.54 | 0.77 | 0.91 | 0.95 | 0.78 | 268 |
| 4204 | 0.92 | 0.94 | 0.94 | 0.90 | 0.97 | 0.97 | 0.97 | 0.95 | 236 |
| 4205 | 0.98 | 0.97 | 0.98 | 0.98 | 0.98 | 0.98 | 0.98 | 0.98 | 208 |
| 4206 | 0.99 | 0.98 | 0.99 | 0.99 | 0.99 | 0.99 | 0.98 | 0.99 | 183 |
| 4207 | 0.99 | 0.98 | 0.99 | 0.99 | 0.99 | 0.99 | 0.99 | 0.99 | 171 |
| 4208 | 0.99 | 0.98 | 0.99 | 0.99 | 0.99 | 0.99 | 0.98 | 0.99 | 154 |
| 4209 | 1.00 | 0.98 | 0.99 | 1.00 | 0.99 | 0.99 | 0.99 | 0.99 | 133 |
| 4210 | 1.00 | 0.98 | 0.99 | 1.00 | 0.99 | 0.99 | 0.98 | 0.99 | 132 |
| 4211 | 0.99 | 1.00 | 0.99 | 0.99 | 0.99 | 1.00 | 1.00 | 0.99 | 72 |
| 4212 | 0.99 | 0.99 | 0.99 | 0.98 | 0.98 | 0.99 | 0.99 | 0.99 | 93 |
| 4213 | 0.97 | 0.97 | 0.98 | 0.98 | 0.98 | 0.98 | 0.99 | 0.98 | 142 |
| 4214 | 0.89 | 0.94 | 0.96 | 0.95 | 0.93 | 0.98 | 0.97 | 0.95 | 180 |
| 4215 | 0.82 | 0.84 | 0.86 | 0.85 | 0.68 | 0.91 | 0.96 | 0.84 | 192 |
| 4216 | 0.90 | 0.88 | 0.94 | 0.93 | 0.79 | 0.92 | 0.97 | 0.90 | 175 |
| 4217 | 0.98 | 0.98 | 0.98 | 0.99 | 0.99 | 0.98 | 0.98 | 0.98 | 122 |
| 4218 | 1.00 | 0.99 | 1.00 | 1.00 | 1.00 | 0.99 | 0.99 | 0.99 | 97 |
| 4219 | 1.00 | 1.00 | 1.00 | 1.00 | 1.00 | 1.00 | 0.99 | 1.00 | 73 |
| 4220 | 1.00 | 1.00 | 1.00 | 1.00 | 1.00 | 1.00 | 1.00 | 1.00 | 52 |
| 4221 | 1.00 | 1.00 | 1.00 | 1.00 | 1.00 | 1.00 | 1.00 | 1.00 | 36 |
| 4222 | 1.00 | 1.00 | 1.00 | 1.00 | 1.00 | 1.00 | 1.00 | 1.00 | 30 |
| 4701 | 0.33 | 0.34 | 0.35 | 0.35 | 0.34 | 0.34 | 0.37 | 0.35 | 137 |
| 4702 | 0.75 | 0.85 | 0.98 | 0.98 | 0.82 | 0.91 | 0.99 | 0.90 | 75 |
| 4703 | 1.00 | 1.00 | 1.00 | 1.00 | 1.00 | 1.00 | 1.00 | 1.00 | 16 |
| 4704 | 0.50 | 0.73 | 0.69 | 0.66 | 0.62 | 0.60 | 0.69 | 0.64 | 74 |

Appendix B

Mode shapes

The following appendix illustrates the mode shapes of the South Pylon. Only the mode shapes for the fiber model have been included as the mode shapes for the elastic model being equal, with only slight differences in periods, see table 4.7.

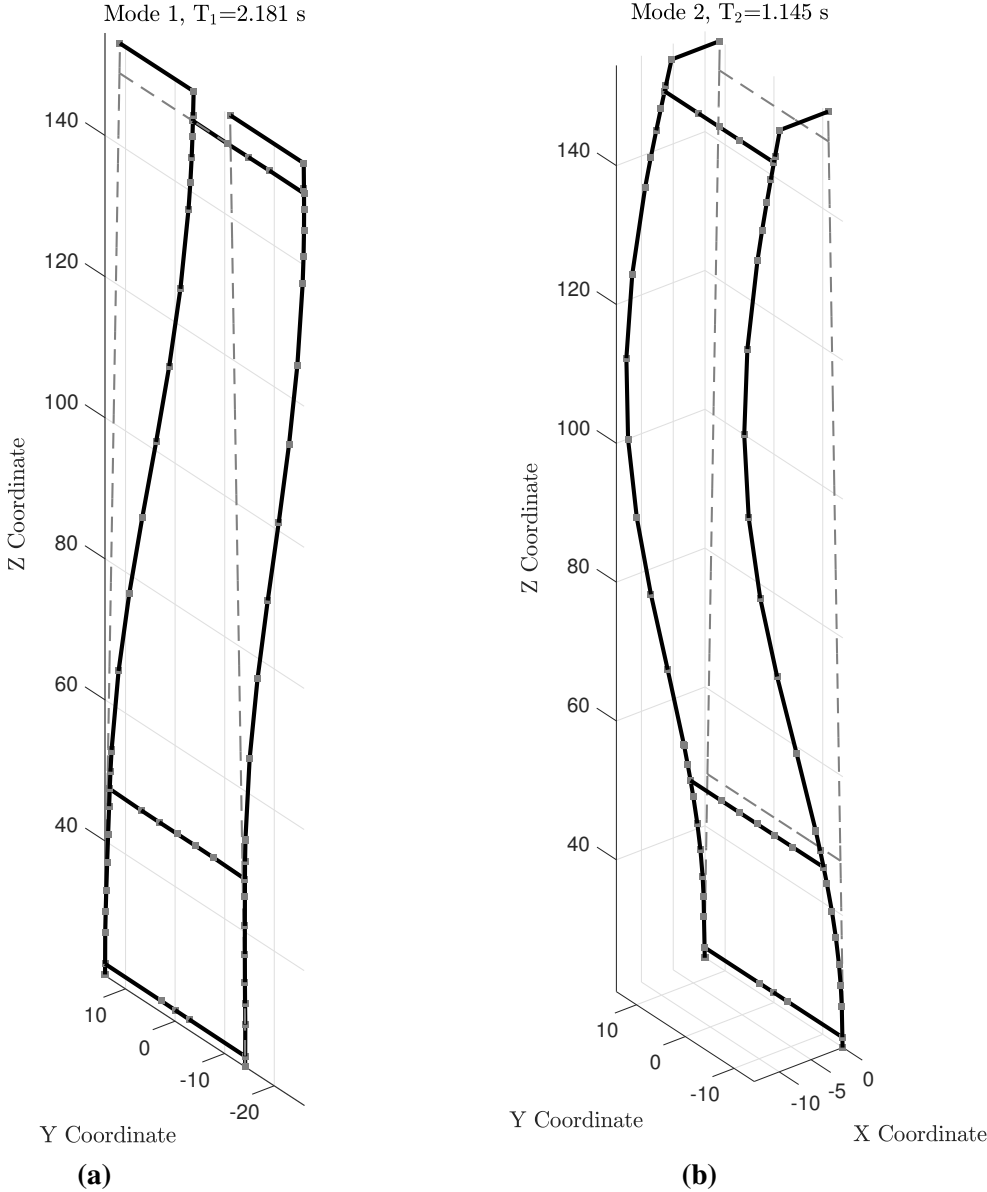


Figure B.1: Mode shapes for the fiber model with cable springs

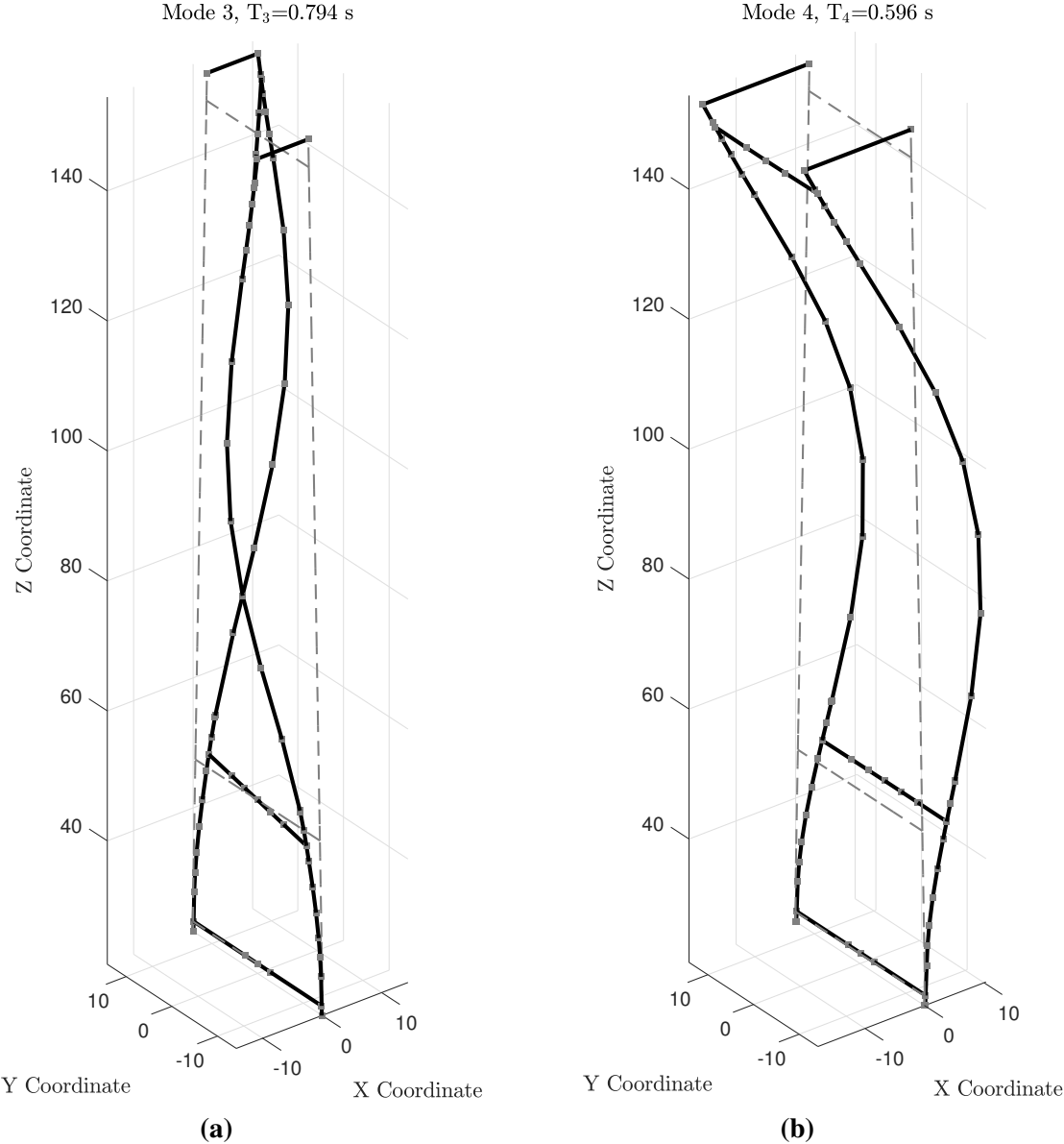


Figure B.2: Mode shapes for the fiber model with cable springs

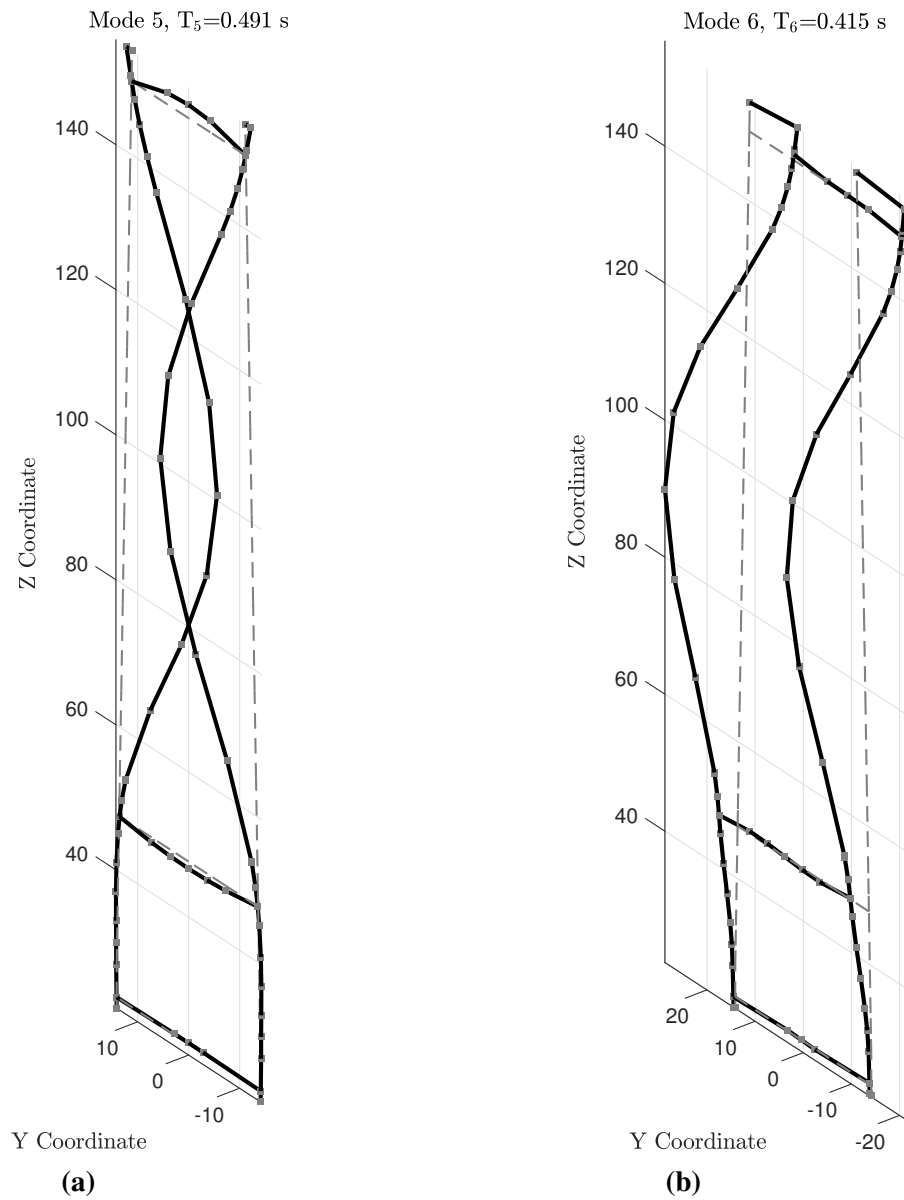


Figure B.3: Mode shapes for the fiber model with cable springs

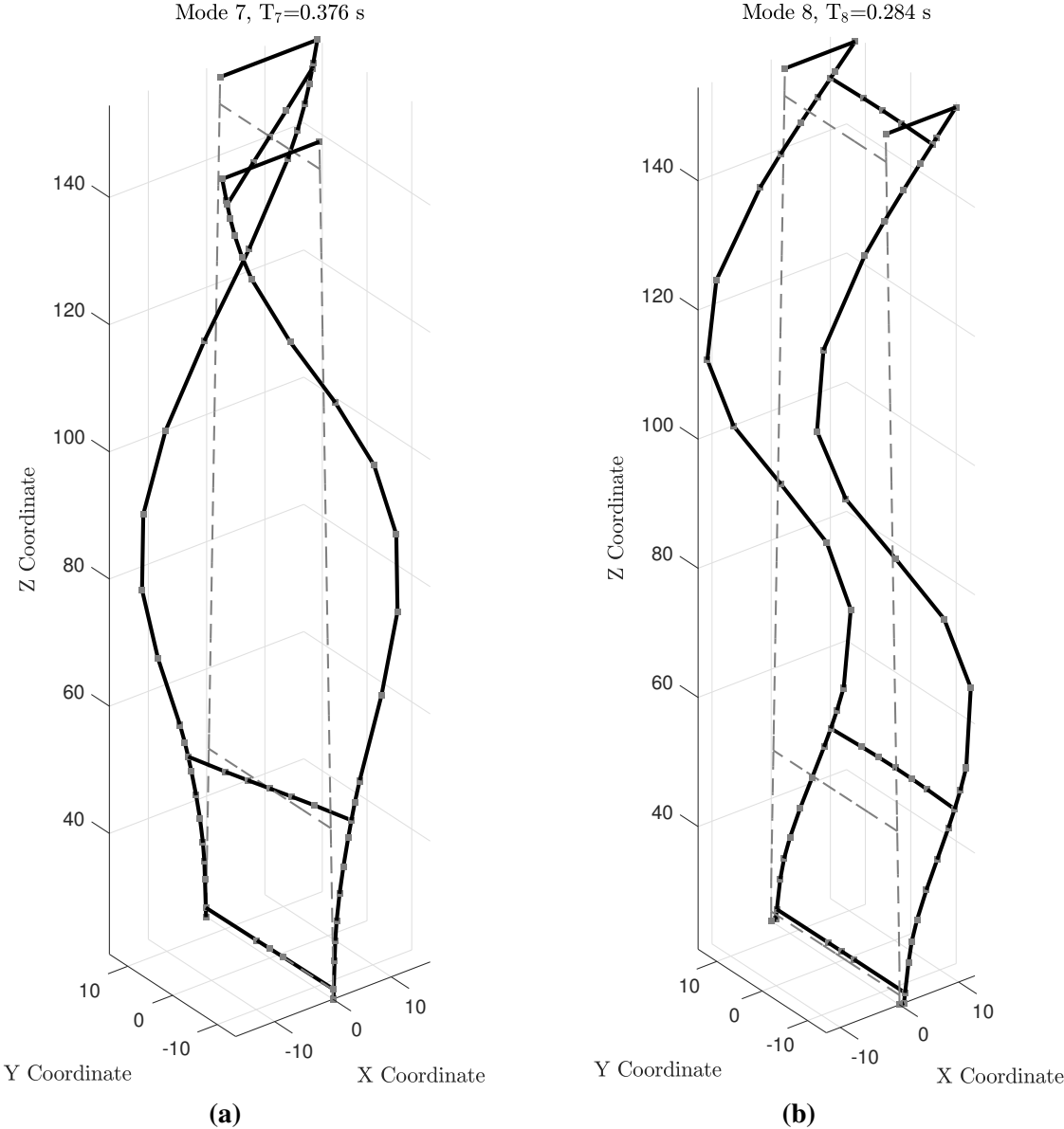


Figure B.4: Mode shapes for the fiber model with cable springs

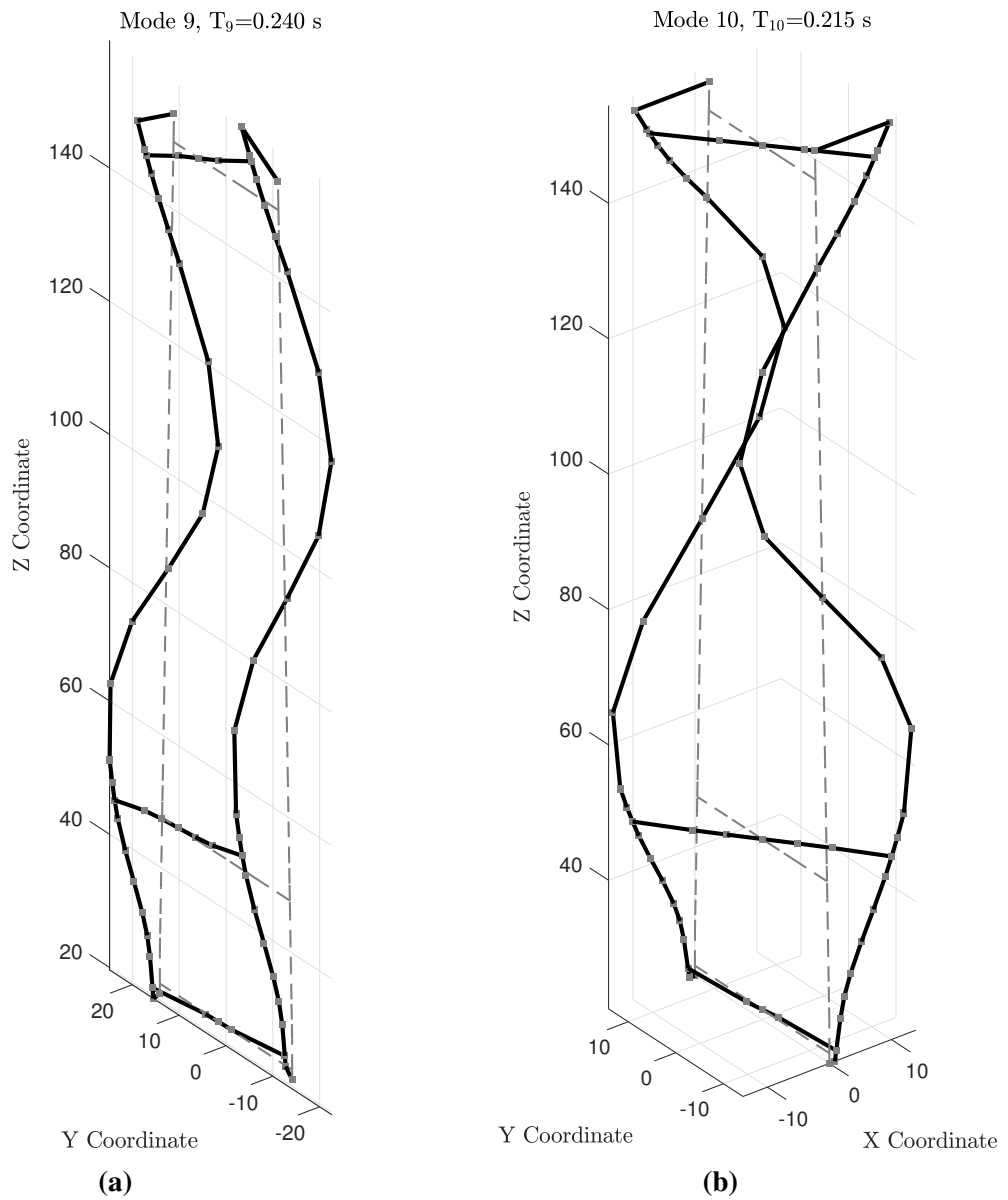


Figure B.5: Mode shapes for the fiber model with cable springs

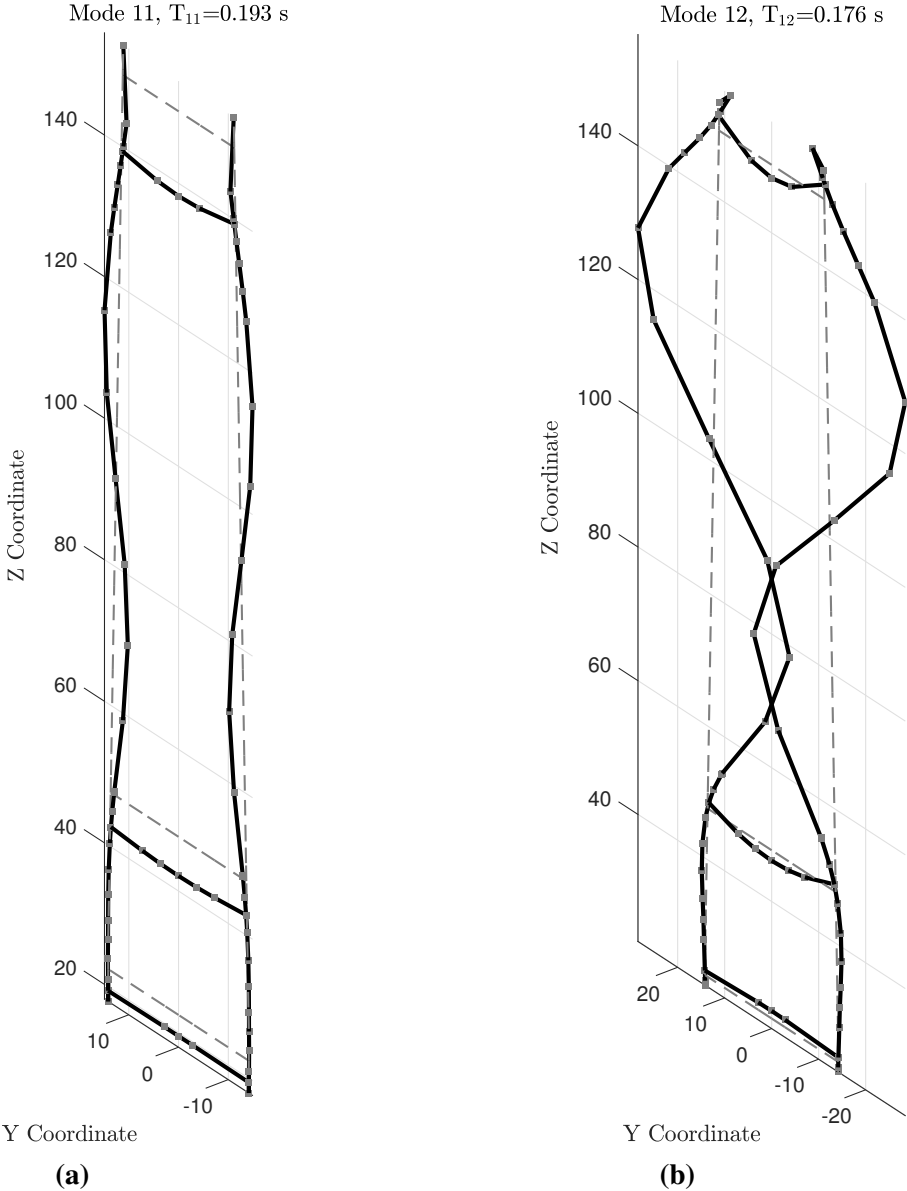


Figure B.6: Mode shapes for the fiber model with cable springs

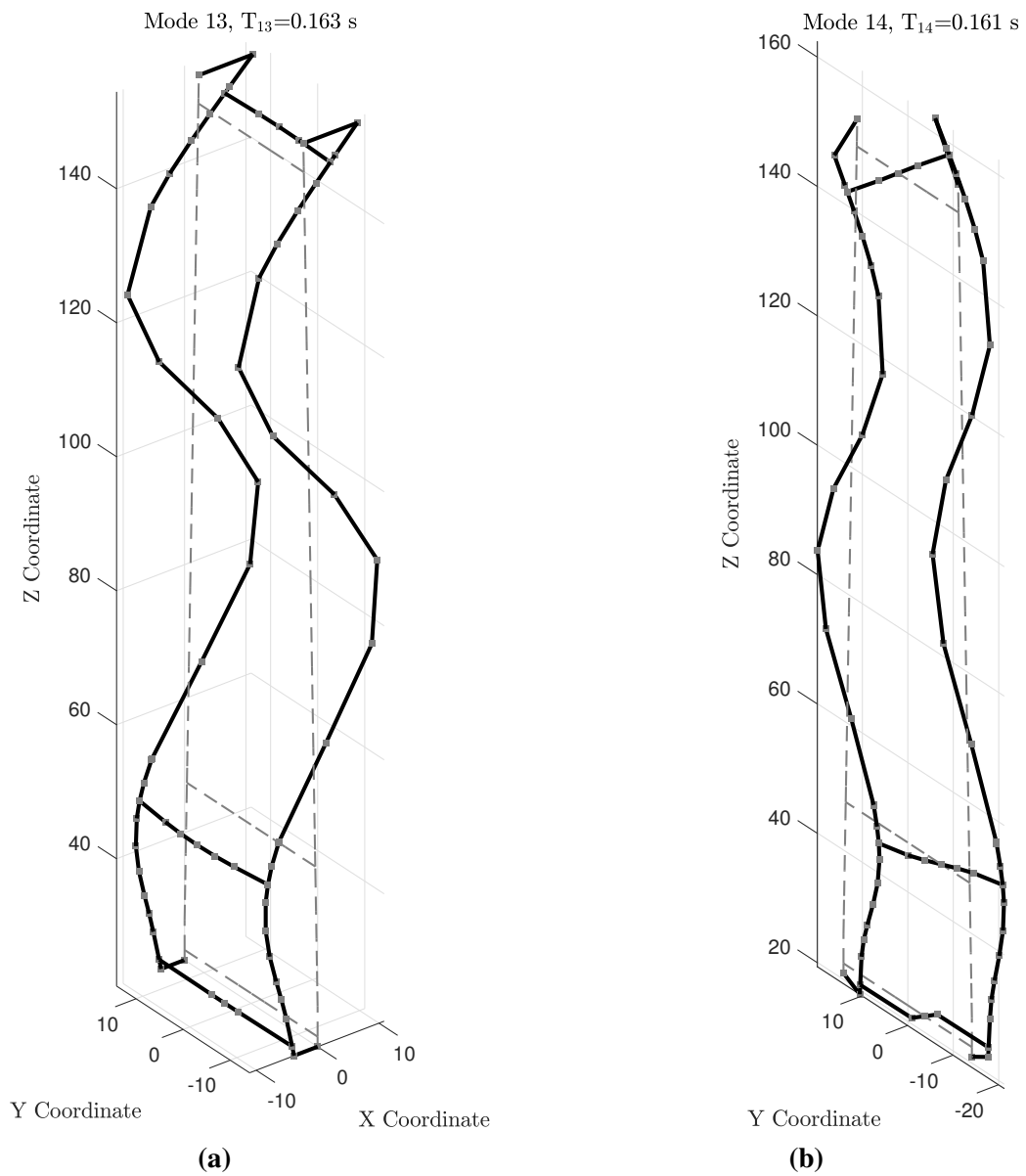


Figure B.7: Mode shapes for the fiber model with cable springs

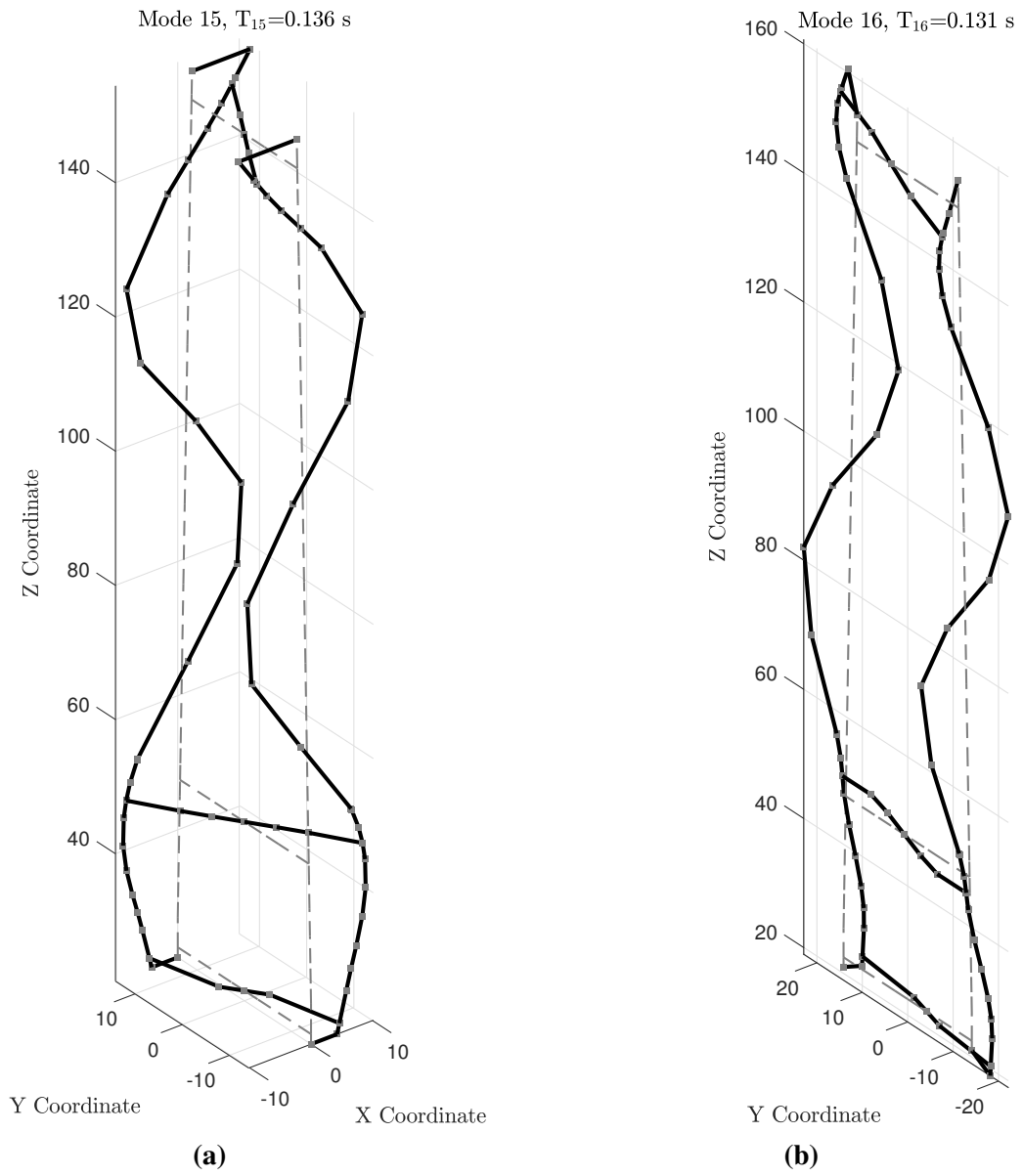


Figure B.8: Mode shapes for the fiber model with cable springs

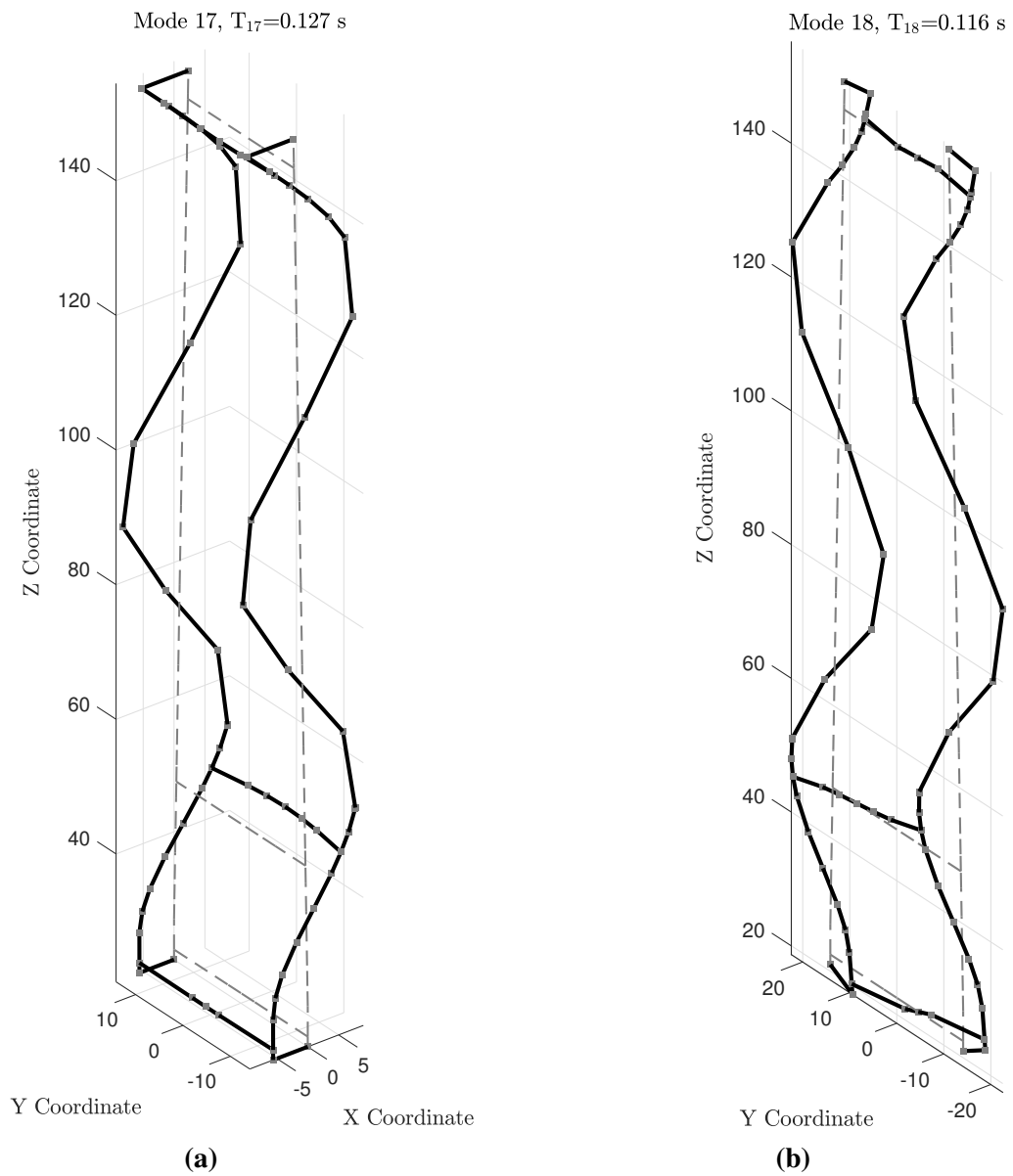


Figure B.9: Mode shapes for the fiber model with cable springs

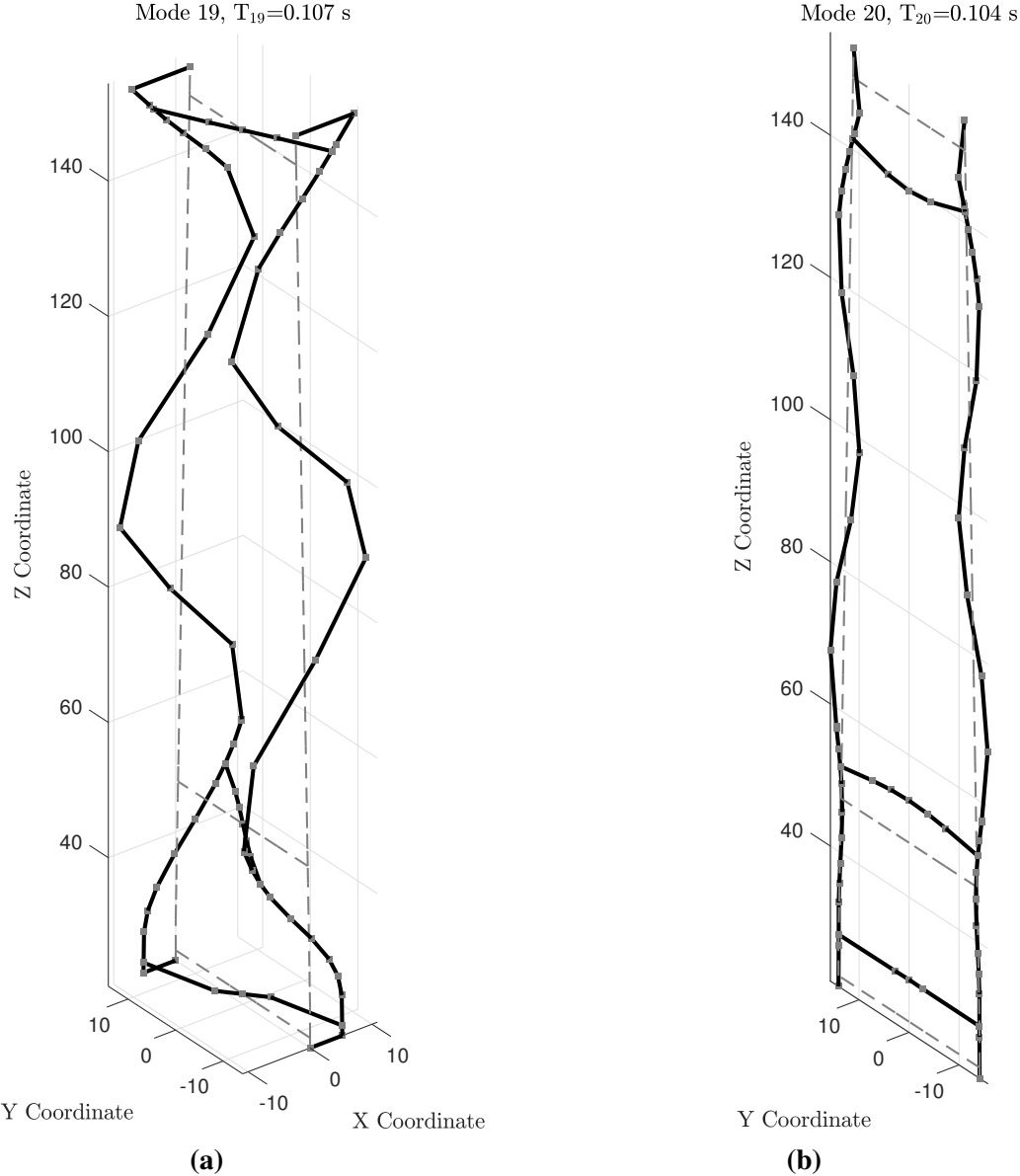


Figure B.10: Mode shapes for the fiber model with cable springs

Appendix C

Cross sections

The following appendix illustrates the various cross sections used in both the fiber model, and for creating the moment-curvature diagrams for use with the Secant Method. The cross sectional properties are listed in table 4.4 in chapter 4. The figures have been created using a MATLAB-script, and are produced in scale and with fixed axes to showcase the relative differences in section dimensions.

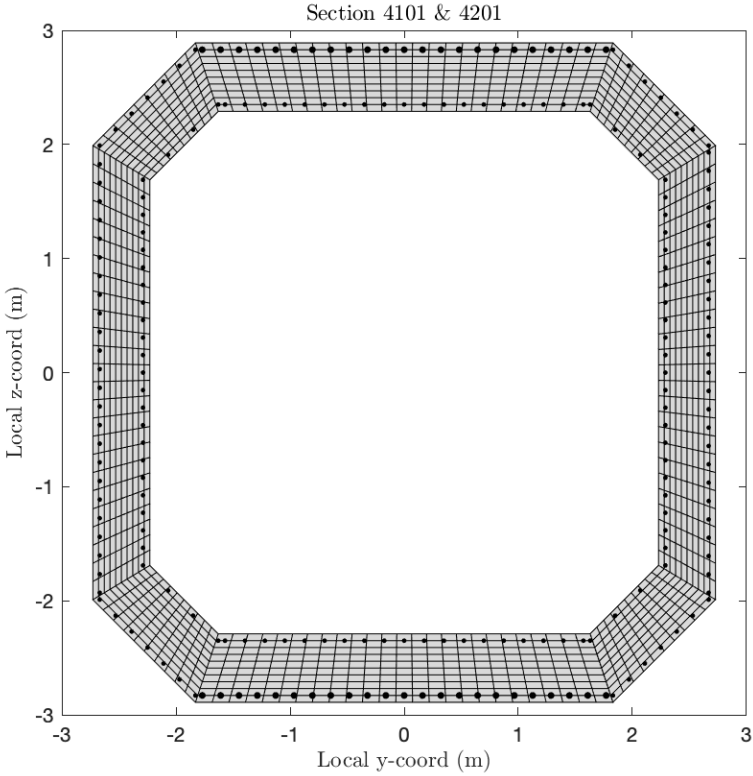


Figure C.1: Section 4101 and 4201

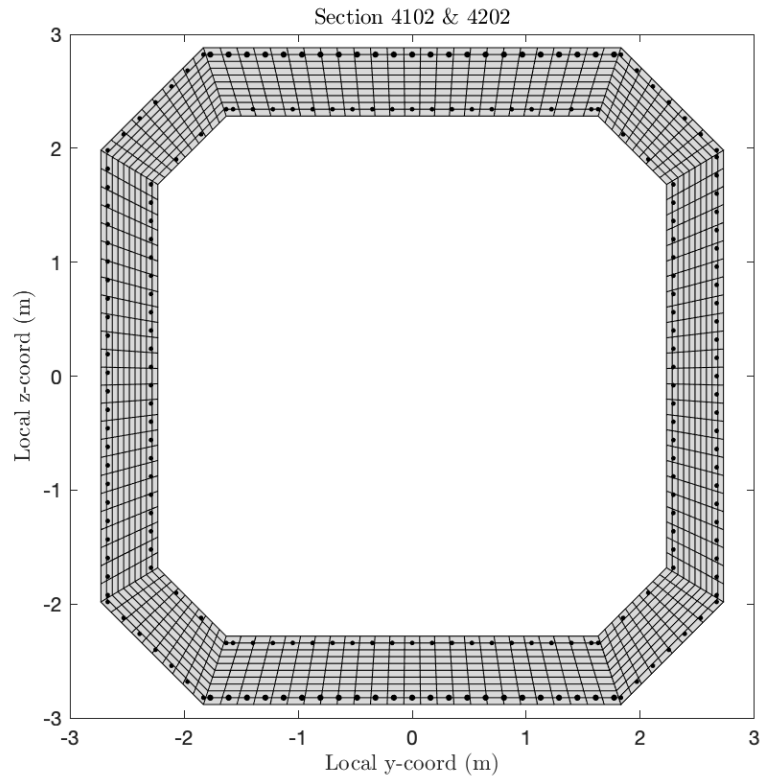


Figure C.2: Section 4102 and 4202

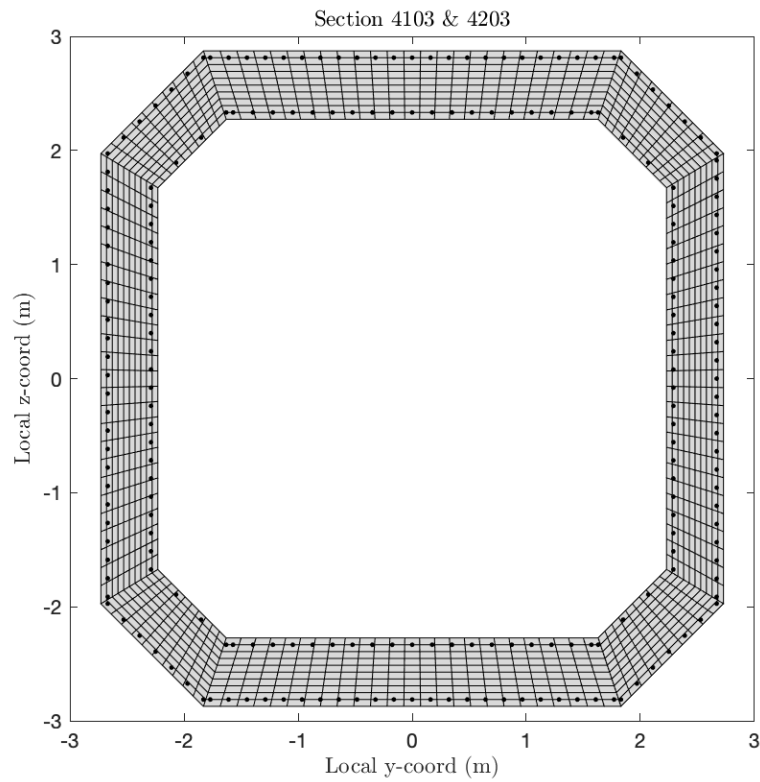


Figure C.3: Section 4103 and 4203

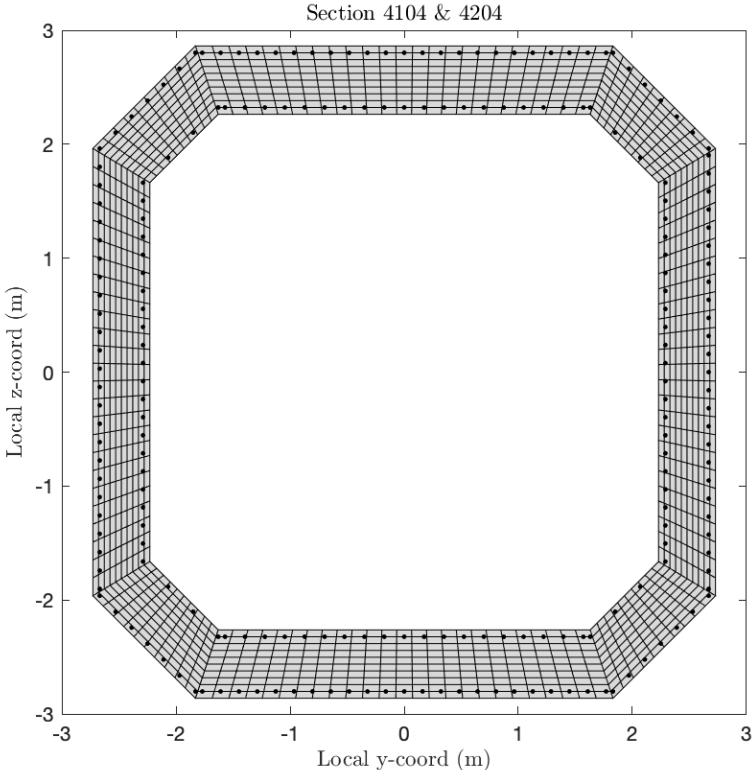


Figure C.4: Section 4104 and 4204

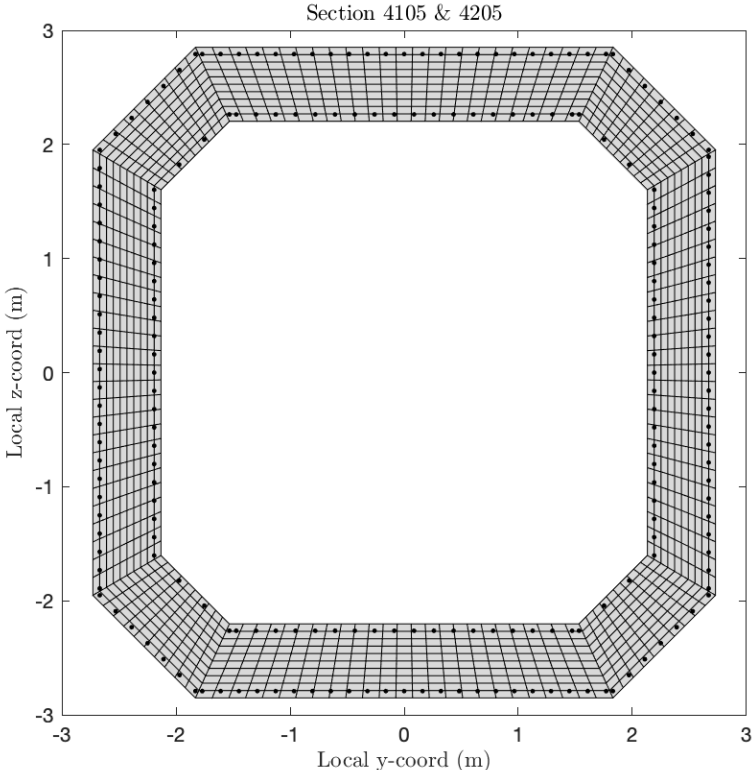


Figure C.5: Section 4105 and 4205

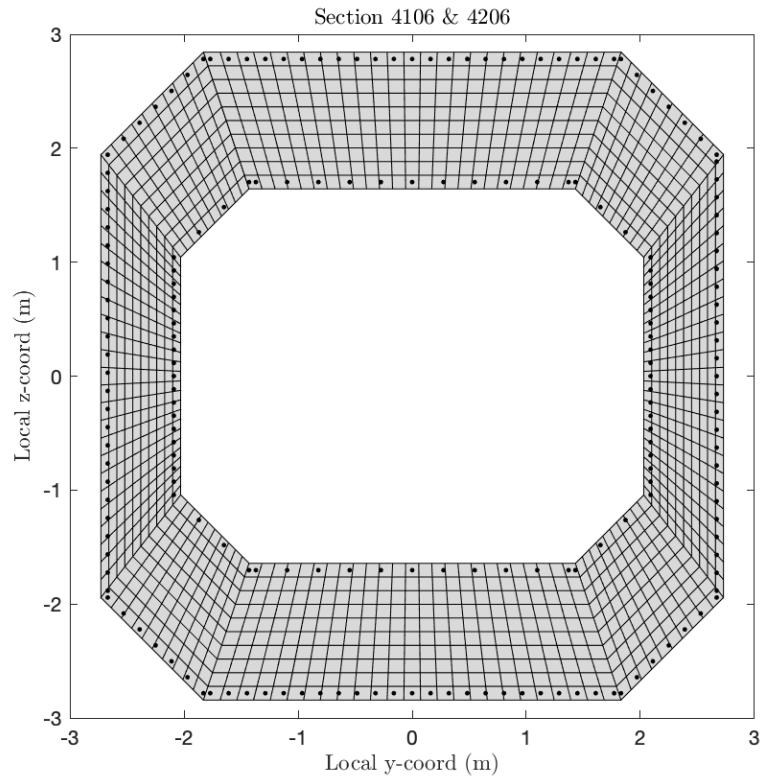


Figure C.6: Section 4106 and 4206

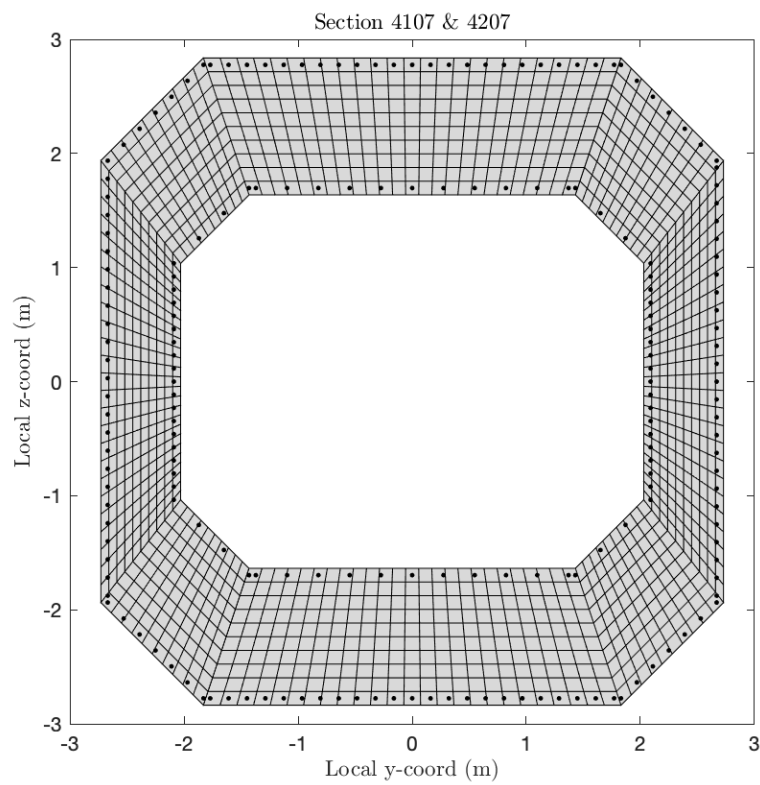


Figure C.7: Section 4107 and 4207

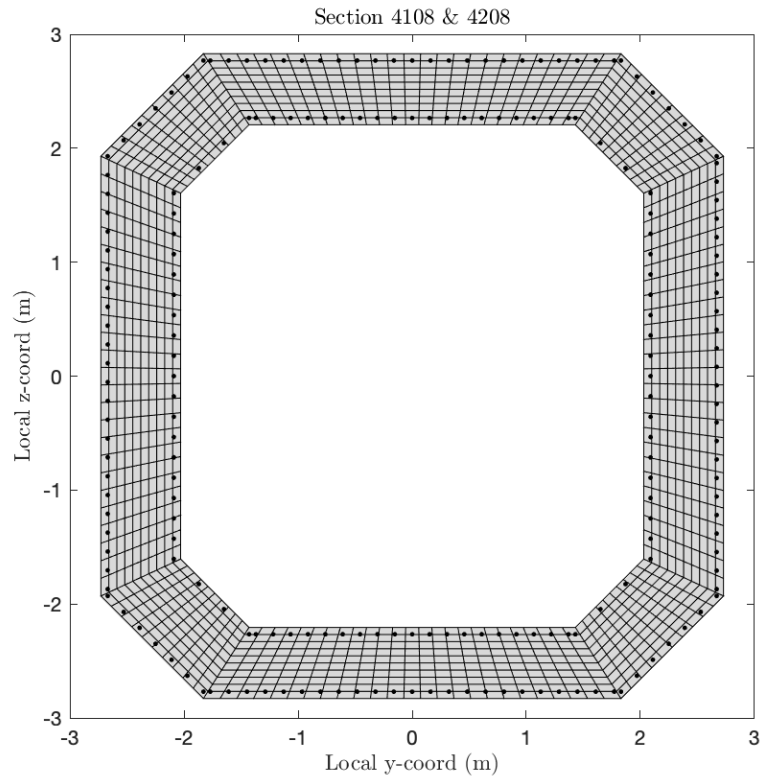


Figure C.8: Section 4108 and 4208

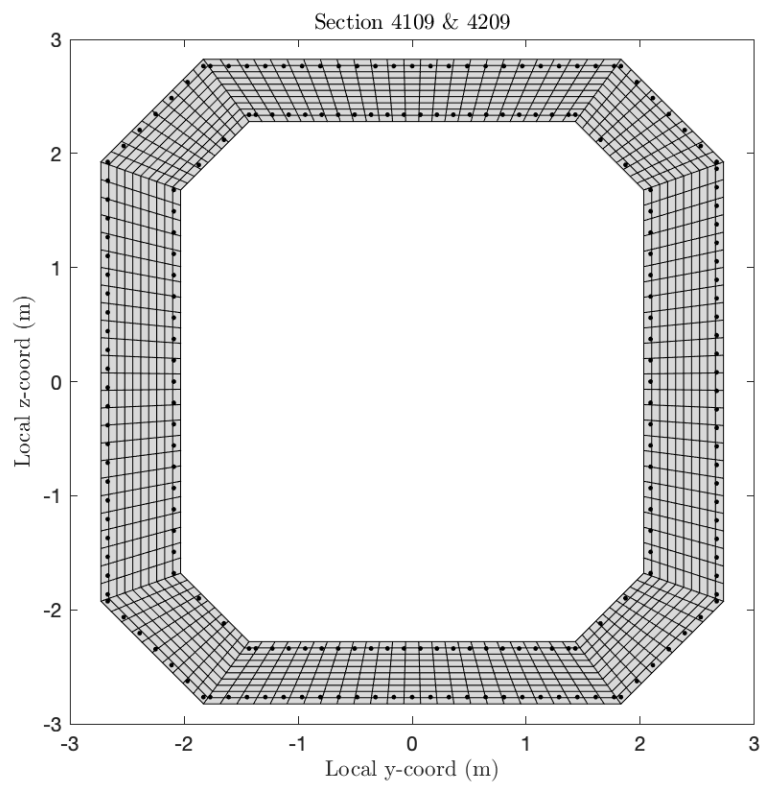


Figure C.9: Section 4109 and 4209

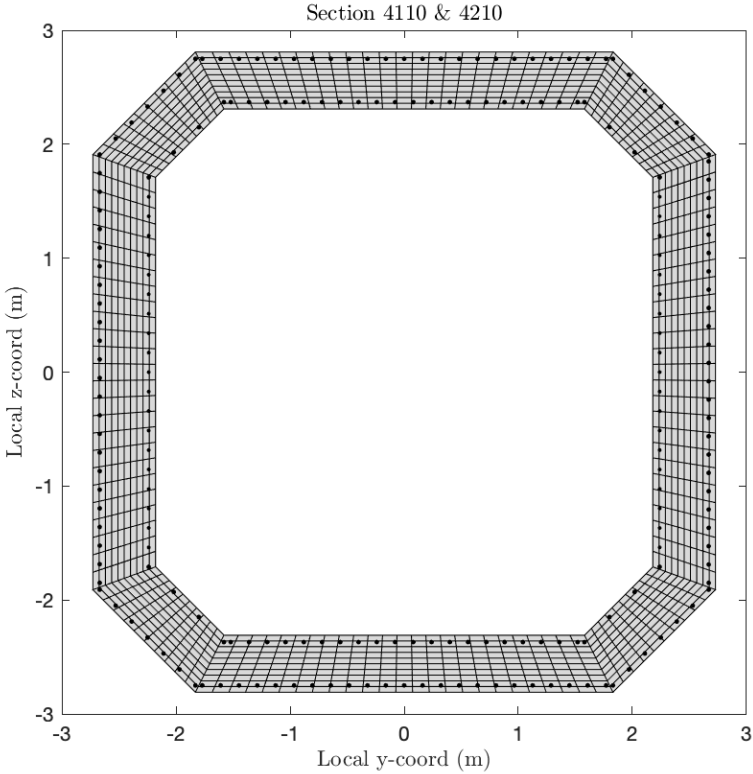


Figure C.10: Section 4110 and 4210

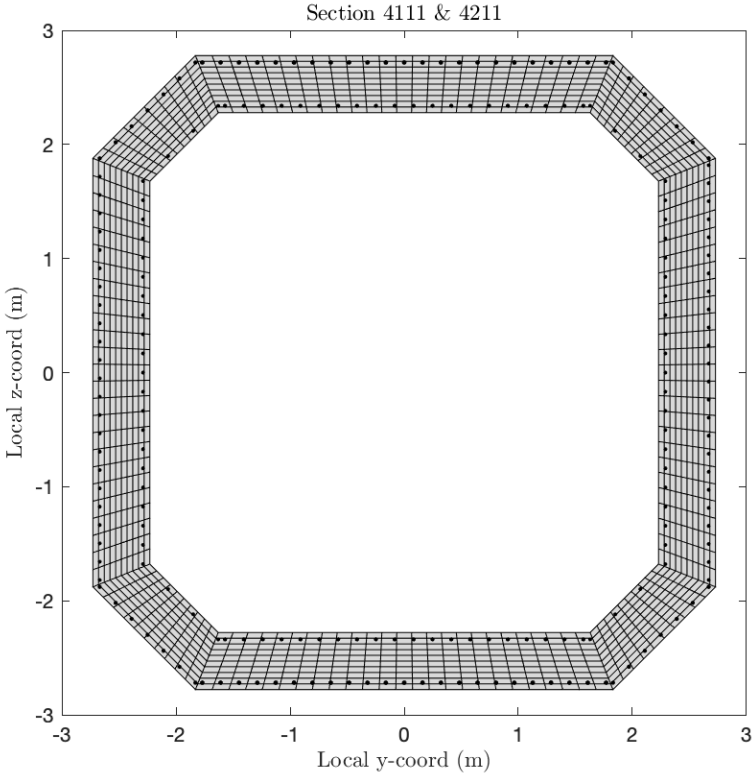


Figure C.11: Section 4111 and 4211

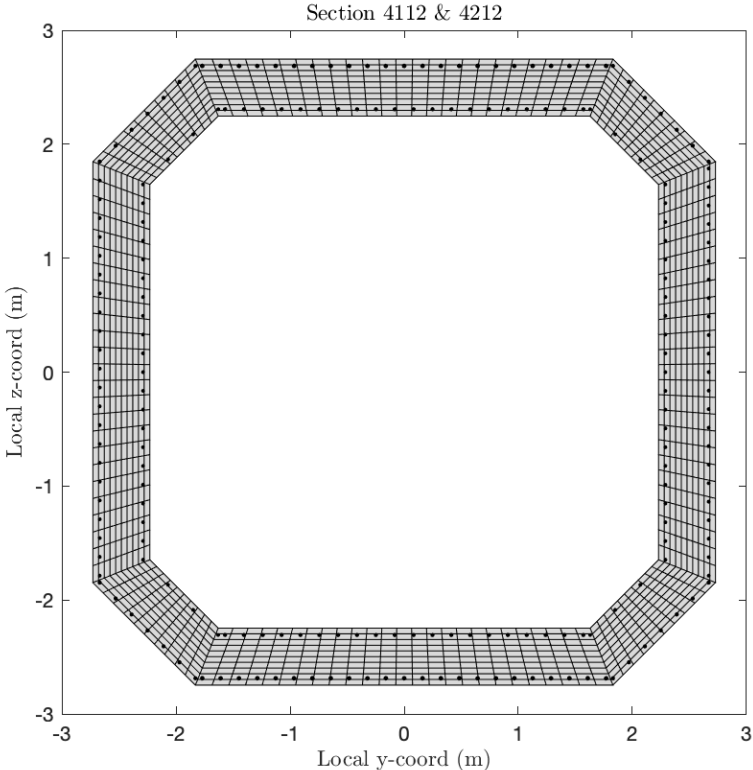


Figure C.12: Section 4112 and 4212

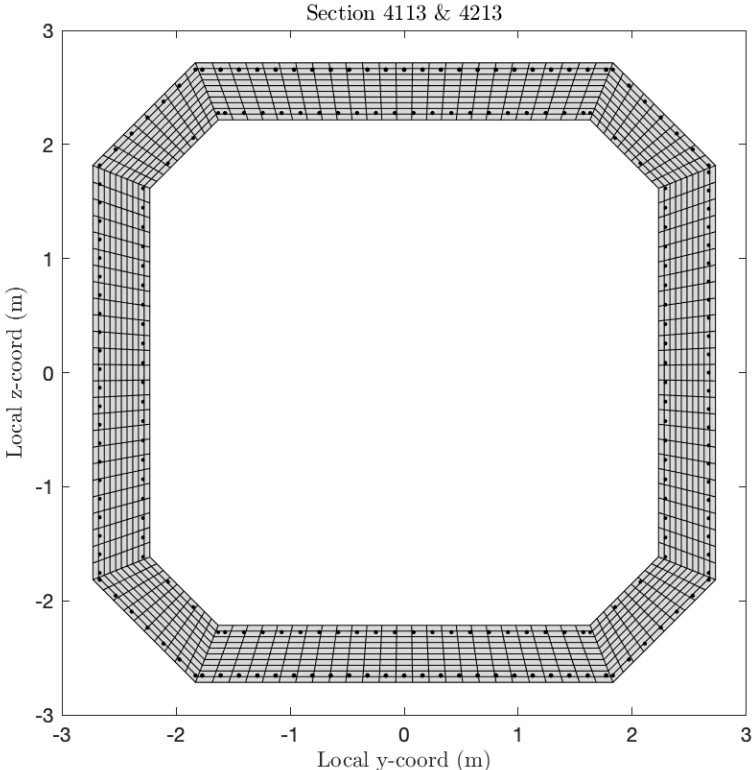


Figure C.13: Section 4113 and 4213

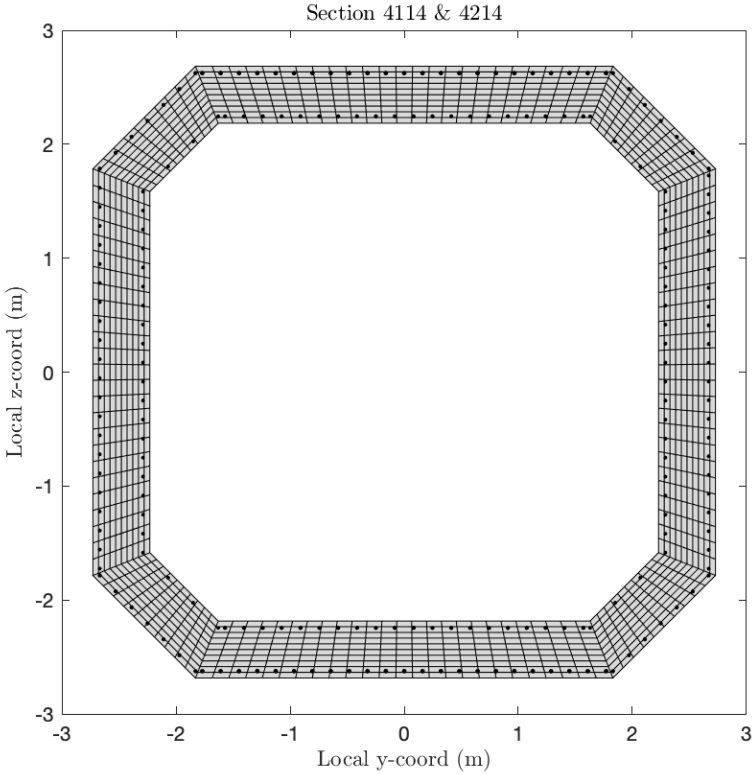


Figure C.14: Section 4114 and 4214

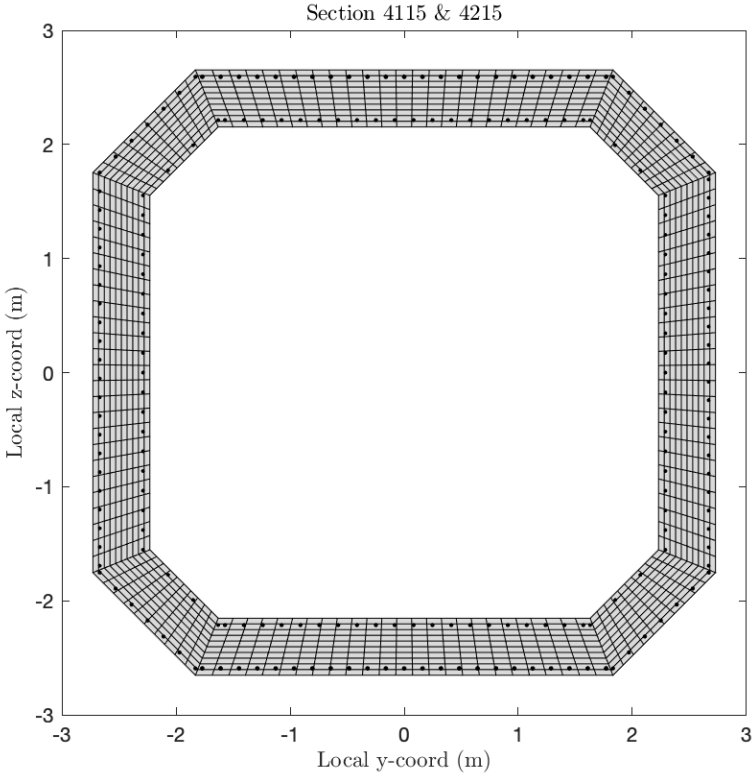


Figure C.15: Section 4115 and 4215

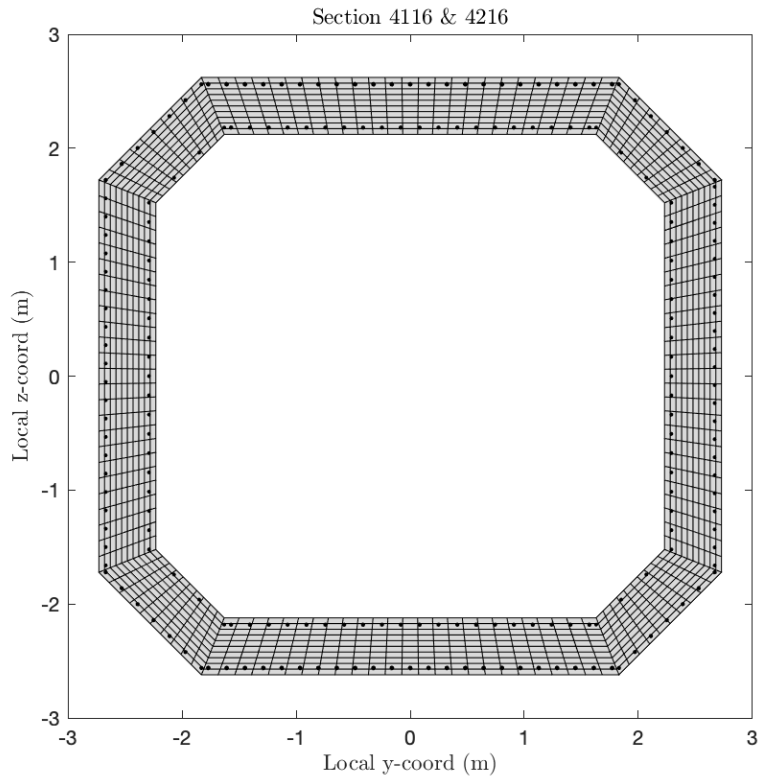


Figure C.16: Section 4116 and 4216

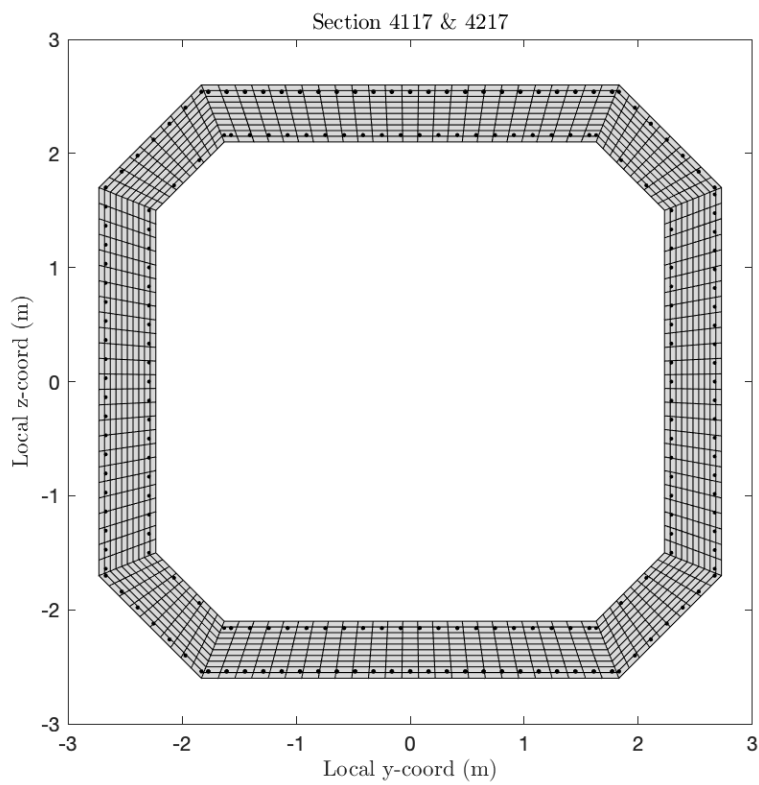


Figure C.17: Section 4117 and 4217

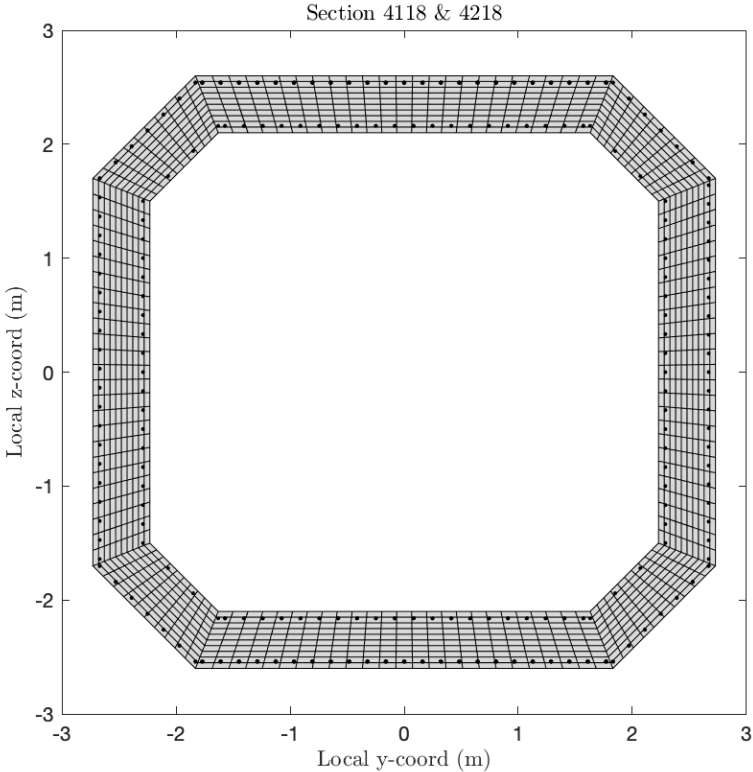


Figure C.18: Section 4118 and 4218

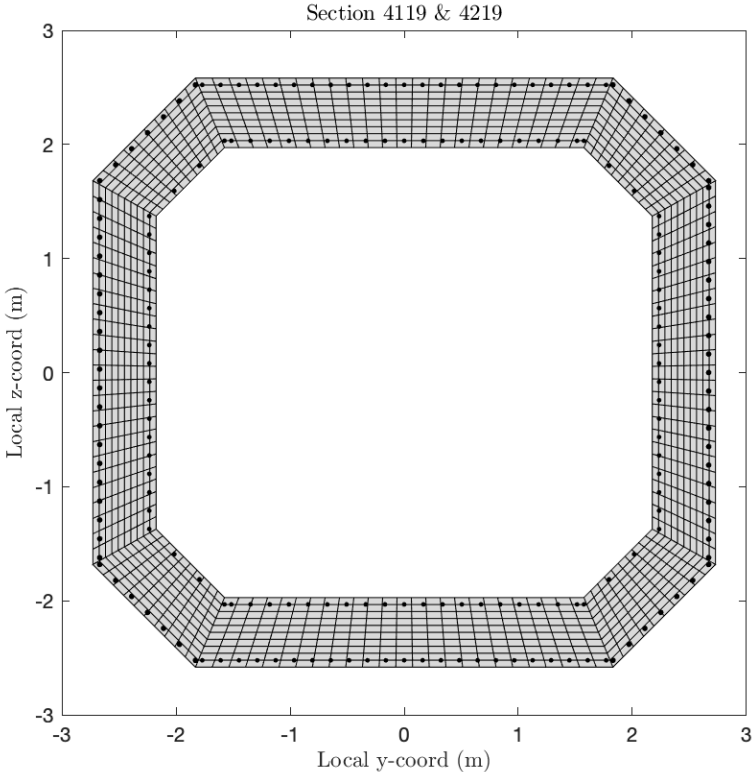


Figure C.19: Section 4119 and 4219

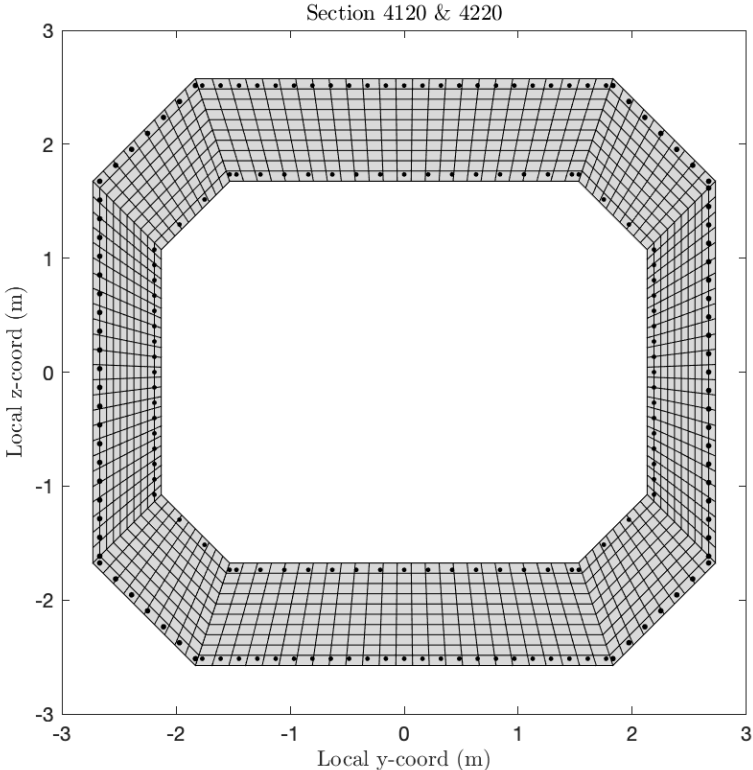


Figure C.20: Section 4120 and 4220

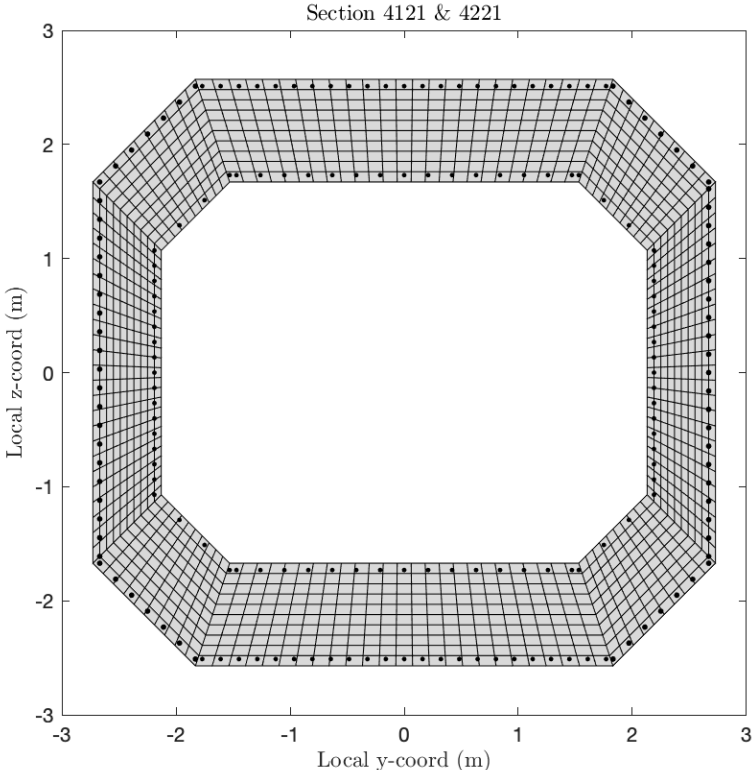


Figure C.21: Section 4121 and 4221

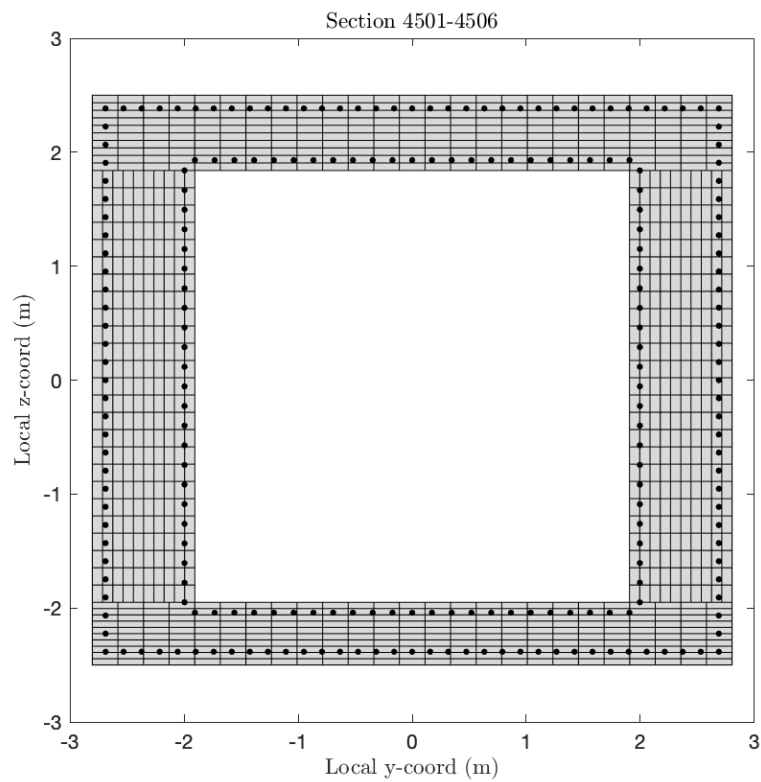


Figure C.22: Section 4501-4506

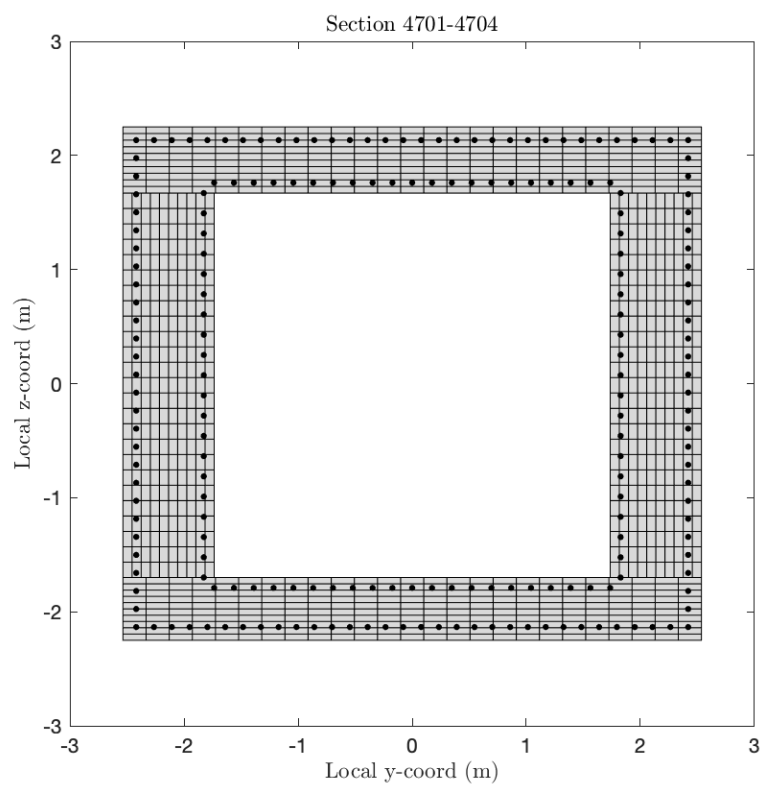


Figure C.23: Section 4701-4704

Appendix D

Moment-Curvature Diagrams

The following appendix lists the moment-curvature diagrams with varying axial loads for interpolation of reduced stiffness in the Secant Method. The diagrams for the cross-beams are only included for illustrative purposes, as they are computed for each iteration with exact axial load due to large variations in axial force levels.

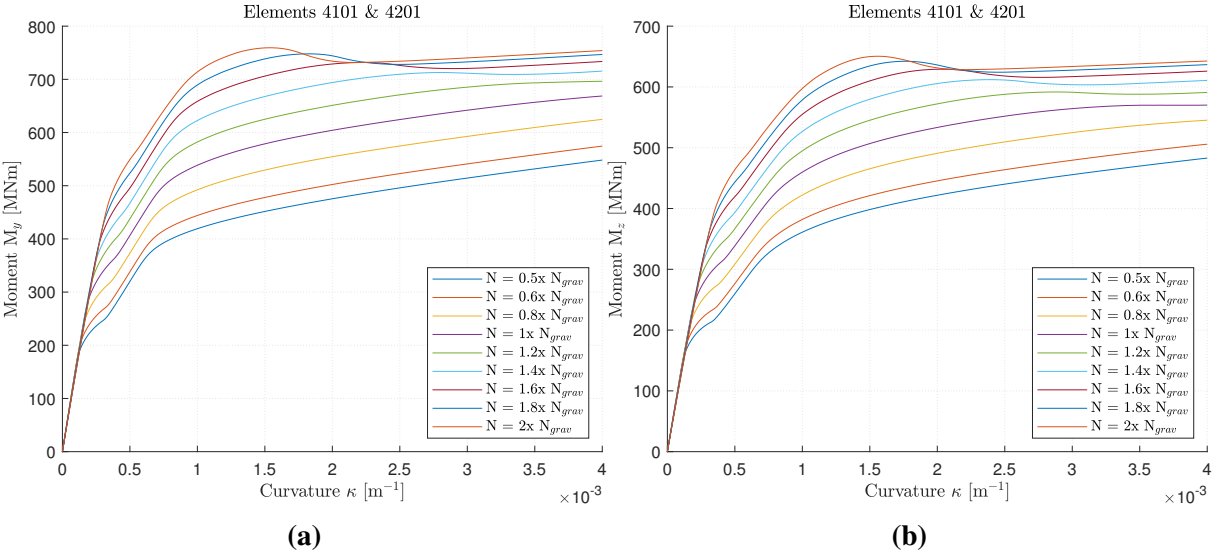


Figure D.1: Moment-curvature relation for element 4101 and 4201 about both local axes

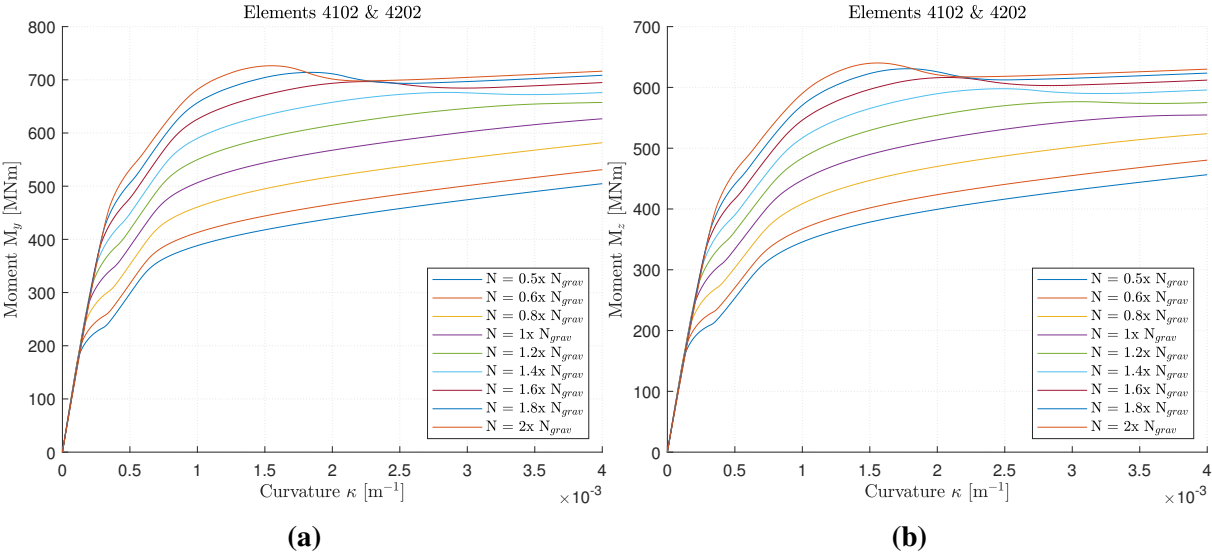


Figure D.2: Moment-curvature relation for element 4102 and 4202 about both local axes

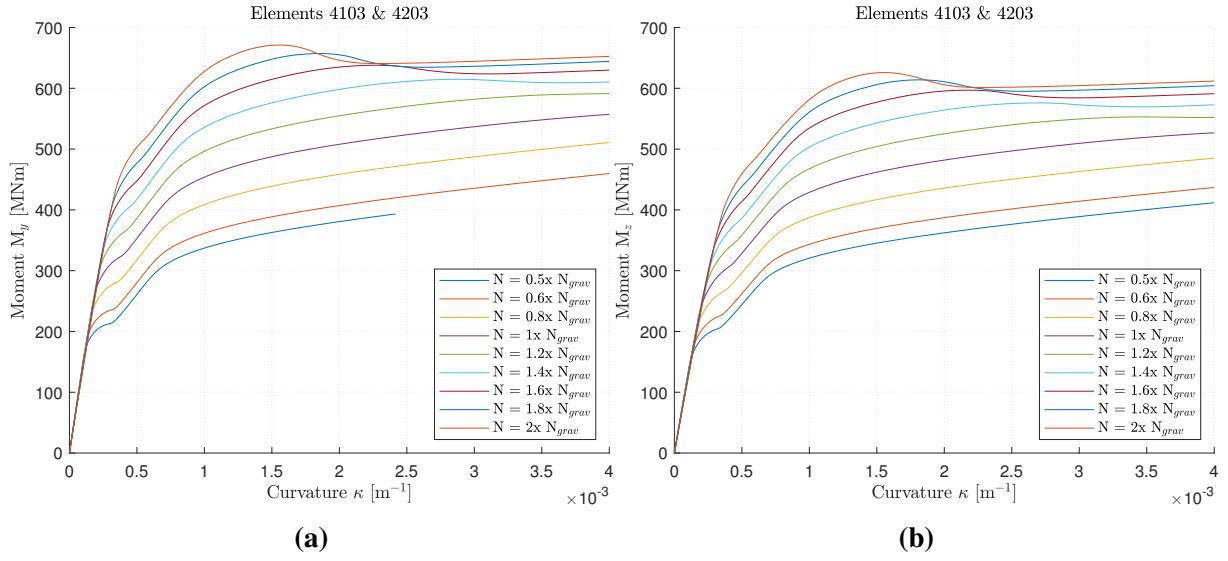


Figure D.3: Moment-curvature relation for element 4103and 4203about both local axes

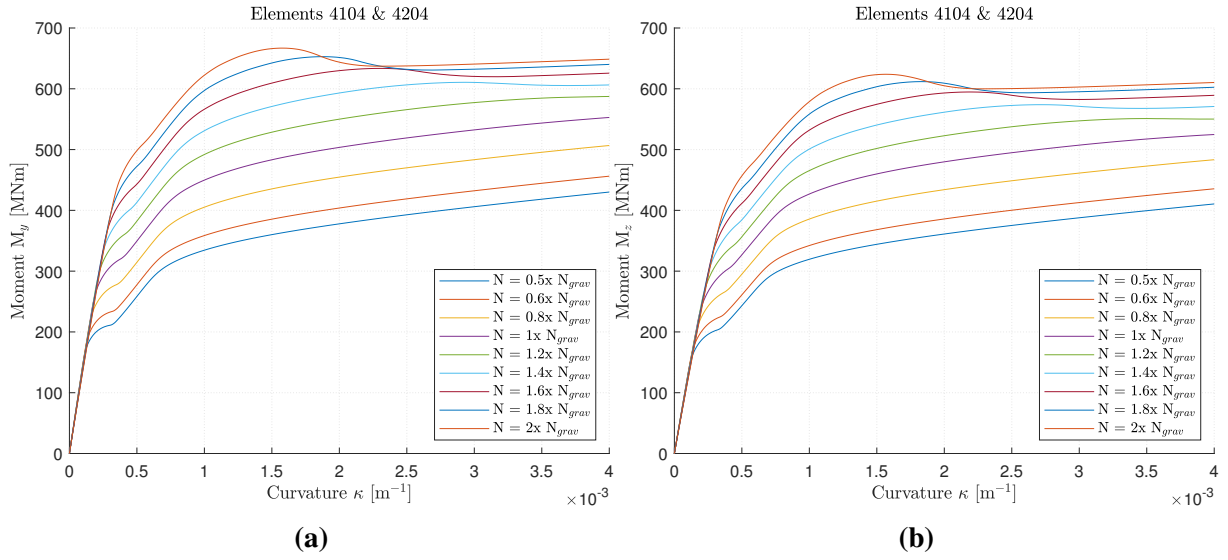


Figure D.4: Moment-curvature relation for element 4104and 4204about both local axes

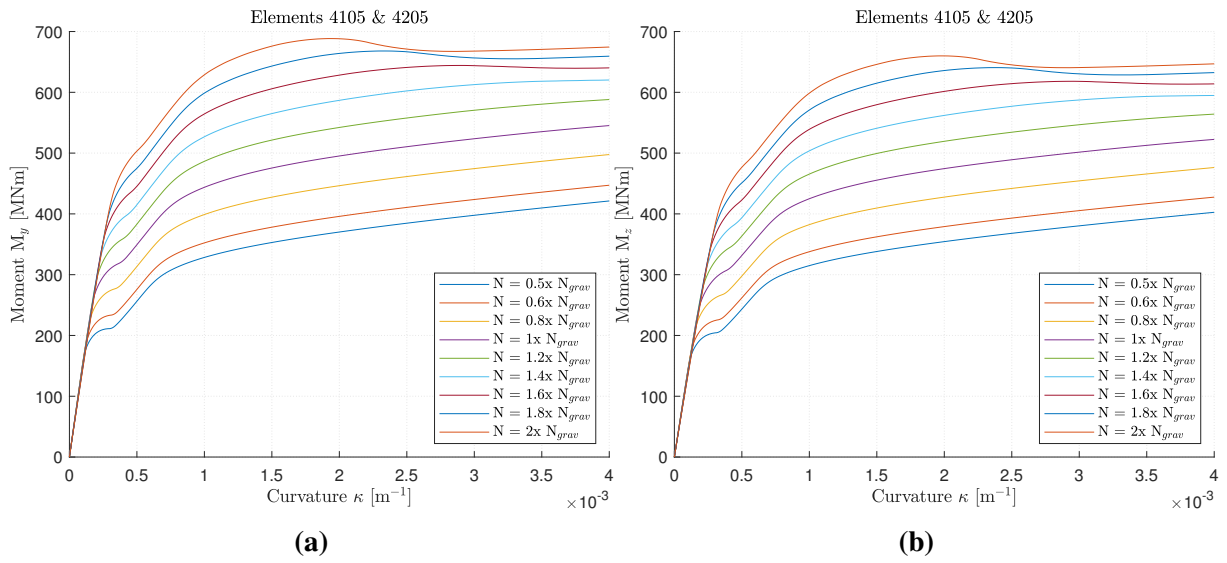


Figure D.5: Moment-curvature relation for element 4105 and 4205 about both local axes

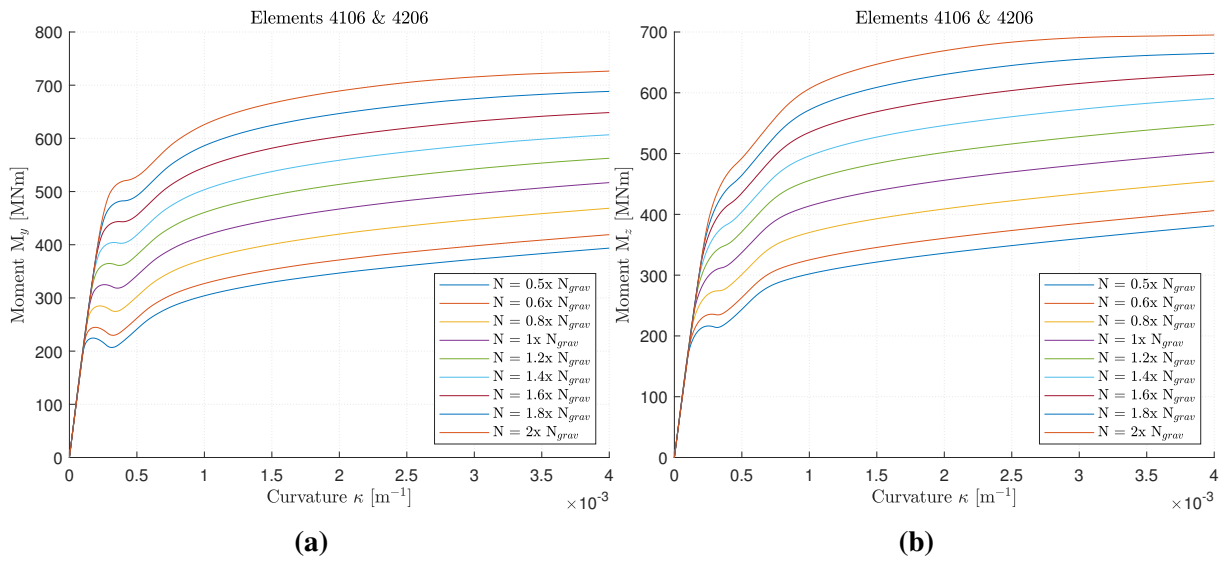


Figure D.6: Moment-curvature relation for element 4106 and 4206 about both local axes

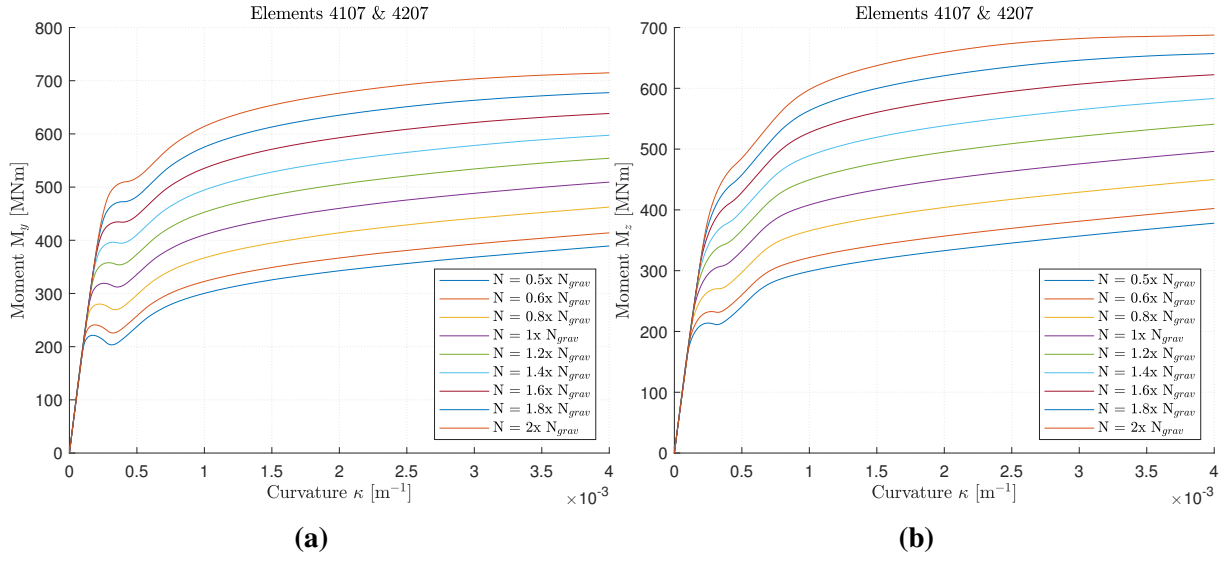


Figure D.7: Moment-curvature relation for element 4107and 4207about both local axes

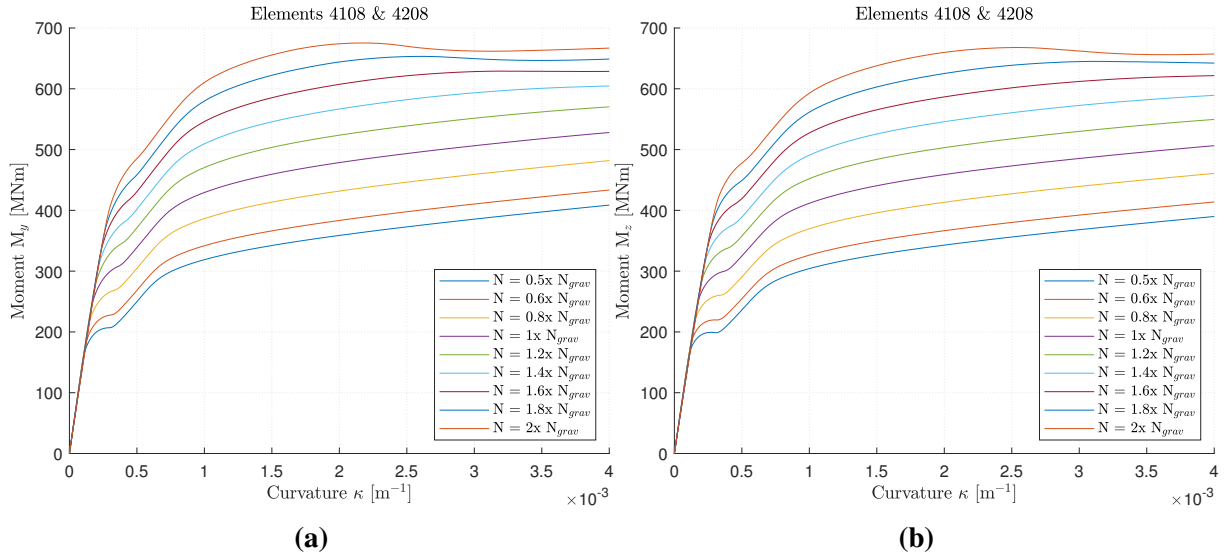


Figure D.8: Moment-curvature relation for element 4108and 4208about both local axes

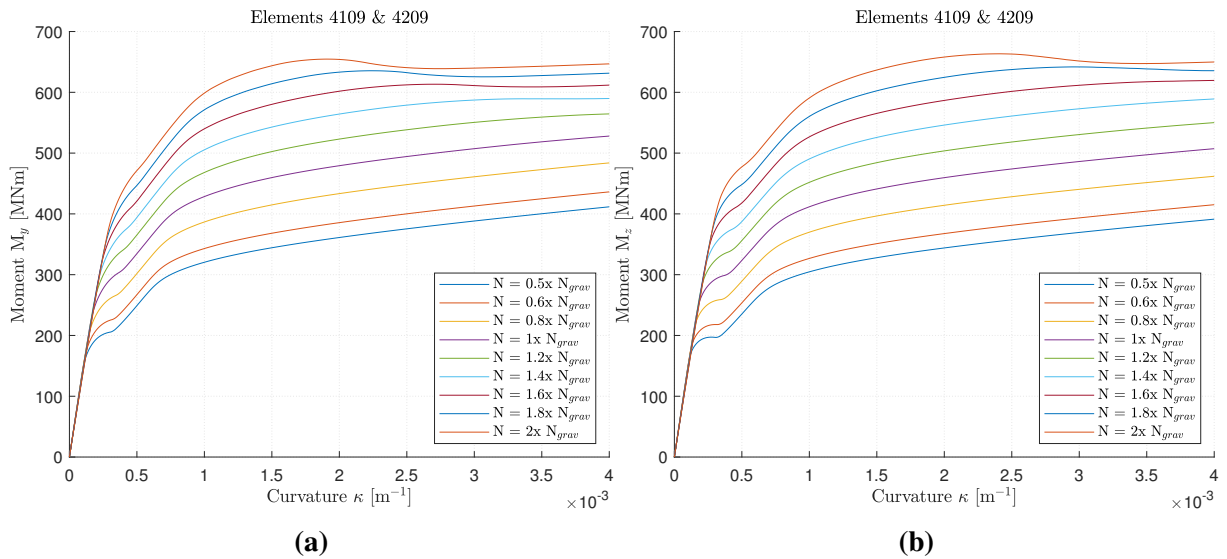


Figure D.9: Moment-curvature relation for element 4109 and 4209 about both local axes

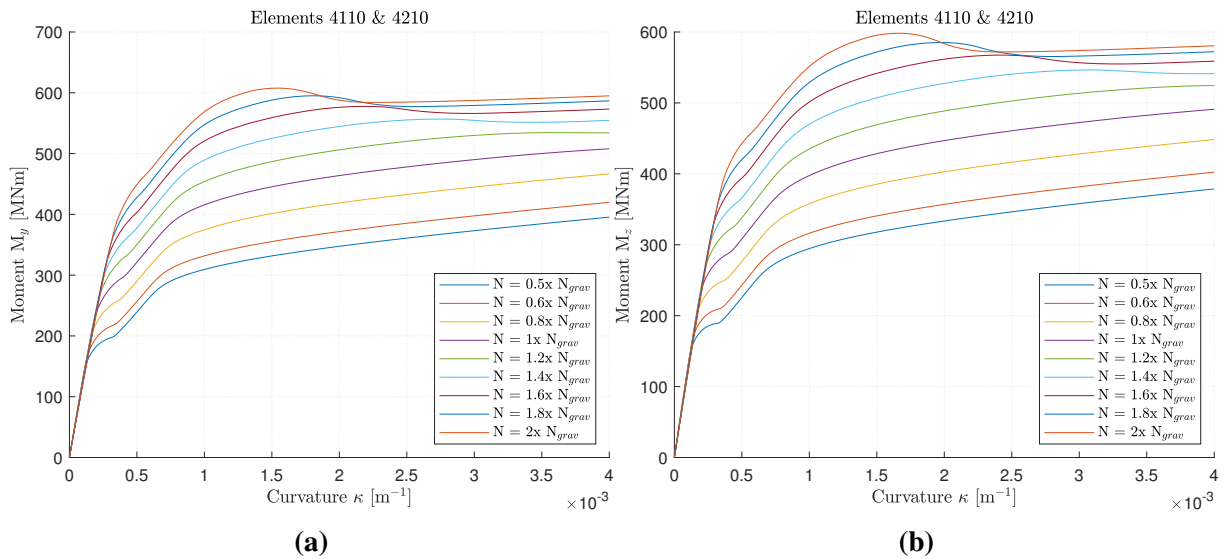


Figure D.10: Moment-curvature relation for element 4110 and 4210 about both local axes

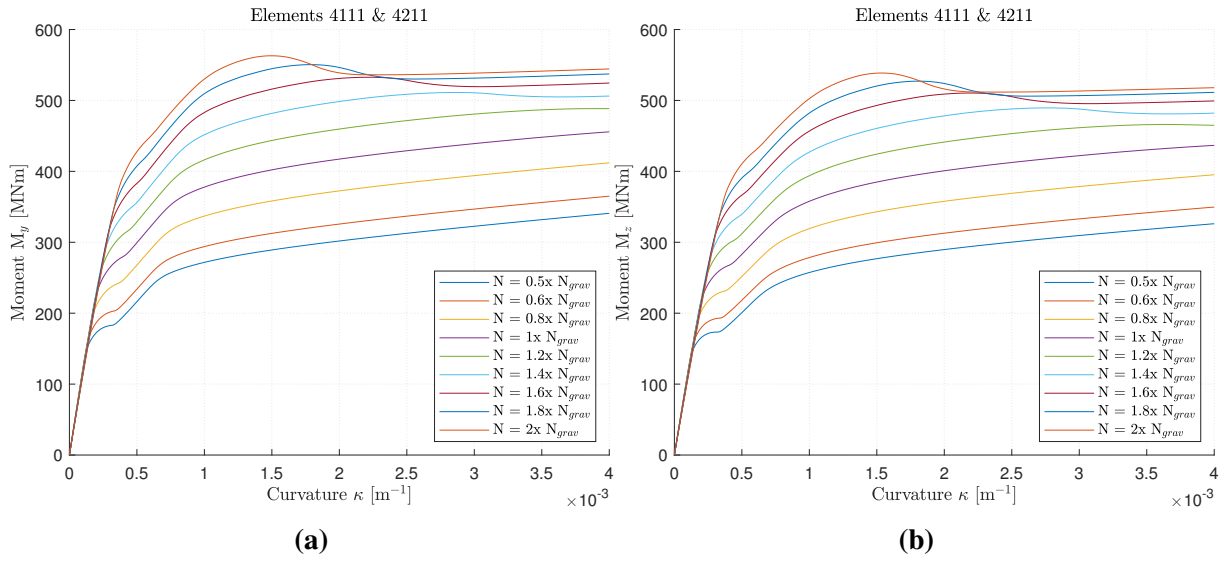


Figure D.11: Moment-curvature relation for element 4111 and 4211 about both local axes

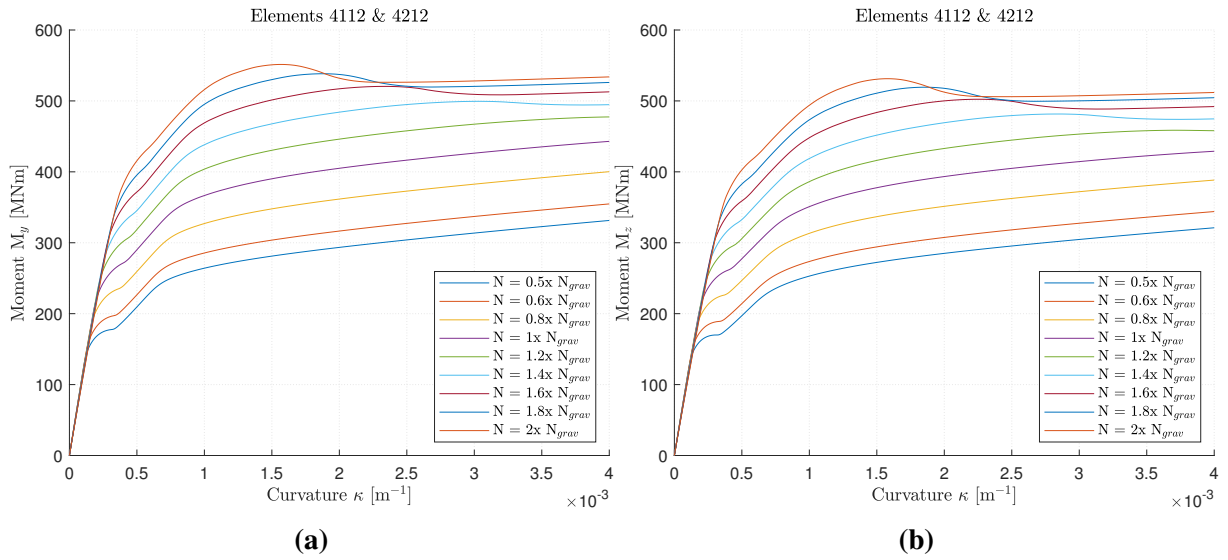


Figure D.12: Moment-curvature relation for element 4112 and 4212 about both local axes

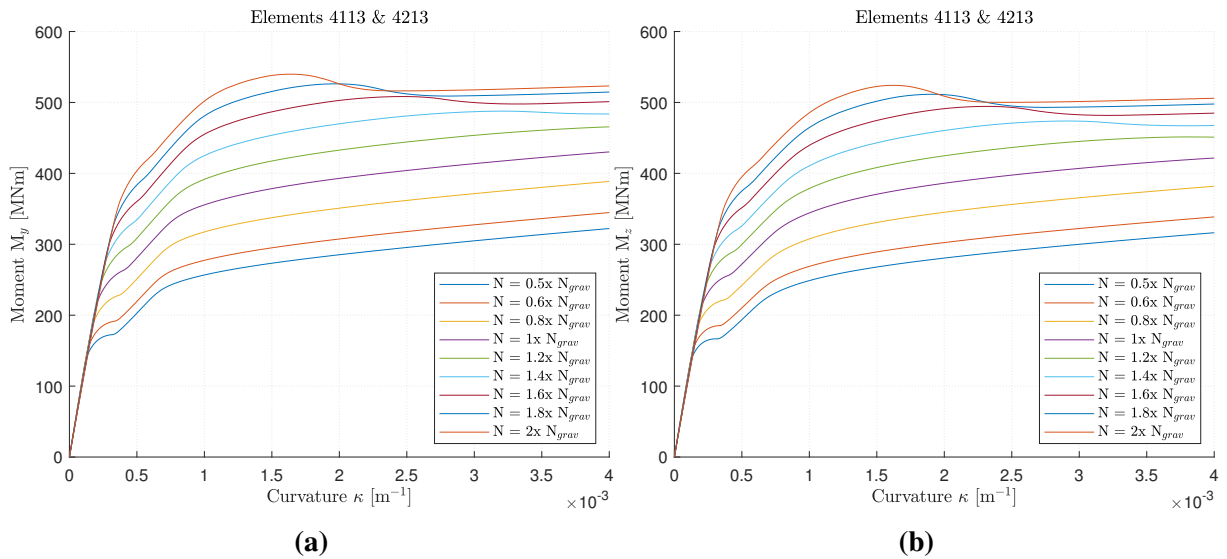


Figure D.13: Moment-curvature relation for element 4113 and 4213 about both local axes

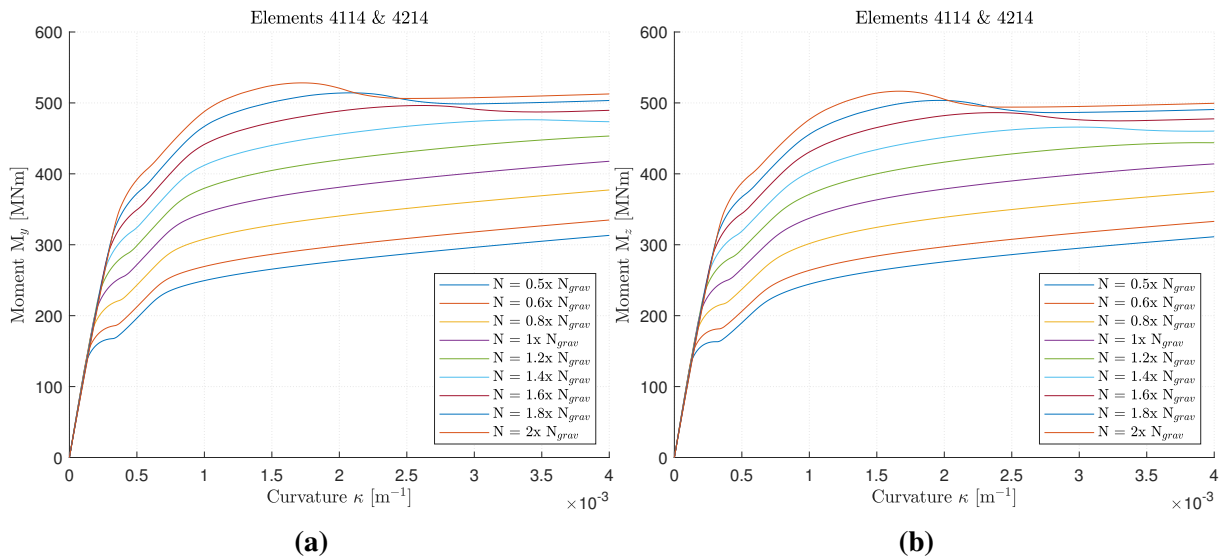


Figure D.14: Moment-curvature relation for element 4114 and 4214 about both local axes

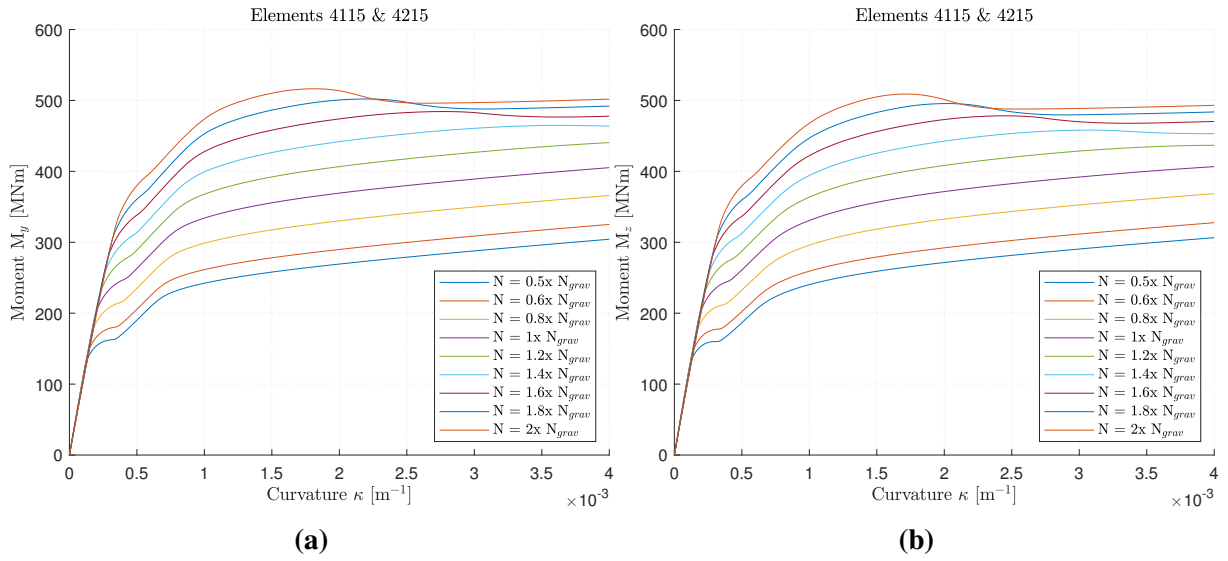


Figure D.15: Moment-curvature relation for element 4115 and 4215 about both local axes

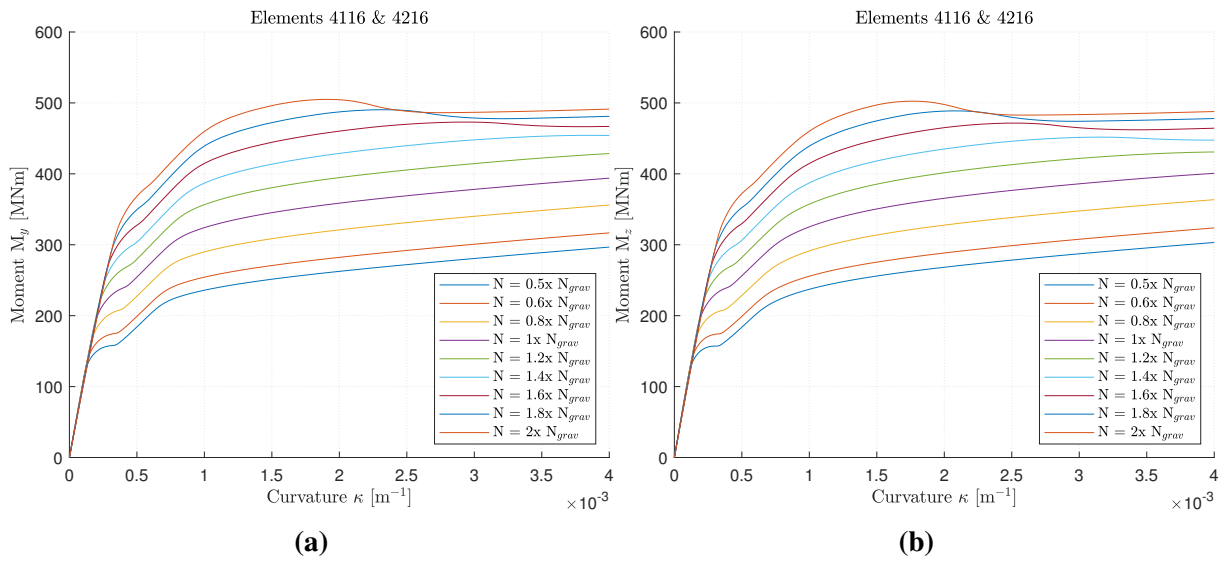


Figure D.16: Moment-curvature relation for element 4116 and 4216 about both local axes

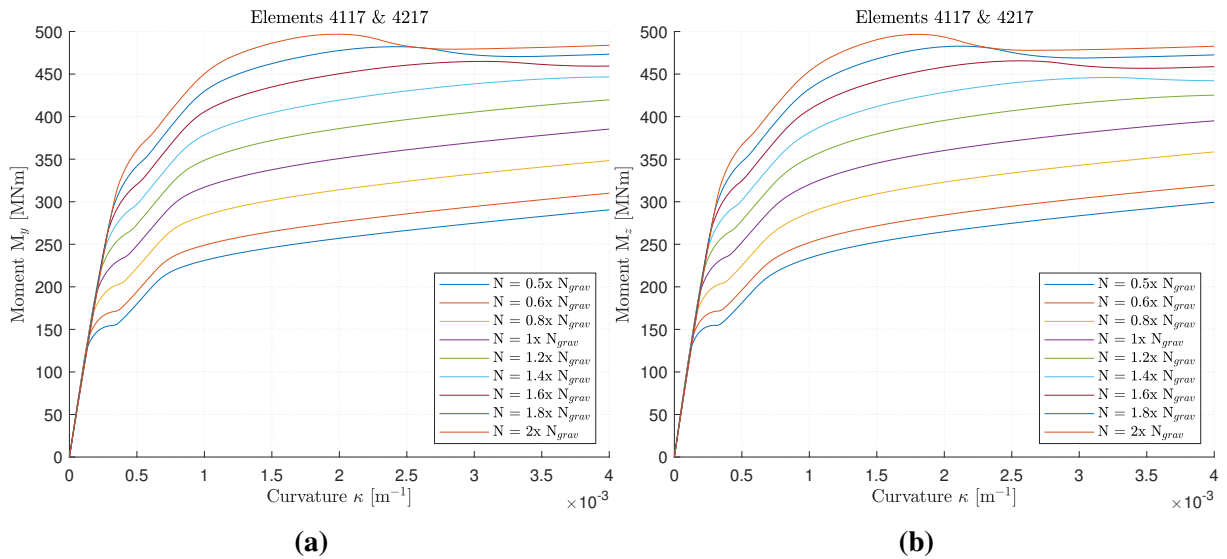


Figure D.17: Moment-curvature relation for element 4117 and 4217 about both local axes

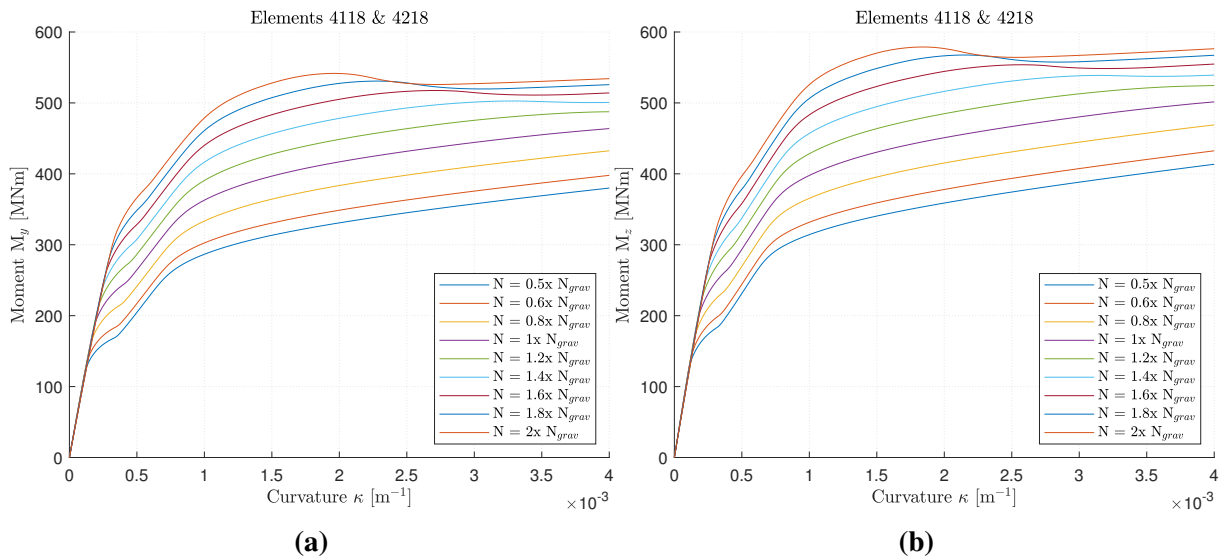


Figure D.18: Moment-curvature relation for element 4118 and 4218 about both local axes

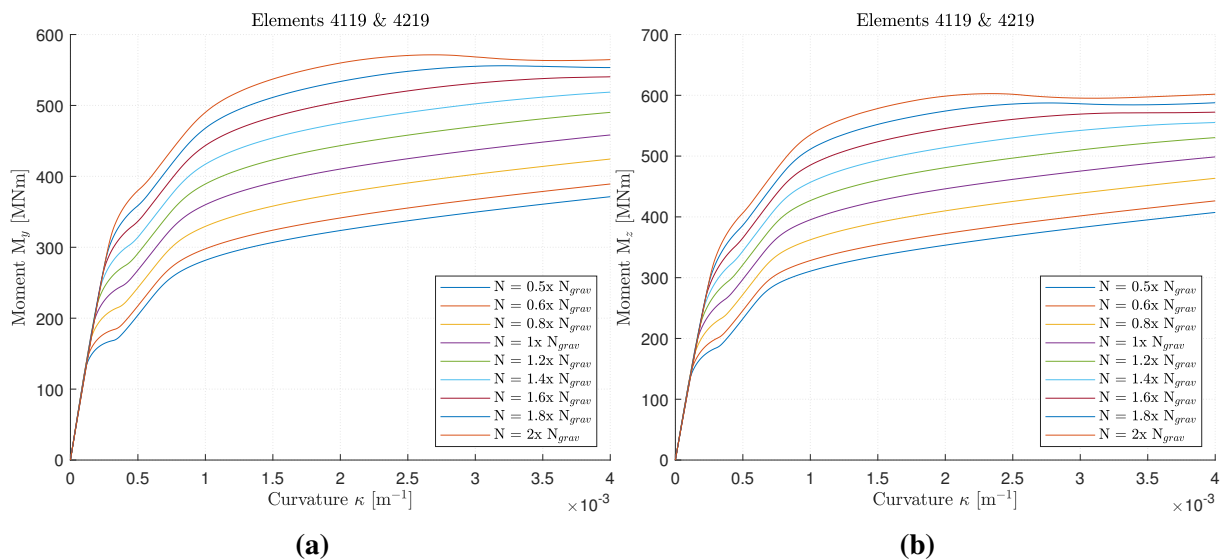


Figure D.19: Moment-curvature relation for element 4119 and 4219 about both local axes

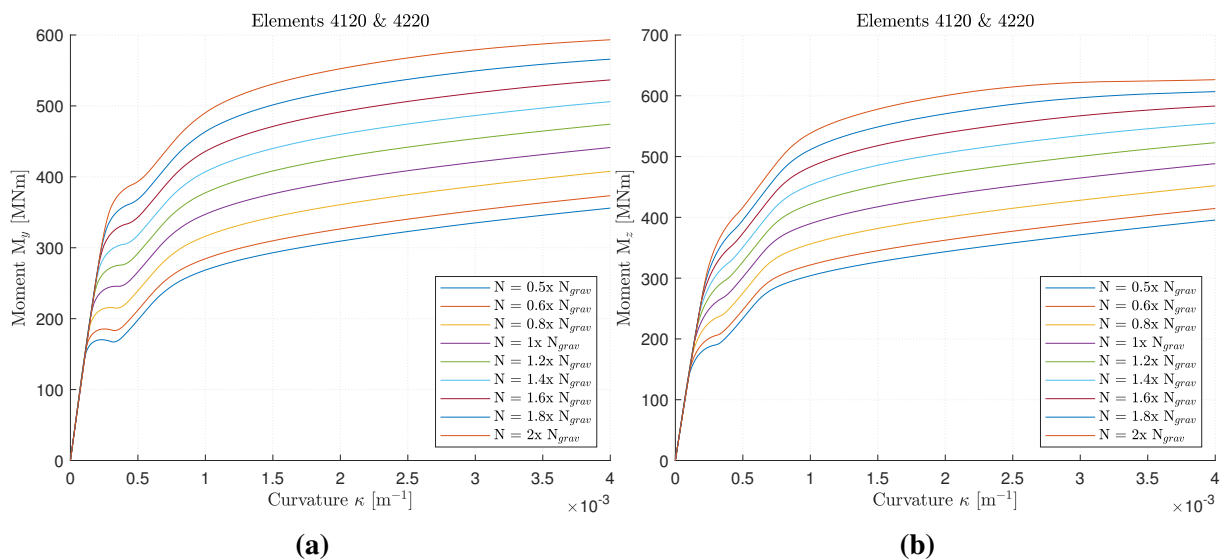


Figure D.20: Moment-curvature relation for element 4120 and 4220 about both local axes

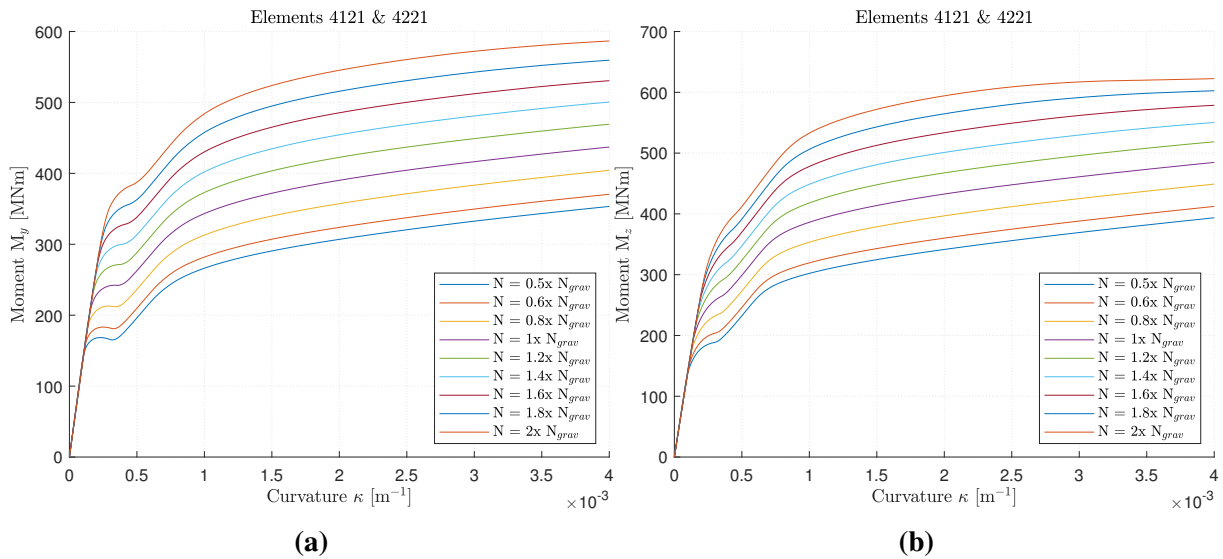


Figure D.21: Moment-curvature relation for element 4121 and 4221 about both local axes

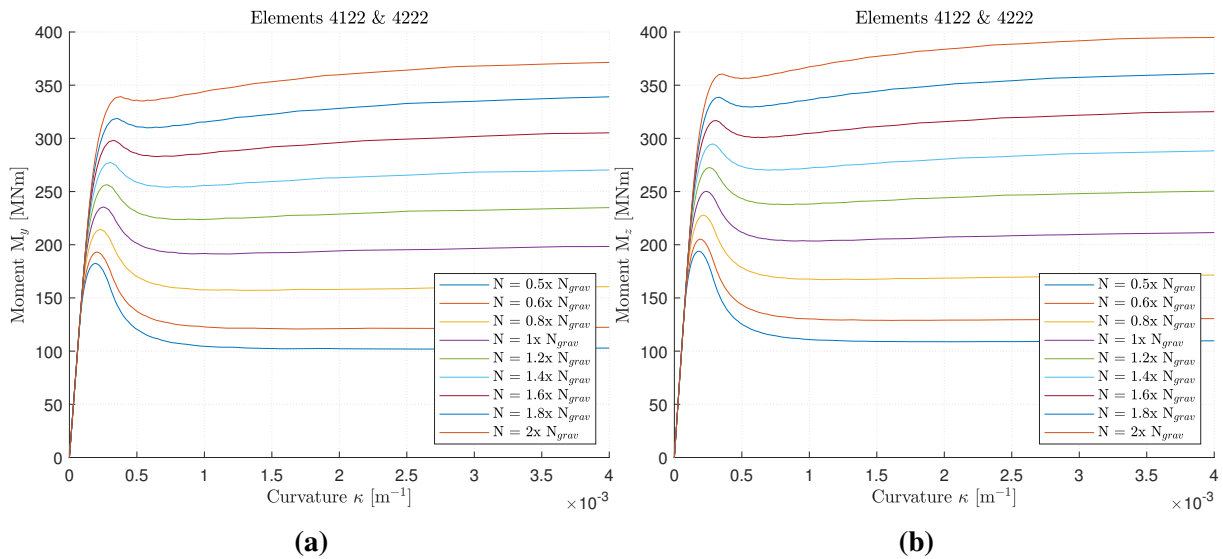


Figure D.22: Moment-curvature relation for element 4122 and 4222 about both local axes

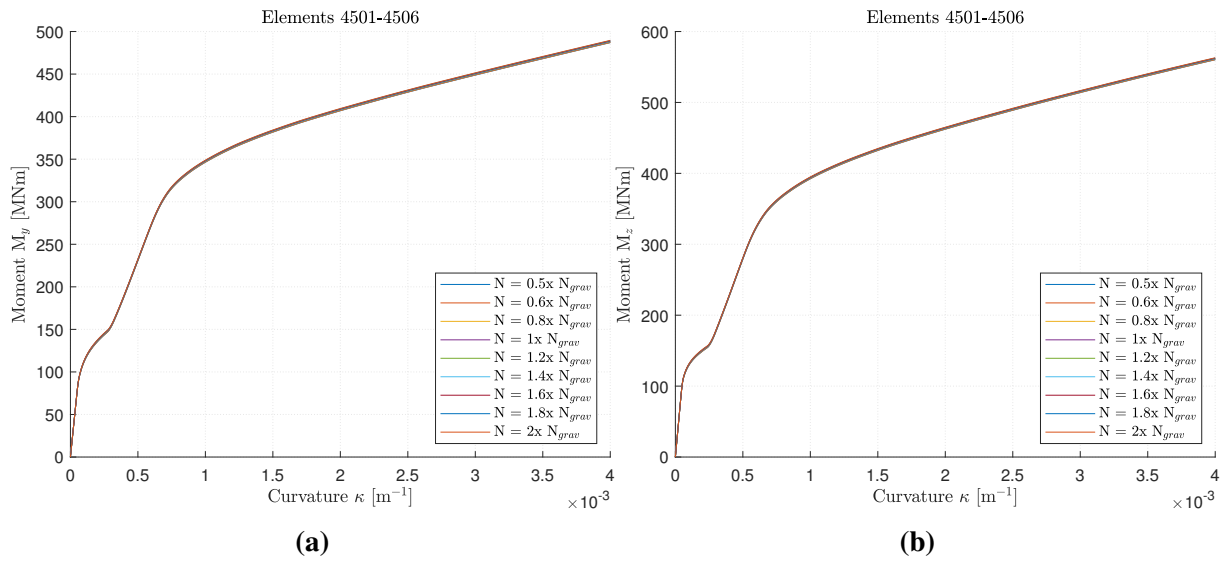


Figure D.23: Moment-curvature relation for element 4501-4506 about both local axes

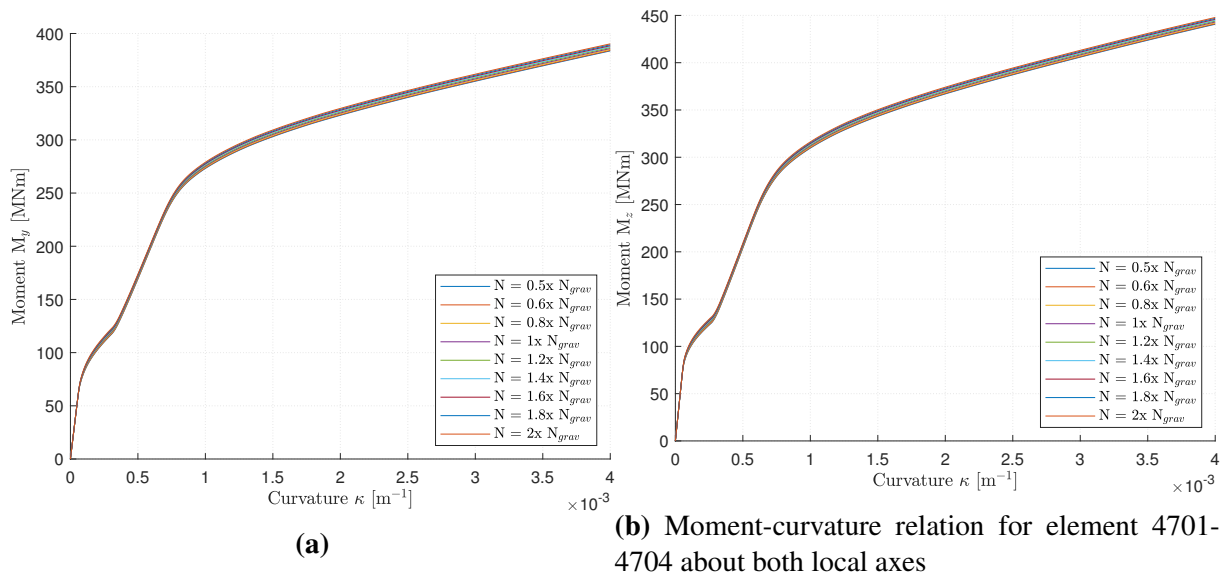


Figure D.24

Appendix E

OpenSees Script

The following script written in the Tcl programming language performed the iterative Secant Method in OpenSees.

```

1  set Resultat_itr {};
2  for {set EQ 1} {$EQ <= 7} {incr EQ 1} {
3      wipe;
4      set record "SP$EQ"
5      set StiffFact_X {}; #Initial Stiffness factors
6      set StiffFact_Y {};
7
8      file delete -force "Results_elastic/Section_$EQ/Ratio"
9      file delete -force "Results_elastic/Section_$EQ/MomentCurvature"
10
11     file mkdir "Results_elastic/Section_$EQ/Ratio"
12     file mkdir "Results_elastic/Section_$EQ/MomentCurvature"
13
14     for {set i 1} {$i<=54} {incr i 1} {
15         lappend StiffFact_X 1
16         lappend StiffFact_Y 1
17     }
18
19     source Units_Riss.tcl
20     puts "" ;
21     puts "BASIC UNITS - $LunitTXT, $FunitTXT, $TunitTXT"
22     set itr 15
23     set fact 0.5
24
25     for {set iter 1} {$iter <= $itr} {incr iter 1} {
26         file delete -force "Results_elastic/Section_$EQ/Ratio/signal.txt"
27         file delete -force "Results_elastic/Section_$EQ/Ratio/signalAxial.txt"
28
29         wipe ;
30
31         puts ":::::::::::::::::::::::::::: Run itr. $iter ::::::::::::::::::::::"
32
33         set Cables "On"; # On for Cables, off to run analysis without suspension cable
34
35         set Results "Results_elastic"
36         file mkdir $Results
37
38         set AnalysisDyn "$Results/DynamicAnalysis_$EQ"
39         file mkdir $AnalysisDyn
40
41         file mkdir "$Results/Section_$EQ"
42
43         # #####
44
45         source Nodes_and_BC_Riss.tcl
46         source Material_Properties_Riss.tcl
47
48         puts "$StiffFact_X"
49         puts "-----"
50
51         puts "$StiffFact_Y"
52         puts "-----"
53
54         source Element_Riss_ini02.tcl
55         source Gravity_Loads_Riss.tcl
56         set modes 30
57         source Modal_analysis_Riss.tcl
58         source TimeHistory_Riss.tcl
59
60         remove recorders;
61
62
63         # Moment curvature analysis with current axial forces
64         set StiffFactDir "$Results/Section_$EQ/Ratio"
65         file mkdir $StiffFactDir
66         # Matlab script obtaining max abs. moment and corresponding axial forces
67
68         if {[catch {exec matlab -nosplash -nodesktop -r
69             "getAxialForces($EQ);quit"}]} {
70             puts "Ignore this $msg"
71         }
72         while {[file exists "$StiffFactDir/signalaxial.txt"] != 1} {

```

```
73     }
74     puts "Axial forces computed!"
75
76     source GetMphi.tcl; # Moment curvature, cross-beams only
77     puts "Moment-curvature for crossbeams computed!"
78
79     # Matlab script calculating secant stiffnesses
80     if {[catch {exec matlab -nosplash -nodesktop -r
81         "GetStiffness_elast_interpol($fact,$iter,$EQ);quit"}]} {
82         puts "Ignore this $msg"
83     }
84
85
86     while {[file exists "$StiffFactDir/signal.txt"] != 1} {
87     }
88     puts "New stiffness computed!"
89
90     set cv [open "$StiffFactDir/conv.txt" r];
91     set conv_data [read $cv];
92     set conv [lindex $conv_data 0]
93     if {$conv > 0} {
94         puts "Conv = $conv, stop after itr=$iter"
95         close $cv
96         lappend Resultat_itr "\n $record converged after $iter itr."
97
98         break
99     }
100    close $cv
101    set StiffFactFileX "ratiosX_$iter.txt"
102    set StiffFactFileY "ratiosY_$iter.txt"
103
104    set fpX [open "$StiffFactDir/$StiffFactFileX" r]; # Update stiffnesses
105    set fpY [open "$StiffFactDir/$StiffFactFileY" r];
106
107    set StiffFact_X [read $fpX]
108    set StiffFact_Y [read $fpY]
109    close $fpX
110    close $fpY
111    if {$iter==$itr} {
112        lappend Resultat_itr "\n $record did not converge, max itr.=$itr"
113    }
114
115    wipe;
116    puts "iter=$iter done!"
117 }
118
119 puts "Analysis complete for record $record"
120 }
121 puts "Analysis complete for all records";
122 puts "$Resultat_itr";
```


Appendix F

MATLAB code

The following script written in MATLAB was invoked once during each iteration of the Secant Method and calculates the updated stiffness ratio using the maximum absolute moment and section response at each element.

```
1
2 function GetStiffness_elast_interpol(fact,itr,Eq)
3
4 Eq_str=num2str(Eq);
5 signal=1;
6 %elemen-tvektor
7 FibElem=[4101 4102 4103 4104 4105 4106 4107 4108 4109 4110 4111 4112 4113 4114 4115
8 4116 4117 4118 4119 4120 4121 4122 4201 4202 4203 4204 4205 4206 4207 4208 4209 4210
9 4211 4212 4213 4214 4215 4216 4217 4218 4219 4220 4221 4222 4501 4502 4503 4504 4505
10 4506 4701 4702 4703 4704];
11 e=length(FibElem);
12
13 Node=[4101 4102 4103 4104 4105 4106 4107 4108 4109 4110 4111 4112 4113 4114 4115
14 4116 4117 4118 4119 4120 4121 4122 4123 4201 4202 4203 4204 4205 4206 4207 4208 4209
15 4210 4211 4212 4213 4214 4215 4216 4217 4218 4219 4220 4221 4222 4223 4502 4503 4504
16 4505 4506 4702 4703 4704];
17 n=length(Node);
18 %Input, henter Mphi, tidshistorie
19 FolderGravity = ['C:\Users\Tarjei\Documents\Gogldr\Masteroppgave,
20 Dynamikk_OpenSees\Scripts\Riss\Results_elastic\Gravity'];
21 FolderMomentCurv = ['C:\Users\Tarjei\Documents\Gogldr\Masteroppgave,
22 Dynamikk_OpenSees\Scripts\Riss\Results_elastic\Section_',Eq_str,'\MomentCurvature'];
23
24 FolderMomentTime = ['C:\Users\Tarjei\Documents\Gogldr\Masteroppgave,
25 Dynamikk_OpenSees\Scripts\Riss\Results_elastic\DynamicAnalysis_',Eq_str,'\Moment'];
26 FolderDynResultsTime = ['C:\Users\Tarjei\Documents\Gogldr\Masteroppgave,
27 Dynamikk_OpenSees\Scripts\Riss\Results_elastic\DynamicAnalysis_',Eq_str];
28
29 %Output, lager tre nye filer
30 nameX= strcat('C:\Users\Tarjei\Documents\Gogldr\Masteroppgave,
31 Dynamikk_OpenSees\Scripts\Riss\Results_elastic\Section_',Eq_str,'\Ratio\ratiosX_',num
32 2str(itr),'.txt');
33 nameDispX= strcat('C:\Users\Tarjei\Documents\Gogldr\Masteroppgave,
34 Dynamikk_OpenSees\Scripts\Riss\Results_elastic\Section_',Eq_str,'\Ratio\dispAccX_',nu
35 m2str(itr),'.txt');
36 name_compX=strcat('C:\Users\Tarjei\Documents\Gogldr\Masteroppgave,
37 Dynamikk_OpenSees\Scripts\Riss\Results_elastic\Section_',Eq_str,'\Ratio\complete_data
38 X_',num2str(itr),'.txt');
39 name_testX=strcat('C:\Users\Tarjei\Documents\Gogldr\Masteroppgave,
40 Dynamikk_OpenSees\Scripts\Riss\Results_elastic\Section_',Eq_str,'\Ratio\test_dataX_',
41 num2str(itr),'.txt');
42
43 fidX=fopen(nameX,'w');
44 fidDispAccX=fopen(nameDispX,'w');
45 fid_compX=fopen(name_compX,'w');
46 fid_testX=fopen(name_testX,'w');
47
48
49 nameY=strcat('C:\Users\Tarjei\Documents\Gogldr\Masteroppgave,
50 Dynamikk_OpenSees\Scripts\Riss\Results_elastic\Section_',Eq_str,'\Ratio\ratiosY_',num
51 2str(itr),'.txt');
52 nameDispY=strcat('C:\Users\Tarjei\Documents\Gogldr\Masteroppgave,
53 Dynamikk_OpenSees\Scripts\Riss\Results_elastic\Section_',Eq_str,'\Ratio\dispAccY_',nu
54 m2str(itr),'.txt');
55 name_compY=strcat('C:\Users\Tarjei\Documents\Gogldr\Masteroppgave,
56 Dynamikk_OpenSees\Scripts\Riss\Results_elastic\Section_',Eq_str,'\Ratio\complete_data
57 Y_',num2str(itr),'.txt');
58 fidY=fopen(nameY,'w');
59 fidDispAccY=fopen(nameDispY,'w');
60 fid_compY=fopen(name_compY,'w');
61
62
63 if itr>=2
64 forrige_ratioX=load(strcat('C:\Users\Tarjei\Documents\Gogldr\Masteroppgave,
65 Dynamikk_OpenSees\Scripts\Riss\Results_elastic\Section_',Eq_str,'\Ratio\ratiosX_',
66 num2str(itr-1),'.txt'));
67 forrige_ratioY=load(strcat('C:\Users\Tarjei\Documents\Gogldr\Masteroppgave,
68 Dynamikk_OpenSees\Scripts\Riss\Results_elastic\Section_',Eq_str,'\Ratio\ratiosY_',
69 num2str(itr-1),'.txt'));
70 elseif itr==1
71 forrige_ratioX=ones(e,1);
72 forrige_ratioY=ones(e,1);
```

```

46 end
47
48
49 for el=1:e
50
51     elem=FibElem(el);
52     str_ele=num2str(elem); %gjør
53     elementnr. til en streng
54
55     MphiX_gravity
56     =load(fullfile(FolderGravity,strcat('MphiX_Gravity_',str_ele,'1.txt')));
57     %henter moment-krumning for element i
58     MphiY_gravity =
59     load(fullfile(FolderGravity,strcat('MphiY_Gravity_',str_ele,'1.txt')));
60     Axial_Gravity_file =load(fullfile(FolderGravity,strcat('N_Ele',str_ele,'.txt')));
61
62     axial_gravity=Axial_Gravity_file(end);
63     Ftime=load(fullfile(FolderMomentTime,strcat('M_Ele',str_ele,'.txt')));
64     %henter Eq-respons for element i
65
66
67
68
69
70
71
72
73
74
75
76
77
78
79
80
81
82
83
84
85
86
87
88
89
90
91
92
93
94

```

```

46 end
47
48
49 for el=1:e
50
51     elem=FibElem(el);
52     str_ele=num2str(elem); %gjør
53     elementnr. til en streng
54
55     MphiX_gravity
56     =load(fullfile(FolderGravity,strcat('MphiX_Gravity_',str_ele,'1.txt')));
57     %henter moment-krumning for element i
58     MphiY_gravity =
59     load(fullfile(FolderGravity,strcat('MphiY_Gravity_',str_ele,'1.txt')));
60     Axial_Gravity_file =load(fullfile(FolderGravity,strcat('N_Ele',str_ele,'.txt')));
61
62     axial_gravity=Axial_Gravity_file(end);
63     Ftime=load(fullfile(FolderMomentTime,strcat('M_Ele',str_ele,'.txt')));
64     %henter Eq-respons for element i
65
66
67
68
69
70
71
72
73
74
75
76
77
78
79
80
81
82
83
84
85
86
87
88
89
90
91
92
93
94

```

```

64 [maxmomentX, i_x]=max(abs(Ftime(:,6))); %Finner max absolutt-moment i tidsserien
65 [maxmomentY, i_y]=max(abs(Ftime(:,7)));
66
67 axial_x=Ftime(i_x,2);
68 axial_y=Ftime(i_y,2);
69 axial_ratio_x=axial_x/axial_gravity;
70 axial_ratio_y=axial_y/axial_gravity;
71 if elem<4500
72     if axial_ratio_x<=0.8
73         x1=0.6; x2=0.8;
74         MphiX1
75         =load(fullfile(FolderGravity,strcat('MphiX_Gravity_',str_ele,'06.txt')));
76         %henter moment-krumning for element i
77         MphiX2
78         =load(fullfile(FolderGravity,strcat('MphiX_Gravity_',str_ele,'08.txt')));
79
80     elseif axial_ratio_x>0.8 && axial_ratio_x<=1
81         x1=0.8; x2=1;
82         MphiX1
83         =load(fullfile(FolderGravity,strcat('MphiX_Gravity_',str_ele,'08.txt')));
84
85         MphiX2
86         =load(fullfile(FolderGravity,strcat('MphiX_Gravity_',str_ele,'11.txt')));
87
88     elseif axial_ratio_x>1 && axial_ratio_x<=1.2
89         x1=1; x2=1.2;
90         MphiX1
91         =load(fullfile(FolderGravity,strcat('MphiX_Gravity_',str_ele,'11.txt')));
92
93         MphiX2
94         =load(fullfile(FolderGravity,strcat('MphiX_Gravity_',str_ele,'14.txt')));
95
96     elseif axial_ratio_x>1.2
97         x1=1.2; x2=1.4;
98         MphiX1
99         =load(fullfile(FolderGravity,strcat('MphiX_Gravity_',str_ele,'14.txt')));
100
101         MphiX2
102         =load(fullfile(FolderGravity,strcat('MphiX_Gravity_',str_ele,'17.txt')));
103
104     end
105
106     if axial_ratio_y<=0.8;
107         y1=0.6; y2=0.8;
108         MphiY1
109         =load(fullfile(FolderGravity,strcat('MphiY_Gravity_',str_ele,'06.txt')));
110         %henter moment-krumning for element i
111         MphiY2
112         =load(fullfile(FolderGravity,strcat('MphiY_Gravity_',str_ele,'08.txt')));
113         %henter moment-krumning for element i

```

```

95     elseif axial_ratio_y>0.8 && axial_ratio_y<=1
96         y1=0.8; y2=1;
97         MphiY1
           =load(fullfile(FolderGravity, strcat('MphiY_Gravity_', str_ele, '08.txt')));
           %henter moment-krumning for element i
98         MphiY2
           =load(fullfile(FolderGravity, strcat('MphiY_Gravity_', str_ele, '1.txt')));
           %henter moment-krumning for element i
99     elseif axial_ratio_y>1 && axial_ratio_y<=1.2
100         y1=1; y2=1.2;
101         MphiY1
           =load(fullfile(FolderGravity, strcat('MphiY_Gravity_', str_ele, '1.txt')));
           %henter moment-krumning for element i
102         MphiY2
           =load(fullfile(FolderGravity, strcat('MphiY_Gravity_', str_ele, '12.txt')));
           %henter moment-krumning for element i
103     elseif axial_ratio_y>1.2
104         y1=1.2; y2=1.4;
105         MphiY1
           =load(fullfile(FolderGravity, strcat('MphiY_Gravity_', str_ele, '12.txt')));
           %henter moment-krumning for element i
106         MphiY2
           =load(fullfile(FolderGravity, strcat('MphiY_Gravity_', str_ele, '14.txt')));
           %henter moment-krumning for element i
107     end
108
109
110     if maxmomentX>=max(MphiX2(:,1))
111         Index_x=find(MphiX2(:,1)==max(MphiX2(:,1)),1);
112         disp('Moment høyere enn Mx-kappa');
113         break;
114     else
115         Index_x1=find(MphiX1(:,1)>maxmomentX, 1); %Finner tilhørende punkt
           på moment-krumning plott
116         Index_x2=find(MphiX2(:,1)>maxmomentX, 1);
117
118         [kappa_x1,M_x1] = polyxpoly([0 2e-3],[maxmomentX
           maxmomentX],[MphiX1(Index_x1,2)
           MphiX1(Index_x1-1,2)], [MphiX1(Index_x1,1) MphiX1(Index_x1-1,1)]);
119         [kappa_x2,M_x] = polyxpoly([0 2e-3],[maxmomentX
           maxmomentX],[MphiX2(Index_x2,2)
           MphiX2(Index_x2-1,2)], [MphiX2(Index_x2,1) MphiX2(Index_x2-1,1)]);
120
121         kappa_x=kappa_x2+(axial_ratio_x-x2)*(kappa_x1-kappa_x2)/(x1-x2);
122     end
123
124     if maxmomentY>=max(MphiY2(:,1))
125         Index_y=find(MphiY2(:,1)==max(MphiY2(:,1)),1);
126         disp('Moment høyere enn My-kappa');
127         break;
128     else
129         Index_y1=find(MphiY1(:,1)>maxmomentY, 1); %Finner tilhørende punkt på
           moment-krumning plott
130         Index_y2=find(MphiY2(:,1)>maxmomentY, 1);
131
132         [kappa_y1,M_y1] = polyxpoly([0 2e-3],[maxmomentY
           maxmomentY],[MphiY1(Index_y1,2)
           MphiY1(Index_y1-1,2)], [MphiY1(Index_y1,1) MphiY1(Index_y1-1,1)]);
133         [kappa_y2,M_y] = polyxpoly([0 2e-3],[maxmomentY
           maxmomentY],[MphiY2(Index_y2,2)
           MphiY2(Index_y2-1,2)], [MphiY2(Index_y2,1) MphiY2(Index_y2-1,1)]);
134
135         kappa_y=kappa_y2+(axial_ratio_y-y2)*(kappa_y1-kappa_y2)/(y1-y2);
136     end
137     fprintf(fid_testX,'%4.0f %5.2f %7.4e %7.4e %7.4e %7.4e
           \r\n',elem,axial_ratio_x,kappa_x1,kappa_x2,kappa_x,maxmomentX);
138 elseif elem < 4700
139     MphiX =load(fullfile(FolderMomentCurv, strcat('MphiX_4501.txt')));
           %henter moment-krumning for element i
140     MphiY =load(fullfile(FolderMomentCurv, strcat('MphiY_4501.txt')));
141     if maxmomentX>=max(MphiX(:,1))
142         Index_x=find(MphiX(:,1)==max(MphiX(:,1)),1);
143         disp('Moment høyere enn Mx-kappa');

```



```

144     else
145         Index_x=find(MphiX(:,1)>maxmomentX, 1);      %Finner tilhørende punkt på
moment-krumning plott
146         [kappa_x,M_x] = polyxpoly([0 1e-3],[maxmomentX
maxmomentX],[MphiX(Index_x,2) MphiX(Index_x-1,2)], [MphiX(Index_x,1)
MphiX(Index_x-1,1)]);
147     end
148
149     if maxmomentY>=max(MphiY(:,1))
150         Index_y=find(MphiY(:,1)==max(MphiY(:,1)),1);
151         disp('Moment høyere enn My-kappa');
152     else
153         Index_y=find(MphiY(:,1)>maxmomentY, 1);      %Finner tilhørende punkt på
moment-krumning plott
154         [kappa_y,M_y] = polyxpoly([0 1],[maxmomentY
maxmomentY],[MphiY(Index_y,2) MphiY(Index_y-1,2)], [MphiY(Index_y,1)
MphiY(Index_y-1,1)]);
155     end
156 else
157     MphiX =load(fullfile(FolderMomentCurv, strcat('MphiX_4701.txt')));
%henter moment-krumning for element i
158     MphiY =load(fullfile(FolderMomentCurv, strcat('MphiY_4701.txt')));
159     if maxmomentX>=max(MphiX(:,1))
160         Index_x=find(MphiX(:,1)==max(MphiX(:,1)),1);
161         disp('Moment høyere enn Mx-kappa');
162     else
163         Index_x=find(MphiX(:,1)>maxmomentX, 1);      %Finner tilhørende punkt på
moment-krumning plott
164         [kappa_x,M_x] = polyxpoly([0 1e-3],[maxmomentX
maxmomentX],[MphiX(Index_x,2) MphiX(Index_x-1,2)], [MphiX(Index_x,1)
MphiX(Index_x-1,1)]);
165     end
166
167     if maxmomentY>=max(MphiY(:,1))
168         Index_y=find(MphiY(:,1)==max(MphiY(:,1)),1);
169         disp('Moment høyere enn My-kappa');
170     else
171         Index_y=find(MphiY(:,1)>maxmomentY, 1);      %Finner tilhørende punkt på
moment-krumning plott
172         [kappa_y,M_y] = polyxpoly([0 1],[maxmomentY
maxmomentY],[MphiY(Index_y,2) MphiY(Index_y-1,2)], [MphiY(Index_y,1)
MphiY(Index_y-1,1)]);
173     end
174 end
175
176 EI_secX= M_x/kappa_x;
177 I_secX=EI_secX/(32.1e9);
178
179 EI_iniX= MphiX_gravity(2,1)/MphiX_gravity(2,2);
180 I_iniX=EI_iniX/(32.1e9);
181
182
183
184 ratioX=EI_secX/EI_iniX;
185
186 EI_secY= M_y/kappa_y;
187 I_secY=EI_secY/(32.1e9);
188
189 EI_iniY= MphiY_gravity(2,1)/MphiY_gravity(2,2);
190 I_iniY=EI_iniY/(32.1e9);
191
192
193
194 ratioY=EI_secY/EI_iniY;
195
196
197
198 %ratio=1-fact*(1-ratio1);
199 ratioX=forrige_ratioX(el)-fact*(forrige_ratioX(el)-ratioX);
200 ratioY=forrige_ratioY(el)-fact*(forrige_ratioY(el)-ratioY);
201
202 %konvegens
203

```

```
204 convX=abs( abs( ratioX )-abs( forrige_ratioX(el) ))/abs(forrige_ratioX(el));
205 convY=abs( abs( ratioY )-abs( forrige_ratioY(el) ))/abs(forrige_ratioY(el));
206
207 if convX>0.05 || convY>0.05
208     signal=signal*0; %blir null hvis ett eller flere av konvergenskravene er over
        terskel
209 end
210
211
212 fprintf(fidX,'%6.3f\r\n', ratioX);
213 fprintf(fidY,'%6.3f\r\n', ratioY);
214
215 fprintf(fid_compX,'%4.0f      %7.4f      %7.4f      %7.4f      %5.3f      %4.3f      %1.0f      %4.2f      %7.4e
%7.4e      %7.4e      \r\n', elem, I_iniX,I_secX,ratioX*I_iniX,ratioX,convX,signal,
axial_ratio_x,maxmomentX, kappa_x,axial_x);
216 fprintf(fid_compY,'%4.0f      %7.4f      %7.4f      %7.4f      %5.3f      %4.3f      %1.0f      %4.2f      %7.4e
%7.4e      %7.4e      \r\n', elem, I_iniY,I_secY,ratioY*I_iniY,ratioY,convY,signal,
axial_ratio_y,maxmomentY,kappa_y, axial_y);
217
218 end
219
220 for no=1:n
221     node=Node(no);
222     DtimeX=load(fullfile(FolderDynResultsTime, strcat('\Displacement\disp_Node_x_', num2str(
node), '.txt'))); %henter Eq-respons for node i
223     DtimeY=load(fullfile(FolderDynResultsTime, strcat('\Displacement\disp_Node_y_', num2str(
node), '.txt')));
224     AtimeX=load(fullfile(FolderDynResultsTime, strcat('\Acceleration\TotalAccel_Node_x_', nu
m2str(node), '.txt'))); %henter Eq-respons for node i
225     AtimeY=load(fullfile(FolderDynResultsTime, strcat('\Acceleration\TotalAccel_Node_y_', nu
m2str(node), '.txt')));
226     maxdispX=max(abs(DtimeX(:,2))); %Finner max absolutt-moment i tidsserien
227     maxdispY=max(abs(DtimeY(:,2)));
228     maxaccX=max(abs(AtimeX(:,2)));
229     maxaccY=max(abs(AtimeY(:,2)));
230     fprintf(fidDispAccX,'%6.2f      %6.2f\r\n', maxdispX, maxaccX);
231     fprintf(fidDispAccY,'%6.2f      %6.2f\r\n', maxdispY, maxaccY);
232
233
234 end
235
236 fclose(fidDispAccX);
237 fclose(fidDispAccY);
238
239 fclose(fidX);
240 fclose(fid_compX);
241 fclose(fidY);
242 fclose(fid_compY);
243
244 conv=['C:\Users\Tarjei\Documents\Gogldr\Masteroppgave,
Dynamikk_OpenSees\Scripts\Riss\Results_elastic\Section_', Eq_str, '\Ratio\conv.txt'];
245 fid_conv=fopen(conv, 'w');
246 fprintf(fid_conv, '%1.0f\r\n', signal);
247 fclose(fid_conv);
248
249 signal_path=['C:\Users\Tarjei\Documents\Gogldr\Masteroppgave,
Dynamikk_OpenSees\Scripts\Riss\Results_elastic\Section_', Eq_str, '\Ratio\signal.txt'];
250 fid_sig=fopen(signal_path, 'w');
251 fclose(fid_sig);
252 fprintf('Iteration %2.0f complete!\n', itr);
253
254 fclose('all');
255
256 end
```

